

EFFECTS OF FLOW REVERSAL ON TWO-DIMENSIONAL TRANSPORT OF EXPLOSIVE CHEMICALS IN SOILS

by

Juan Pablo Gutiérrez Marín

A thesis submitted in partial fulfillment of the requirements for the degree of

MASTER OF SCIENCE
in
CIVIL ENGINEERING
(Environmental and Water Resources Engineering)

UNIVERSITY OF PUERTO RICO
MAYAGÜEZ CAMPUS
May 2008

Approved by:

Ingrid Y. Padilla Cestero, PhD
President, Graduate Committee

Date

Sangchul Hwang, PhD
Member, Graduate Committee

Date

Miguel Pando, PhD
Member, Graduate Committee

Date

Christa von Hillebrandt, MSc
Representative of Graduate Studies

Date

Ismael Pagán Trinidad, MSCE
Director, Department of Civil Engineering and Surveying

Date

ABSTRACT

The effects of water infiltration and evaporation on the fate and transport of explosive-related chemicals (ERCs) in soils were studied. The experiments were conducted in two 100 cm uniform cylindrical columns packed with homogeneous sand, and instrumented with air and water pressure sensors and sampling ports to monitor hydraulic conditions and ERCs concentration profiles in soil. TNT and DNT crystals were placed in a porous membrane and buried as a point source near the surface of the soil. Infiltration of water containing a conservative tracer was followed by evaporation periods. Spatial and temporal concentration distributions of conservative solutes were used to evaluate transport behavior of TNT and DNT in soils. Results indicate that physical transport is spatially and temporally variable. Results also indicate that: water movement near TNT and DNT buried source highly influence their fate and transport in soils and near soil-atmospheric surfaces; water flux associated with higher water contents enhance source dissolution, volatilization, and movement of TNT and DNT solutes; flux-dependent dissolution kinetics control the TNT and DNT concentrations in soil water and vapor; sorption processes slows down the movement of solutes in infiltrating water; dissolution limitations and greater sorption and volatilization losses tend to decrease TNT and DNT concentrations with time after infiltration periods; greater water contents and temperatures result in enhance transport of TNT and DNT; reverse flow during infiltration and evaporation periods result in greater dispersion of solutes.

RESUMEN

Los efectos de la infiltración y de la evaporación del agua en el destino y el transporte de los compuestos químicos relacionados a explosivos (ERCs) en suelos fueron estudiados. Los experimentos fueron desarrollados en una columna cilíndrica uniforme de 100 cm de longitud empaçada con arena homogénea, y equipada con sensores de presión de aire y de agua y puntos de muestreo para monitorear las condiciones hidráulicas y los perfiles de concentraciones de ERCs en el suelo. Los cristales de TNT y DNT fueron localizados en una membrana porosa y se enterraron como fuente puntual cerca de la superficie del suelo. La infiltración del agua, la cual contiene un trazador conservativo, fue seguida por períodos de evaporación. Las distribuciones espaciales y temporales de la concentración de solutos conservadores fueron utilizadas para evaluar el comportamiento del transporte de TNT y del DNT en suelos. Los resultados indicaron que el transporte físico es variable espacial y temporalmente. Los resultados además indican que: el movimiento de agua alrededor de la fuente enterrada de TNT y DNT influye altamente su destino y transporte en suelos y cerca de las superficies suelo-atmósfera; el flujo de agua asociado con altos contenidos de agua mejora la disolución de la fuente, volatilización y movimiento de TNT y DNT; la flujo-dependencia de las cinéticas de disolución controlan las concentraciones de TNT y DNT en agua y vapor; los procesos de adsorción retardan el movimiento de los solutos en el agua infiltrada; limitaciones en la disolución y mayores pérdidas por adsorción y volatilización tienden a disminuir las concentraciones de TNT y DNT con el tiempo después de períodos de infiltración; mayores contenidos de agua y temperaturas resultan en la optimización del transporte de TNT y DNT; el reverso de flujo durante los períodos de infiltración y evaporación resultan en mayores dispersiones de los solutos.

Copyright © 2008 by Juan Pablo Gutiérrez Marín. All rights reserved. Printed in the United States of America. Except as permitted under the United States Copyright Act of 1976, no part of this publication may be reproduced or distributed in any form or by any means, or stored in a data base or retrieved system, without the prior written permission of the publisher.

“To my parents for their unconditional support,
for their confidence in my skills and dexterities.
To my God for be my guidance during my
decision-makings in my entire life. ”

ACKNOWLEDGEMENTS

This project was achieved thanks to God and to the contribution of many people who believed in me. I feel an immense debt with my graduate committee; Dr. Ingrid Padilla from who I have learned a lot, gained my complete admiration and was able to address my research and my studies with success, Dr. Sangchul Hwang, who was able to create an extraordinary confidence and an unconditional support and assistance in further the achievement of the research goals and my professional growth, and Dr. Miguel Pando who dedicated his valuable time to review the advance of my project and who supported its adequate performance.

To my friends and partners from the Environmental Engineering Laboratory, from the Civil Engineering and Surveying Department and other persons that supported and advised me during this time, full of happiness, hard work and sometimes despair, I want to recognize a big part of this achievement.

Especially I want to express gratitude to my beloved parents and to my sisters Sandra and Nati, who supported me since I decided to conduct my graduate studies faraway from home. They are the reason to be a better person and professional. I want to express my gratefulness to my girlfriend, Yisset, because of her entire support, dedication and unbelievable love. I am extremely thankful with Puertorrican people, because they extended their hands and received me so friendly in the Isla del Encanto. Finally, I want to thank to the Department of Defense from the United States, who supported this project been possible the culmination of my studies.

TABLE OF CONTENT

LIST OF TABLES	VIII
LIST OF FIGURES	IX
LIST OF APPENDIXES	XVII
LIST OF SYMBOLS AND ABBREVIATIONS	XVIII
1 INTRODUCTION	2
1.1 Justification.....	2
1.2 Objectives	5
2 LITERATURE REVIEW	6
2.1 Landmines	7
2.1.1 <i>Landmine Chemical Emissions</i>	9
2.2 Fate and Transport of ERCs in Soils	10
2.2.1 <i>Advective and Dispersive Transport</i>	11
2.2.1.1 Advection.....	11
2.2.1.2 Dispersion.....	13
2.2.2 <i>Mass Transfer and Reactive Processes</i>	17
2.2.2.1 Mass Transfer	18
2.2.2.2 Sorption	19
2.2.2.3 Transformations of TNT and DNT in Soils	21
2.3 Fate and Transport Equations for ERCs in Soils	23
2.4 Soil and Environmental Factors Affecting the ERCs Transport.....	25
2.4.1 <i>Temperature</i>	27
2.4.2 <i>Soil Water Content</i>	28
2.5 Modeling Transport of Explosives in Soil.....	30
3 METHODOLOGY.....	33
3.1 Experimental Setup	33
3.1.1 <i>Column Instrumentation</i>	38
3.1.1.1 Pressure Sensors	39
3.1.1.2 Temperature Sensors.....	42
3.1.1.3 Data Logger	43
3.2 Soil Properties	44
3.3 Transport Experiments	47
3.4 Environmental Conditions.....	52
3.5 Chemical Reagents and Analysis	53
3.5.1 <i>Reagents</i>	53
3.5.2 <i>Chemical Analysis</i>	54
3.5.3 <i>NaCl Concentrations</i>	54
3.5.4 <i>ERCs Concentrations</i>	55
3.5.4.1 Aqueous Standards Preparation	57
3.5.4.2 Vapor Standards Preparation	58
3.6 Microbial Analysis	58

3.7	Data Analysis.....	59
3.7.1	<i>Conservative Solute</i>	59
3.7.1.1	Numerical Simulation.....	61
3.7.1.1.1	Initial and Boundary Conditions.....	61
3.7.1.1.2	Parameters Optimization.....	62
4	RESULTS AND DISCUSSION.....	63
4.1	Pressures.....	63
4.2	Soil Hydraulic Properties.....	67
4.3	Soil-Water Contents.....	71
4.4	Soil-Water Flux.....	75
4.5	Breakthrough Curves.....	78
4.5.1	<i>NaCl BTCs</i>	78
4.5.2	<i>Aqueous TNT/DNT BTCs</i>	89
4.5.3	<i>Vapor TNT/DNT BTCs</i>	101
4.5.4	<i>Microbial Activity Test Realized during Experiment 4 (WC 0.28 and 25°C)</i>	106
4.5.5	<i>ERC Degradation</i>	107
4.6	NaCl Simulation.....	108
4.7	Integrated Discussion of Results.....	112
5	CONCLUSIONS.....	118
6	RECOMMENDATIONS.....	121
7	REFERENCES.....	123
	APPENDIXES.....	133

LIST OF TABLES

Table 1.	TNT and DNT Chemical Properties.....	18
Table 2.	Comparison of Solute Transport Simulation Codes.....	30
Table 3.	Calibration Equation used for Pressure Sensors.....	42
Table 4.	Physical Characteristics of Isabela Sand.....	44
Table 5.	Chemical Characteristics of Isabela Sand.....	44
Table 6.	Description of Experimental Conditions.....	48
Table 7.	Temporal Pressure Variations during Evaporation Periods for Ports 4 and 3.....	65
Table 8.	Estimated K_s from Steady-State Pressure Data for Saturated Flow Conditions.....	69
Table 9.	Soil Hydraulic Properties Obtained Using ROSETTA Computer Program.....	70
Table 10.	Water Flux from toward the End of Evaporation Period.....	78
Table 11.	Parameters Obtained from NaCl BTCs using the Method of Moments during Infiltration Process.....	83
Table 12.	Average of Pore Water Velocities and Effective Water Contents throughout the Column during Infiltration Process.....	84
Table 13.	TNT and DNT Mass Estimated from Moment Analyses of BTCs in Port 4.....	99
Table 14.	Vapor-Phase TNT and DNT Average Concentrations.....	103
Table 15.	Simulated Pressure Heads and Water Contents during Infiltration Process.....	109
Table 16.	Estimated Transport Parameters for NaCl during Infiltration Process.....	112

LIST OF FIGURES

Figure 1.	Landmines: Plastic and Metal	8
Figure 2.	Environmental Fate and Transport for Buried Landmines.....	10
Figure 3.	TNT Metabolism by Bacteria: Aerobic (a) and Anaerobic (b)	22
Figure 4.	Experimental Setup for Column 1 (a) and (b); and Setup for Column 2 (c)	34
Figure 5.	Simulation of Evaporation using Air Sweeping System	35
Figure 6.	Location of Water-Gas Samplers and Water-Gas Pressure Transducers for Column 1 (a) and Column 2 (b).	36
Figure 7.	Water and Gas Samplers	37
Figure 8.	Experimental Setup for Saturated during Infiltration (a) and Evaporation (b) Events; and for Unsaturated Conditions during Infiltration (c) and Evaporation (d) Events.	38
Figure 9.	Calibration Curves for Pressure Sensors	40
Figure 10.	Theoretical Pressure vs. Measured Pressure for Water Sensors.....	41
Figure 11.	Theoretical Pressure vs. Measured Pressure for Gas Sensors	41
Figure 12.	Calibration Curves for Thermocouples	42
Figure 13.	Data Logger Connections	43
Figure 14.	Particle Size Distribution for Isabela Sand.....	45
Figure 15.	Water Content Simulated in Hydrus 1D for Constant Flows of 2 (a), 10 (b), and 20 (c) mL/min.....	49
Figure 16.	Location of the Landmine in the Column of Soil.....	49
Figure 17.	Vapor Collection in a Septum Injector using SPME Fiber	52
Figure 18.	Sample Injection to Conductivity Detector	55
Figure 19.	Peak Simple Calibration for NaCl Concentration Determination	55
Figure 20.	Calibration Curves for Standards Prepared from TNT-DNT in Crystals (a) and TNT-DNT in Solutions in Acetonitrile	57
Figure 21.	Pressures during Infiltration (a) and Evaporation (b) Processes under Saturated Conditions at 25°C (Exp 3)	65
Figure 22.	Pressures during Infiltration (a) and Evaporation (b) Processes in the First Stage of the Experiment under Saturated Conditions at 35°C (Exp 6).....	65
Figure 23.	Pressures during Infiltration (a) and Evaporation (b) Processes in the Second Stage of the Experiment under Saturated Conditions at 35°C (Exp 6).....	66
Figure 24.	Pressures during Infiltration (a) and Evaporation (b) Processes under 75% of Saturation at 25°C (Exp 4).....	66
Figure 25.	Pressures during Infiltration (a) and Evaporation (b) Processes under 60% of Saturation at 25°C (Exp 7).....	66
Figure 26.	Pressures during Infiltration (a) and Evaporation (b) Processes under 60% of Saturation at 35°C (Exp 8).....	67
Figure 27.	Pressures during Infiltration (a) and Evaporation (b) Processes under 45% of Saturation at 25°C (Exp 5).....	67
Figure 28.	Total Hydraulic Heads vs Elevations	69
Figure 29.	Estimated SWCC for Isabela Sand.....	70
Figure 30.	Estimated non-Saturated Hydraulic Conductivities Function K(h) for Isabela Sand.....	71
Figure 31.	Soil Water Content at 25°C during: Infiltration Process for Exp 1 (a), Exp 2 (b), Exp 3 (c), Exp 4 (d), Exp 5 (e), Exp 7 (f); and Evaporation Process for Exp 1 (g), Exp 2 (h), Exp 3 (i), Exp 4 (j), Exp 5 (k), Exp 7 (l).....	74

Figure 32.	Soil Water Content at 35°C during: Infiltration Process for Exp 6 (a), Exp 8 (b); and Evaporation Process for Exp 6 (c), Exp 8 (d).....	75
Figure 33.	Total Hydraulic Heads during Infiltration (a) and Evaporation (b) Processes under 75% of Saturation at 25°C (Exp 4).....	76
Figure 34.	Total Hydraulic Heads during Infiltration (a) and Evaporation (b) Processes under 45% of Saturation at 25°C (Exp 5).....	76
Figure 35.	Total Hydraulic Heads during Infiltration (a) and Evaporation (b) Processes under 60% of Saturation at 25°C (Exp 7).....	77
Figure 36.	Total Hydraulic Heads during Infiltration (a) and Evaporation (b) Processes under 60% of Saturation at 35°C (Exp 8).....	77
Figure 37.	NaCl BTC during Infiltration (a) and Evaporation (b) Processes under Saturated Conditions at 25°C (Exp 3).....	80
Figure 38.	NaCl BTC during Infiltration (a) and Evaporation (b) Processes in the First Stage of the Experiment under Saturated Conditions at 35°C (Exp 6).....	81
Figure 39.	NaCl BTC during Infiltration (a) and Evaporation (b) Processes in the Second Stage of the Experiment under Saturated Conditions at 35°C (Exp 6).....	81
Figure 40.	NaCl BTC Arrival during Infiltration Process under Saturated Conditions at 25°C (Exp 3).....	87
Figure 41.	NaCl BTC Arrival (a) and Elution (b) during Infiltration Process under Saturated Conditions at 35°C (Exp 6).....	87
Figure 42.	NaCl BTC Arrival during Infiltration Process under 75% of Saturation at 25°C (Exp 4).....	87
Figure 43.	NaCl BTC Arrival (a) and Elution (b) during Infiltration Process under 60% of Saturation at 25°C (Exp 7).....	88
Figure 44.	NaCl BTC Arrival (a) and Elution (b) during Infiltration Process under 60% of Saturation at 35°C (Exp 8).....	88
Figure 45.	NaCl BTC Arrival (a) and Elution (b) during Infiltration Process under WC 0.17 at 25°C (Exp 5).....	88
Figure 46.	NaCl BTC Arrival in Port 4 during Infiltration Process under Different Water Contents at 25°C.....	89
Figure 47.	TNT _w BTC during Infiltration (a) and Evaporation (b) Processes under Saturated Conditions at 25°C (Exp 3).....	90
Figure 48.	DNT _w BTC during Infiltration (a) and Evaporation (b) Processes under Saturated Conditions at 25°C (Exp 3).....	90
Figure 49.	TNT _w BTC during Infiltration (a) and Evaporation (b) Processes under 75% of Saturation at 25°C (Exp 4).....	90
Figure 50.	DNT _w BTC during Infiltration (a) and Evaporation (b) Processes under 75% of Saturation at 25°C (Exp 4).....	91
Figure 51.	TNT _w (a) and DNT _w (b) BTCs during Infiltration Process under 60% of Saturation at 25°C (Exp 7).....	91
Figure 52.	DNT _w BTC during Infiltration Process under 60% of Saturation at 35°C (Exp 8).....	91
Figure 53.	TNT _w (a) and DNT _w (b) BTCs during Infiltration Process under 45% of Saturation at 25°C (Exp 5).....	92
Figure 54.	TNT _w vs. DNT _w during: Infiltration Process for Port 4 (a), Port 3 (b), Port 2 (c) and Port 1 (d); during Evaporation Process for Port 4 (e), Port 3 (f), Port 2 (g) and Port 1 (h), under Saturated Conditions at 25°C (Exp 3).....	94
Figure 55.	NaCl vs. TNT _w during Infiltration Process for Port 4 (a), Port 3 (b), Port 2 (c) and Port 1 (d), under 45% of Saturation at 25°C (Exp 5).....	96

Figure 56.	NaCl vs. DNT_W during Infiltration Process for Port 4 (a), Port 3 (b), Port 2 (c) and Port 1 (d), under 45% of Saturation at 25°C (Exp 5).....	96
Figure 57.	NaCl vs. TNT_W during: Infiltration Process for Port 4 (a), Port 3 (b), Port 2 (c) and Port 1 (d); during Evaporation Process for Port 4 (e), Port 3 (f), Port 2 (g) and Port 1 (h), under Saturated Conditions at 25°C (Exp 3).....	97
Figure 58.	NaCl vs. TNT_W during: Infiltration Process for Port 4 (a), Port 3 (b), Port 2 (c) and Port 1 (d) under Saturated Conditions at 25°C (Exp 3).....	99
Figure 59.	NaCl vs. TNT_W during: Infiltration Process for Port 4 (a), Port 3 (b), Port 2 (c), Port 1 (d) and Port 0 (e) in the Second Stage of the Experiment under Saturated Conditions at 35°C (Exp 6).....	100
Figure 60.	TNT_W vs. DNT_W during: Infiltration Process for Port 4 (a), Port 3 (b), Port 2 (c), Port 1 (d) and Port 0 (e), in the First Stage of the Experiment under Saturated Conditions at 35°C (Exp 6).....	101
Figure 61.	TNT_G (a) and DNT_G (b) BTCs during Evaporation Process under 45% of Saturation at 25°C (Exp 5).....	102
Figure 62.	DNT_W vs. DNT_G during Infiltration Process for Port 4 (a), Port 3 (b), Port 2 (c) and Port 1 (d) under 45% of Saturation at 25°C (Exp 5).....	104
Figure 63.	TNT_W vs. TNT_G during Infiltration Process for Port 3 (a), Port 2 (b) and Port 1 (c) under 45% of Saturation at 25°C (Exp 5).....	105
Figure 64.	TNT_G (a) and DNT_G (b) BTCs in the Surface of the Soil during Evaporation Process in the Second Stage of the Experiment under Saturated Conditions at 35°C (Exp 6).....	105
Figure 65.	DNT_W vs. DNT_G during Infiltration Process for Port 4 (a) and Port 3 (b), under 60% of Saturation at 35°C (Exp 8).....	106
Figure 66.	DNT_W vs. DNT_G BTC in the Surface of the Soil during Evaporation Process in the Second Stage of the Experiment under Saturated Conditions at 35°C (Exp 6).....	106
Figure 67.	Port 2 without (a) and with (b) initial addition of explosive solution (5 mg/L TNT-DNT).....	107
Figure 68.	Degradation on Soil Surface.....	107
Figure 69.	Explosives Chromatogram from Aqueous Phase Samples.....	108
Figure 70.	Simulated Pressure Heads for Saturated Conditions (a) and 60% of Saturation (b) at 25°C.....	109
Figure 71.	Simulated Water Contents for Saturated Conditions (a) and 60% of Saturation (b) at 25°C.....	110
Figure 72.	Measured vs Simulated Relative NaCl Concentrations Using Mobile-Immobile Model (MIM) for Saturated Conditions (a) and 60% of Saturation (b) at 25°C.....	111
Figure 73.	Pressures during Infiltration Process under Saturated Conditions at 25°C (Exp 1).....	134
Figure 74.	Total Hydraulic Heads during Infiltration Process under Saturated Conditions at 25°C (Exp 1).....	134
Figure 75.	NaCl BTC during Infiltration Process under Saturated Conditions at 25°C (Exp 1).....	135
Figure 76.	TNT_W BTC during Infiltration Process under Saturated Conditions at 25°C (Exp 1).....	135
Figure 77.	DNT_W BTC during Infiltration Process under Saturated Conditions at 25°C (Exp 1).....	135
Figure 78.	Pressures during Infiltration (a) and Reverse Flow (b) Processes under Saturated Conditions at 25°C (Exp 2).....	136
Figure 79.	Total Hydraulic Heads during Infiltration (a) and Reverse Flow (b) Processes under Saturated Conditions at 25°C (Exp 2).....	136
Figure 80.	NaCl BTC during Infiltration and Reverse Flow Processes under Saturated Conditions at 25°C (Exp 2).....	137

Figure 81.	TNT _w BTC during Infiltration and Reverse Flow Processes under Saturated Conditions at 25°C (Exp 2)	137
Figure 82.	Pressures during Infiltration (a) and Evaporation (b) Processes under Saturated Conditions at 25°C (Exp 3)	138
Figure 83.	Total Hydraulic Heads during Infiltration (a) and Reverse Flow (b) Processes under Saturated Conditions at 25°C (Exp 2)	138
Figure 84.	NaCl BTC during Infiltration (a) and Evaporation (b) Processes under Saturated Conditions at 25°C (Exp 3)	139
Figure 85.	TNT _w BTC during Infiltration (a) and Evaporation (b) Processes under Saturated Conditions at 25°C (Exp 3)	139
Figure 86.	DNT _w BTC during Infiltration (a) and Evaporation (b) Processes under Saturated Conditions at 25°C (Exp 3)	140
Figure 87.	NaCl vs. TNT _w during: Infiltration Process for Port 4 (a), Port 3 (b), Port 2 (c) and Port 1 (d); during Evaporation Process for Port 4 (e), Port 3 (f), Port 2 (g) and Port 1 (h), under Saturated Conditions at 25°C (Exp 3).....	141
Figure 88.	NaCl vs. DNT _w during: Infiltration Process for Port 4 (a), Port 3 (b), Port 2 (c) and Port 1 (d); during Evaporation Process for Port 4 (e), Port 3 (f), Port 2 (g) and Port 1 (h), under Saturated Conditions at 25°C (Exp 3).....	142
Figure 89.	TNT _w vs. DNT _w during: Infiltration Process for Port 4 (a), Port 3 (b), Port 2 (c) and Port 1 (d); during Evaporation Process for Port 4 (e), Port 3 (f), Port 2 (g) and Port 1 (h), under Saturated Conditions at 25°C (Exp 3).....	143
Figure 90.	Pressures during Infiltration (a) and Evaporation (b) Processes under 75% of Saturation at 25°C (Exp 4).....	144
Figure 91.	Total Hydraulic Heads during Infiltration (a) and Evaporation (b) Processes under 75% of Saturation at 25°C (Exp 4).....	144
Figure 92.	NaCl BTC during Infiltration (a) and Evaporation (b) Processes under 75% of Saturation at 25°C (Exp 4).....	145
Figure 93.	TNT _w BTC during Infiltration (a) and Evaporation (b) Processes under 75% of Saturation at 25°C (Exp 4).....	145
Figure 94.	DNT _w BTC during Infiltration (a) and Evaporation (b) Processes under 75% of Saturation at 25°C (Exp 4).....	145
Figure 95.	NaCl vs. TNT _w during: Infiltration Process for Port 4 (a), Port 3 (b), Port 2 (c) and Port 1 (d); during Evaporation Process for Port 2 (e) and Port 1 (f), under 75% of Saturation at 25°C (Exp 4).....	146
Figure 96.	NaCl vs. DNT _w during: Infiltration Process for Port 4 (a), Port 3 (b), Port 2 (c) and Port 1 (d); during Evaporation Process for Port 2 (e) and Port 1 (f), under 75% of Saturation at 25°C (Exp 4).....	147
Figure 97.	TNT _w vs. DNT _w during: Infiltration Process for Port 4 (a), Port 3 (b), Port 2 (c) and Port 1 (d); during Evaporation Process for Port 2 (e) and Port 1 (f), under 75% of Saturation at 25°C (Exp 4).....	148
Figure 98.	TNT _G (a) and DNT _G (b) BTCs during Evaporation Process under 75% of Saturation at 25°C (Exp 4).....	149
Figure 99.	Pressures during Infiltration (a) and Evaporation (b) Processes under 45% of Saturation at 25°C (Exp 5).....	150
Figure 100.	Total Hydraulic Heads during Infiltration (a) and Evaporation (b) Processes under 45% of Saturation at 25°C (Exp 5).....	150
Figure 101.	NaCl BTC during Infiltration Process under 45% of Saturation at 25°C (Exp 5).....	151

Figure 102.	TNT _W (a) and DNT _W (b) BTCs during Infiltration Process under 45% of Saturation at 25°C (Exp 5).....	151
Figure 103.	NaCl vs. TNT _W during Infiltration Process for Port 4 (a), Port 3 (b), Port 2 (c) and Port 1 (d), under 45% of Saturation at 25°C (Exp 5).....	152
Figure 104.	NaCl vs. DNT _W during Infiltration Process for Port 4 (a), Port 3 (b), Port 2 (c) and Port 1 (d), under 45% of Saturation at 25°C (Exp 5).....	153
Figure 105.	TNT _W vs. DNT _W during Infiltration Process for Port 4 (a), Port 3 (b), Port 2 (c) and Port 1 (d), under 45% of Saturation at 25°C (Exp 5).....	154
Figure 106.	TNT _G BTC during Infiltration (a) and Evaporation (b) Processes under 45% of Saturation at 25°C (Exp 5).....	154
Figure 107.	DNT _G BTC during Infiltration (a) and Evaporation (b) Processes under 45% of Saturation at 25°C (Exp 5).....	155
Figure 108.	TNT _W vs. TNT _G during Infiltration Process for Port 3 (a), Port 2 (b) and Port 1 (c) under 45% of Saturation at 25°C (Exp 5).....	155
Figure 109.	DNT _W vs. DNT _G during Infiltration Process for Port 4 (a), Port 3 (b), Port 2 (c) and Port 1 (d) under 45% of Saturation at 25°C (Exp 5).....	156
Figure 110.	Pressures during Infiltration (a) and Evaporation (b) Processes in the First Stage of the Experiment under Saturated Conditions at 35°C (Exp 6).....	157
Figure 111.	Total Hydraulic Heads during Infiltration (a) and Evaporation (b) Processes in the First Stage of the Experiment under Saturated Conditions at 35°C (Exp 6).....	157
Figure 112.	NaCl BTC during Infiltration (a) and Evaporation (b) Processes in the First Stage of the Experiment under Saturated Conditions at 35°C (Exp 6).....	158
Figure 113.	TNT _W BTC during Infiltration (a) and Evaporation (b) Processes in the First Stage of the Experiment under Saturated Conditions at 35°C (Exp 6).....	158
Figure 114.	DNT _W BTC during Infiltration (a) and Evaporation (b) Processes in the First Stage of the Experiment under Saturated Conditions at 35°C (Exp 6).....	159
Figure 115.	NaCl vs. TNT _W during: Infiltration Process for Port 4 (a), Port 3 (b), Port 2 (c), Port 1 (d) and Port 0 (e), in the First Stage of the Experiment under Saturated Conditions at 35°C (Exp 6).....	160
Figure 116.	NaCl vs. TNT _W during Evaporation Process for Port 4 (a), Port 3 (b), Port 2 (c) and Port 1 (d), in the First Stage of the Experiment under Saturated Conditions at 35°C (Exp 6).....	161
Figure 117.	NaCl vs. DNT _W during Infiltration Process for Port 4 (a), Port 3 (b), Port 2 (c), Port 1 (d) and Port 0 (e), in the First Stage of the Experiment under Saturated Conditions at 35°C (Exp 6).....	162
Figure 118.	NaCl vs. DNT _W during Evaporation Process for Port 4 (a), Port 3 (b), Port 2 (c) and Port 1 (d), in the First Stage of the Experiment under Saturated Conditions at 35°C (Exp 6).....	163
Figure 119.	TNT _W vs. DNT _W during Infiltration Process for Port 4 (a), Port 3 (b), Port 2 (c), Port 1 (d) and Port 0 (e), in the First Stage of the Experiment under Saturated Conditions at 35°C (Exp 6).....	164
Figure 120.	TNT _W vs. DNT _W during Evaporation Process for Port 4 (a), Port 3 (b), Port 2 (c) and Port 1 (d), in the First Stage of the Experiment under Saturated Conditions at 35°C (Exp 6).....	165
Figure 121.	TNT _G (a) and DNT _G (b) BTCs in the Surface of the Soil during Evaporation Process in the First Stage of the Experiment under Saturated Conditions at 35°C (Exp 6).....	165
Figure 122.	TNT _W vs. TNT _G BTC in the Surface of the Soil during Evaporation Process in the First Stage of the Experiment under Saturated Conditions at 35°C (Exp 6).....	166

Figure 123.	DNT _W vs. DNT _G BTC in the Surface of the Soil during Evaporation Process in the First Stage of the Experiment under Saturated Conditions at 35°C (Exp 6)	166
Figure 124.	Pressures during Infiltration (a) and Evaporation (b) Processes in the Second Stage of the Experiment under Saturated Conditions at 35°C (Exp 6).....	166
Figure 125.	Total Hydraulic Heads during Infiltration (a) and Evaporation (b) Processes in the Second Stage of the Experiment under Saturated Conditions at 35°C (Exp 6).....	167
Figure 126.	NaCl BTC during Infiltration (a) and Evaporation (b) Processes in the Second Stage of the Experiment under Saturated Conditions at 35°C (Exp 6).....	167
Figure 127.	TNT _W BTC during Infiltration (a) and Evaporation (b) Processes in the Second Stage of the Experiment under Saturated Conditions at 35°C (Exp 6).....	167
Figure 128.	DNT _W BTC during Infiltration (a) and Evaporation (b) Processes in the Second Stage of the Experiment under Saturated Conditions at 35°C (Exp 6).....	168
Figure 129.	NaCl vs. TNT _W during Infiltration Process for Port 4 (a), Port 3 (b), Port 2 (c), Port 1 (d) and Port 0 (e), in the Second Stage of the Experiment under Saturated Conditions at 35°C (Exp 6)	169
Figure 130.	NaCl vs. TNT _W during Evaporation Process for Port 4 (a), Port 3 (b), Port 2 (c) and Port 1 (d), in the Second Stage of the Experiment under Saturated Conditions at 35°C (Exp 6).....	170
Figure 131.	NaCl vs. DNT _W during Infiltration Process for Port 4 (a), Port 3 (b), Port 2 (c) and Port 1 (d), in the Second Stage of the Experiment under Saturated Conditions at 35°C (Exp 6).....	171
Figure 132.	NaCl vs. DNT _W during Evaporation Process for Port 4 (a), Port 3 (b), Port 2 (c) and Port 1 (d), in the Second Stage of the Experiment under Saturated Conditions at 35°C (Exp 6).....	172
Figure 133.	TNT _W vs. DNT _W during Infiltration Process for Port 4 (a), Port 3 (b), Port 2 (c), Port 1 (d) and Port 0 (e), in the Second Stage of the Experiment under Saturated Conditions at 35°C (Exp 6)	173
Figure 134.	TNT _W vs. DNT _W during Evaporation Process for Port 4 (a), Port 3 (b), Port 2 (c) and Port 1 (d), in the Second Stage of the Experiment under Saturated Conditions at 35°C (Exp 6).....	174
Figure 135.	TNT _G (a) and DNT _G (b) BTCs in the Surface of the Soil during Evaporation Process in the Second Stage of the Experiment under Saturated Conditions at 35°C (Exp 6).....	174
Figure 136.	TNT _W vs. TNT _G BTC in the Surface of the Soil during Evaporation Process in the Second Stage of the Experiment under Saturated Conditions at 35°C (Exp 6).....	175
Figure 137.	DNT _W vs. DNT _G BTC in the Surface of the Soil during Evaporation Process in the Second Stage of the Experiment under Saturated Conditions at 35°C (Exp 6).....	175
Figure 138.	Pressures during Infiltration (a) and Evaporation (b) Processes under 60% of Saturation at 25°C (Exp 7).....	176
Figure 139.	Total Hydraulic Heads during Infiltration (a) and Evaporation (b) Processes under 60% of Saturation at 25°C (Exp 7).....	176
Figure 140.	NaCl BTC during Infiltration Process under 60% of Saturation at 25°C (Exp 7).....	177
Figure 141.	TNT _W (a) and DNT _W (b) BTCs during Infiltration Process under 60% of Saturation at 25°C (Exp 7).....	177
Figure 142.	NaCl vs. TNT _W during Infiltration Process for Port 4 (a), Port 3 (b), Port 2 (c) and Port 1 (d), under 60% of Saturation at 25°C (Exp 7).....	178
Figure 143.	NaCl vs. DNT _W during Infiltration Process for Port 4 (a), Port 3 (b), Port 2 (c) and Port 1 (d), under 60% of Saturation at 25°C (Exp 7).....	179

Figure 144.	TNT _w vs. DNT _w during Infiltration Process for Port 4 (a), Port 3 (b), Port 2 (c) and Port 1 (d), under 60% of Saturation at 25°C (Exp 7).....	180
Figure 145.	TNT _G (a) and DNT _G (b) BTCs during Evaporation Process under 60% of Saturation at 25°C (Exp 7).....	180
Figure 146.	Pressures during Infiltration (a) and Evaporation (b) Processes under 60% of Saturation at 35°C (Exp 8).....	181
Figure 147.	Total Hydraulic Heads during Infiltration (a) and Evaporation (b) Processes under 60% of Saturation at 35°C (Exp 8).....	181
Figure 148.	NaCl BTC during Infiltration Process under 60% of Saturation at 35°C (Exp 8).....	182
Figure 149.	DNT _w BTC during Infiltration Process under 60% of Saturation at 35°C (Exp 8).....	182
Figure 150.	NaCl vs. DNT _w during Infiltration Process for Port 4 (a) and Port 3 (b), under 60% of Saturation at 35°C (Exp 8).....	182
Figure 151.	TNT _G (a) and DNT _G (b) BTCs during Infiltration Process under 60% of Saturation at 35°C (Exp 8).....	183
Figure 152.	TNT _G (a) and DNT _G (b) BTCs during Evaporation Process under 60% of Saturation at 35°C (Exp 8).....	183
Figure 153.	DNT _w vs. DNT _G during Infiltration Process for Port 4 (a) and Port 3 (b), under 60% of Saturation at 35°C (Exp 8).....	183
Figure 154.	TNT/DNT Water Calibration Curves for ECD Sensitivity 1 and Sensitivity 10.....	184
Figure 155.	TNT/DNT Water Calibration Curves for TSD Sensitivity 12.....	184
Figure 156.	TNT/DNT Gas Calibration Curves for ECD Sensitivity 1.....	185
Figure 157.	Simulated Pressure Heads (a) and Water Contents (b) for Saturated Conditions at 25°C (N1=Port 5, N2=Port 4, N3=Port 3, N4=Port 2, N5=Port 1, and N6=Port 0).....	187
Figure 158.	Measured vs Simulated Relative NaCl Concentrations Using Mobile-Immobile Model (MIM) for Saturated Conditions at 25°C (For Simulated Data: N1=Port 5, N2=Port 4, N3=Port 3, N4=Port 2, N5=Port 1, and N6=Port 0; For Experimental Data: C13=Port 4, C15=Port 3, C17=Port 2, C19=Port 1, and C21=Port 0).....	188
Figure 159.	Simulated Pressure Heads (a) and Water Contents (b) for 75% of Saturation at 25°C (N1=Port 5, N2=Port 4, N3=Port 3, N4=Port 2, N5=Port 1, and N6=Port 0).....	190
Figure 160.	Measured vs Simulated Relative NaCl Concentrations Using Mobile-Immobile Model (MIM) for 75% of Saturation at 25°C (For Simulated Data: N2=Port 4, N3=Port 3, N4=Port 2, N5=Port 1, and N6=Port 0; For Experimental Data: C13=Port 4, C15=Port 3, C17=Port 2, C19=Port 1, and C21=Port 0).....	191
Figure 161.	Simulated Pressure Heads (a) and Water Contents (b) for 45% of Saturation at 25°C (N1=Port 5, N2=Port 4, N3=Port 3, N4=Port 2, N5=Port 1, and N6=Port 0).....	193
Figure 162.	Measured vs Simulated Relative NaCl Concentrations Using Mobile-Immobile Model (MIM) for 45% of Saturation at 25°C (For Simulated Data: N2=Port 4, N3=Port 3, N4=Port 2, N5=Port 1, and N6=Port 0; For Experimental Data: C13=Port 4, C15=Port 3, C17=Port 2, C19=Port 1, and C21=Port 0).....	194
Figure 163.	Simulated Pressure Heads (a) and Water Contents (b) for Saturated Conditions at 25°C (N1=Port 5, N2=Port 4, N3=Port 3, N4=Port 2, N5=Port 1, and N6=Port 0).....	196
Figure 164.	Measured vs Simulated Relative NaCl Concentrations Using Mobile-Immobile Model (MIM) for Saturated Conditions at 25°C (For Simulated Data: N2=Port 4, N3=Port 3, N4=Port 2, N5=Port 1, and N6=Port 0; For Experimental Data: C13=Port 4, C15=Port 3, C17=Port 2, C19=Port 1, and C21=Port 0).....	197
Figure 165.	Simulated Pressure Heads (a) and Water Contents (b) for 60% of Saturation at 25°C (N1=Port 5, N2=Port 4, N3=Port 3, N4=Port 2, N5=Port 1, and N6=Port 0).....	199

Figure 166.	Measured vs Simulated Relative NaCl Concentrations Using Mobile-Immobile Model (MIM) for 60% of Saturation at 25°C (For Simulated Data: N2=Port 4, N3=Port 3, N4=Port 2, N5=Port 1, and N6=Port 0; For Experimental Data: C13=Port 4, C15=Port 3, C17=Port 2, C19=Port 1, and C21=Port 0)	200
Figure 167.	Simulated Pressure Heads (a) and Water Contents (b) for 60% of Saturation at 35°C (N1=Port 5, N2=Port 4, N3=Port 3, N4=Port 2, N5=Port 1, and N6=Port 0).....	202
Figure 168.	Measured vs Simulated Relative NaCl Concentrations Using Mobile-Immobile Model (MIM) for 60% of Saturation at 35°C (For Simulated Data: N2=Port 4, N3=Port 3, N4=Port 2, N5=Port 1, and N6=Port 0; For Experimental Data: C13=Port 4, C15=Port 3, C17=Port 2, C19=Port 1, and C21=Port 0)	203

LIST OF APPENDIXES

Appendix A. Graphs Obtained from Experimental Data	134
Appendix B. TNT/DNT Water Calibration Curves	184
Appendix C. TNT/DNT Gas Calibration Curves	185
Appendix D. Mass Balance Information for Inverse Solution Results from NaCl Transport at Saturated Conditions and 25°C (Exp 3).....	186
Appendix E. Mass Balance Information for Inverse Solution Results from NaCl Transport at 75% of Saturation and 25°C (Exp 4)	189
Appendix F. Mass Balance Information for Inverse Solution Results from NaCl Transport at 45% of Saturation and 25°C (Exp 5)	192
Appendix G. Mass Balance Information for Inverse Solution Results from NaCl Transport at Saturated Conditions and 35°C (Exp 6).....	195
Appendix H. Mass Balance Information for Inverse Solution Results from NaCl Transport at 60% of Saturation and 25°C (Exp 7)	198
Appendix I. Mass Balance Information for Inverse Solution Results from NaCl Transport at 60% of Saturation and 35°C (Exp 8)	201
Appendix J. Pressure and Temperature Sensors Wiring Diagram for Data Logger and Multiplexer	204

LIST OF SYMBOLS AND ABBREVIATIONS

BEDs	-	buried explosives devices
BTC	-	breakthrough curve
CDE	-	convection-dispersion equation
DNT	-	2,4 dinitrotoluene
ECD	-	electron capture detector
ERCs	-	explosive related chemicals
GC	-	gas chromatography
HPLC	-	high pressure liquid chromatography
ID	-	internal diameter
mg/L	-	miligram(s) per liter
MIM	-	mobile-immobile model
mL	-	milliliter(s)
mL/min	-	mililiter(s) per minute
mM	-	milimolar
MOM	-	method of moments
ppm	-	part per million
SC	-	specific conductance
SPME	-	solid phase micro extraction
SWCC	-	soil-water characteristic curve
SS	-	stainless steel
TSB	-	tryptic soy broth
TNT	-	2,4,6 trinitrotoluene
TSD	-	thermionic specific detector
UXO	-	unexploded ordnance
µg/L	-	microgram(s) per liter

1 INTRODUCTION

The use and production of conventional weapons such as buried explosive devices (BEDs) in military conflicts and training results in the release of weapon-related chemicals into the environment. Some of these chemicals pose detrimental effects to the environment and public health (Massol et al., 2005; US EPA, 2002). It is, therefore, imperative to effectively detect explosive-related contaminants, and remove them from the environment. Fate and transport processes control the mobility and persistence of these contaminants, and ultimately influence detection and remedial actions.

Assertive detection of explosive-related chemicals (ERCs) from BEDs is also of great importance to ensure safety of military personnel, civilian population, and the environment. Chemical, biological, and infrared detection require the presence of ERCs near the soil-atmospheric surface. The presence of ERCs near the surface depends on source characteristics and on fate and transport processes that affect their movement in soils.

The dynamics of fate and transport of ERCs in soils is complex, involving multiple interrelated processes that vary with environmental conditions. To adequately predict the concentration distribution in soils and near soil surfaces, it is necessary to have accurate knowledge of the dynamic behavior of these processes under variable environmental conditions.

1.1 Justification

Contamination of soils and groundwater with ERCs results from: the release of munition constituents from blast particles during training and testing; munitions disposal/burial sites

associated with military ranges and munition storage sites; deterioration of unexploded ordnance (UXO); open burning and detonation of ordnance; and wastewater contaminated with explosive compounds during ordnance production (US EPA, 2002). ERCs also enter the soil environment through leakage of casing material and cracks in BEDs, and from desorption of chemicals from contaminated surfaces (Leggett et al., 2000 and 2001). Predominate analyte emitted from many BEDs include 2,4,6-Trinitrotoluene (TNT) and 2,4-Dinitrotoluene (Leggett et al., 2001).

Once in the soil environment, TNT and DNT move in soil by advection, dispersion, and diffusion processes. Advection, dispersion, and solute diffusion in the water phase dominate transport during wet conditions, whereas gas-phase diffusion control their movement at low water contents during dry conditions (Anaya et al., 2007; Torres et al., 2007). The mobility and persistence of ERCs in soils are also influenced by retention, mass transfer and degradation processes (Comfort et al., 1995; Miyares and Jenkins, 2000; Phelan and Webb, 2002; Phelan et al., 2001; Price et al., 2002; Pennington and Patrick, 1990).

Fate and transport processes are influenced by soil and environmental conditions, including rainfall, atmospheric pressure, wind, relative humidity, temperature, water content, plant coverage, sun light, and soil type (Anaya et al., 2007). These conditions are dynamic and interrelated (i.e., not independent variables). They influence hydrologic and biological processes, such as infiltration, plant growth, and evapotranspiration, which further affect the net transport of water in soils. Any variable permutation of these processes result in magnitude and directional changes on water flow, which controls the advective and dispersive transport of ERCs in soils (Webb et al., 1999; Webb and Phelan, 2000).

Accurate knowledge of ERCs fate and transport is necessary to assess contamination potential to: protect drinking water supplies from toxic contaminants; develop remediation strategies; and facilitate the detection of buried explosives. Although studies have been conducted to assess and quantify the fate and transport behavior of ERCs in soils (Comfort et al. 1995; Hawari et al. 2000; Pennington and Patrick, 1990; Phelan et al., 2000; Dontsova et al., 2006) most of the experimental work has focused on simplistic and non-variable conditions and have not looked at the effect of interrelated (i.e., not independent) factors that vary in space and time (Phelan et al., 2000). Few studies have been conducted to evaluate the effect of variable environmental conditions on the fate and transport of ERC point sources near the soil-atmospheric surface, such as those emanating from buried landmines and UXO (Anaya et al., 2007). Limited studies have been conducted to evaluate the effect of flow reversal in the fate and transport of ERCs through variable-saturated porous media (Phelan et al., 2000 and 2001; Havis et al., 1992; Wildenschild and Jensen, 1999). Numerical model studies (Webb et al., 1998 and 1999; Phelan and Webb, 1997) have concentrated on the average response of transport parameters, but have not been validated with data. A need, thus, exists to (1) develop a physical experimental platform that will generate accurate data and information on the effect of interrelated environmental factors on the fate and transport ERCs in soil, and (2) evaluate the effect of flow reversal during infiltration and evaporation events on the fate and transport of ERCs in soils.

1.2 Objectives

The general goal is to characterize and quantify the effect of interrelated environmental and soil factors on the fate and transport of TNT and DNT, emanating from buried point sources. The specific objectives are to:

- Determine the fate and transport behavior of TNT and DNT in soil under different conditions of temperature and water content, when subjected to infiltration and evaporation events.
- Determine the effect of flow reversal caused by infiltration and evaporation processes on the fate and transport behavior of tracer solutes and TNT and DNT in soils.
- Estimate the dispersion coefficient and the average solute velocity as a function of environment conditions.

2 LITERATURE REVIEW

ERCs may enter the soil environment from poor disposal and waste management practices at ammunition production facilities (Comfort et al., 1995; Pennington and Patrick, 1990) and/or through chemical leakage and detonation of explosives devices, such as landmines and UXO (Cragin and Leggett, 2003; Leggett et al., 2000 and 2001; Jenkins et al., 1999 and 2001). In fact, chemical detection of landmines and UXO rely on the emissions of signatures from these devices (Jenkins et al., 1999; Cragin and Leggett, 2003; Leggett et al., 2001; Phelan and Webb, 1998 and 2002). Chemical entry of ERCs into the soil environment from these devices occurs as single or multiple point sources.

Once in the soil environment, ERCs may migrate as dissolved solutes and vapors, undergo physiochemical reactions (e.g., sorption, precipitation), and be transformed to other forms (Brannon et al., 1999; Comfort et al., 1995; Phelan and Webb, 2002; Petersen et al., 1996; Price et al., 2002). Their fate and transport in soils depend on advective, dispersive, sorptive, mass transfer, and transformations processes.

Fate and transport processes of ERCs in soils are interrelated with each other and are influenced by environmental factors (Anaya et al., 2007). Accurate knowledge of the fate and transport behavior and their variations with environmental conditions is necessary to effectively predict the spatial and temporal concentration distribution of ERCs in soils.

Numerical models have been developed and applied to describe and predict the fate and transport behavior of ERCs in soils (Webb et al., 1998 and 1999; Dontsova et al., 2006).

Accuracy of model predictions, however, depends on the certainty of fate and transport parameter values.

This study aims to determine the effect of environmental variables on the fate and transport behavior of ERCs emanating from point sources, such as landmines. This chapter provides a review of previous work found in the literature on: landmines and their chemical signatures; fate and transport of ERCs in soils; soil and environmental factors affecting the fate and transport of ERCs in soils; and numerical modeling of ERC fate and transport in soils.

2.1 Landmines

Landmines are explosive devices placed on or below the land surface and designed to explode when triggered (Keeley, 2006). Hundreds of millions of landmines have been abandoned in more than 60 countries, becoming a threat to the human safety, health and environment (Yoshikawa et al., 2002).

Landmines are composed of a triggered mechanism, a detonator or ignitor, main and booster charge, and the casing (Keeley, 2006). The composition of land mines is variable, ranging from those that contain a significant amount of metal (a metal case filled with explosive) to those that are essentially all dielectric (a plastic case filled with explosive) (Bourgeois and Smith, 1998). In Colombia, the majority of the antipersonnel mines are artisan, made with wood, lamina of steel, plastic and PVC. The artisan mines are the best option to decimate the adversary in an irregular conflict and their cost adjusts easily to the low budget of this type of combatant.

The antipersonnel mines are not easy to see, and are buried, hidden in the scrubs, and placed in the trees or in the middle of water (Unicef, 2007).



Figure 1. Landmines: Plastic and Metal

Source: Sandia National Laboratories, 2007.
Rensselaer Polytechnic Institute, 2007.

The main charge contains explosive chemicals. Approximately 80% of mines manufactured in the world contain TNT or mixtures of explosives containing TNT (Fisher and Cumming, 2001; Cumming et al. 2001). The mass of TNT contained in these mines ranges from as little as 7 grams up to 13 kilograms. This mass of TNT produces vapors of signature compounds that can be released into the soil for decades (Cumming et al., 2001). TNT is manufactured by nitration of toluene with a nitric acid solution. The toluene is derived from the distillation of crude oil, and may have impurities such as benzene. The synthesis process favors the production of TNT, but other isomers (chemicals with same molecular formula, but with different structures) can be formed in smaller quantities. Different TNT production and purification processes will produce different amounts of isomeric impurities (Phelan and Webb, 2002). Of the ERCs found in TNT, the most prevalent found in the vapor phase include TNT, DNT, 2,6-

DNT, 1,3-Dinitrobenzene, and 1,3,5-Dinitrobenzene (Fisher and Cumming, 2001; Pennington et al. 2003).

2.1.1 Landmine Chemical Emissions

Transfer of landmine chemicals to soil involves both leakage and permeation (both together are termed landmine flux). Leakage occurs through openings in the case. Leakage is the rate at which gases or vapors pass through an opening or crack. Permeation occurs by vapor diffusion through the thickness of the polymeric material. It does not happen through metal such as steel (Phelan and Webb, 2002). Some mines have small holes, which allow vapors a direct escape path to the soil. These openings also provide a path for direct contact of the explosive main charge package with water, such as with an extended rainfall, which can release a large amount of chemicals to the soil (Phelan and Webb, 2002).

Due to the different kind of landmines, the chemical emissions to the environment are variable. Landmine signature chemicals are released into the soil through surface contamination of landmine cases, by vapor phase diffusion of chemical through the mine casing material, and by leakage through cracks, seams and holes in the mine (Fisher and Cumming, 2001). Flux varies for different casing materials and compounds. Higher vapor fluxes have been reported when temperature increases, ranging from 10^{-3} to 10^0 $\mu\text{g}/\text{mine-d}$ for TNT and from 10^{-1} to 10^1 $\mu\text{g}/\text{mine-d}$ for DNT, for a temperature range between -3 to 34°C (Leggett et al., 2001). Higher DNT and TNT emission flux have been observed for mines submerged in water (10^0 and 10^2 $\mu\text{g}/\text{mine-d}$ at 21.5°C) than exposed to the gas phase (10^{-2} and 10^1 $\mu\text{g}/\text{mine-d}$ at 21.5°C) for two types of mines (PMA2 and PPM2) (Cragin and Leggett, 2003).

2.2 Fate and Transport of ERCs in Soils

The mobility and persistence of ERCs in soils are controlled by fate and transport processes (Figure 2) involving advection, dispersion, mass transfer, and various reactions (Brannon et al., 1999; Comfort et al., 1995; Phelan and Webb, 2002). Advective and dispersive processes relate to the movement of the chemicals with and within the bulk fluids (water, air), and control the direction and magnitude of this movement. Chemical, physical, and biological reactive processes influence the fate of the chemicals and overall transport. These processes include sorption, precipitation, and transformations. Mass transfer among available environmental compartments (e.g., water, air, organic matter, air-water interface) could strongly influence the rate at which ERCs move in the soil.

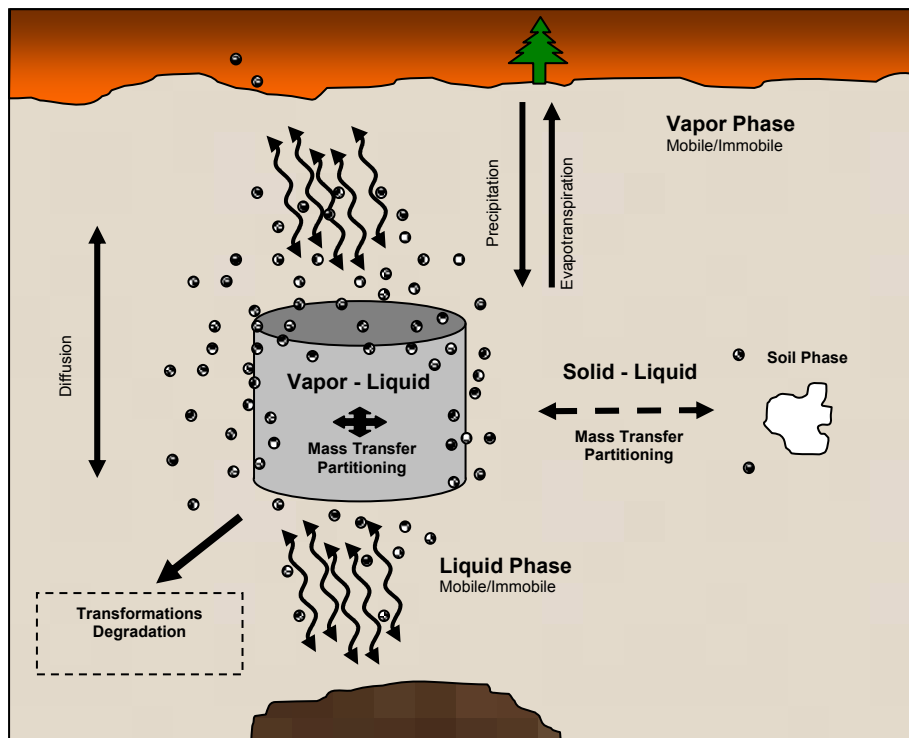


Figure 2. Environmental Fate and Transport for Buried Landmines

2.2.1 Advective and Dispersive Transport

The movement of ERCs in soils is governed by advective and dispersive transport process occurring in the water and gaseous phases. This movement is influenced by soil properties and conditions, as well as flow, chemical sources/sinks, and boundary conditions (e.g., rainfall, infiltration, evaporation, boundary flux). Soil water content and flux, which are controlled by infiltration, redistribution, and evaporation processes, have been found to significantly influence advective and dispersive transport (Padilla et al., 1999; Vanderborght et al., 2000).

2.2.1.1 Advection

Advection describes the transport of a chemical with a flowing fluid (air or water) within the soil. It results in a bulk movement of the chemical in the direction of the fluid movement. Mathematically, chemical advection is described as the product of the chemical concentration (C) in the bulk fluid and the velocity of the fluid (v).

The velocity of the fluid in porous media depends on hydraulic gradients (dh/dL) and the physical and hydraulic properties and conditions of the soil, including hydraulic conductivities ($K_{x,y,z}$), porosity (n), and the water content (θ_w). The advecting velocity is commonly described with Darcy's Law (Fetter, 1999):

$$q = -K \frac{dh}{dL} \quad [1]$$

where h is the hydraulic head ($h=z+P$), z is the elevation above the bottom, P is the pressure head and L is the length.

In unsaturated soil, soil-water pressure and hydraulic conductivities are a function of water content. The functional relationship between pressure heads and water content is given by the water characteristic curve (WCC), which is described by a number of functional forms (Jury and Horton, 2004; Bachmann et al., 2002). Among the most commonly functional forms used to relate water content, hydraulic conductivity, and soil-water pressure, are the van Genuchten functions:

$$\theta(h) = \theta_r + \frac{\theta_s - \theta_r}{\left(1 + |\alpha h_c|^n\right)^m} \quad [2]$$

$$K(h_c) = K_s \theta^{1/2} \left[1 - \left(1 - \theta^{1/m}\right)^m\right]^2 \quad [3]$$

The pressure head in unsaturated soil is related to the capillary, or soil-water pressure (P_c),

$$h_c = \frac{P_c}{\rho_w g} = \frac{2\sigma_{lg} \cos(\varphi)}{r\rho_w g} \quad [4]$$

where σ_{lg} is the surface tension of the liquid–gas interface tension; φ is the contact angle; r is the average radius of the liquid–gas interface; θ is the volumetric water content; θ_r is the irreducible minimum water content; θ_s is the volumetric water content at saturation; h_c is the pressure head or matric potential; n , m and α are van Genuchten soil parameters; $K(\theta)$ is the unsaturated hydraulic conductivity at water content (θ); and K_s is the saturated hydraulic conductivity.

Unsaturated water flow in one-dimension is described by applying Darcy’s Law into the continuity equation, resulting in Richards’s equation (Jury and Horton, 2004):

$$\frac{\partial \theta}{\partial t} = \frac{\partial}{\partial z} \left[K(h) \left(\frac{\partial h}{\partial z} + 1 \right) \right] \quad [5]$$

where h is the total hydraulic head ($h_T = z + P_c$), z is the elevation above the bottom, P_c is the pressure head and L is the length.

2.2.1.2 Dispersion

Dispersion is a general term applied to the observed spreading of a chemical plume and results in movement of chemicals from areas of high concentration to low concentrations. It is generally attributed to mechanical dispersion and molecular diffusion. Dispersion processes occur in both the water and gaseous phase. Molecular diffusion controls the dispersive processes at very low water contents and limited flow conditions, whereas mechanical dispersion dominates under advective conditions.

Molecular diffusion is caused by random movement of particles in a fluid, and it is commonly described by Fick's first Law (Fetter, 1999):

$$F = -D_d \left(\frac{dC}{dx} \right) \quad [6]$$

where F is the mass flux of solute per unit area per time; D_d is the diffusion coefficient, C is the solute concentration and x is the length.

In porous media, molecular diffusion is restricted by the tortuous path forced by the solids. To account for this, an effective diffusion coefficient, D^* , must be used (Fetter, 1999). D^* is a function of water content and the soil media. Generally, aqueous molecular diffusion controls transport processes under limited water flow conditions. Gaseous molecular diffusion controls the transport of volatile (or semi-volatile) compounds under limited flow or low water contents (Torres et al., 2007). For volatile organic compounds, such as trichloroethylene (TCE), vapor-

phase diffusion is an important transport mechanism. Choi et al. (2002) developed a series of field measurements and computer simulations in order to compare diffusion and advection fluxes at a TCE-contaminated field site at Picatinny Arsenal in northcentral New Jersey. In agreement with the solute transport simulations, TCE vapors are transported by advection and diffusion at essentially all times for all the simulation events, but the magnitude of the advective flux was usually small compared to that of the diffusive flux. Diffusive vapor transport of ERCs in unsaturated soil is limited due to their low vapor pressure (Phelan and Webb, 2002), but it is the controlling transport mechanism in low water contents (Grifoll et al., 2005; Phelan and Webb, 2002; Torres et al., 2007).

Mechanical dispersion is a macroscopic spreading caused by the multiple variations in flow path velocity and tortuosity (McGrath, 1995). It generally results in chemicals moving from high to low concentrations and, like diffusion, is commonly described by Fick's Law (Fetter, 1999). Assuming that the amount of mechanical dispersion is a function of the average linear pore-water velocity (v), a coefficient of mechanical dispersion, D_m^* , can be defined longitudinally (direction of flow) and transversally (perpendicular to flow):

$$\text{Coefficient of longitudinal mechanical dispersion} = \alpha_i v_i \quad [7]$$

where α_i is the dynamic dispersivity in the i direction and v_i is the average linear velocity in the i direction.

$$\text{Coefficient of transverse mechanical dispersion} = \alpha_j v_i \quad [8]$$

where α_j is the dynamic dispersivity in the j direction and v_i is the average linear velocity in the i direction.

The dispersivity is generally considered to be an intrinsic property of the media under fully saturated media, but has been shown to vary with water content for unsaturated media (Padilla et al. 1999). Porous media with greater heterogeneities is generally characterized by higher dispersivity values, reflecting velocity variations. The inclusion of greater amount of heterogeneities as the flow paths get longer has been related to the “scale effect of dispersion”, which results in greater dispersivity values as the scale of the average flow path is increased (Fetter, 1999). In unsaturated media, preferential flow path cause greater velocity variations (Šimůnek et al., 2003) and, thus, greater dispersivity values (Padilla et al., 1999; Porro et al., 1993). In the presence of large macropores, dispersivity values for a flux-average system were also a function of flow rates, with higher dispersivity at higher flow rates (Vanderborght et al., 2000). As with the saturated case, greater dispersivity values have been observed in unsaturated media as the scale of flow path length increases (Wierenga and van Genuchten, 1989).

Lower number of flow paths and greater velocity variation in unsaturated media may induce differential concentrations between low and high velocity flow paths and exchange of solutes between regions of high pore water velocities and comparatively immobile regions (Bond and Wierenga, 1990; Padilla et al., 1999). The immobile region may contain water that is stagnant, or it may contain water that is flowing much slower than that in the mobile region (Skaggs and Leij, 2002). Immobile water can affect the solute transport producing asymmetric breakthrough curves (BTCs) if the time to achieve a complete mixing is large compared with the

advection time for a determinate distance. In addition to earlier initial BTCs and tailing, the presence of immobile water results in greater dispersion of solutes (Bond and Wierenga, 1990). Strong evidence has been shown for the presence of immobile water fraction under steady state conditions but not under unsteady conditions (Bond and Wierenga, 1990). The amount of immobile water and exchange between mobile and immobile water depends on water content and flow (Padilla et al., 1999).

Advective (convective) and dispersive processes influence the transport of all chemicals in a system, but are generally characterized using non-reactive tracers. They are integrated mathematically in the convection-dispersion equation (CDE).

$$\frac{\partial \theta C}{\partial t} = \frac{\partial}{\partial z} \left(\theta D \frac{\partial C}{\partial z} \right) - \frac{\partial v \theta C}{\partial z} \quad [9]$$

Equation (9), which assumes that the transport of solutes has reached the Fickian regime, describes well the solute transport in homogeneous, fully saturated media at the scales generally studied (Padilla et al., 1999). Lower number of flow paths and greater velocity variation in unsaturated media, however, require greater flow path lengths before attaining the Fickian regime (Padilla et al., 1999; Roth and Hammel, 1996). As a result, solute transport may produce asymmetric BTCs and long effluent tailing and can not be adequately described by the CDE.

The mobile-immobile model (MIM) has been applied to describe transport behavior producing asymmetric BTCs (Bond and Wierenga, 1990; Padilla et al., 1999). The approach leads to a two-region convection-dispersion equation with a first-order solute-exchange process

between the mobile and immobile regions (van Genuchten and Wierenga, 1976; Wierenga and van Genuchten, 1989):

$$\theta_m \frac{\partial C_m}{\partial t} + \theta_{im} \frac{\partial C_{im}}{\partial t} = \theta_m D_m \frac{\partial^2 C_m}{\partial z^2} - \theta_m v_m \frac{\partial C_m}{\partial z} \quad [10]$$

$$\theta_{im} \frac{\partial C_{im}}{\partial t} = \alpha_{mim} (C_m - C_{im}) \quad [11]$$

where the subscripts m and im refer to mobile and immobile liquid phases, respectively, $D_m = D_h / \beta = (D - D_w \tau_w) / \beta$ (where β is mobile water fraction, θ_m/θ), v_m is mobile pore water velocity (where $v_m = q / \theta_m$), and α_{mim} is a first-order mass transfer coefficient which accounts for diffusion between the mobile and immobile water regions. Values for β have been reported to decrease as water content decreases in unsaturated systems (Padilla et al., 1999). The mass transfer coefficient has been related to the interfacial area between the two regions, volume and geometry of the immobile water, and velocity (e.g. Armstrong et al., 1994; Bajracharya and Barry, 1997). Notice that if $\theta_{im}=0$, equation (11) reduces to the CDE (equation 9) and will be referred to as the CDE equilibrium model; otherwise it is referred to as the non-equilibrium or MIM model.

2.2.2 Mass Transfer and Reactive Processes

In addition to advective and dispersive transport, the migration and persistence of ERCs in soils are influenced by mass transfer and physical, chemical, and biological reaction processes. Mass transfer among available environmental compartments (e.g., water, air, soil, organic matter, air-water interface) affects the rate at which ERCs move and react in the soil. Reactive processes

include sorption, dissolution, precipitation, and transformations. All of these processes influence the fate of the chemical and overall transport.

2.2.2.1 Mass Transfer

Once in the soil environment, ERCs may dissolve in soil-water, volatilize into soil-air, partition onto the soil and the environment compartments, including the soil-water interface. This requires a mass transfer between its initial state, and other available compartments in the soil. This mass transfer may be rate-limited (Torres et al., 2007) or may occur relatively rapid, reaching equilibrium.

Rate limited mass transfer has been reported for ERCs dissolution (Dontsova et al., 2006; Morley et al., 2006; Lynch et al., 2002), volatilization (Torres et al., 2007), and soil sorption (Dontsova et al., 2006). Mass transfer limitations result in tailing of chemical BTC, and time-dependent concentrations, which are below respective equilibrium concentrations.

Under equilibrium conditions, the maximum amount of solute dissolved in water is dictated by its solubility (S); whereas the maximum amount of vapor is dictated by the chemical's vapor pressure (P_v). TNT has lower solubility and vapor pressure than DNT (Table 1).

Table 1. TNT and DNT Chemical Properties

T (°C)	DNT			TNT		
	Solubility (mg/L) ^(a)	Vapor Pressure (mg/L) ^(b)	K_H	Solubility (mg/L) ^(a)	Vapor Pressure (mg/L) ^(b)	K_H
25	199.056	2.126E-03	1.068E-05	127.240	1.096E-04	8.610E-07
35	301.553	7.188E-03	2.384E-05	195.826	3.878E-04	1.980E-06

Source: (a) Phelan and Barnett, 2001.
(b) Pella, 1977.

Solubility and vapor pressure for both chemicals tend to increase with increasing temperature (Phelan and Webb, 2002). The ratio of the amount of chemicals that exist in the gas phase (C_g) to that in the aqueous phase (C_w) at equilibrium is given by Henry's constant (K_H) (Schwarzenbach et al., 2003).

$$K_H = \frac{C_g}{C_w} \quad [12]$$

K_H dictates the concentration in the gas and aqueous phases at equilibrium. It is also a function of temperature. K_H for DNT is greater than for TNT (Table 1).

The amount of chemical taken up or released by soil is controlled by sorption processes. Because of their complexity and variability, these processes are discussed below as a separate section.

2.2.2.2 Sorption

Sorption involves equilibrium and non-equilibrium interactions between ERCs solutes and vapors and the soil organic matter, mineral surface, and air-water interfaces (Costanza and Brusseau, 2000; Erikson and Skyllberg, 2001; Ravikrishna et al., 2002; Pennington and Patrick, 1990). Sorption processes are responsible for delaying the transport of ERCs, and concentrating ERCs around landmines (Jenkins et al., 2000; George et al., 1999). At equilibrium, soil-water sorption is described often by linear distribution coefficient (K_d , cm^3/g), defined as the ratio of chemical sorbed to the soil (C_s , $\mu\text{g}/\text{g}$) over than in water (C_w , $\mu\text{g}/\text{g}$) (Fetter, 1999):

$$K_d = \frac{C_s}{C_w} \quad [13]$$

Phelan and Barnett (2001) developed batch experiments in a soil mainly composed by sand, to determine TNT and DNT soil-water partitioning, and soil-vapor partitioning in soils. The results obtained suggested a linear adsorption coefficient for low concentrations (0.5-2 mg/L) and for higher concentrations (25-150 mg/L) suggested a Freundlich or Langmuir model. K_d fitted values were $0.9 \text{ cm}^3/\text{g}$ and $0.5 \text{ cm}^3/\text{g}$ for TNT and DNT, respectively. Pennington and Patrick (1990) developed batch TNT adsorption isotherms indicating that soil-water partitioning coefficient fits the Langmuir adsorption model having an average value of $4.0 \text{ cm}^3/\text{g}$ for all the soils used in the study. Sheremata et al. (1999) studied the sorption and desorption characteristics of TNT, using three soils. K_d values were different depending on the soil, being $6.38 \text{ cm}^3/\text{g}$ and $223.63 \text{ cm}^3/\text{g}$ for topsoil and illite, respectively. The topsoil was composed mainly of sand (83%) instead of illite which is 100% clay. Comfort et al. (1995) determined long-term sorption of TNT residues in soil using unsaturated soil columns containing uncontaminated soil and layers of contaminated and uncontaminated soils. They found that TNT sorption and degradation were concentration-dependent. Also they concluded that the assumptions of linear adsorption and adsorption-desorption might not be valid for predicting TNT transport in munitions-contaminated soils. Solid-vapor sorption (K_d') for TNT and DNT is strongly impacted by the soil moisture content with declining K_d' values exponentially by a factor of 100,000 as the soil moisture increase (Phelan and Barnett, 2001; Phelan et al., 2001).

In unsaturated soil, solutes may accumulate at the air-water interface (Costanza and Brusseau, 2000). Although this accumulation has been reported for volatile organic compounds (Costanza and Brusseau, 2000; Hoff et al., 1993 a,b), no studies have been found addressing the magnitude of ERC accumulation at the air-water interface.

2.2.2.3 Transformations of TNT and DNT in Soils

Transformation reactions include biotic and abiotic processes (Brannon et al., 1999; Hawari et al., 2000; Price et al., 2002), and are influenced by sorption, solute availability (Eriksson and Skyllberg, 2001), oxidation conditions (Pennington and Patrick., 1990), residence time, and other environmental factors, such as water content and soil type (Phelan and Webb, 2002). Biotic conditions significantly enhance TNT disappearance relative to disappearance under abiotic conditions (Myers et al., 1998).

Biotic transformation occurs under aerobic and anaerobic conditions (Figure 3), but studies suggest that the transformation rates are strongly dependent on the redox potential (Eh), with lower Eh values resulting in higher rates (Myers et al., 1998; Cattaneo et al., 2000). TNT degradation results in the formation of aminometabolites: 4-amino-2,6-dinitrotoluene (4ADNT), 2-amino-4,6-DNT (2ADNT), 2,4-diamino-6-nitrotoluene (2,4-DANT), 2,6-diamino-4-nitrotoluene (2,6-DANT) mainly due to the reductions of nitro moieties to amino groups (Myers et al., 1998; Cattaneo et al., 2000; Pennington et al., 2003). Reductive degradation of 2,4-DNT generates 4-methyl-3-nitroaniline (Pennington et al., 2003). TNT is reduced to monoamino transformation products under abiotic conditions (Brannon et al., 1997). Complete reduction to diamine byproducts occurs under anaerobic conditions (Pennington et al., 2003). Biodegradation of dinitrotoluene (2,4 -and 2,6- DNT) and aminometabolites (4ADNT and 2ADNT) also produces nitrate and nitrite (Cattaneo et al., 2000).

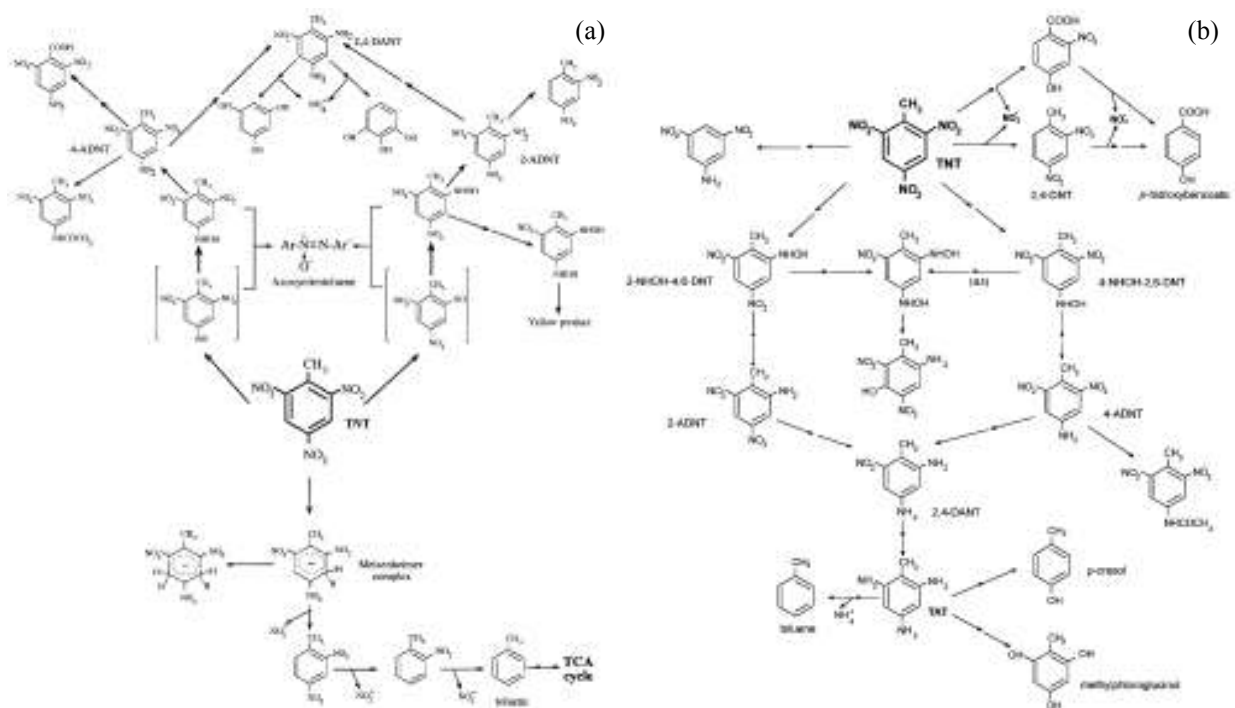


Figure 3. TNT Metabolism by Bacteria: Aerobic (a) and Anaerobic (b)

Source: Esteve-Núñez et al., 2001.

Abiotic transformations of TNT through photodecomposition are developed on sun-light environments (Hwang et al., 2000, Larson et al., 2000) and photocatalized systems (Dillert et al., 1995; Schmelling et al., 1996). TNT exposed to light is submitted mainly to photo-oxidation, producing 1,3,5-trinitrobenzene (1,3,5-TNB) during the transformation process (Hwang et al., 2000, Dillert et al., 1995). Enhanced degradation of nitroaromatic compounds have also been attributed to their reactivity when photochemically excited (Larson et al., 2000). Photodegradation of nitroaromatic compounds has been shown to be influenced by solution pH, alkalinity, and the presence of surface-active agents (Larson et al., 2000; Schmelling et al., 1996). The reduction of TNT increases as the pH of the media increases (Brannon et al., 1997).

2.3 Fate and Transport Equations for ERCs in Soils

Fate and transport processes affecting the mobility of ERCs in soils are incorporated into fate and transport equations that can be applied to describe and predict the spatial and temporal distribution of ERC concentrations in soils (Fetter, 1999):

$$\begin{aligned} \frac{\partial}{\partial t}(\theta_{mw} C_{mw} + f\rho_b C_s + A_{aw}(\theta_w)C_{aw}) = \\ \frac{\partial}{\partial z}\left(\theta_{mw} D_{mw}^* \frac{\partial C_{mw}}{\partial z}\right) - \frac{\partial}{\partial z}(\theta_{mw} v_{mw}) + \Sigma \frac{\partial \theta_{mw} C_{mw}}{\partial \alpha} \Big|_{rxn} - m_{t_w/s} - m_{t_w/g} - m_{t_{mw}/imw} \end{aligned} \quad [14]$$

$$\frac{\partial}{\partial t}(\theta_{imw} C_{imw} + (1-f)\rho_b C_s) = \Sigma \frac{\partial \theta_{imw} C_{imw}}{\partial \alpha} + m_{t_{mw-imw}} \quad [15]$$

$$\frac{\partial}{\partial t}(\theta_g C_g) = \frac{\partial}{\partial z}\left(\theta_g D_g^* \frac{\partial C_g}{\partial z}\right) - \frac{\partial}{\partial z}(\theta_g v_g) + \Sigma \frac{\partial \theta_g C_g}{\partial \alpha} \Big|_{rxn} + m_{t_w/g} - m_{t_{g/s}} \quad [16]$$

$$C_s = K_d(\theta_w)C_{mw,imw} \quad (\text{linear sorption}) = K_f(\theta_w)C_{mw,imw}^n \quad (\text{non-linear sorption}) \quad [17]$$

$$C_{aw} = K_{ia} C_{mw,imw} \quad [18]$$

$$D_{mw,g}^* = D_{mw,g}^o \tau_{mw,g}(\theta_{mw,g}) + \xi_{mw,g}(\theta) v_{mw,g} \quad [19]$$

$$v_{mw,g} = -\frac{K_{mw,g}(\theta_{mw,g})}{\phi} \frac{dh}{dx}, \quad h = \frac{P_c(\theta_w)}{\gamma} + z \quad [20]$$

For 1st order reactions / mass transfer

$$\Sigma \frac{\partial \mathcal{C}}{\partial \alpha} \Big|_{rxn} = -\mu_1 C_{mw,imw} \Big|_{Bio} - \mu_2 C_{w,g} \Big|_{Photo} - \mu_3 C_{mw,imw,g} \Big|_{Chem} - \mu_4 C_{mw,imw,g} \Big|_T + \mu_{\#} C_{mw,imw,g} \Big|_{prod} \quad [21]$$

$$m_{i/j} \alpha \lambda_{i/j} (xC_i - yC_j) \quad [22]$$

where C is concentration, θ is the fluid content, ρ_b is the bulk density, f is the fraction of soil in sorption equilibrium with water, $A(\theta)$ is the saturation dependent air-water interfacial area, D^* is the total effective dispersion coefficient, v is fluid velocity, $rxns$ refers to transformation reactions, m is mass transfer, K_d and K_f are linear partition and nonlinear sorption coefficient between soil and water, K_{ia} is a linear partition coefficient between water and the air-water interface, $t(\theta)$ is the saturation-dependent tortuosity coefficient for molecular diffusion, $\varepsilon(\theta)$ is the saturation-dependent dispersivity coefficient, $K(\theta)$ is saturation-dependent fluid conductivity coefficient, $h(\theta)$ is the fluid energy head, γ is the specific gravity, μ is the degradation constant, and λ is the mass transfer coefficient. The subscripts mw , imw , s , aw , and g refer to the mobile water, immobile water, solid phase, air-water interface, and gas phase, respectively. Subscripts Bio , $Photo$, $Chem$, T , $Prod$ refer to biodegradation, photodegradation, chemical degradation, thermal degradation and production terms, respectively.

Equation (14) describes movement in mobile water, and incorporates mobile water and mass transfer terms of chemicals between mobile water and immobile water ($m_{t_{mw/imw}}$), water and air ($m_{t_{w/g}}$), and water and soil ($m_{t_{w/s}}$). Transport in the gas phase (with respective mass transfer terms) is described in equation (16).

To effectively predict the concentration distributions of ERCs in soils and near soil surfaces, it is necessary to have good understanding of the values of the parameters included in equations (14) through (22) and their interrelated behavior.

2.4 Soil and Environmental Factors Affecting the ERCs Transport

Fate and transport processes of ERCs in soils are influenced by chemical characteristics and interrelated soil and environmental conditions, including: rainfall, temperature, atmospheric pressure, wind, relative humidity, solar radiation, plant coverage, soil water content, and soil properties (Phelan and Webb, 2002; Webb and Phelan, 2000). These conditions are dynamic and interrelated (i.e., not independent) variables and have an effect on hydrologic and biological processes, such as infiltration, plant growth, and evapotranspiration, which further affect the net transport of water in soils (Webb et al., 1999; Webb and Phelan, 2000). Previous simulations studies have shown that diurnal and seasonal weather variations significantly affect the transport and concentration distribution of explosive chemicals in soils (Webb and Phelan, 2000). During infiltration of rainfall, ERCs held in soil-water are mixed with infiltrating water and generally advected downward. The chemicals sorbed to soil particles and desorb until the soil-water partitioning relationship is satisfied. Evaporation periods may induce upward flow and solute advection. Movement of air in soils induced by wind and barometric pressure can also advect vapors downward into and upward out of surface soils (Phelan and Webb, 2002). The optimal transport conditions for ERCs detection are when water is moving upward through soils (Phelan and Webb, 2002). Transport near soil surfaces (Anaya et al., 2007) and flux of explosive chemicals at the soil surface (Phelan et al., 2001) are also affected by cycles of soil wetting and draining.

Phelan and Webb (1998) studied the impact on the fate and transport of explosive chemical when the soil was submitted to a heavy precipitation followed by a dry season. They found that

the heavy precipitation lowered the surface flux by seven orders of magnitude, but the evaporation returned the surface flux approximately to the pre-monsoon surface flux. Phelan et al. (2001) in another study using a soil column injected a point source of DNT to determine the transport of the explosive chemical through the length of the column. The data showed the dramatic decline in DNT vapor concentrations as the surface soil moisture declined; which then rebounded upon wetting. The laboratory data were compared with the results of a simulation showing an excellent correlation.

Amrhein et al. (1996) studied the potential effect of rainfall and evapotranspiration on contaminant migration in the unsaturated soil zone using a deterministic dynamic modeling approach. They determined that diffusion, dispersion and convection contributed to different levels to the flux of the contaminant upward and downward the soil column, during various parts of the year. The temporal variability of both the volatilization flux and the amount of chemical remaining in the unsaturated soil zone are significantly impacted by the dynamics of rainfall and the period of initial contamination.

Reichman et al. (2000) simulated the fate of pesticides in silty clay and sandy soils, during diurnal cycling of soil drying and wetting, varying the environmental conditions. The diurnal variations in parathion and dieldrin volatilization fluxes approximated the diurnal variation in water evaporation rate, which itself was closely related to the diurnal variation in solar radiation. The volatilization fluxes of these two pesticides were higher for the wet soil, for which the evaporation rate was higher.

This research evaluates the effect of temperature and water content in the fate and transport of ERCs during rainfall and evaporation processes that result in flow reversal events. Therefore, the implications of both factors are described below.

2.4.1 Temperature

Soil temperature is a critical factor influencing physical, chemical, and biological processes in soils. Soil hydraulic properties are influenced by temperature (Jury and Horton, 2004) by affecting fluid densities, viscosity (Hopmans and Dane, 1986), surface tensions, contact angles (Bachmann et al., 2002; Grant and Salehzadeh, 1996). As temperature increases, hydraulic conductivities for a given water content tend to increase (Hopmans and Dane, 1986) and capillary pressures tend to decrease (Hopmans and Dane, 1986; Bachmann et al., 2002; Grant and Salehzadeh, 1996), resulting in greater drainage and water movement. Soil temperature also affects many fate and transport processes in soils. The surface temperature of the soil affects the chemical signature at the surface. For example, at higher temperatures, the vapor-liquid partitioning coefficient, or Henry's coefficient, will be higher, and more of the mass would partition in the gas phase (Phelan and Webb, 2002). Dissolution, degradation and sorption rates, are also higher at higher temperatures (Lynch et al., 2002; Phelan and Webb, 2002; Miyares and Jenkins, 2000). The local water vapor pressure will also be increased, possibly leading to higher evaporation rates, which will increase the chemical vapor flux rate into the boundary layer (Phelan and Webb, 2002).

2.4.2 Soil Water Content

Water mass transfer in the soil occurs through a balance of the water added to the soil through net precipitation (precipitation minus runoff), water evaporated at the soil surface, and water that flows through the system to the underlying soil units. Retention and transport of water in the soil is influenced by the soil characteristics, such as the amount of clay present, and by other properties such as the porosity and the unsaturated soil characteristic curves (Phelan and Webb, 2002). Weather condition affects the soil water content dramatically from variations in precipitation, radiation, atmospheric water vapor pressure (the term relative humidity is often used, that is simply the water vapor pressure divided by the saturated value), wind, and atmospheric temperatures. Soil water content tend to increase during precipitation events, and decrease during evaporation. Evaporation tends to increase with increasing atmospheric temperatures, and decreasing relative humidity.

Soil water content influences hydraulic properties, water and air flux, and fate and transport properties. Lower water contents increase capillary pressures, reduces hydraulic conductivities and water flux (Jury and Horton, 2004), and increases gas phase permeabilities (Fetter, 1999). Lower water contents may also result in greater preferential flow (Padilla et al., 1999). Consequently, solute transport in the water phase is reduced at low water contents, where as vapor transport is enhanced. Lower water contents result in lower water advection and diffusion, but higher vapor phase diffusion of ERCs (Webb and Phelan, 2001; Jenkins et al., 1999). Dispersivity values have been reported to increase as water content decrease (Padilla et al., 1999).

Water content also influences mass transfer and reaction processes. Sorption of TNT and DNT onto soil tends to be constant at higher water content, but increase dramatically below a specified water content (e.g. below 8%) (Phelan and Webb, 2002). Phelan and Webb (2002) reported that dry soils will sorb about 10,000 times more landmine signature chemicals than damp soils. This depresses the vapor levels by the same amount. In damp soils, about 80 to 90% of the mass of TNT and DNT is found sorbed to the soil particles, about 10 to 20% is found in the soil water, and only 10-6% is found in the vapor. The soil acts as a temporary storage reservoir for the landmine signature chemicals, releasing them when dew or rain falls, and collecting more as soil water evaporates.

Laboratory measurements of TNT, DNT and DNB found that degradation rates are also dependent on water content (Phelan and Webb, 2002). In this study, soil moisture contents less than 1% preserve the chemicals, whereas higher water content increased degradation rates.

There are competing effects between the soil surface temperature and the soil surface water content as illustrated by an increase in soil surface temperature. While this increase will lead to an increase in Henry's constant, which in turn leads to a higher gas-phase chemical concentration, the higher soil surface temperature also leads to a decrease in the surface moisture content due to evaporation. Lower water contents, however, may enhance sorption, and reduce ERC transport. The net effect of an increased soil surface temperature on the gas phase chemical concentration depends on the interaction between temperature and moisture content (Phelan and Webb, 2002).

2.5 Modeling Transport of Explosives in Soil

Several numerical codes have been applied to model fate and transport processes in variable-saturated soils, including: T2TNT (Phelan et al., 2000, 2001), LEACHM (Hutson and Wagenet, 1989), HYDRUS 2D (Šimůnek et al., 2006; Dontsova et al., 2006; Jenkins et al., 2007), FEHM (Zyvoloski et al., 1988; Borrero et al., 2004; Irrazábal et al., 2005 and 2007), and SESOIL (Bonazountas and Wagner, 1984). These codes apply fate and transport equations in water and gas phases, but differ in the number of processes that are included (Table 2).

Table 2. Comparison of Solute Transport Simulation Codes

Process	Simulation Code				
	HYDRUS 2D	LEACHM	T2TNT	SESOIL	FEHM
Water Flow					
Saturated/Unsaturated	x				x
Mobile/Immobile phases	x				x
Macropore flow					x
Root water uptake	x	x	x		
Multidimensional flow	x		x		x
Soil-Hydraulic Model					
Dual porosity	x				x
Dual permeability					x
Hysteresis	x				
Heat Transport					
	x		x		x
Solute Processes					
Multiple solutes	x	x			x
Dissolution	x			x	x
Adsorption	x	x		x	x
Multi-site sorption	x	x			x
Vaporization/Volatilization	x	x	x	x	x
Dispersion (Water/Gas)	x	x	x	x	x
Diffusion (Water/Gas)	x		x	x	x
Degradation	x	x	x	x	x
Dual porosity transport	x				x
Rate-limited mass transfer	x		x		x
Reaction	x				x
Multidimensional flux	x		x		x
Inverse Solution					
	x	x			x

HYDRUS solves numerically the Richards' equation for saturated-unsaturated water flow and the convection-dispersion equation for heat and solute transport (Šimůnek et al., 2006). The solute transport equations consider convective-dispersive transport in the liquid phase, as well as diffusion in the gaseous phase. The program may be used to analyze water and solute movement in unsaturated, partially saturated, or fully saturated porous media. This program allows determining the solute parameters since the program includes a Marquardt-Levenberg type parameter optimization algorithm for inverse estimation of soil hydraulic and/or solute transport and reaction parameters from measured transient or steady-state flow and/or transport data. The governing flow and transport equations are solved numerically using Galerkin-type linear finite element schemes (Šimůnek et al., 2006).

Dontsova et al. (2006) studied the dissolution and transport of ERCs in saturated soil columns, in which Hydrus 1D was used to determine the fate and transport parameters. During the analysis high values of correlation coefficients were achieved between the measured data and the fitted using the Hydrus 1D code. Jenkins et al. (2007) used Hydrus 1D to determine the transport parameters by fitting the experimental propellants breakthrough curves obtaining high correlation values. Degradation and adsorption coefficients for propellants were determined by using Hydrus 1D, achieving values similar to values reported in other studies.

Phelan et al. (2001) modeled with T2TNT the DNT soil transport and surface flux when submitted to evaporation process. The data showed as was expected a DNT vapor concentrations decreased as the surface soil moisture decreased. They achieved high correlation values between the experimental data and the simulated results, demonstrating the accuracy of T2TNT model

predictions under well controlled laboratory conditions. They concluded that T2TNT is adequate to evaluate the environmental impacts to the chemical signature emanating from buried landmines. Phelan et al. (2000) used T2TNT to evaluate the conditions that impact chemical signature transport from DNT. The model was validated using experimental data. Numerical simulation showed excellent comparison to the surface flux and soil concentration data, concluding that under well controlled conditions, the T2TNT code very closely simulates the chemical transport of DNT in near surface soils.

Borrero et al. (2004) modeled numerically the transport of the chemical signature compounds from buried landmines in a three-dimensional minefield array under unsaturated conditions by using FEHM code. The simulations were developed submitting the explosives to infiltration and evaporation periods. They used parameter values from TNT and DNT reported by other authors obtained from experimental data, achieving results as was expected considering the information from other studies. Irrazábal et al. (2005) used FEHM to study the effect of an inclined terrain in the fate and transport of explosives chemicals when submitted to infiltration and evaporation processes. Irrazábal et al. (2007) studied the effect of environmental conditions (water content, temperature, relative humidity and UV-VIS radiation) on the chemical signature of TNT in soil. They used experimental data to validate the results obtained through numerical simulation using FEHM code, concluding that using the code represented well the chemical signature of the explosive.

3 METHODOLOGY

The research objectives were accomplished by conducting solute transport experiments in laboratory-scale soil columns subjected to infiltration, evaporation and reverse flow conditions. The soil column system permits 1D flow and 2D solute transport. It incorporates a uniform cylindrical stainless steel column (100 cm long and 19 cm ID) packed with a homogeneous sandy soil. Transport experiments involved introducing a point source of TNT and DNT under the soil surface and inducing infiltration, evaporation, and reverse flow events, while monitoring aqueous and vapor concentrations of TNT and DNT, and other related chemicals. Spatial and temporal breakthroughs were analyzed comparatively and analytically. The breakthroughs/data were analyzed numerically using HYDRUS-2D code.

All the experimental work and analysis were conducted at the Environmental Engineering Laboratory at the University of Puerto Rico, Mayagüez. The laboratory is equipped with the physical transport modes, instrumentation for system control, hydraulic data measurement, chemical analytical equipment, and computational resources necessary for this research.

3.1 Experimental Setup

The experimental setup consists of a solution-delivery and air-sweeping systems, vertically-placed sand columns, and vacuum and waste chambers (Figure 4). The solution delivery system delivers the aqueous solution to the column and consists of solution reservoirs connected to liquid delivery pump. For saturated conditions the solution delivery pump was comprised of a high pressure liquid chromatography (HPLC) pump (Series III, LabAlliance)

connected to the top of the column. For unsaturated conditions the solution was pumped using a peristaltic pump (Model 7553-70, Cole-Parmer Instrument Co.) connected through a nozzle to distribute the water over the surface area of the column. This system is only active when infiltration conditions were imposed in the column. The air sweeping system delivers dry air across the soil surface to enhance evaporation. It consists of an air-sweeping chamber fitted to the top of the column and connected to an air-delivery line on one face and an outlet line on the opposite face (Figure 5). The air-delivery line is connected to the air-outlet of a vacuum (Model 2545B-01, Welch). The air is passed first through a moisture trap with Drierite (Anhydrous Calcium Sulfate, W.A. Hammond Drierite Company Ltd.) packed in a Plexi-glass tube in order to remove the moisture contained in air.

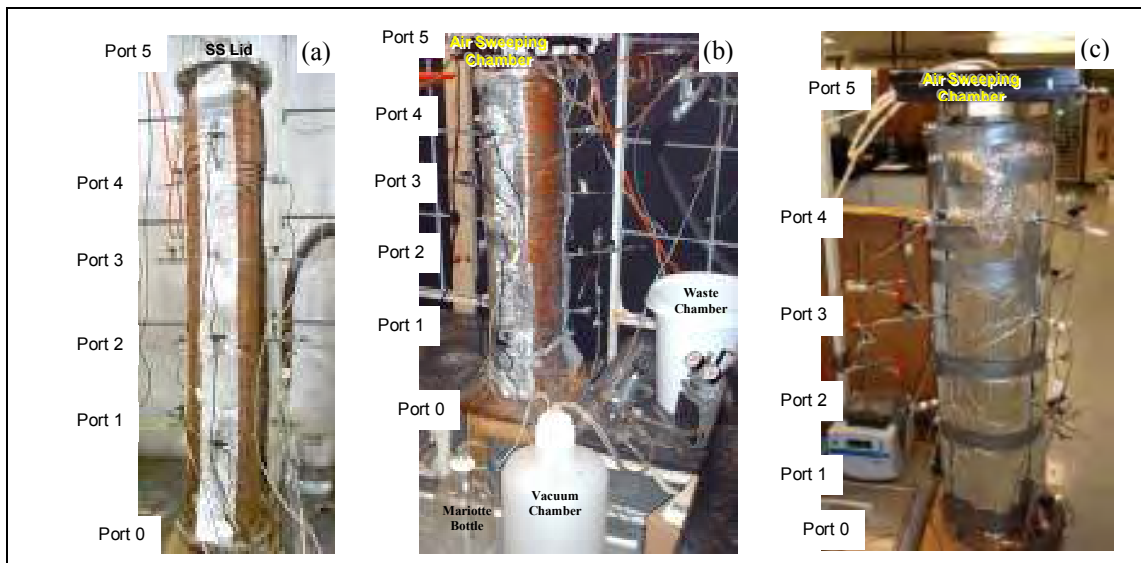


Figure 4. Experimental Setup for Column 1 (a) and (b); and Setup for Column 2 (c)

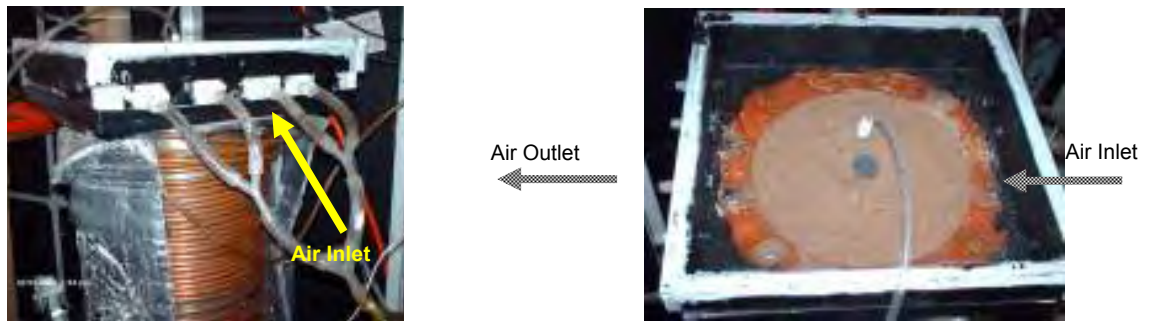


Figure 5. Simulation of Evaporation using Air Sweeping System

The sand columns (Figure 4) consist of a stainless steel (SS) tube (100 cm long by 19 cm ID) closed at both ends with SS caps. SS porous plates with average pore sizes of 10 and 100 μm and bubbling pressures of 103 and 24 mbars were placed at the bottom and top ends of the columns, respectively, to provide support for the porous media and maintain unsaturated water flux conditions at the bottom and atmospheric conditions at the top. Two soil columns were used: Column 1 contained sampling port clusters located at 19.5, 39.0, 58.5, and 78 cm from the bottom. Each cluster contains a water-pressure sampler, a liquid sampler, and a gas pressure and vapor sampler. The sampling clusters in column 2 were located at 19.5, 39.0, 58.5, and 78 cm from the bottom of the column and included a water pressure sampler, a liquid sampler, a gas pressure sampler, and a gas-phase sampler. The liquid and vapor samplers were used to measure the spatial and temporal concentration distribution of ERCs and other chemicals in the water and gas phases. Pressure samplers were used to monitor soil-water content and pressures and soil-gas pressure, and determine flow conditions. The samplers consist of stainless steel porous cups to selectively sample the water or the gas phases in the soil (Padilla et al., 2006). The water and air samplers consist of 5 μm and 100 μm stainless steel porous cups, respectively, which were inserted 6.5 cm into the column (Figures 6 and 7). The pressure samplers were coupled with a

digital pressure gauge connected to a data acquisition system controlled by a computer and a data logger (Model CR23, Campbell Sci., UT). Experimental temperatures were achieved in the soil column by circulating water of a set temperature through copper coils. A coil of copper tubing connected to a refrigerated circulating bath (Model RTE 10, NesLab Corp.) and covered by a thermal insulation material, surrounds the columns to control the temperature in the soil. Although, delivery lines and coils were insulated, some heat losses were observed between the water temperature in the bath and the attained in column. Temperatures of 25°C ($\pm 1^\circ\text{C}$) and 35°C ($\pm 1^\circ\text{C}$) were attained by setting the water bath temperature at 32°C ($\pm 3^\circ\text{C}$) and 45°C ($\pm 3^\circ\text{C}$), respectively. Because of heat losses through the coil and variations in temperature-dependent water densities, more constant temperatures were attained through the column of the bath water was introduced through the bottom of the coil. The temperature was measured with type-K thermocouples located on the outside of the column next to ports 4 and 1 (Figure 4). Thermocouples were placed to avoid contact with coil.

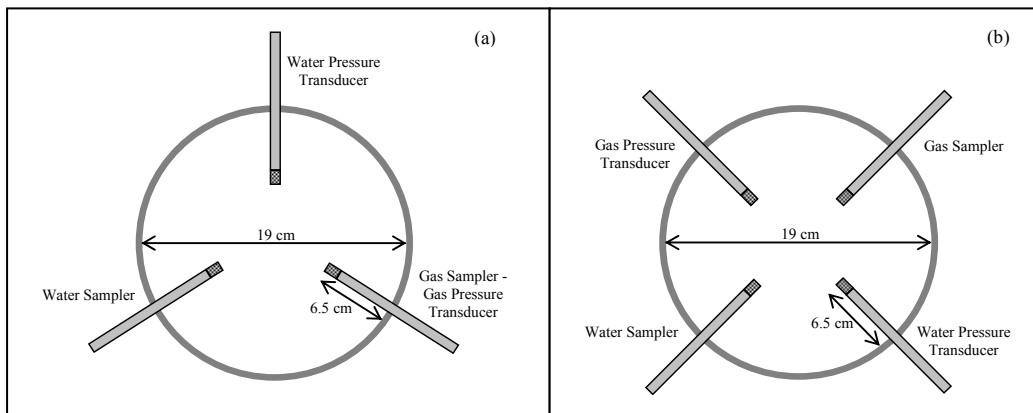


Figure 6. Location of Water-Gas Samplers and Water-Gas Pressure Transducers for Column 1 (a) and Column 2 (b).



Figure 7. Water and Gas Samplers

The top of the column was fitted with a SS lid for infiltration during saturated experiments (Figure 8a) and the air sweeping chamber for evaporation during saturated experiments and for infiltration-evaporation events during unsaturated experiments (Figure 8b, 8c and 8d). Both, the lid and the chamber, were fitted with a ¼” inlet at the top to deliver the aqueous solution during infiltration periods.

The bottom of the column is connected to a vacuum and waste chamber to establish a constant head boundary for water flow at the bottom of the column during the infiltration periods and achieve specific soil-water tensions and water contents in the sand for given water flow rates. During the evaporation periods the bottom of the column is connected to a Mariotte water reservoir which supplies water at a constant head (Figures 8b and 8d).

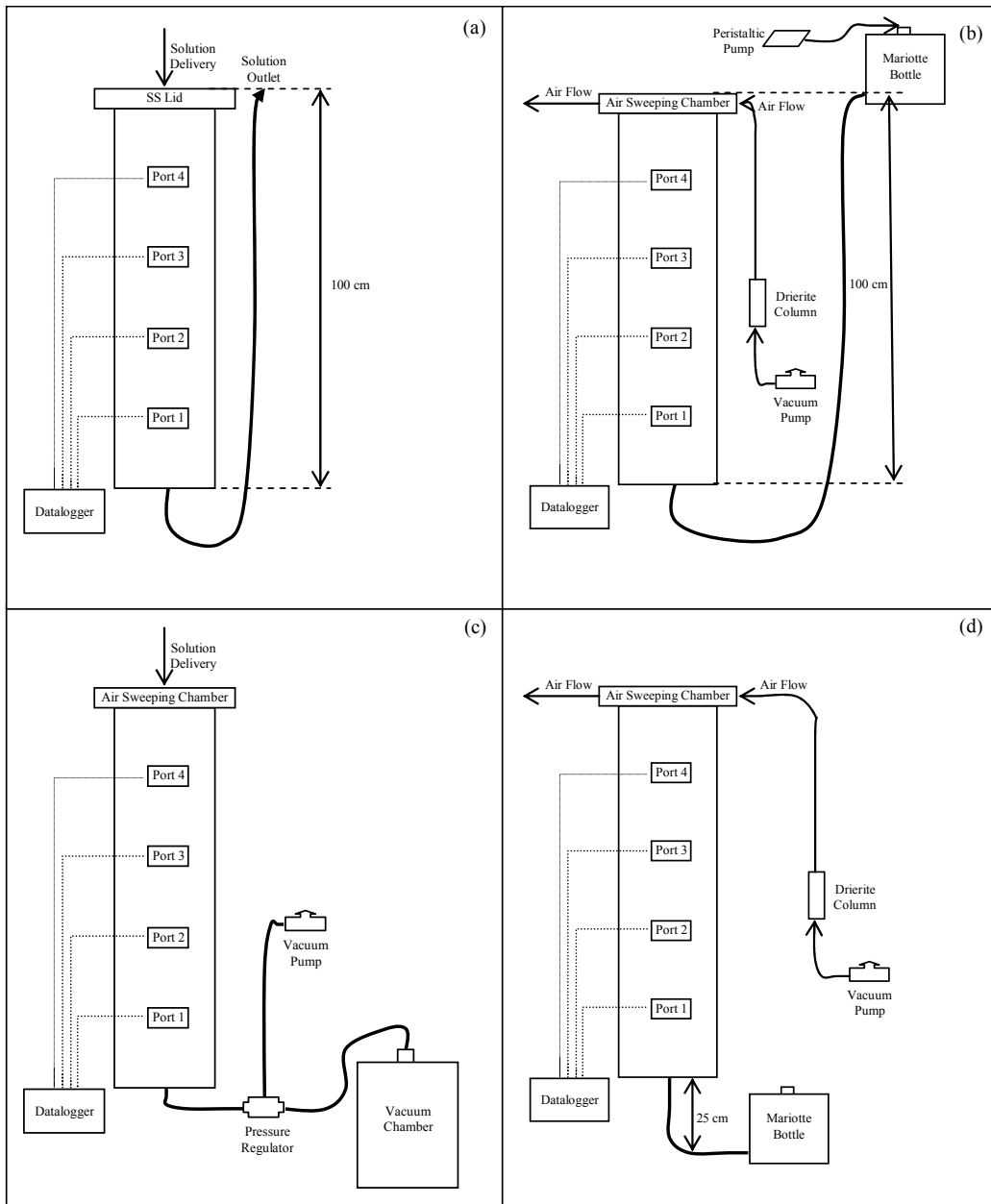


Figure 8. Experimental Setup for Saturated during Infiltration (a) and Evaporation (b) Events; and for Unsaturated Conditions during Infiltration (c) and Evaporation (d) Events.

3.1.1 Column Instrumentation

As previously discussed, the soil column was instrumented with: (1) pressure sensors to measure soil water and gas pressures; (2) thermocouples sensors to determine the system

temperature; and (3) a data acquisition system used to collect and store pressure and temperature data. This section discusses the calibration and the setup of the data acquisition system.

3.1.1.1 Pressure Sensors

The pressure samplers were coupled with digital pressure gauges or pressure transducers. The pressure transducers used were SS-housed pressure sensors (Model 230PC, Micro Switch). Pressure sensors were cabled to the Campbell Scientific CR23 data logger, which measured signal voltage from the sensor. To determine pressures, a relationship must be established between the measured signal and the pressure.

Calibration of the pressure sensors was conducted by connecting the sensors to a SS manifold system used to set and control pressures. The manifold was connected to a vacuum pump (Model 2545B-01, Welch) to a (+/-) pressure regulator (Model 44-50, Siemens), and to a digital manometer (Model 407910, Extech Instruments) used to monitor pressures. Pressure was increased or decreased and voltage signal for given pressure was recorded. This was repeated for several pressures to develop the calibration curve function relating pressure and signal voltage (Figure 9). Calibration functions were highly linear.

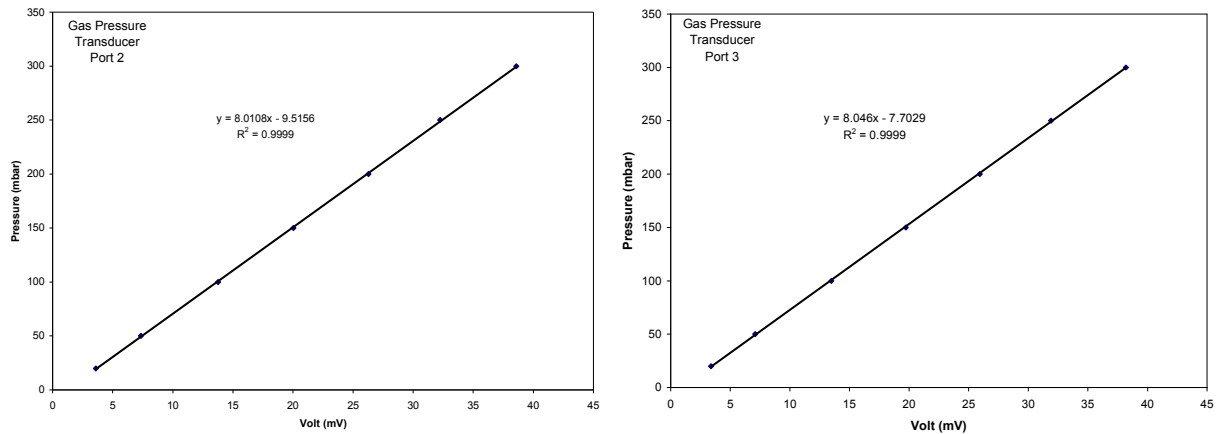


Figure 9. Calibration Curves for Pressure Sensors

To validate pressure measurements in situ (once samplers were installed in soil column), the column was saturated from the bottom, and imposing a static head on the soil water, static heads of 20, 40, 60 and 80 cm above the top of the column were used. The validation pressures measurements were somewhat biased from the theoretical pressures (Figures 10 and 11). Pressures determined in situ were generally higher than expected for water pressure sensors, but slightly lower for the gas-pressure sensors. The sensors were re-calibrated using off-situ (manifold) and in-situ data. The final calibration functions are given in table 3.

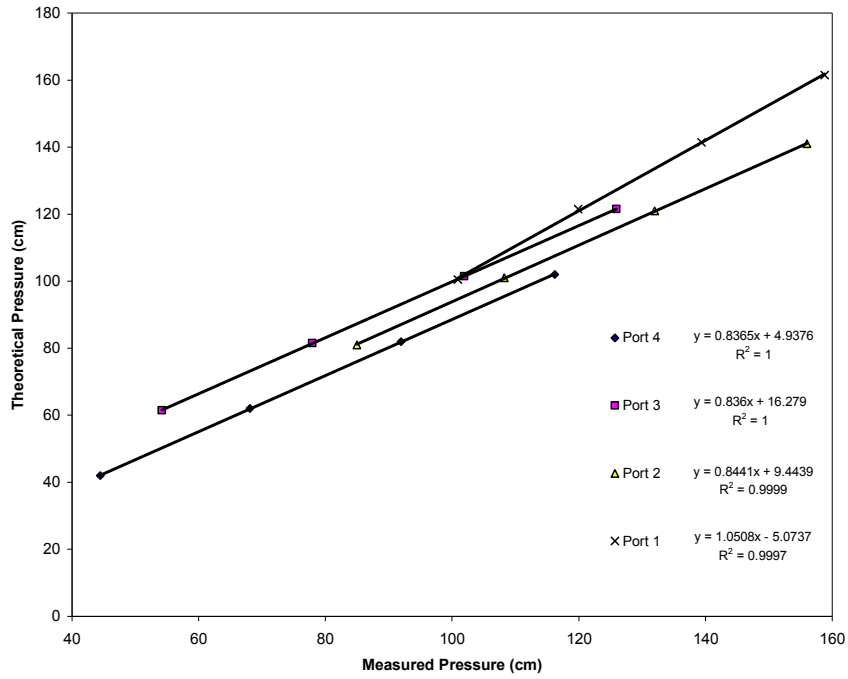


Figure 10. Theoretical Pressure vs. Measured Pressure for Water Sensors

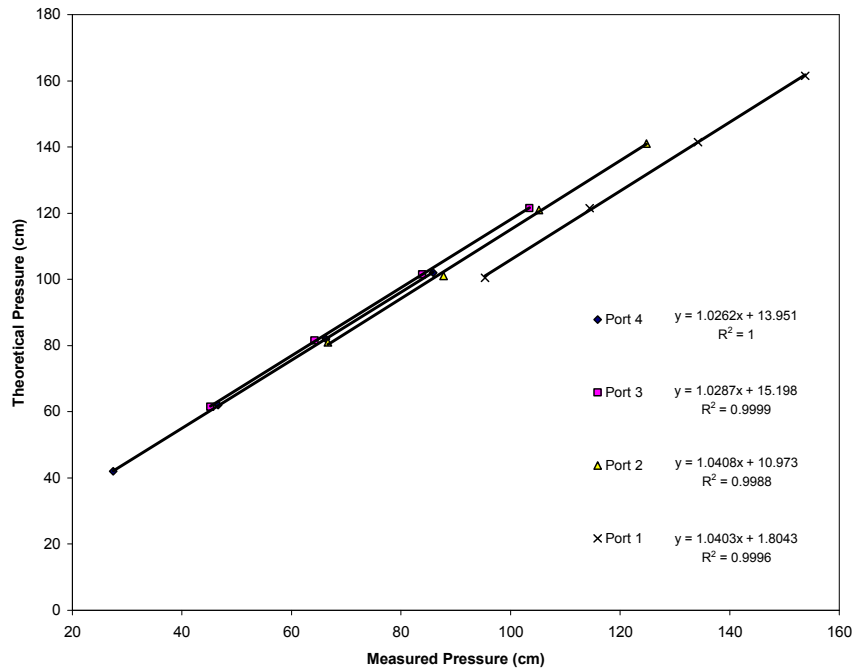


Figure 11. Theoretical Pressure vs. Measured Pressure for Gas Sensors

Table 3. Calibration Equation used for Pressure Sensors

Pressure Transducer	Port	Initial Equation	Correcting multiplying for	Equation corrected
Gas	4	$y = 8.0598x - 5.5203$	$1.0262x + 13.951$	$y = 8.27097x + 8.28607$
	3	$y = 8.046x - 7.7029$	$1.0287x + 15.198$	$y = 8.27692x + 7.27403$
	2	$y = 8.0108x - 9.5156$	$1.0408x + 10.973$	$y = 8.33764x + 1.06916$
	1	$y = 8.0512x + 1.1866$	$1.0403x + 1.8043$	$y = 8.37569x + 3.03868$
Water	4	$y = 9.8299x + 1.1870$	$0.8365x + 4.9376$	$y = 8.22271x + 5.93053$
	3	$y = 9.8577x - 13.1349$	$0.8360x + 16.2790$	$y = 8.24104x + 5.29522$
	2	$y = 9.8959x - 13.4218$	$0.8441x + 9.4439$	$y = 8.35313x - 1.88544$
	1	$y = 8.0352x - 3.3885$	$1.0508x - 5.0737$	$y = 8.44344x - 1.51309$

3.1.1.2 Temperature Sensors

Thermocouples were calibrated by immersing them into water set at different temperatures and recording the respective measured voltage output. The calibration curves were highly linear (Figure 12).

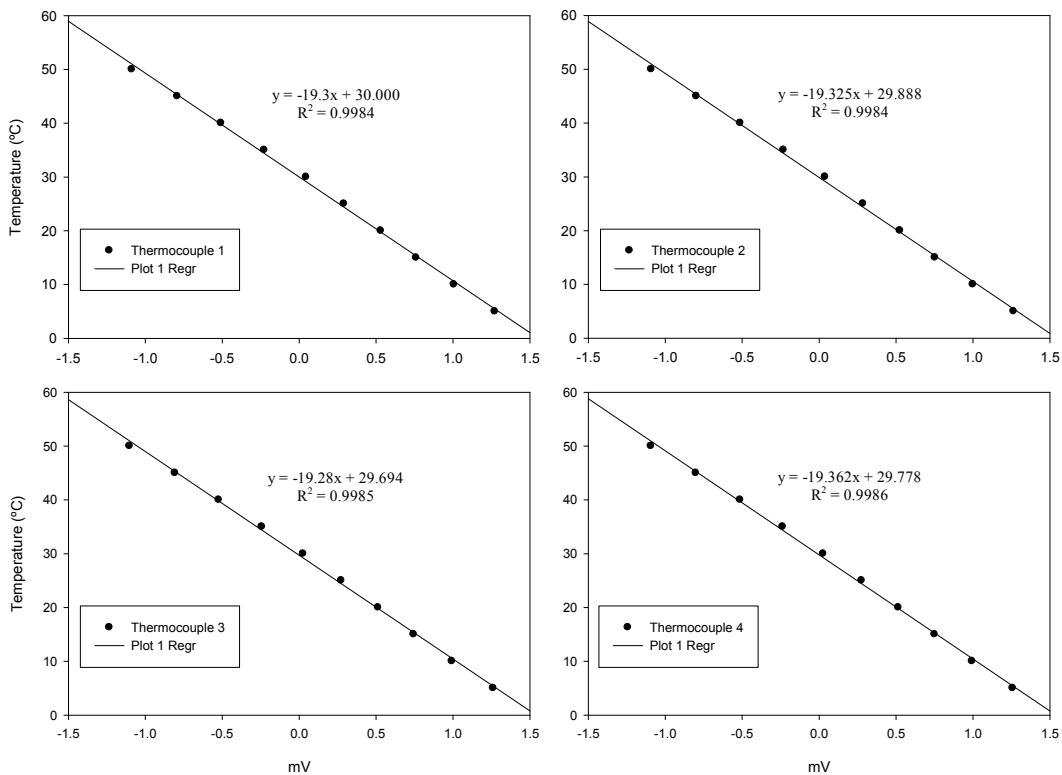


Figure 12. Calibration Curves for Thermocouples

3.1.1.3 Data Logger

Temperature and pressure sensors were cabled to a CR23X data logger (Campbell Scientific, Utah) to monitor, collect, and store data (Figure 13). A 16-channel (4-wire) or 32-channel (2-wire) relay multiplexer was connected to channel 1 to expand the number channel available for sensors. Each sensor was connected to a particular channel. Pressure and temperature sensors required single channels. The pressure sensors had 4 wires: a ground (black); a voltage (red); an output “A” (white); and an output “B” (green). The ground was connected to the Ground insert; the voltage was connected to the V12 insert; the output “A” to the High insert; and the output “B” to the Low insert. Temperature sensors had 2 wires: an output “A” (red); and an output “B” (white). The output “A” was connected to the High insert and the output “B” was connected to the Low insert of a particular channel in the data logger.

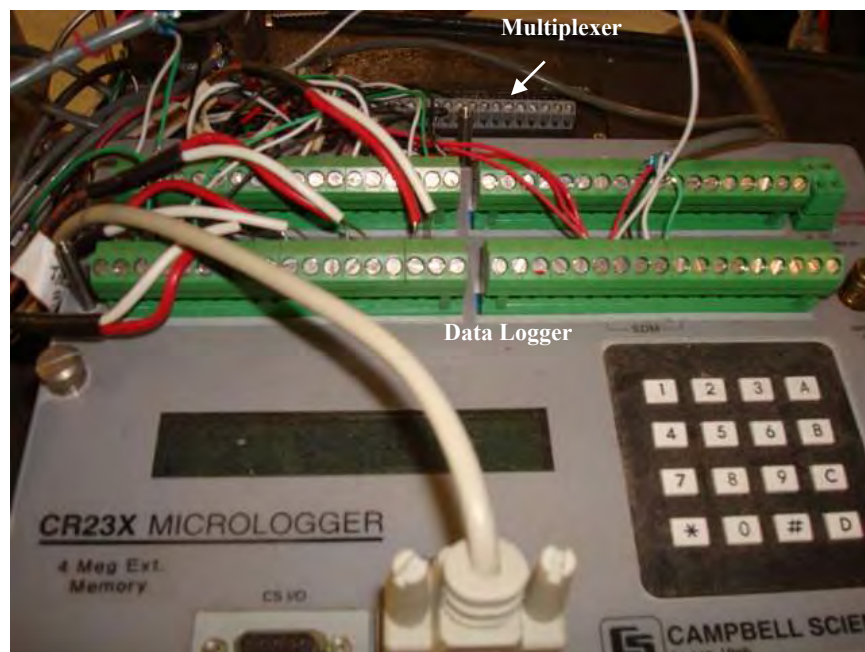


Figure 13. Data Logger Connections

3.2 Soil Properties

Transport experiments were conducted in stainless steel columns packed with beach sand from Isabela, Puerto Rico. This sand consists mainly of quartz and calcite. Physical and chemical soil properties are listed in Tables 4 and 5. It is noted that the measured specific gravity of this sand is higher than expected (Myers et al., 1998).

Table 4. Physical Characteristics of Isabela Sand

Soil	USCS Classification	Specific Gravity (g/cm ³)	Specific Surface Area m ² /g	Mineralogy
Isabela Sand	SP	2.83	1.687	Quartz/calcite

Source: Modified from Molina et al. (2006)

Note: SP – Sand Poorly Graded

Table 5. Chemical Characteristics of Isabela Sand

Ca (ppm)	Mg (ppm)	Na (ppm)	HCO ₃ ⁻ (mg/kg)	CO ₃ (mg/kg)	Cl ⁻ (ppm)	FOC (%)	OM (%)	TFe (mg/kg)	TN (mg/kg)	pH	CEC (mg/100g)
275.00	36.40	36.40	2.00	<1.00	59.00	0.07	0.47	6125.70	<713.00	8.83	2.10

Source: Modified from Molina et al. (2006)

The particle size distribution for the Isabela sand (Figure 14) was determined by Molina et al. (2006) using sieve analysis. Isabela sand is primarily composed of 92.6% sand sizes, and 7.4% of fines (silts and clays).

It is important to achieve a homogenous density through the column height, since packing and compactions densities affect the hydraulic and transport properties of the soil, and consequently could affect the transport of ERCs in the soil column. The sand was packed in the stainless steel column following a procedure developed by Rodríguez et al. (2006) to achieve consistent and reproducible bulk densities and soil porosities. This procedure applies mechanical compaction energies to wet sand (5% w/w water content) using a piston-driven mechanism. The sand was packed to a bulk density of 1.65 g/cm³ and a media porosity of 41%. These values are

within acceptable bulk density and porosity range for natural sandy soils (Fetter, 1999; Phelan and Webb, 1998).

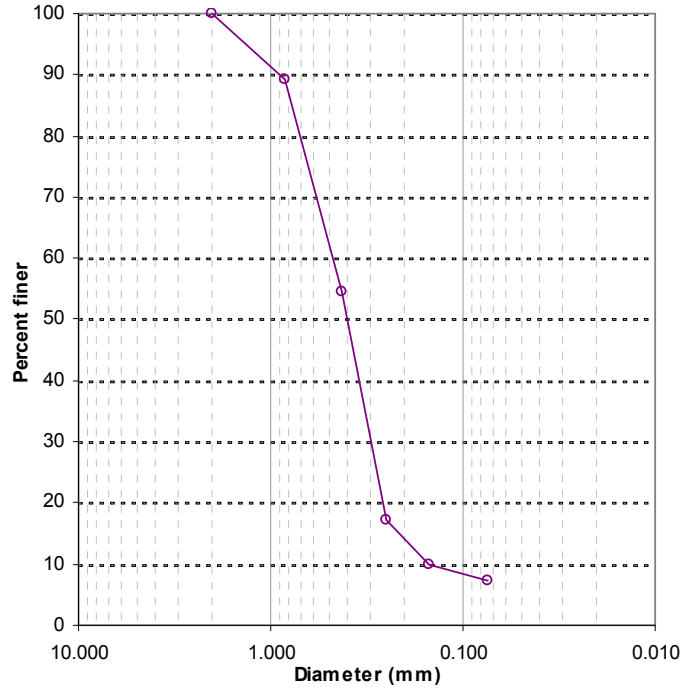


Figure 14. Particle Size Distribution for Isabela Sand

Source: Molina et al. (2006)

The bulk density and media porosity were calculated using the following equations:

$$\rho_b = \frac{M_s}{V_s} \quad [23]$$

where ρ_b is the bulk density (g/cm^3), M_s is the mass of soil particles (g) and V_s is the volume of soil (cm^3).

$$n = 1 - \frac{\rho_b}{\rho_p} \quad [24]$$

where n is the volumetric porosity (cm^3/cm^3) and ρ_p is the particle density.

After packing, the soil was initially degassed using a CO₂ flow of 228 mL/min. It was thereafter saturated from the bottom up with a 4.0 mM NaCl solution, which was pumped at a 2 mL/min constant flow with a HPLC pump (Series III, LabAlliance).

The Soil-Water Characteristic Curve (SWCC) was estimated using pedotransfer functions (PTF) incorporated in the ROSETTA code (Schaap et al., 2001). PTFs generate soil characteristics from other, easily measured and more available soil property data. ROSETTA generates the van Genuchten parameters (α , m , n , θ_r ; equation (2)) from particle-size distribution (Figure 14) and dry density (1.65 g/cm³) data. Estimates of saturation-dependent hydraulic conductivities were generated using the van Genuchten parameters and an estimated saturated hydraulic conductivity (K_s).

Values of K_s were measured during saturated flow experiments conducted at different flow rates (Q). In these experiments constant flow rates of 2 and 40 mL/min were introduced at the top of the column over the cross-sectional area (A) normal to the flow. The bottom of the column was connected to a saturated tube discharging to the atmosphere at an elevation of 1 cm above the top of the column (101 cm above the reference level at the bottom of the column). At steady-state flow, total hydraulic heads (h) were determined between ports (dL) of respective hydraulic heads. Saturated hydraulic conductivities were estimated as,

$$K_s = -\frac{Q}{A\left(\frac{dh}{dL}\right)} \quad [25]$$

3.3 Transport Experiments

Transport experiments involved introducing a TNT/DNT point source below the soil surface, and inducing infiltration, evaporation and reverse flow events, while monitoring chemical concentrations in the aqueous and gaseous phases. A total of eight (8) experiments were conducted under different source, water content, flow, and temperature conditions (Table 6). Two experiments under saturated conditions (Exp. 1 and 2) injected an aqueous TNT point source solution (30 mg/L) TNT solution 22 cm below the soil surface near the center of the column at a 0.4 mL/min constant flow. To measure TNT concentrations in each sampling point, a 2 mL sample was extracted every 5 minutes. The sample analyses were made by using Solid Phase Micro Extraction. Downward flow transport experiments were conducted under steady state flow conditions by passing a 20 mM NaCl solution at 40 mL/min at the top of the column, simulating saturated infiltration process. Once the NaCl reached the bottom of the column, the flow was reversed by pumping a 4 mM NaCl solution at 40 mL/min from the bottom. The effect of 20 mM NaCl solution on the fate and transport processes of ERCs is considered negligible. Brannon et al. (2005) studied the influence of salt concentration in dissolution rates, adsorption and transformation rates of some ERCs as TNT, RDX and HMX. They concluded that even though high NaCl concentration can decrease the explosives dissolution rates it is considered neglected. The salt concentration used during their experiments was 20 ppt, therefore the differences in dissolution rates expected for our experiments are neglected considering that the changes in the solution injected were about 0.1 ppt.

The other six (6) transport experiments (Table 6) involve burying a point source containing TNT and DNT crystals and allowing water to flow through the soil and the source under

infiltration or evaporation conditions. These experiments were conducted at different water contents and temperature conditions (Table 6). Four column-averaged water contents (~45, 60, 75 and 100% saturation) were used at a 25°C constant temperature. Two column-averaged water contents (~60 and 100% saturation) were used at 35°C. Unsaturated water contents were achieved by varying the flow rate at the top of the column during infiltrating periods, while maintaining a -25 cm constant suction head at the bottom of the column during the entire experiment. The flow rates required to achieve particular saturation (i.e., 45, 60, 75% approximately) under an imposed constant pressure condition of -24.52 mbar (-25 cm of H₂O) were determined from flow simulations using HYDRUS 1D (Šimůnek et al., 2005). The simulation assumed homogeneous porous media characterized by the soil properties described in section 3.2. Results from HYDRUS 1D (Figure 15) suggest the use of 2, 10 and 20 mL/min flow rates at the top of the column to obtain water contents of 0.17, 0.23 and 0.28 (45, 60 and 75%), respectively.

Table 6. Description of Experimental Conditions

Experiment Number	Temperature (°C)	Degree of Saturation (%)	ERC Source ^(1,2)	Flow Regime					Chemical Analysis	
				Infiltration ⁽³⁾		Reverse Flow		Evaporation ⁽⁴⁾	NaCl Tracer ⁽⁵⁾	ERC ⁽⁶⁾
				Rate (cm/min)	Period (min)	Rate (cm/min)	Period (min)	Period (min)		
1	25	100	AS	0.141	532				CP	SPME
2	25	100	AS	0.141	200	0.141	180		CP	SPME
3	25	100	SPS	0.007	6150			84270	FTCC	LLE
4	25	75	SPS	0.071	1004			74536	FTCC	LLE
5	25	45	SPS	0.007	7080			44360	FTCC	LLE
6 ⁽⁷⁾	35	100	SPS	0.007	27300			99740	FTCC	LLE
7	25	60	SPS	0.035	7320			64880	FTCC	LLE
8	35	60	SPS	0.035	7380			64880	FTCC	LLE

(1) AS = Aqueous Solution (30 mg/L) injected at 0.4 mL/min

(2) SPS = Solid-Phase Source (TNTmass / DNT mass)

(3) Infiltration Rate (cm/min) = Q/A, where A=283.4 cm²

(4) Evaporation Rates were measured during experiments and are reported under the Results and Discussion chapter

(5) Measurements made using a conductivity probe (CP) or flow-through conductivity cell (FTCC)

(6) ERC solutes in legend samples were extracted using SPME or liquid/liquid extraction (LLE) methods and analyzed with GC/ECD

(7) Experiment 6 consisted of 2 saturated infiltration/evaporation cycles.

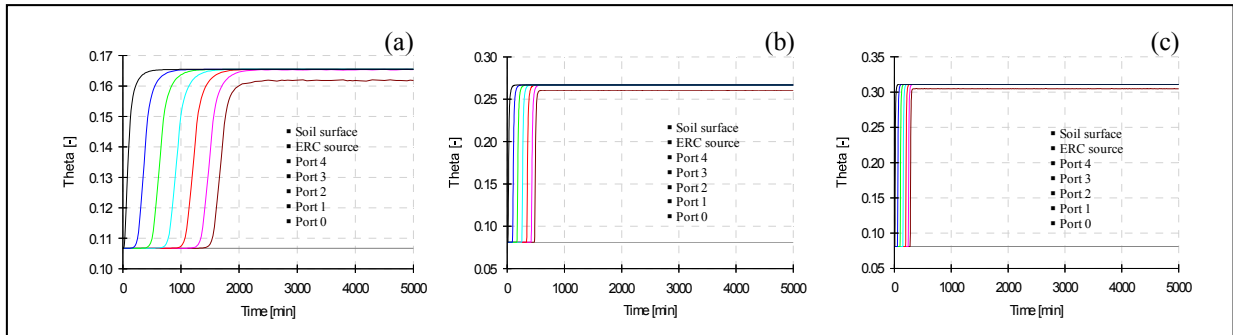


Figure 15. Water Content Simulated in Hydrus 1D for Constant Flows of 2 (a), 10 (b), and 20 (c) mL/min

TNT and DNT crystals were placed in a nylon bag (pore size $\sim 49 \mu\text{m}$), simulating a landmine point source. The source was buried at the center of the column, 13 cm from the soil surface (9 cm above Port 4). Burial involved placing a 60 mL plastic syringe (body + plunger) (Figure 16) vertically in the center of the column during soil packing of upper 13 cm column interval. The end of the syringe housing the outlet nozzle was sliced off to form a uniform circular opening with same diameter as syringe body (28.5 mm). After packing to the top of the column, the plunger was removed from the syringe tube, the TNT/DNT source was placed at the bottom of the syringe tube, the tube was removed, and the bore hole was filled and compacted with soil wet at 5 %.



Figure 16. Location of the Landmine in the Column of Soil

Prior to each experiment, the sandy soil was thermally washed to remove any residues of ERCs. Soil was then saturated.

For saturated experiments, the simulated landmine was buried by initially saturating the column, then lowering the water table to Port 4 (22 cm below the soil surface) before burying the simulated landmine. The water table was thereafter raised to the top again. Once the water table reached the top, infiltration process was started at time zero (0). For unsaturated experiments, the column is drained to desired average water content by adjusting the flow rate of the 4 mM NaCl solution and applying a -25 cm constant suction at the bottom. When the pressures in the column reached equilibrium, the landmine was inserted without stopping the water flow. The beginning of the experiment (time 0) is considered to be at the time the source is completely buried.

Transport experiment started by imposing infiltration events initially, followed by evaporation events. Infiltration conditions were imposed by injecting a 20 mM NaCl tracer solution at the top of the column until the NaCl front reached the bottom of the column (Port 0). Evaporation conditions were imposed after infiltration periods by discontinuing the delivery of the infiltrating solution, and passing dry air through the air-sweeping system on top of the column (Figure 5). Under saturated conditions, a constant head was maintained at the top of the column to replenish the evaporated water. The replenishment source was a NaCl solution of different concentration to the final infiltrating solution. For experiments 3 and 4 the final infiltrating solution was 16 mM. The evaporation replenishment NaCl solution was set to 4 mM. For experiments 5 through eight, the infiltrating solution was set at 20 mM for displacement of resident background water and set back to background solution (4 mM) thereafter for elution of the initially infiltrated 20 mM solution. This was done to conduct a complete miscible displacement BTC during infiltration periods and better characterize advective and dispersive

processes. For these experiments, a 20 mM solution was set as the evaporation replenishment source. Under unsaturated conditions, a constant tension head was maintained at the bottom of the column to replenish the evaporated water.

Experiment 6 consisted of 2 saturated infiltration/evaporation cycles. After period 1 (20040 minutes), reverse flow was induced for 26280 minutes from the bottom of the column during evaporation period. This flow was mistakenly imposed through an increasing variable-head boundary. A second infiltration cycle was imposed thereafter for 7260 minutes, followed by a second 73460 minutes evaporation event.

Aqueous and vapor samples were collected temporally and spatially during the experiments. Aqueous samples were withdrawn through the liquid sampling ports using a manual syringe. Sample volumes of 27 mL were taken for the reverse flow experiments (Exp. 1 and 2, table 7) conducted under saturated conditions. A volume of 1 mL was withdrawn for all other experiments (Exp. 3-8, table 7). Vapor samples were obtained by withdrawing 1 mL of air samples through the gas samplers and introducing a Solid Phase Micro Extraction (SPME) fiber Polydimethylsiloxane/divinylbenzene (65 μm film coating from Supelco) supported in a fiber holder assembly (Supelco, Sigma-Aldrich Chemie GmbH) into a septum nut fitting (VICI, Tx) located in the vapor sampler (Figure 17). The SPME fiber was left sampling (sorbing) vapor within the sampler for a period of 4 minutes, and later desorbed in a GC for analysis. The concentration was plotted vs. time to establish BTC at each sampling point. The BTC was then analyzed using moments analysis and numerical models as described below.

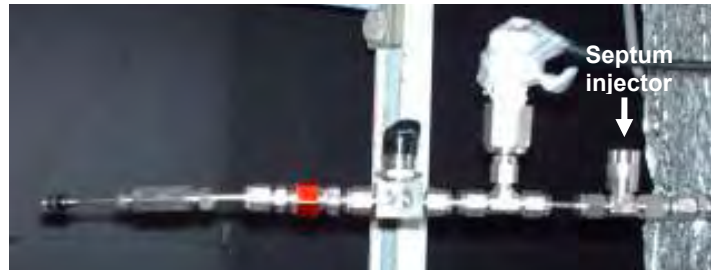


Figure 17. Vapor Collection in a Septum Injector using SPME Fiber

3.4 Environmental Conditions

Transport experiments were conducted under different environmental conditions of water content, water flow, temperature, and evaporation fluxes (Table 7). Temperature in the soil was assumed to be the same as that measured in the column. Infiltration water flux (q) was estimated from flow (Q) measurements and surface area of the column (283.4 cm^2).

$$q = \frac{Q}{A} \quad [26]$$

Water flow velocities were estimated from water flux and water content (θ_w) estimates,

$$v = \frac{q}{\theta_w} \quad [27]$$

Water content was estimated from soil-water tension measurements by applying the van Genuchten equation and parameters (equation 2). Evaporation fluxes were estimated by solving the Richard's equation (equation 1), using the unsaturated hydraulic conductivities obtained by solving the van Genuchten equation (equation 3).

The amount of air flowing near the soil surface during evaporation periods (air-sweeping flow) was estimated by applying the Poisson equation, using the pressure gradient between two points of the flow line,

$$Q = \frac{\pi \cdot r^4 \cdot \Delta P}{8L \cdot \mu} \quad [28]$$

where, r is the pipe radius, ΔP is the change of pressure between the two points, μ is the dynamic viscosity of the fluid (air) and L is the distance between the two points selected (Roberson and Crowe, 1990). Pressure gradients of 11 and 7 mbars were measured in the delivery line ($r = 0.95\text{cm}$) yielding an estimated flow rate of 14.35 L/min. This flow was divided in four equidistant lines located on the inflowing face of the box. Four outlet points with the same diameter were placed on the opposite (outflowing) face to produce laminar flow near the soil surface.

3.5 Chemical Reagents and Analysis

Transport experiments were conducted using NaCl solution as an unreactive aqueous tracer, and DNT and TNT and target ERCs.

3.5.1 Reagents

TNT (30% minimum water) and DNT crystals with a purity >99% were purchased from Chem Service (West Chester, PA), whereas TNT and DNT standard solutions (concentration in acetonitrile) were from the Restek corp (Bellefonte, PA). Isopentyl acetate anhydrous, tryptic soy broth (TSB), and agar were acquired from the Sigma-Aldrich (St. Louis, MO). Sodium chloride

certified by ACS was purchased from the Fisher Scientific (Fair Lawn, NJ). Distilled and deionized water was obtained from an operational water distillation unit that provides Type I water. Other chemicals used were reagent grade or better.

3.5.2 Chemical Analysis

Spatial and temporal concentrations of NaCl, TNT, and DNT in the soil water and air (only ERCs vapors) phases, were estimated by analyzing water and vapor samples taken from samplers and outlet ports in the soil column system. Generally, NaCl concentrations were analyzed using conductivity detectors, whereas ERC solutes and vapors were analyzed using gas chromatography techniques.

3.5.3 NaCl Concentrations

Aqueous NaCl concentrations in each sampling port were analyzed by measuring the specific conductance (SC) of the sample and applying a calibrated function relating SC and NaCl concentration. NaCl concentration in the reverse-flow experiments were measured by placing a 25 cm³ sample into a 40 mL plastic vial and measuring its SC (in μSICm) with a conductivity probe connected to a conductivity meter (Model 162, Orion). NaCl concentrations in all the experiments (Exp. 3-8) were measured using a flow-through conductivity detector (Model 550, Alltech). The conductivity detector was connected to a HPLC pump delivering a constant flow of 2.0 mL/min of deionized and degassed water. A 0.2 mL of each sample was injected in a high pressure switching valve (Model 7000, Rheodyne) (Figure 18) which delivers the samples in the detector. A Peak Simple Chromatography Data System (Model 203, SRI) was used to obtain the signal from the detector, integrate the pulse response, and determine the SC of the sample. The

conductivity detector was calibrated with 2, 4, 10, 16, 20 and 22 mM NaCl solutions. Figure 19 shows the calibration curve used to determine the NaCl concentration during the transport experiments.

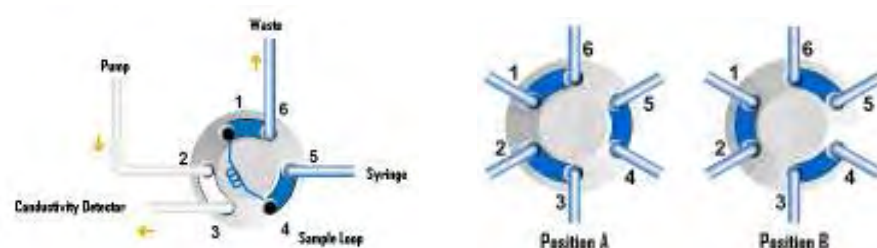


Figure 18. Sample Injection to Conductivity Detector

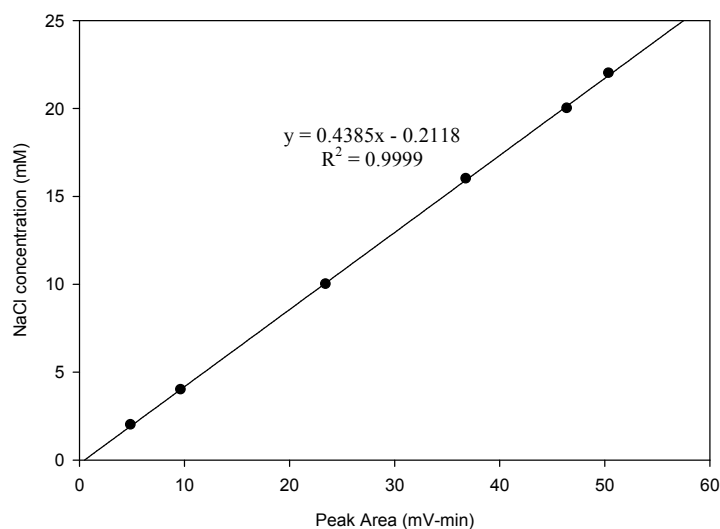


Figure 19. Peak Simple Calibration for NaCl Concentration Determination

3.5.4 ERCs Concentrations

TNT and DNT concentrations were analyzed using various extraction methods and GC techniques. Aqueous TNT and DNT sample concentrations in reverse flow experiments (Exp. 1 and 2, table 7) were analyzed using SPME extraction, followed by analysis in a GC equipped with a thermionic specific detector (Model CP-3800, Varian Inc). SPME was performed using a

SPME autosampler (Model 8400, Varian Inc), which inserted the SPME fiber into the sample for 3 minutes, and then injected into the GC analyte desorption and analysis. The desorption time was set to 5 minutes, the detector temperature was set at 300°C. The oven was initially set at 100°C. ERC analytes in all other experiments (Exp. 3-8) were extracted from aqueous samples through liquid-liquid extractions. Liquid-liquid extraction involves the use of isoamyl acetate as the extractions solvent. Extractions were done at a 1:2 sample/solvent ratio by mixing for 15 minutes, followed by a separation period of 5 minutes. Once extracted, the ERC in the extract was analyzed in a gas chromatography (GC) (Model CP-3800, Varian Inc) equipped with an electron capture detector (ECD) and a thermionic specific detector (TSD). As the concentrations were variable ranging from µg/L to mg/L it was necessary to use both detectors at different sensitivities, setting in all cases the injector temperature at 250°C. The detectors temperatures were set at 300°C and 250°C for ECD and TSD, respectively. The oven was initially set at 100°C for 1 minute, ramped to 150°C at 10°C/min, and ramped again to 200°C at 20°C/min for a total time of 11 minutes. Both injector/detector systems used an ATTM-1 (dimethylpolysiloxane) chromatography column (6 m length, 0.53 mm diameter and 1.5 µm of thickness) for ECD and a CP-Sil 5CB chromatography column (15 m length, 0.25 mm diameter and 0.1 µm of thickness) for TSD. Explosive concentrations were determined using liquid-liquid extraction calibration curves.

After withdrawing gas samples, vapor samples were extracted by inserting a SPME fiber Polydimethylsiloxane/divinylbenzene (65 µm film coating from Supelco) into the sampler for 4 minutes. The sampling time was decided considering the results obtained in other studies (Torres et al., 2007) who determined that a time of 4 minutes was adequate to detect DNT and TNT

concentrations as low as ng/L. The samples were analyzed with a SRI 8610C Gas Chromatograph equipped with a micro electron capture detector and a 0.25 mm x 15 m RTX XLB column (Restek). The injector and detector temperatures were set at 265°C and 300°C, respectively. The oven was initially set at 160°C for 30 seconds, ramped to 175°C at 3°C/min, and ramped again to 195°C at 7°C/min. Explosive concentrations were determined using SPME calibration curves.

3.5.4.1 Aqueous Standards Preparation

For the analysis of the explosive concentrations in water, a mixture of DNT and TNT crystals was dissolved in a 4 mM NaCl solution to prepare TNT-DNT standards. The standards were then extracted and analyzed following the same method as for sample analysis. The calibration curves obtained from standards prepared with explosive crystals (Chem Service) were compared with calibration curves obtained from standard solutions in acetonitrile (Restek) to determine if the crystals were completely diluted in the aqueous solution (Figure 20). Similar results in the calibration curves (Figure 20) validated the use of standards prepared from TNT and DNT crystals.

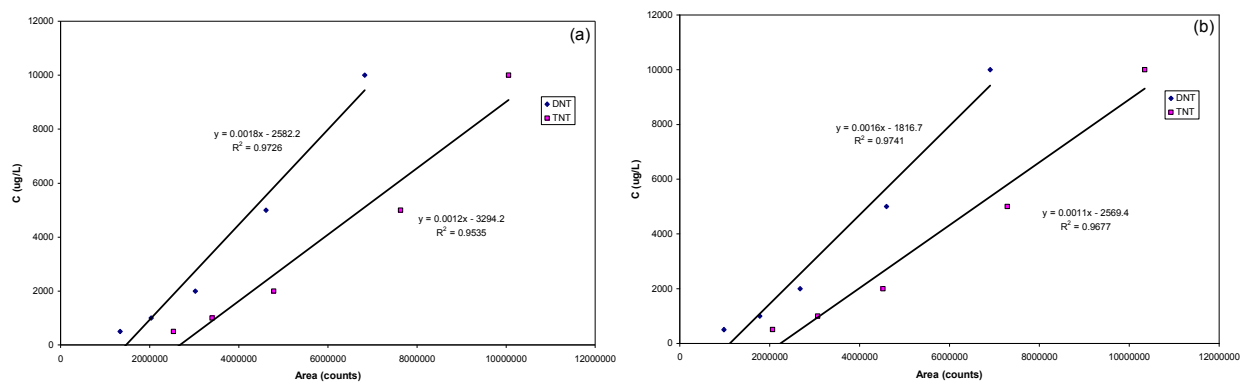


Figure 20. Calibration Curves for Standards Prepared from TNT-DNT in Crystals (a) and TNT-DNT in Solutions in Acetonitrile

3.5.4.2 Vapor Standards Preparation

Vapor standards were prepared from liquid standards, using an 8 mL DNT – TNT mixture which was placed into a 25 mL vial and maintained for at least 10 days to equilibrate the gas and water phases. After equilibrium, the headspace was sampled and analyzed using the SPME method previously described. Headspace concentrations in the vials were calculated as follows:

$$C_A = \frac{C_{W,0}}{\left(\frac{1}{K_H} + \frac{V_A}{V_W}\right)} \quad [29]$$

where, K_H is the Henry's Law constant, $C_{W,0}$ is the initial aqueous concentration, and V_A and V_W are the gas and water volumes, respectively. The K_H values used were of 8.61×10^{-7} for TNT and 1.07×10^{-5} for DNT at 25°C (Table 1).

3.6 Microbial Analysis

Biological degradation is an important factor that may affect the fate and transport of ERCs in soils. Although the evaluation of biological activity was not included into the goals of this study, knowledge of the existence (or absence) of biological activity related to ERC degradation provide important information on the fate and transport behavior of ERCs in the experiments. Therefore, qualitative analysis of heterotrophic microorganism activity was conducted, where agar plate counting was performed in the presence or absence of a TNT-DNT solution on the surface of the agar media. The agar media was prepared with 0.3% (w/v) TSB and 1.5% (w/v) agar solution. For each sampling port, water samples were withdrawn and diluted using 0.9% (w/v) NaCl solution, yielding dilution ratios in the range of 10^{-3} and 10^{-6} . The diluted samples

were applied to the agar plates with and without the ERCs coatings. The ERCs coating was made by spreading 0.5 mL of the TNT-DNT solution in acetone at 5 mg/L each, and allowing the acetone to evaporate. All microbial experiments were conducted in the abiotic and sterile environment. Then, the microorganisms were counted by using a colony counter (Model 3325, Leica).

3.7 Data Analysis

The fate and transport experiments generated spatial and temporal pressure and concentration data. Pressure data was used to estimate water content (see section 3.4) and hydraulic heads (equation 3). Hydraulic gradients were used to quantify water flux and advection processes. Spatial and temporal concentration breakthroughs were analyzed comparatively and analytically to determine transport behavior of solutes and ERCs under the imposed conditions. Analytical assessment involved using the method of moments for temporal concentration distribution. Breakthroughs were also analyzed numerically using HYDRUS 2D code (Šimůnek et al., 2006).

3.7.1 Conservative Solute

The method of moments for temporal concentration distributions was used to characterize the NaCl breakthrough data. Experimental absolute moments, M_n , are obtained through numerical integration of the breakthrough data using the trapezoidal rule (Padilla et al, 1999).

$$M_n = \int_0^{\infty} t^n C(z, t) dt \quad [30]$$

Using this method, the zero (M_0) and first (M_1) moments are calculated as:

$$M_0 = \int_0^{\infty} C(z, t) dt = \sum \left(\frac{C_i + C_{i+1}}{2} \right) (t_{i+1} - t) \quad [31]$$

$$M_1 = \int_0^{\infty} tC(z, t) dt = \sum \left(\frac{C_i t_i + C_{i+1} t_{i+1}}{2} \right) (t_{i+1} - t) \quad [32]$$

The first normalized absolute moment of the input pulse and the effluent concentration signal are used to estimate the mean arrival time of the center of NaCl mass (μ) (Padilla et al, 1999).

$$\mu = \frac{M_I^{II}}{M_0^{II}} - \frac{M_I^I}{M_0^I} \quad [33]$$

where the I and II superscripts refer to the moments of the input and output signals, respectively. The mean arrival time is used in conjunction with the column length L to calculate the pore water velocity ($v = L/\mu$). An effective water content θ_e is estimated from the Darcy flux divided by the moment-derived pore water velocity (Padilla et al, 1999).

$$\theta_e = \frac{Q}{A \cdot v} \quad [34]$$

The v and D values were obtained from inverse modeling using HYDRUSs 2D. These values are used to calculate dispersivity (ε),

$$D = \varepsilon \cdot v + D^* \quad [35]$$

3.7.1.1 Numerical Simulation

NaCl infiltration data was simulated using a non-equilibrium mobile-immobile model (MIM). The MIM was used because comparative and analytical assessment indicated preferential flow in the column.

3.7.1.1.1 Initial and Boundary Conditions

The initial condition for water flow was set to a linear pressure head distributed through the column height from 0 at the upper boundary to 100 at the lower boundary. It is assumed that the initial NaCl concentration through the column is constant (4mM). The simulations were developed using relative NaCl concentrations, normalized to initial concentration (C_o).

$$\frac{C}{C_o} = \frac{C - C_o}{C_f - C_o} \quad [36]$$

where C_f is the inlet concentration (20 mM). Initial concentrations in the model were therefore set to zero.

The upper boundary condition was set for water flow to a constant flux and a third-type boundary condition was used for the solute condition. A third-type boundary condition is used when the solute flux along a boundary is specified (Šimůnek et al., 2006). The lower boundary condition was set for water flow to constant head, knowing that in the bottom is maintained a 100 cm head during the saturated experiments and to -25 cm head for unsaturated experiments.

3.7.1.1.2 Parameters Optimization

The immobile saturated water content ($\theta_{s,im}$) and the immobile water retention ($\theta_{r,im}$) are parameters not fitted during the simulations, but modified until obtaining an adequate model fitting.

D_L , θ_{imw} , and ω parameters were fitted using the inverse module within the HYDRUS-2D software package. HYDRUS-2D uses the Marquart–Levenberg optimization algorithm to achieve the best fit of the parameters (Šimůnek et al., 2006).

4 RESULTS AND DISCUSSION

To accomplish the goals of this research transport experiments were conducted at 25°C and 35°C under different water contents. Results of hydraulic properties and conditions are discussed initially to establish flow behavior in the system. Temporal chemical distribution represented by breakthrough curves (BTC) for NaCl, TNT, and DNT are thereafter presented to establish the fate and transport behavior of ERCs under specific flow, water content, and temperature conditions.

4.1 Pressures

Soil-water pressures data collected during the experiments allow determining the water content of the soil and hydraulic conductivities. Soil-water pressures did not show significant variations during infiltration periods of constant flow, but show significant variations during evaporation periods in unsaturated media (Figures 21-27). Higher soil water pressures were observed for higher temperature (35°C) under saturated infiltration conditions (Figures 21 and 22). The higher pressures at higher temperatures is unexpected and may be caused by expansion of entrapped air, or measurement errors resulting from hydraulic variations of pressure samplers. Soil-water pressures during evaporation periods at saturation for 25°C remain relatively constant at about the same values as during infiltration. At higher temperatures (Figure 22), soil-water pressures during evaporation events were, however, lower than during infiltration. The lower pressures at higher temperatures during evaporation are attributed to higher evaporation rates. Similar behavior was observed for two infiltration/evaporation cycles conducted during experiment (6) (Figures 22 and 23).

As expected, lower soil-water pressures are observed for unsaturated experiments (Figures 24-27). The values tend to be lower for lower water-flux experiments (i.e., lower degree of saturation), and to decrease in time during evaporation periods. Lower pressure values during evaporation periods are observed closest to the evaporation (top) surface and are induced by evaporation water losses. Greater decrease with time near evaporative surfaces are observed for systems subjected to lower initial infiltration fluxes (i.e., lower degree of saturation) and higher temperature. Soil water pressure measurements at 35°C (Figure 26) indicate that pressures decrease rapidly during evaporation. For soil water pressures lower than about -40 cm, the water pressures attain the bubbling pressure of the stainless steel sampler and the measurements do not reflect soil-water pressure conditions.

After infiltration events, soil water pressures near the surface tend to decrease. The rate of decrease (Table 7) depends on initial infiltration flux conditions and depth. Greater increase is observed in sampling ports closest to the surface and for systems subjected to lower infiltration flux (i.e., lower degree of saturation). For ports close to the bottom, soil water pressures increase initially and then decrease to near constant levels. Pressure measurements close to the surface indicate that evaporative losses are greater than the water replenishment rate from the bottom of the column and never attain equilibrium. Measurements close to the bottom attain equilibrium indicating that the rate of upward movement near the water source is similar to the rate of water replenishment. Greater decrease in soil-water pressure with depth for lower saturation conditions indicate lower drainage influenced from above.

Table 7. Temporal Pressure Variations during Evaporation Periods for Ports 4 and 3

Experiment		Temperature (°C)	Initial Degree of Saturation (%)	dP/dt (cm/min)	
				Early-time	Late-time
4	Port 4	25	75	0.0157	0.0005
	Port 3			0.0144	0.0002
5	Port 4	25	45	0.0113	0.0042
	Port 3			0.0072	0.0006
7	Port 4	25	60	0.0240	0.0045
	Port 3			0.0150	0.0008
8	Port 4	35	60	0.0352	0.0030
	Port 3			0.0166	0.0022

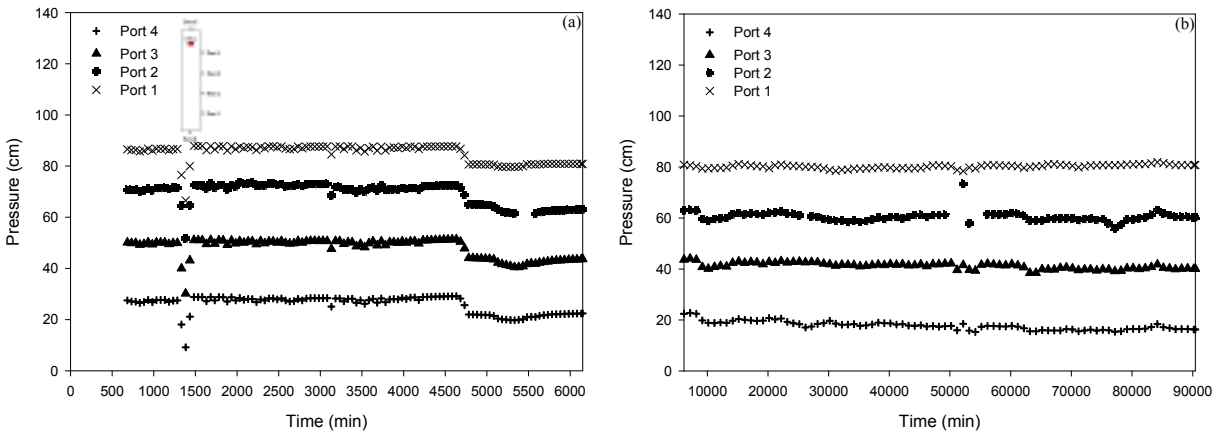


Figure 21. Pressures during Infiltration (a) and Evaporation (b) Processes under Saturated Conditions at 25°C (Exp 3)

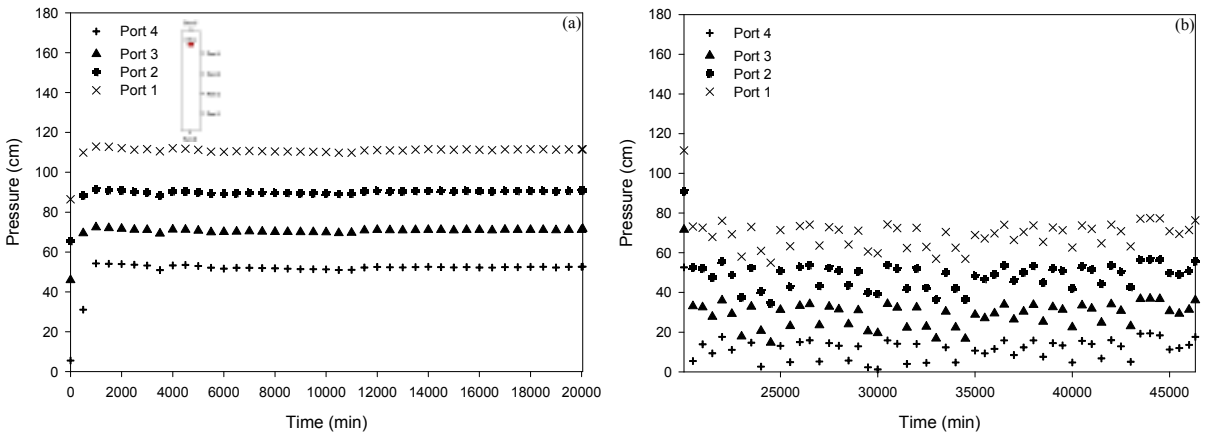


Figure 22. Pressures during Infiltration (a) and Evaporation (b) Processes in the First Stage of the Experiment under Saturated Conditions at 35°C (Exp 6)

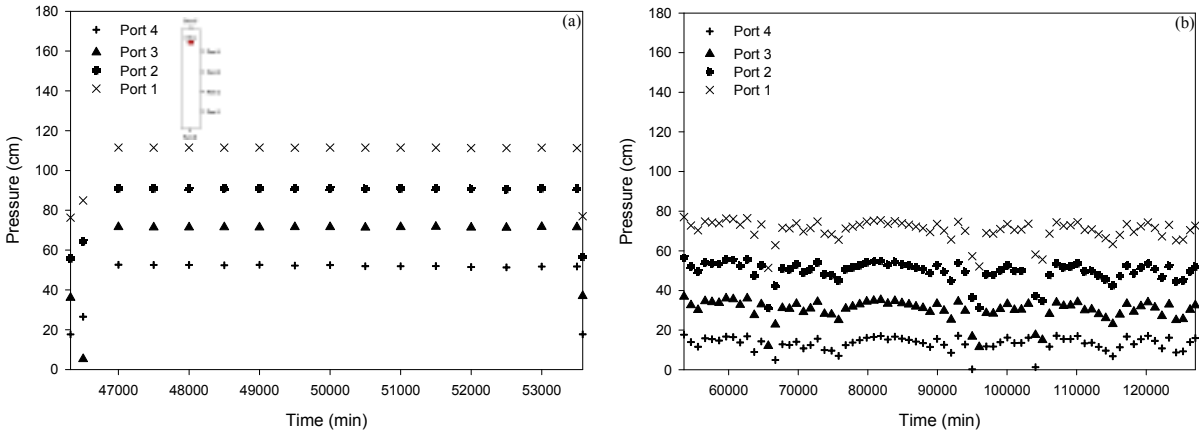


Figure 23. Pressures during Infiltration (a) and Evaporation (b) Processes in the Second Stage of the Experiment under Saturated Conditions at 35°C (Exp 6)

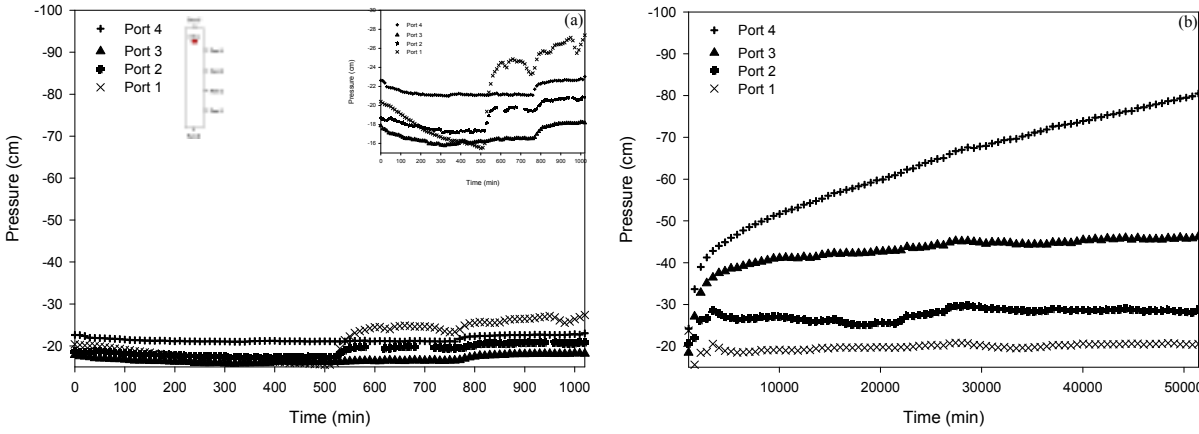


Figure 24. Pressures during Infiltration (a) and Evaporation (b) Processes under 75% of Saturation at 25°C (Exp 4)

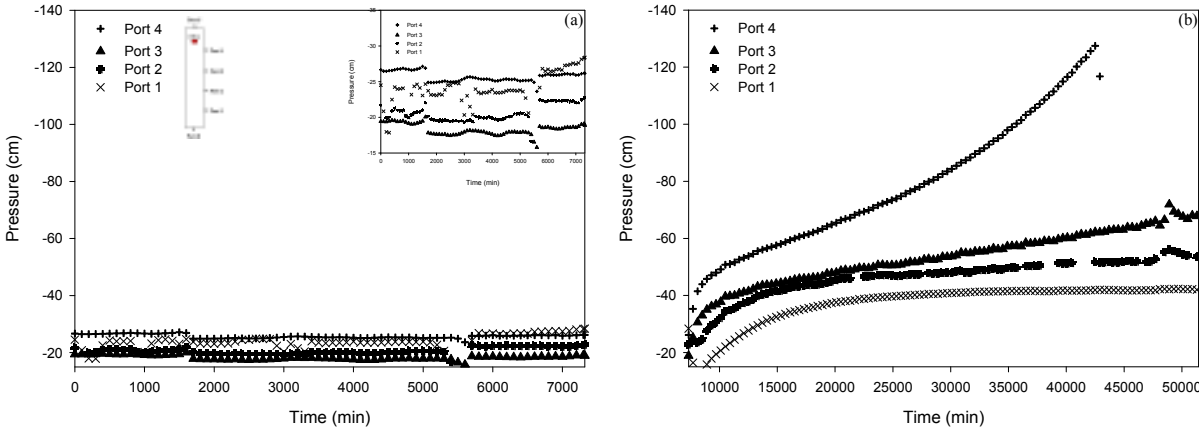


Figure 25. Pressures during Infiltration (a) and Evaporation (b) Processes under 60% of Saturation at 25°C (Exp 7)

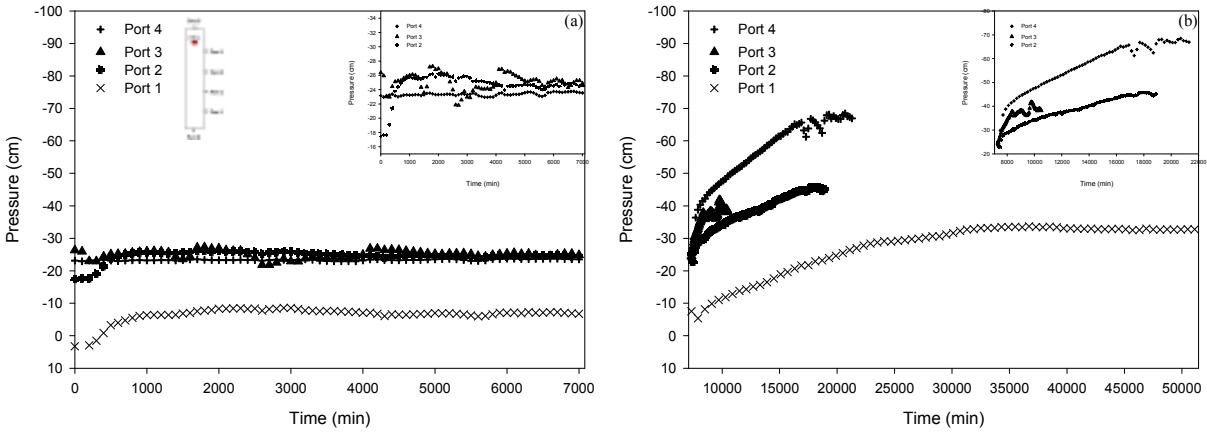


Figure 26. Pressures during Infiltration (a) and Evaporation (b) Processes under 60% of Saturation at 35°C (Exp 8)

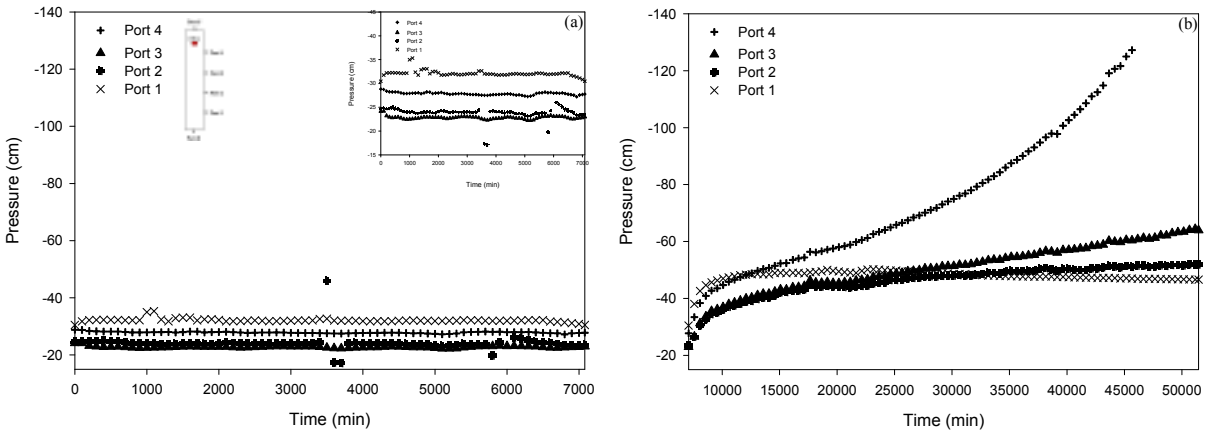


Figure 27. Pressures during Infiltration (a) and Evaporation (b) Processes under 45% of Saturation at 25°C (Exp 5)

4.2 Soil Hydraulic Properties

Saturated hydraulic conductivities were determined by applying hydraulic head data ($h = P_c + z$) calculated from measured pressures and flow rates to equation (1). Pressure measurements during the experiments (Table 8) suggest that measurements errors were higher than the head difference between ports. It was, consequently, not possible to determine hydraulic gradients from adjacent ports. Potential measurements errors may be caused by entrapped air

(from water deaeration) in the pressure transducer lines. For saturated experiments at 25°C (Exp. 1 and 2, Table 6), a general gradient of 0.08 was determined from a plot of elevation vs head (Figure 28). From this value, the saturated conductivity was estimated as 1.77 cm/min (3×10^{-2} cm/s), which is within the range reported for well sorted sands (10^{-3} - 10^{-1} cm/s) (Fetter, 2001). The average saturated hydraulic conductivity estimated from the average gradients calculated for all possible combinations of heads which satisfied downward flow for these two experiments (Exp. 1 and 2) is 4.5 cm/min (7.5×10^{-2} cm/s), which is also within the range of reported values. Hydraulic gradient for saturated experiments 3 and 6 are expected to be lower than experiments 1 and 2 because of the lower water flux (Table 6). As a result there is possibly much larger errors in measurement. Although not physically possible gradients in opposite direction to flow may result from these errors. For these experiments (3 and 6), gradients were estimated as the average for all combinations of heads which satisfied downward flow (i.e., higher heads at higher elevations). No significant difference in saturated hydraulic conductivities is observed for different flow rates and temperatures (Table 8). Generally, hydraulic conductivities are expected to increase as temperature increases because of the much lower fluid viscosity (Hopmans and Dane, 1986). The estimated saturated conductivities from the experiments are, however, influenced by pressure measurement errors, and show no significant differences.

Table 8. Estimated K_s from Steady-State Pressure Data for Saturated Flow Conditions

Z (cm)	Ports Location	Experiment											
		1 (q=0.141 cm/min)			2 (q=0.141 cm/min)			3 (q=0.007 cm/min)			6 (q=0.007 cm/min)		
		P (cm)	h_T (cm)	K_s (cm/min)	P (cm)	h_T (cm)	K_s (cm/min)	P (cm)	h_T (cm)	K_s (cm/min)	P (cm)	h_T (cm)	K_s (cm/min)
100	Top												
78	P ₄	127.94	205.94	23.204 0.983 1.324	125.65	203.65	0.578 0.163 0.898	29.24	107.24	5.926 0.027	55.56	133.56	0.121 0.286
58.5	P ₃	147.32	205.82		152.51	211.01		52.26	110.76		73.92	132.42	
39	P ₂	164.02	203.02		155.13	194.13		75.91	114.91		93.60	132.60	
19.5	P ₁	181.44	200.94		185.38	204.88		90.33	109.83		115.61	135.11	
0	Dattum												
Estimated Column Average		155.18	203.93	4.500	154.67	203.42	4.500	61.93	110.68	2.977	84.67	133.42	0.203
Standard Deviation		22.89	2.40	9.000	24.43	6.98	9.000	26.86	3.19	4.171	25.82	1.23	0.117

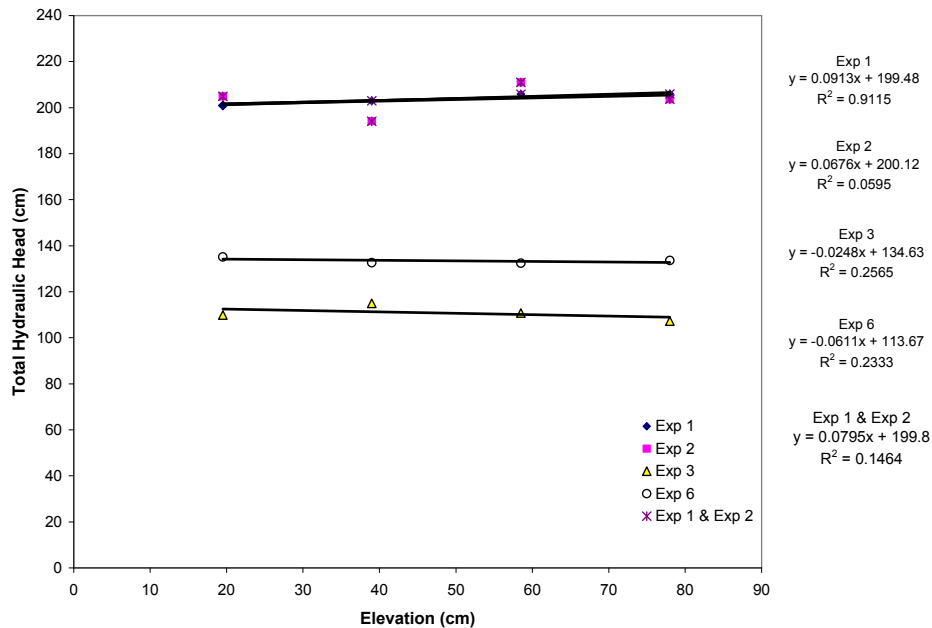


Figure 28. Total Hydraulic Heads vs Elevations

Under saturated flow conditions, water contents were indirectly obtained from the soil water characteristic curve (SWCC) generated with ROSETTA (Figure 29). Unsaturated hydraulic conductivities (Figure 30) were estimated from the ROSETTA-generated van

Genuchten parameters (Table 9). The SWCC and van Genuchten parameters generated for the Isabela sand are given in Table 9.

Table 9. Soil Hydraulic Properties Obtained Using ROSETTA Computer Program

Parameter	Value
θ_r	0.0492
θ_s	0.3371
α	0.0335
n	2.8176
K_s	14.325

The saturated hydraulic conductivity estimated with ROSETTA (0.24 cm/min) was within the range estimated from experimental measurements. ROSETTA-estimated saturated water content (thus porosity) was lower (34%) than the estimated with equation (24). It is suspected that the sand particle density (ρ_p) may be lower than measured. If a value of $\rho_p=2.6$ (commonly used for sandy soils; Myers et al., 1998) is used with a bulk density of 1.65 g/cm^3 to estimate porosity from equation (24), a porosity value of 36% would be estimated. This would be closer to the value given by ROSETTA, and conforms better to the data obtained for NaCl BTCs (discussed at a later section).

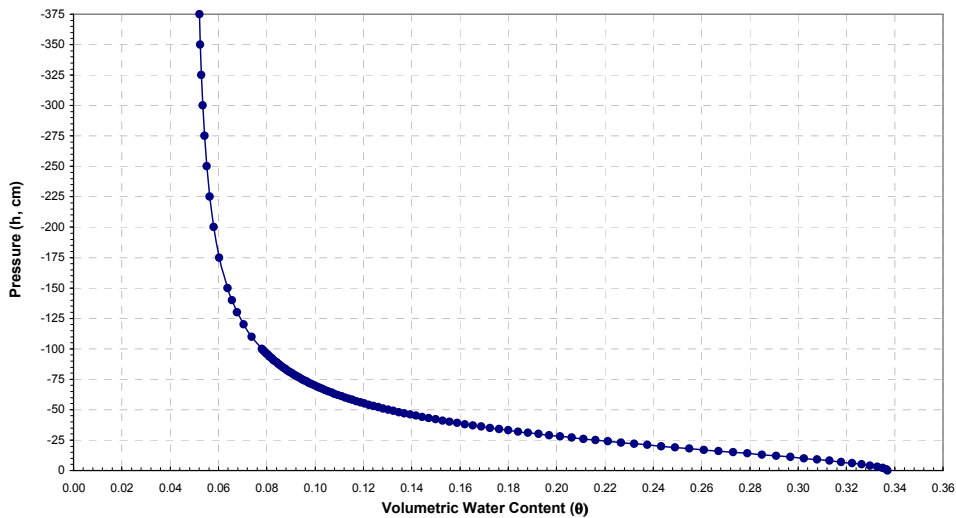


Figure 29. Estimated SWCC for Isabela Sand

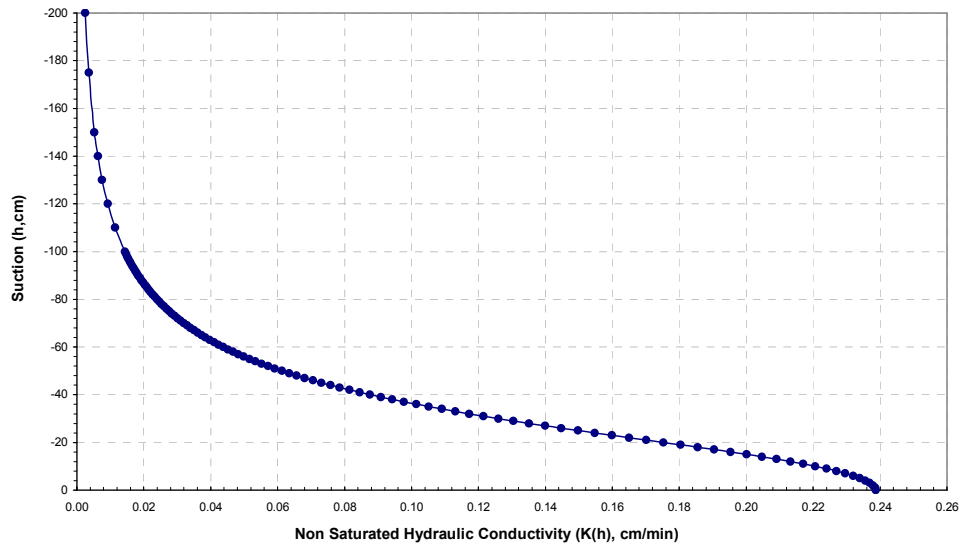


Figure 30. Estimated non-Saturated Hydraulic Conductivities Function $K(h)$ for Isabela Sand

4.3 Soil-Water Contents

Soil-water contents through the column during infiltration and evaporation events are shown in Figures 31 and 32 for 25 and 35°C, respectively. Infiltration pressures reached steady-state conditions relatively rapidly and steady water contents are only shown as a function of depth (not time) at 25°C (Figures 31 a, b, c, d, e) and 35°C (Figures 32 a and b). Water contents are assumed constant through depth for saturated experiments. Assuming homogeneous media the saturated water content (thus porosity) is assumed as 34%, which is the value obtained from ROSETTA.

For unsaturated experiments, water contents are determined from measured soil-water pressures and the ROSETTA-generated SWCC water contents show variations along the depth of the column at 25°C (Figures 31 d, e, f, j, k, l) and 35°C (Figures 32 b and d) for infiltration and evaporation periods. Because soil-water pressure reach constant values relatively rapid for

infiltration events, soil water contents are assumed constant through the infiltration periods. They, however, vary with time for evaporation periods (Figures 31 j, k, l and 32 d).

Soil water content variations during the infiltration experiments result from flow processes under non-unit hydraulic gradients and soil heterogeneity. Although somewhat variable, water contents under unsaturated infiltration tend to decrease with depth for temperatures at 25°C (Figure 31). As expected, lower average water contents throughout the column are observed for lower water flux rates (Table 6).

Water contents during evaporation periods tend to decrease with time for the higher water content (i.e., higher infiltration water flux) experiments at 25°C (Figure 31 j and l). The temporal trend depends on elevation for the lower water content (Figure 31 k) experiment at 25°C and the higher temperature condition (Figure 25 d). Generally, water contents decreased with soil elevation (i.e., increased with depth), reflecting the effect of top and bottom boundary conditions, and soil hydraulic properties. These results suggest that during evaporation events the main process affecting flow movement is drainage. At higher temperatures (35°C) lower soil water contents are however, observed at the beginning of the experiment at the base of the soil. This phenomenon can be explained because of the lower water retention capacity of the soil at higher temperatures, which results in greater drainage.

Comparison of Figures 31(l) and 32(d) for experiments developed for similar boundary conditions and water flux but different temperatures show higher soil water contents at higher temperatures. The higher water contents are a reflectance of higher soil water pressures and may not necessarily result from higher water contents. Indeed it is suspected that these values result

from measurement errors caused by changes in the hydraulic properties of the stainless-steel samplers. For 5 μm size porous cups the theoretical bubbling pressures are 287.7 and 281.5 mbar for 25°C and 35°C, respectively. The bubbling pressures measured before experimental period ranged between 116 and 125 mbar at 25°C, and during experimental period bubbling pressures ranged from 128 to 130 mbar at 25°C and from 38 to 69 mbar at 35°C. It must be considered that the Capillarity equation from Grant and Salehzadeh (1996) is used to calculate the bubbling pressures. This equation suggests that the liquid-gas interfacial tension is temperature-dependent. The ratio between the theoretical and pre-experiment bubbling pressures is almost 2:1, suggesting that the contact angle is higher than 0° and/or there are higher pore sizes than the specified by the provider. To determine the theoretical bubbling pressures was used a 0° contact angle, which corresponds to the interfacial angle between water and sand. However, the contact angle between water and stainless steel is expected to be greater to 15° assuming that is hydrophilic (Roero, 2004). This would reduce the estimated water contents. It is also possible that soil water pressures reached the bubbling pressures of the samplers, resulting in erroneous water pressure measurements.

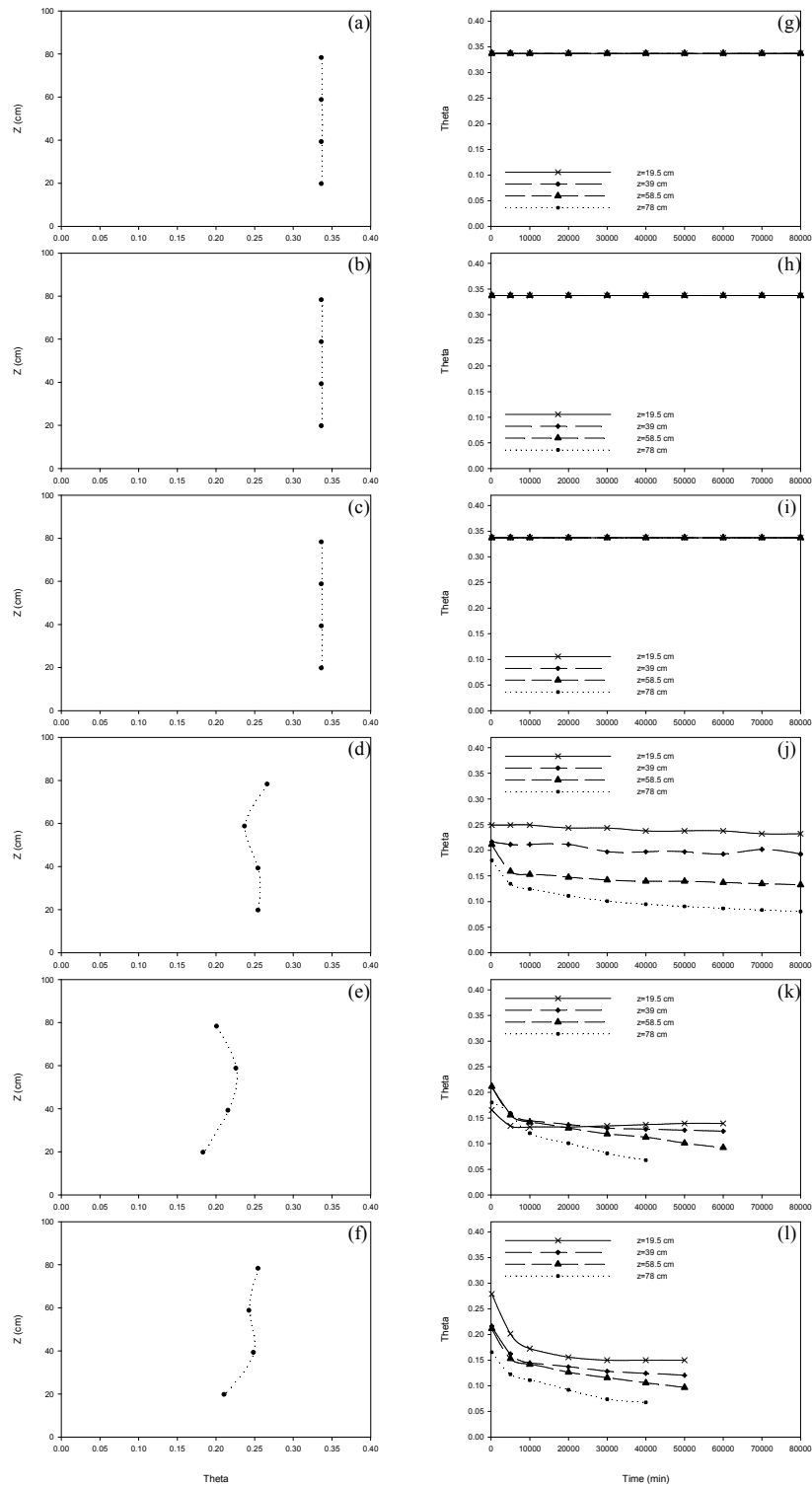


Figure 31. Soil Water Content at 25°C during: Infiltration Process for Exp 1 (a), Exp 2 (b), Exp 3 (c), Exp 4 (d), Exp 5 (e), Exp 7 (f); and Evaporation Process for Exp 1 (g), Exp 2 (h), Exp 3 (i), Exp 4 (j), Exp 5 (k), Exp 7 (l)

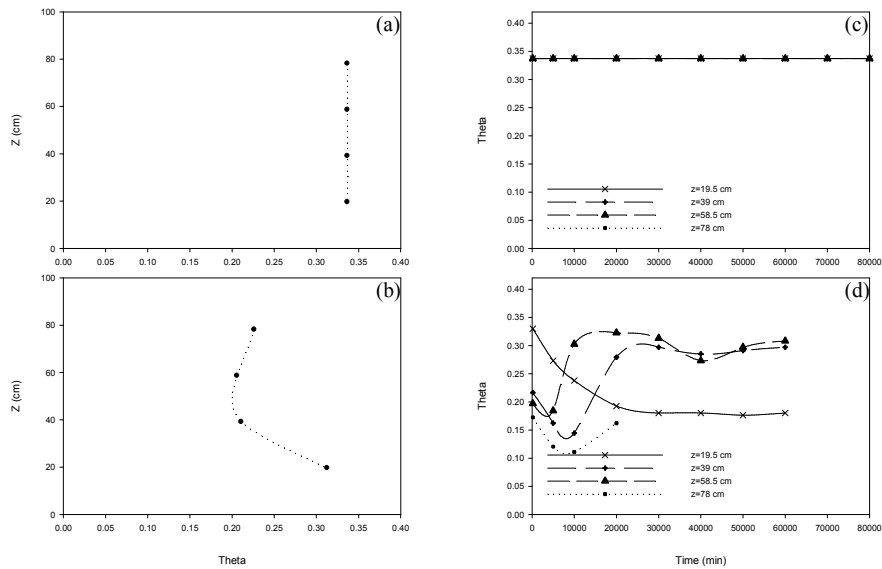


Figure 32. Soil Water Content at 35°C during: Infiltration Process for Exp 6 (a), Exp 8 (b); and Evaporation Process for Exp 6 (c), Exp 8 (d)

4.4 Soil-Water Flux

Water flux during infiltration experiments were estimated as the infiltration volumetric flow rate (Q) over the column area (A), assuming 1D uniform flow over the column area. Evaporation flux for unsaturated conditions was estimated from hydraulic gradients at upper ports (port 3 and 4) and an average $K(\theta)$ estimated from the SWCC parameters. Evaporation water fluxes for saturated conditions were estimated from replenishment volumes in the Mariotte's bottle.

Downward head gradients for unsaturated infiltration (Figures 33 through 36) show downward water flux, possibly of different magnitudes with depth. During the evaporation period, total heads decrease with time (Figures 33b, 34b, 35 b and 36b). Initial gradients after the onset of the evaporation period indicate drainage of the water column. Greater temporal changes

for the upper ports indicate that water is being drained to lower portions of the soil and water pressures are being influenced by surface evaporations. At some time during the evaporation period, total head gradients are reversed near the surface of the soil, involving upward evaporative fluxes.

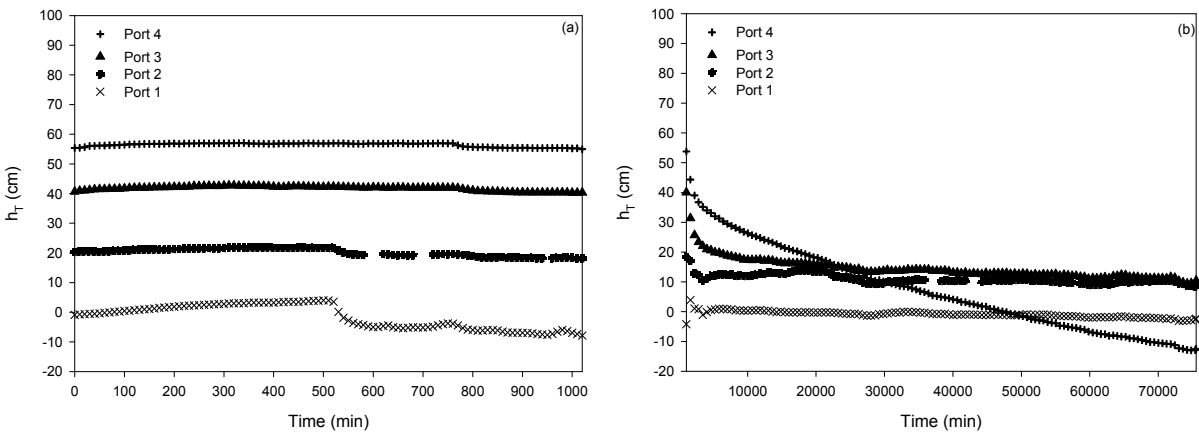


Figure 33. Total Hydraulic Heads during Infiltration (a) and Evaporation (b) Processes under 75% of Saturation at 25°C (Exp 4)

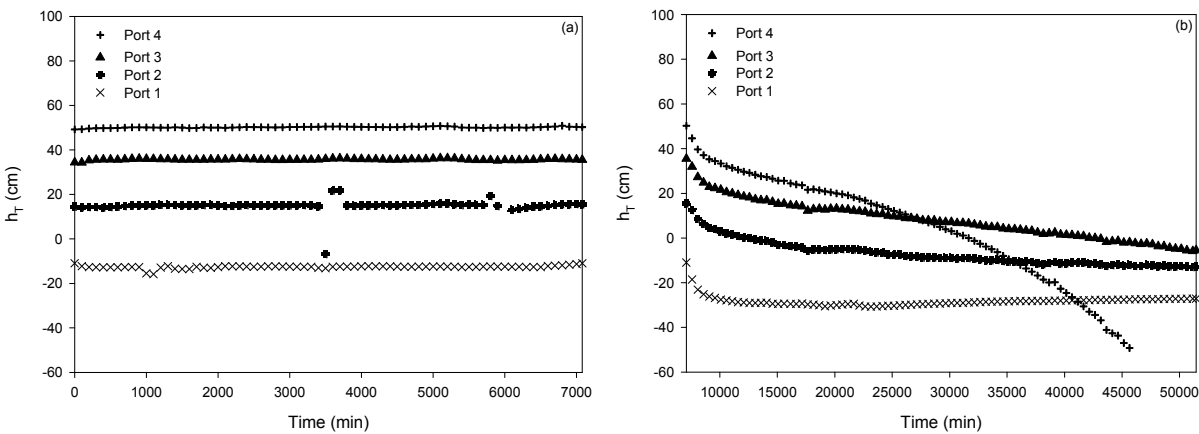


Figure 34. Total Hydraulic Heads during Infiltration (a) and Evaporation (b) Processes under 45% of Saturation at 25°C (Exp 5)

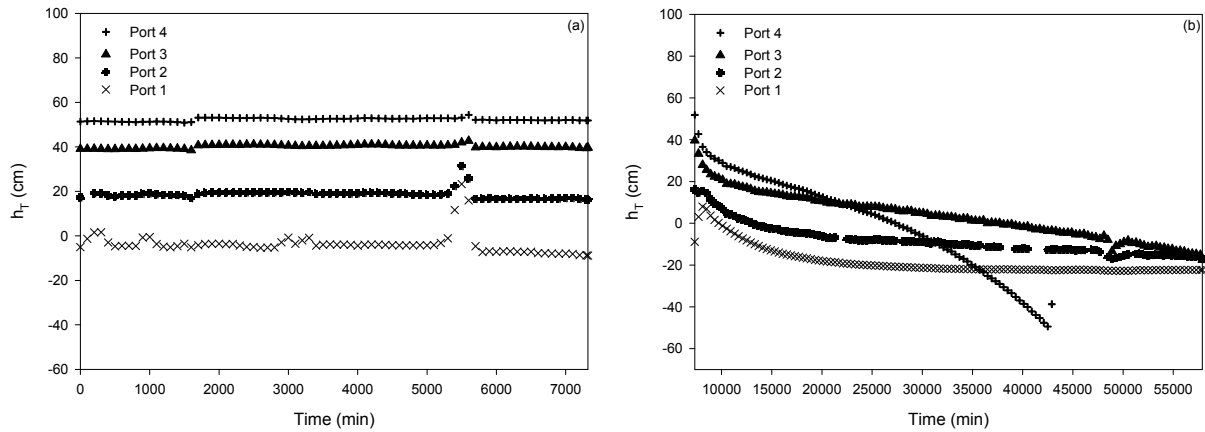


Figure 35. Total Hydraulic Heads during Infiltration (a) and Evaporation (b) Processes under 60% of Saturation at 25°C (Exp 7)

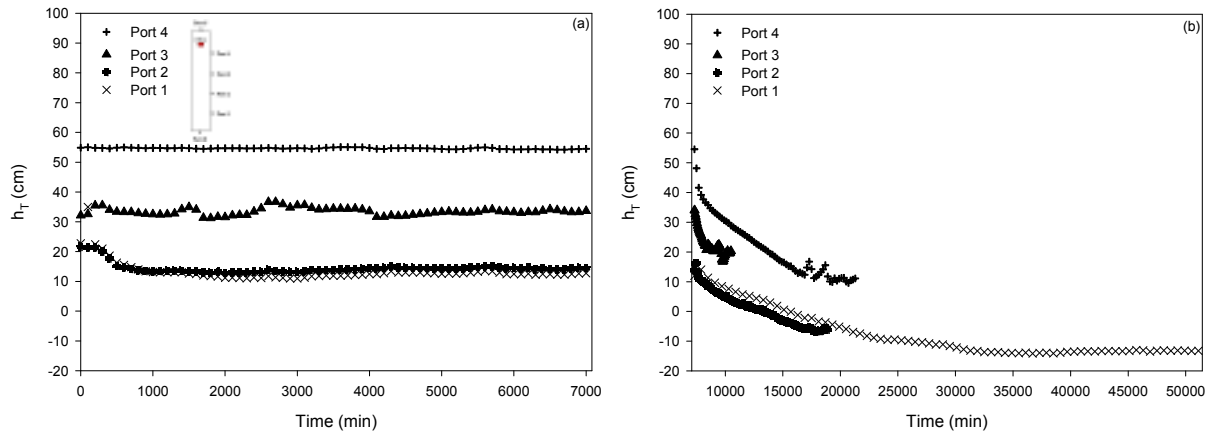


Figure 36. Total Hydraulic Heads during Infiltration (a) and Evaporation (b) Processes under 60% of Saturation at 35°C (Exp 8)

Estimated water evaporation fluxes (Table 10) indicate lower water fluxes for saturated than unsaturated conditions. Generally as water content decreases, evaporation fluxes are expected also to decrease as lower amount of water is available for evaporation (greater amount of water retained by soil) at lower water contents. Lower-than-expected estimates of evaporation flux at saturation may be caused by measurements error in the Mariotte's bottle. The large area of the bottle precluded the accurate measurement in water level readings.

For saturated conditions, higher temperatures result in higher evaporation flux (Table 10). For unsaturated conditions, the higher temperatures induce greater drainage. Under these conditions the upward evaporative flux is counterbalanced by downward drainage.

Table 10. Water Flux from toward the End of Evaporation Period

Experiment	P (cm)		dh/dL	K(h) (cm/min)		K(h) average (cm/min)	q (cm/min)
	Port 4	Port 3		Port 4	Port 3		
3							0.022
4	-90.89	-48.98	2.149	0.018	0.063	0.041	0.087
5	-128.60	-60.53	3.491	0.008	0.043	0.025	0.089
6							0.034
7	-129.00	-62.40	3.415	0.008	0.040	0.024	0.082
8	-49.13	-38.17	0.562	0.063	0.094	0.079	0.044

Note: For experiments 3 and 6, water fluxes were calculated from replenishment volumes in the Mariotte's bottle

4.5 Breakthrough Curves

Temporal concentration distributions or breakthrough curves (BTCs) were analyzed for NaCl, TNT and DNT to determine the transport behavior of conservative and reactive chemicals throughout the column under different experimental conditions imposed. NaCl BTCs represent the transport behavior of aqueous conservative tracers (move as water) in principally downward (1D) flow. TNT and DNT BTCs represent the fate and transport behavior of ERCs from a point source and its assume to occur in at least two dimensions.

4.5.1 NaCl BTCs

NaCl BTCs were used to determine the mean arrival time of the center of solute mass (μ). The mean arrival time is used in conjunction with the column length L to calculate the pore

water velocity (v). An effective water content ($\theta_e = q/v$) is, thereafter, estimated from pore water velocity and water flux measurements ($q = Q/A_e$).

NaCl BTCs were analyzed for infiltration process. Limited measurable and highly variable flow conditions (e.g., drainage and evaporative flux) precludes the use of BTCs generated during evaporation events. Limited water samples were obtained for unsaturated experiments during the evaporation period. Samples were only obtained for bottom ports (port 1 and port 2). Limited sampling volume (~2 mL) precluded the analyses for NaCl, thus these samples were only analyzed for ERCs.

NaCl BTCs during saturated infiltration and evaporation events at 25°C (Figure 37) show downward advection transport throughout the entire columns during infiltration events. Greater dispersion around the center of mass (wider temporal concentration distribution) is observed at greater depth for infiltration periods. Initially, decreasing NaCl concentrations for the lower column ports (ports 1, 2 and 3) during evaporation periods in unsaturated conditions show upward displacement of 20 mM resident solution with the lower NaCl background solution used as evaporation replenish source. Lower and later decrease is observed for higher elevation port. It is attributed to delayed upward movement of background solution. NaCl concentrations near the evaporative surface (and farther away from the evaporation replenishment source) tend to remain constant initially, followed by a significant increase in concentration above the concentration of the infiltrating solution. This is caused by solute accumulation concentration as water evaporates. Solute concentration is also observed in the lower column ports at later times.

Higher-than-inlet NaCl concentrations are initially observed in the infiltration BTCs (Figure 37 a). For organic compounds this behavior has been attributed to a phenomenon denominated “rollup” effect (Thibaud et al., 1993) caused by initial different affinities between the substances and the soil when water is initially infiltrated.

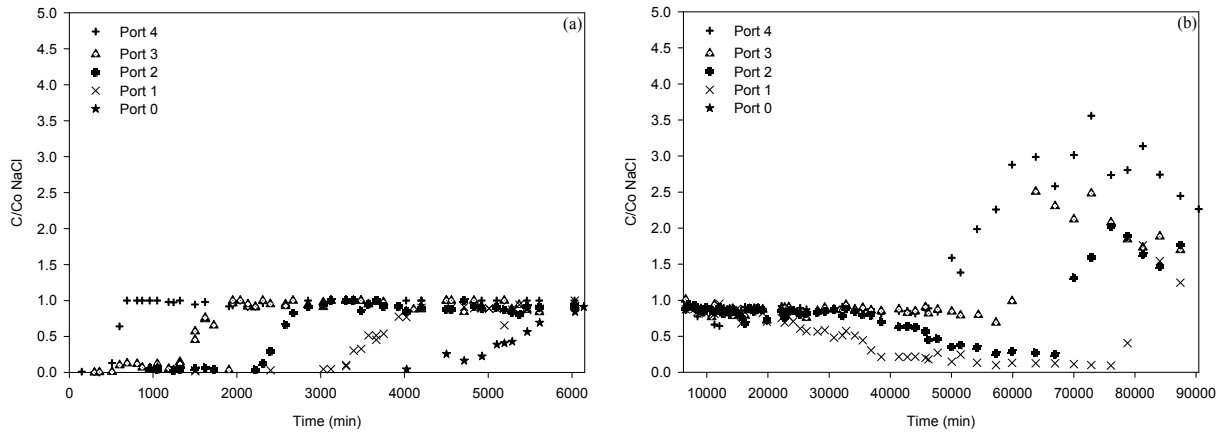


Figure 37. NaCl BTC during Infiltration (a) and Evaporation (b) Processes under Saturated Conditions at 25°C (Exp 3)

NaCl BTCs at higher temperatures (Figures 38 and 39) suggest similar transport behavior processes to those at lower temperatures (Figure 37) with some particular differences: higher “roll up” effects during infiltration periods; increasing NaCl concentrations from the bottom up during evaporation periods; and higher accumulation concentrations near the evaporative surfaces. Increasing NaCl concentrations from the bottom up during evaporation periods result from upward displacement of the 4 mM resident solution at the end of the infiltration period with a higher (20 mM) NaCl background solution used as evaporative replenishment source. The higher accumulation concentration is attributed to greater evaporative flux and greater initial salt concentration in the replenishment water.

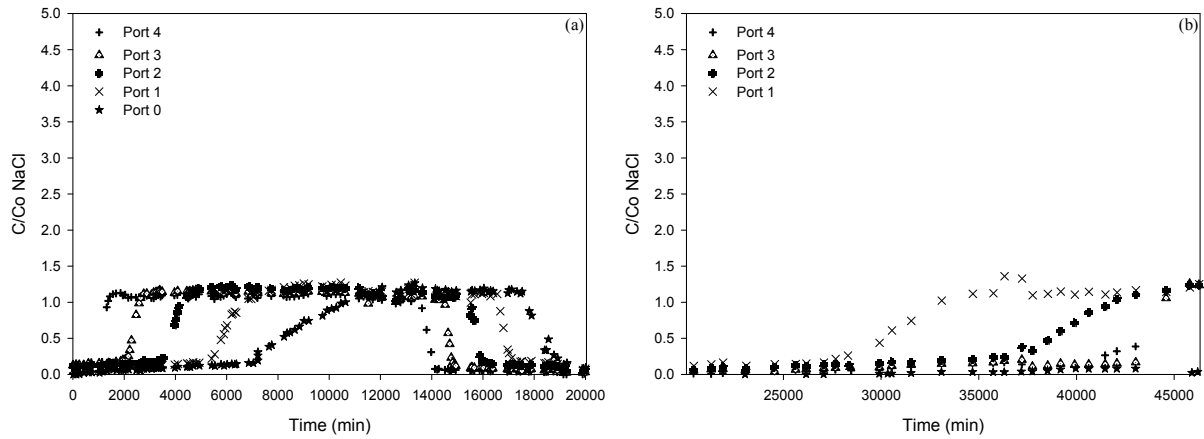


Figure 38. NaCl BTC during Infiltration (a) and Evaporation (b) Processes in the First Stage of the Experiment under Saturated Conditions at 35°C (Exp 6)

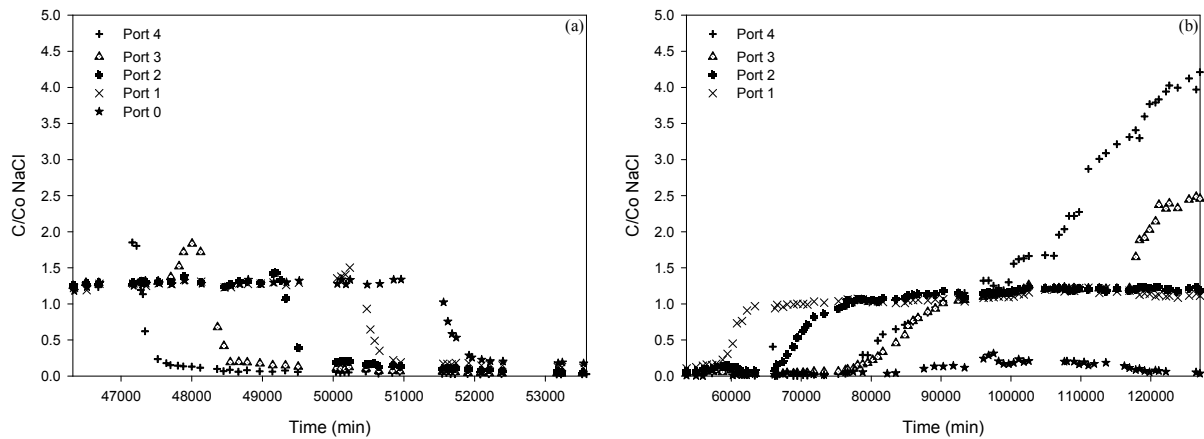


Figure 39. NaCl BTC during Infiltration (a) and Evaporation (b) Processes in the Second Stage of the Experiment under Saturated Conditions at 35°C (Exp 6)

NaCl BTCs were analyzed using the method of moments on temporal concentration distributions. Zeroth and the first moments were determined for the displacement of background solution (termed frontal elution, Table 12) and the complete elution of a NaCl slug injection (termed slug elution, Table 12). Frontal elution moments were estimated as:

$$M_n = \int_{t=0}^{t=t^*} \left(1 - \frac{C}{C_0}\right) t^n dt \quad [37]$$

where t^* is the time at which C/C_0 reaches 1. The moments for slug elution were determined as:

$$M_n = \int_0^{\infty} \frac{C}{C_0} t^n dt \quad [38]$$

Both methods of analysis were used because not all the experiments had slug data distribution. The soil parameters obtained during the analysis of moments for the NaCl BTCs achieved through the experimental period are presented in Table 11. The results obtained from both analysis (Table 12) show significant differences, most likely caused by the lack of data from the displaced mass that carries on to truncated moments of the frontal elution causing considerable integration errors (Jawitz, 2004; Young and Ball, 2000). The ratio between mass measured and theoretical mass shows that the data obtained using the frontal elution differ significantly from the expected mass. It was, consequently, decided to modify experimental techniques to include slug injections during infiltration events. Table 12 shows the high variability in the pore water velocities and effective water in depth, due to non-unit hydraulic gradients and soil heterogeneity.

Temporal moments of slug injection indicate slightly greater mass recovery that injected (Table 11). The difference is mostly attributed to integration errors and error caused by the assumption of direct relationship between NaCl concentration and specific conductance. Although, it is assumed that this error is small, the presence of any electrically conductive (e.g., Ca^{+2}) specie will affect the conductance measurement.

Table 11. Parameters Obtained from NaCl BTCs using the Method of Moments during Infiltration Process

Experiment	Parameter	Slug					Front				
		Port 4	Port 3	Port 2	Port 1	Port 0	Port 4	Port 3	Port 2	Port 1	Port 0
1	Mean Arrival Time (μ)	ND	ND	ND	ND	ND	33.21	95.97	141.96	183.19	234.53
	Pore Water Velocity (v)	ND	ND	ND	ND	ND	0.66	0.43	0.43	0.44	0.43
	Effective Water Content (θ_e)	ND	ND	ND	ND	ND	21.29	32.62	32.83	32.10	33.09
	Total Mass Measured (mg)	ND	ND	ND	ND	ND	1816.65	1830.41	2469.80	2847.94	17844.32
	Theoretical Mass (mg)	ND	ND	ND	ND	ND	613.03	1156.41	1699.78	2243.15	2786.52
	Mass Ratio (Measured/Theor)	ND	ND	ND	ND	ND	2.96	1.58	1.45	1.27	6.40
2	Mean Arrival Time (μ)	ND	ND	ND	ND	ND	25.96	62.63	118.48	159.81	ND
	Pore Water Velocity (v)	ND	ND	ND	ND	ND	0.85	0.66	0.51	0.50	ND
	Effective Water Content (θ_e)	ND	ND	ND	ND	ND	16.65	21.29	27.40	28.01	ND
	Total Mass Measured (mg)	ND	ND	ND	ND	ND	1395.10	1820.32	2562.56	3060.62	ND
	Theoretical Mass (mg)	ND	ND	ND	ND	ND	613.03	1156.41	1699.78	2243.15	ND
	Mass Ratio (Measured/Theor)	ND	ND	ND	ND	ND	2.28	1.57	1.51	1.36	ND
3	Mean Arrival Time (μ)	ND	ND	ND	ND	ND	336.57	894.20	1587.27	2332.82	4331.19
	Pore Water Velocity (v)	ND	ND	ND	ND	ND	0.07	0.05	0.04	0.03	0.02
	Effective Water Content (θ_e)	ND	ND	ND	ND	ND	10.79	15.20	18.36	20.44	30.55
	Total Mass Measured (mg)	ND	ND	ND	ND	ND	798.15	2189.86	3183.70	4578.31	5067.75
	Theoretical Mass (mg)	ND	ND	ND	ND	ND	655.95	1237.35	1818.76	2400.17	2981.58
	Mass Ratio (Measured/Theor)	ND	ND	ND	ND	ND	1.22	1.77	1.75	1.91	1.70
4	Mean Arrival Time (μ)	ND	ND	ND	ND	ND	32.38	67.43	100.80	112.56	425.24
	Pore Water Velocity (v)	ND	ND	ND	ND	ND	0.68	0.62	0.61	0.72	0.24
	Effective Water Content (θ_e)	ND	ND	ND	ND	ND	10.38	11.46	11.66	9.86	30.00
	Total Mass Measured (mg)	ND	ND	ND	ND	ND	990.41	2327.16	3413.45	3868.49	4462.34
	Theoretical Mass (mg)	ND	ND	ND	ND	ND	617.63	1165.08	1712.53	2259.97	2807.42
	Mass Ratio (Measured/Theor)	ND	ND	ND	ND	ND	1.60	2.00	1.99	1.71	1.59
5	Mean Arrival Time (μ)	384.33	875.77	1086.83	1376.15	2202.28	171.03	420.17	550.87	676.57	1208.26
	Pore Water Velocity (v)	0.06	0.05	0.06	0.06	0.05	0.13	0.10	0.11	0.12	0.08
	Effective Water Content (θ_e)	12.32	14.89	12.57	12.06	15.53	5.48	7.14	6.37	5.93	8.52
	Total Mass Measured (mg)	6544.52	6498.37	6509.53	6566.90	6451.63	502.51	1337.40	1647.30	2129.45	3600.49
	Theoretical Mass (mg)	6184.76	6184.76	6184.76	6184.76	6184.76	634.49	1196.88	1759.27	2321.66	2884.05
	Mass Ratio (Measured/Theor)	1.06	1.05	1.05	1.06	1.04	0.79	1.12	0.94	0.92	1.25
6	Mean Arrival Time (μ)	1243.31	2132.68	3337.10	4828.94	6675.86	680.66	1177.70	1908.08	2915.48	4235.78
	Pore Water Velocity (v)	0.02	0.02	0.02	0.02	0.01	0.03	0.04	0.03	0.03	0.02
	Effective Water Content (θ_e)	20.43	18.58	19.78	21.69	24.13	11.19	10.26	11.31	13.09	15.31
	Total Mass Measured (mg)	12768.63	13144.72	13194.66	12365.99	10769.19	983.68	1812.16	3032.77	4759.93	7057.26
	Theoretical Mass (mg)	11546.30	11546.30	11546.30	11546.30	11546.30	659.01	1243.14	1827.26	2411.39	2995.51
	Mass Ratio (Measured/Theor)	1.11	1.14	1.14	1.07	0.93	1.49	1.46	1.66	1.97	2.36
7	Mean Arrival Time (μ)	231.34	378.07	569.46	562.28	801.86	239.76	189.63	188.39	222.06	325.48
	Pore Water Velocity (v)	0.10	0.11	0.11	0.14	0.12	0.09	0.22	0.32	0.36	0.31
	Effective Water Content (θ_e)	37.09	32.13	32.93	24.64	28.28	38.44	16.12	10.89	9.73	11.48
	Total Mass Measured (mg)	29808.31	30629.04	31470.26	30404.04	31433.51	1018.53	1540.31	2451.49	3633.94	5554.15
	Theoretical Mass (mg)	28641.60	28641.60	28641.60	28641.60	28641.60	613.03	1156.41	1699.78	2243.15	2786.52
	Mass Ratio (Measured/Theor)	1.04	1.07	1.10	1.06	1.10	1.66	1.33	1.44	1.62	1.99
8	Mean Arrival Time (μ)	224.42	357.07	509.62	611.08	917.91	42.40	89.31	166.23	214.66	367.86
	Pore Water Velocity (v)	0.10	0.12	0.12	0.13	0.11	0.52	0.46	0.37	0.38	0.27
	Effective Water Content (θ_e)	35.98	30.35	29.47	26.77	32.37	6.80	7.59	9.61	9.41	12.97
	Total Mass Measured (mg)	32356.97	33231.59	33016.42	33888.34	34201.81	747.37	1562.97	2807.63	3797.22	6036.85
	Theoretical Mass (mg)	28641.60	28641.60	28641.60	28641.60	28641.60	613.03	1156.41	1699.78	2243.15	2786.52
	Mass Ratio (Measured/Theor)	1.13	1.16	1.15	1.18	1.19	1.22	1.35	1.65	1.69	2.17

ND - No Determined

Table 12. Average of Pore Water Velocities and Effective Water Contents throughout the Column during Infiltration Process

Experiment	Parameter	Slug		Front	
		Column-Average value	Standar Deviation	Column-Average value	Standar Deviation
1	Pore Water Velocity (v, cm/min)	--	--	0.48	0.10
	Effective Water Content (θ_{e^*} , %)	--	--	30.39	5.10
2	Pore Water Velocity (v, cm/min)	--	--	0.63	0.16
	Effective Water Content (θ_{e^*} , %)	--	--	23.34	5.39
3	Pore Water Velocity (v, cm/min)	--	--	0.04	0.02
	Effective Water Content (θ_{e^*} , %)	--	--	19.07	7.38
4	Pore Water Velocity (v, cm/min)	--	--	0.57	0.19
	Effective Water Content (θ_{e^*} , %)	--	--	14.67	8.60
5	Pore Water Velocity (v, cm/min)	0.05	0.01	0.11	0.02
	Effective Water Content (θ_{e^*} , %)	13.47	1.61	6.69	1.19
6	Pore Water Velocity (v, cm/min)	0.02	0.00	0.03	0.00
	Effective Water Content (θ_{e^*} , %)	20.92	2.12	12.23	2.00
7	Pore Water Velocity (v, cm/min)	0.12	0.02	0.26	0.11
	Effective Water Content (θ_{e^*} , %)	31.01	4.74	17.33	12.05
8	Pore Water Velocity (v, cm/min)	0.11	0.01	0.40	0.10
	Effective Water Content (θ_{e^*} , %)	30.99	3.44	9.28	2.39

NaCl BTCs normalized to distance (using por volumes = tL/v , v estimated from the moment method) in different ports during infiltration and evaporation events (Figures 40 through 45) show faster solute infiltration and preferential flow near the surface induced by soil disturbance during source burial. However, the preferential flow paths pattern near the surface is even more severe as soil dries. NaCl shows earlier initial arrival and more tailing as water content decreases (Figure 46).

Several observations can be made from the solute arrival times estimates for infiltration processes (Table 11) using frontal and slug elution methods. These observations are summarized in the following assertions:

- Pore water velocities estimated with the frontal method are generally higher than for slug method. The frontal method only evaluates the displacement velocities of the resident pore

background water (with the arrival front of the 20 mM tracer). The slug method integrates the pore water velocities of the solute slug during the displacement of the resident pore background water with the NaCl arrival front and the displacement of the 20 mM solution with background water (elution front). Differences are attributed to greater temporal and spatial sampling volumes in the slug method. It is assumed that slug velocities are more representative of the average flow conditions in the columns. Because several experiments did not have NaCl slug data, general trends are analyzed for the frontal elution method.

- Pore water velocities estimated with the frontal method, generally suggest greater velocities, thus lower effective water contents, closest to the soil surface (port 4) than the other ports. Lower effective water content estimates than saturated porosity ($n=0.34-0.41$, depending on method analysis for saturated conditions (Exp. 1, 2, 3 and 6)) suggest that the entire volume is not participating in flow processes and that preferential flow exists in the system under saturated conditions.
- Lower and more uniform (in depth) pore water velocities estimated for the slug moment method results in higher θ_e estimates, suggesting a greater volume of the medium participating in flow processes.
- Pore water velocities are not significantly different for experiments conducted at 25°C and 35°C. Velocity differences are expected at different temperatures because of the temperature dependency of the water density (ρ_w) and dynamic viscosity (μ_w). Based on variations in ρ_w and μ_w with temperature, saturated hydraulic conductivities at 35°C ($K_{s(35^\circ\text{C})}$) can be estimated from values at 25°C as:

$$K_{s(35^{\circ}C)} = K_{s(25^{\circ}C)} \frac{\rho_{w,25^{\circ}C}}{\rho_{w,35^{\circ}C}} \frac{\mu_{w,35^{\circ}C}}{\mu_{w,25^{\circ}C}} = K_{s(25^{\circ}C)} \times 1.2 \quad [39]$$

where ρ_w and μ_w values are given by Roberson and Crowe (1990). Based on this relationship, the hydraulic conductivity values at 35°C are expected to be slightly (1.2 times) greater than those at 25°C. Comparison of water velocities for saturated experiments (Exp. 3 and 6, Table 11) show no observable difference between the two. For the unsaturated case (Exp. 7 and 8, Table 11), the water velocities at 35°C are slightly higher (~1.5 times) than those at 25°C. The higher velocities can result from ρ_w and μ_w temperature-dependence and from differences in saturation-dependent hydraulic conductivities for unsaturated flow. Slightly different pore water velocities for higher temperature in the unsaturated medium may also result from changes in pressure heads and gradients.

During infiltration process, dispersion increases with depth due to greater velocity variations as water contents change with depth and decreases with increasing water content. Greater dispersion is observed for evaporation (Figures 38 and 39) than infiltration (Figure 37) periods. During evaporation, greater dispersion is observed at longer distances from the bottom of the column. This is attributed to greater velocity variations caused by depth-dependent variable flow and multiple dispersive mechanisms (mechanical and diffusive).

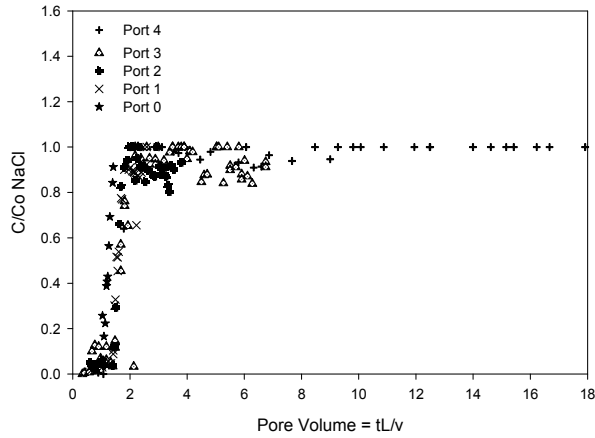


Figure 40. NaCl BTC Arrival during Infiltration Process under Saturated Conditions at 25°C (Exp 3)

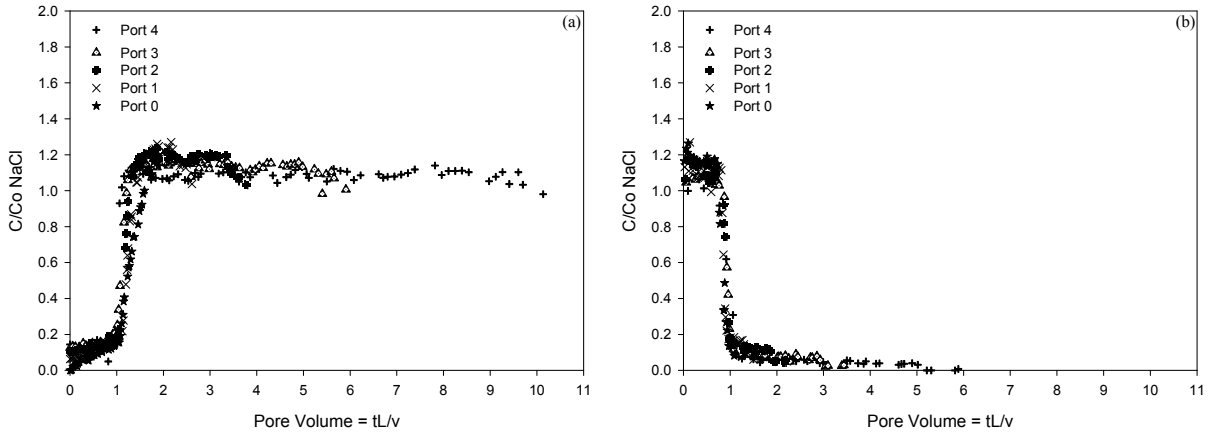


Figure 41. NaCl BTC Arrival (a) and Elution (b) during Infiltration Process under Saturated Conditions at 35°C (Exp 6)

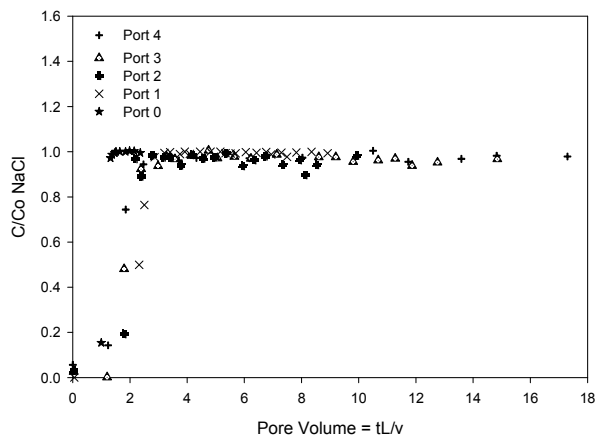


Figure 42. NaCl BTC Arrival during Infiltration Process under 75% of Saturation at 25°C (Exp 4)

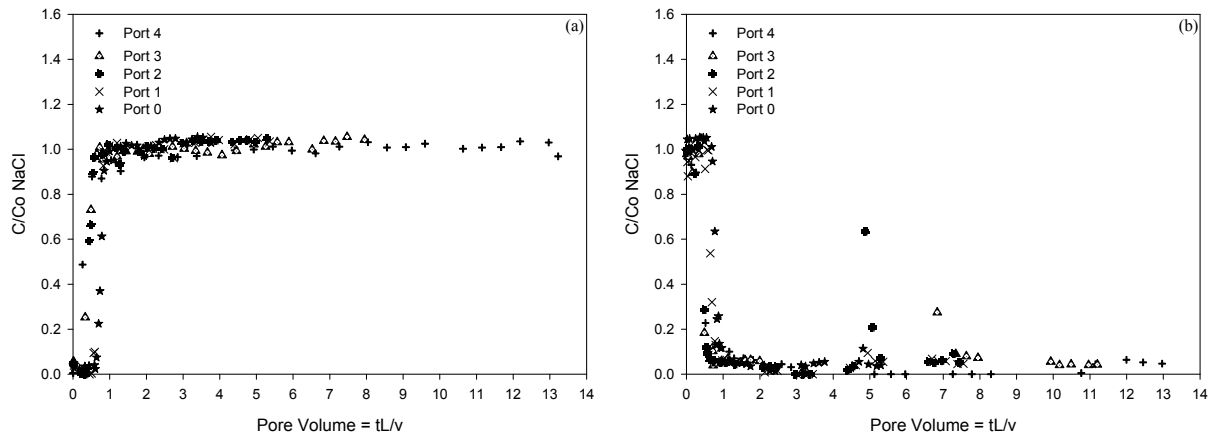


Figure 43. NaCl BTC Arrival (a) and Elution (b) during Infiltration Process under 60% of Saturation at 25°C (Exp 7)

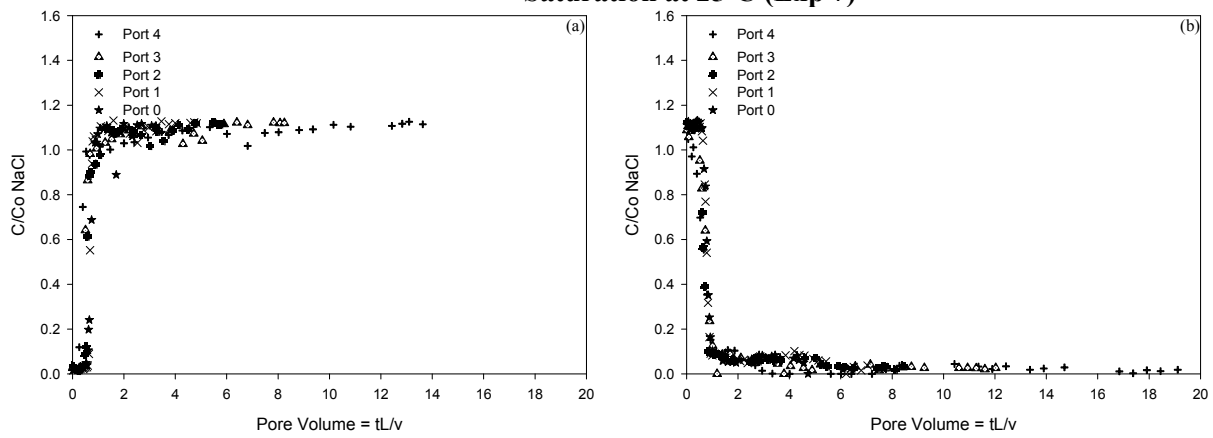


Figure 44. NaCl BTC Arrival (a) and Elution (b) during Infiltration Process under 60% of Saturation at 35°C (Exp 8)

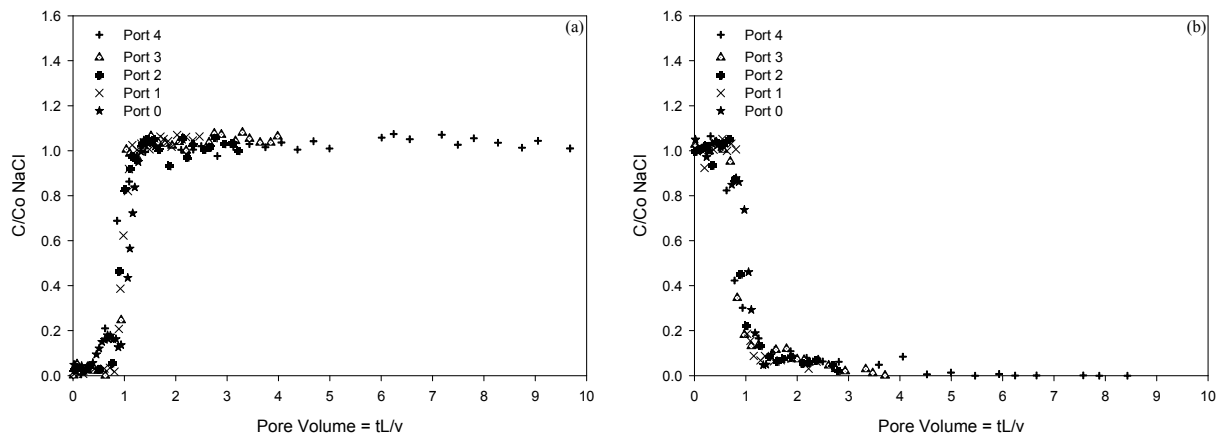


Figure 45. NaCl BTC Arrival (a) and Elution (b) during Infiltration Process under WC 0.17 at 25°C (Exp 5)

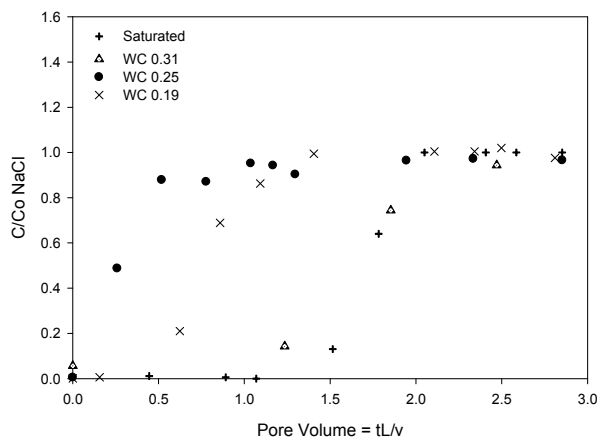


Figure 46. NaCl BTC Arrival in Port 4 during Infiltration Process under Different Water Contents at 25°C

4.5.2 Aqueous TNT/DNT BTCs

The temporal distributions of TNT and DNT in water through the column (Figures 47 through 53) show high concentration variability. This variability is mostly attributed to spatial and temporal variations in fate and transport processes, which will be later discussed. For saturated conditions (Figures 47a and 48 a), TNT and DNT during infiltration events are initially detected in the upper most port (port 4). TNT and DNT concentrations at this location, which is closest to the DNT/TNT source (~10 cm from source), initially increase with time, reaching nearly constant concentrations of about 12 and 14 mg/L, respectively. Solute breakthroughs at deeper locations are generally eluted in an order related to the depth location, but at lower concentrations than in the upper-most port. Concentrations in port 3 are generally the most variable. At later infiltration times TNT and DNT solute concentrations in the lower-most port (port 1) tend to be higher than those measured in higher ports (port 3 and port 2).

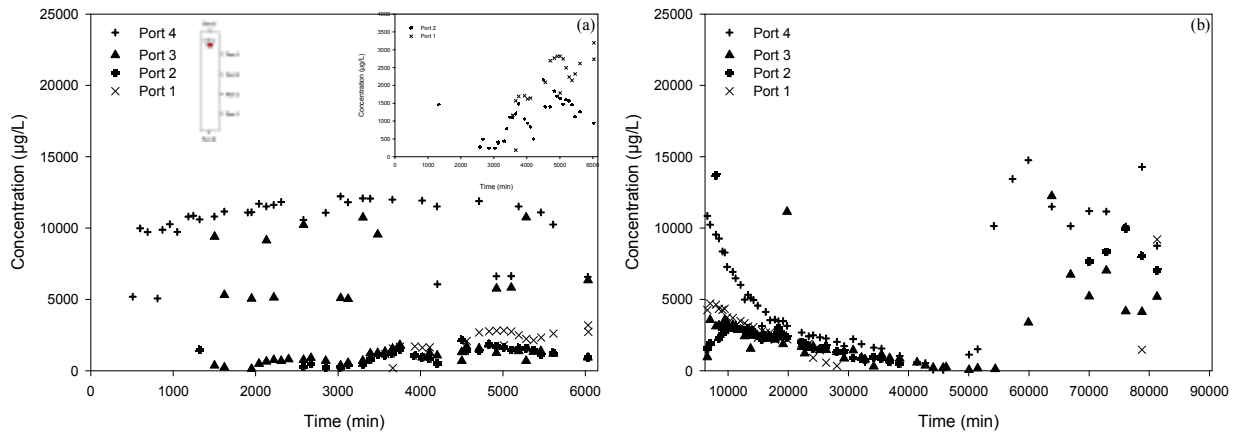


Figure 47. TNT_w BTC during Infiltration (a) and Evaporation (b) Processes under Saturated Conditions at 25°C (Exp 3)

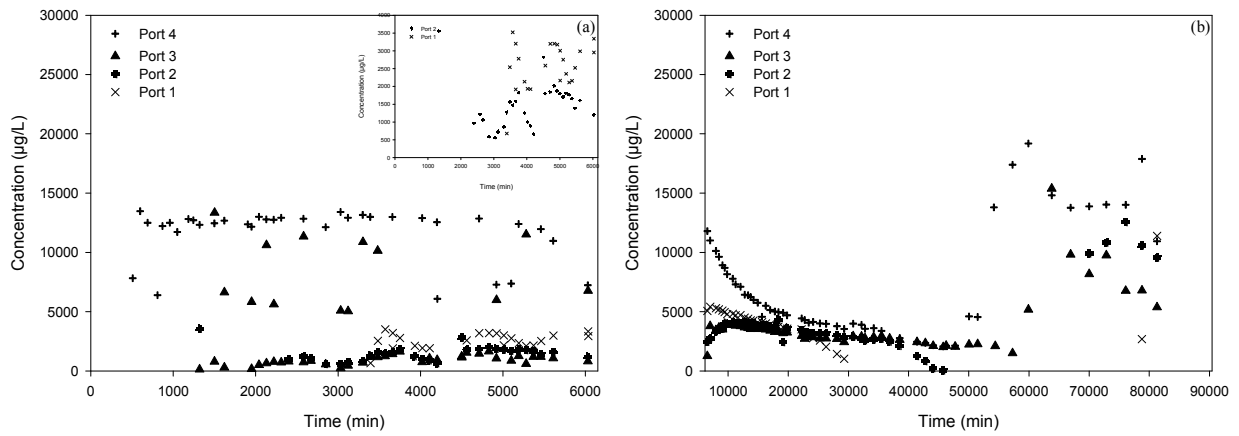


Figure 48. DNT_w BTC during Infiltration (a) and Evaporation (b) Processes under Saturated Conditions at 25°C (Exp 3)

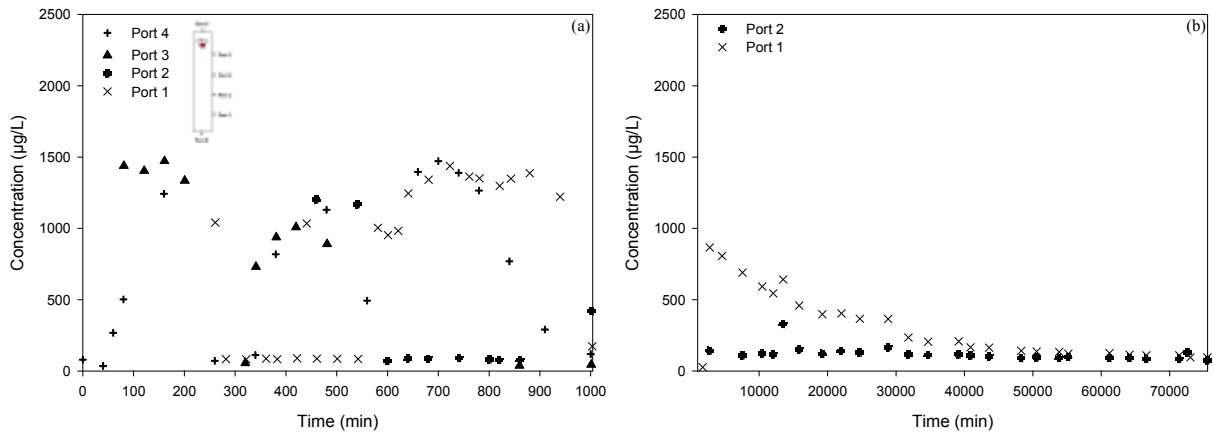


Figure 49. TNT_w BTC during Infiltration (a) and Evaporation (b) Processes under 75% of Saturation at 25°C (Exp 4)

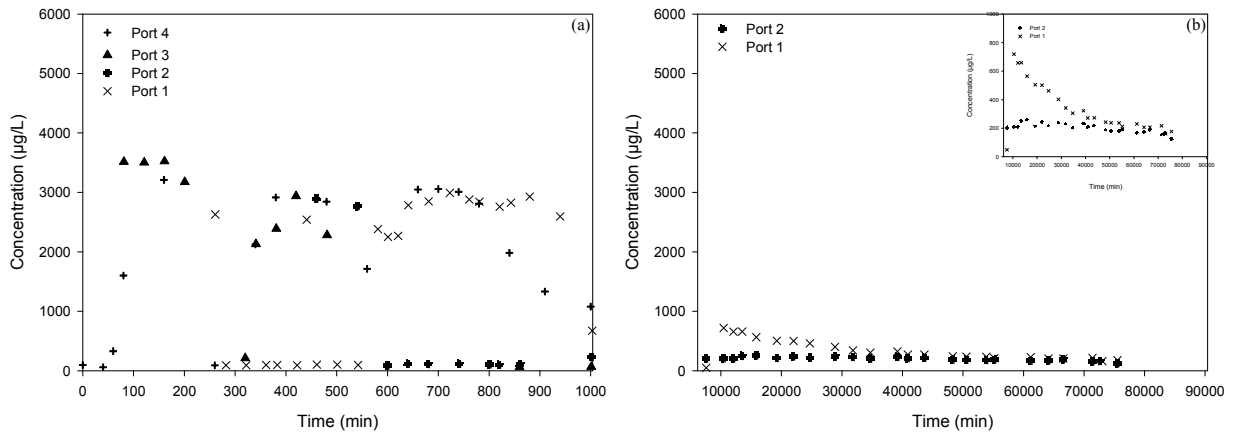


Figure 50. DNT_w BTC during Infiltration (a) and Evaporation (b) Processes under 75% of Saturation at 25°C (Exp 4)

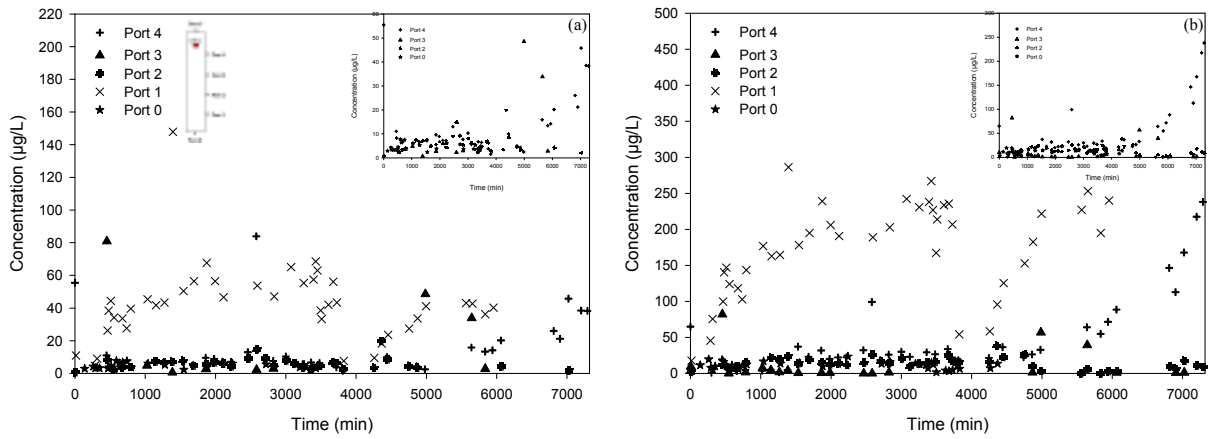


Figure 51. TNT_w (a) and DNT_w (b) BTCs during Infiltration Process under 60% of Saturation at 25°C (Exp 7)

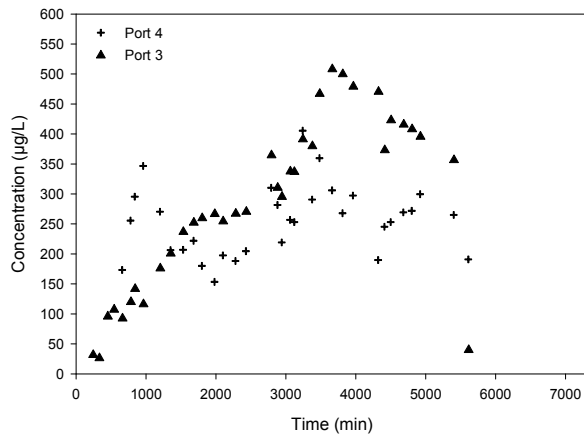


Figure 52. DNT_w BTC during Infiltration Process under 60% of Saturation at 35°C (Exp 8)

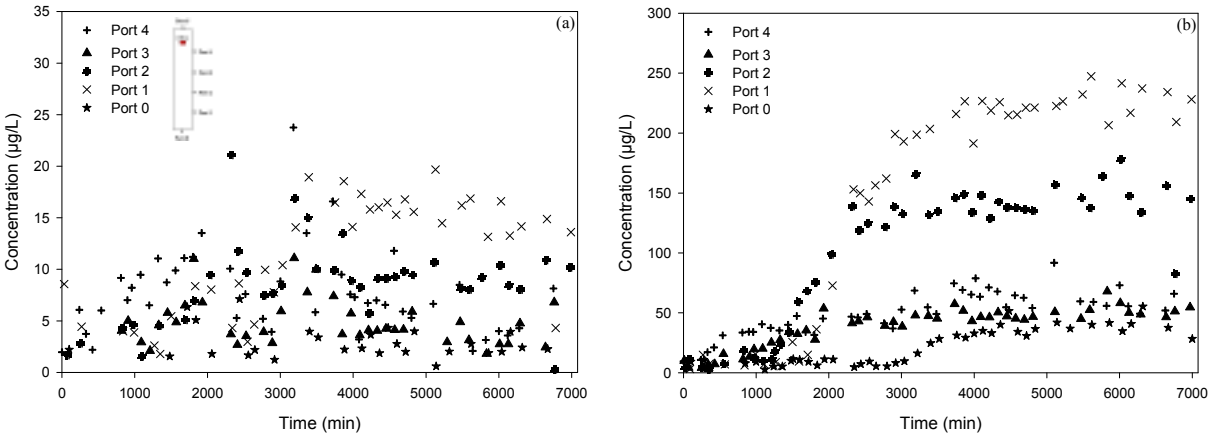


Figure 53. TNT_w (a) and DNT_w (b) BTCs during Infiltration Process under 45% of Saturation at 25°C (Exp 5)

The general order of elution (i.e., earlier for closer-downstream locations) indicate that TNT and DNT solutes are moving with infiltrating water. The lower-than-solubility concentrations (see Table 1) indicate that the dissolution processes of TNT and DNT is rate limited. The higher DNT solute concentrations (Figure 54) is attributed to the higher dissolution capacity of DNT than TNT. Similar behavior in concentration variations of TNT and DNT indicate that both solutes are influenced by similar transport processes.

Lower solute concentrations at lower depth (i.e., greater transport distance) is attributed to preferential flow and incomplete mixing of the solute during initial transport distance after dissolution source. Because the upper-most sampling port is directly below the ERC source, solute at this location do not have enough mixing time and concentrations are high. As solutes continue to move downward they mix with solute-free water and concentrations are lowered. The high variability in concentrations at port 3 is attributed to preferential flow paths. Higher concentrations at latter infiltration times in the lowest-most port suggest solute accumulation

near the outflow boundary. This may also result from greater mass arrival through time as preferential flow paths converge toward the outflow boundary.

During evaporation processes, unsaturated conditions (Figures 47b and 48b), TNT and DNT solute concentrations tend to decrease initially in the upper ports. For the lower ports, the concentrations increase initially after the onset of the evaporation period and then decrease. Solute concentrations in all ports increase significantly after a long evaporation period (>50,000 minutes).

Initial concentration decrease in the upper ports and increase in the lower ports are associated with downward movement of the solute during flow redistribution after infiltration and onset of evaporation periods. Decreasing concentrations in the lower-most ports are also associated with the upward movement of a solute-free solution as evaporation takes place. Significant increase in concentrations after long evaporation periods is attributed to solute accumulation caused by water evaporation. Temporally this significant increase is observed initially at the upper-most port and later at deeper locations.

TNT and DNT concentrations in unsaturated infiltration (Figures 49 through 53) indicate lower solute concentrations as water content decreases. The lower concentrations are attributed to rate-limited dissolution and increasing preferential flow as water content decreases. The greater preferential flow results in lower water flux through the TNT/DNT source causing lower dissolution flux. Because flow is only concentrated in preferential flow paths, there is greater velocities in those flow paths (than if the flow was evenly distributed). Greater velocities result in lower concentrations if the dissolution process is rate-limited.

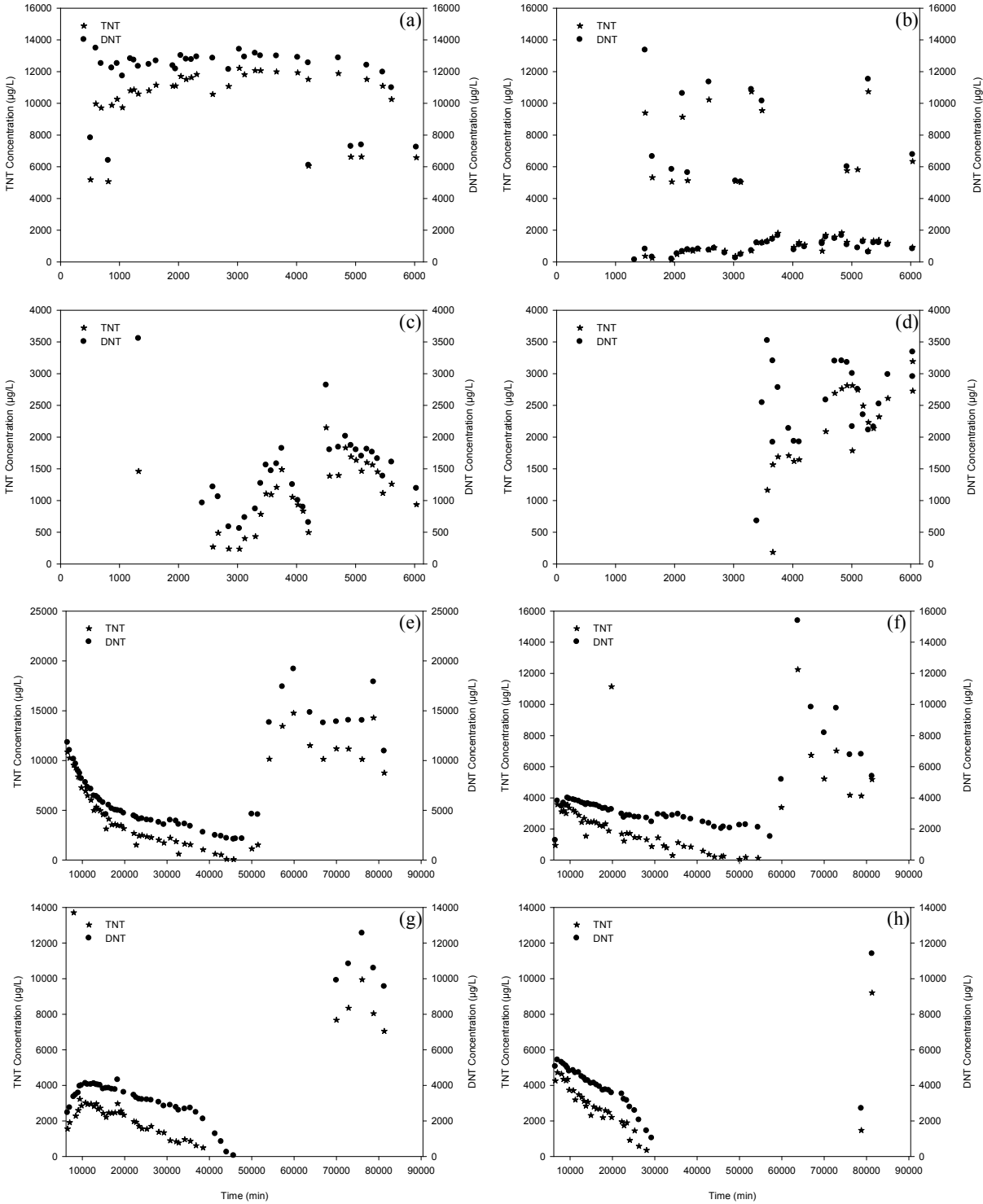


Figure 54. TNT_W vs. DNT_W during: Infiltration Process for Port 4 (a), Port 3 (b), Port 2 (c) and Port 1 (d); during Evaporation Process for Port 4 (e), Port 3 (f), Port 2 (g) and Port 1 (h), under Saturated Conditions at 25°C (Exp 3)

TNT and DNT concentrations during evaporation periods in unsaturated conditions tend to decrease with time to an asymptotic value (Figures 49b and 50b). During this period only the bottom ports were possible to sample due to drainage of the upper sections of the soil. Lower temporal concentrations are attributed to drainage losses during flow redistribution and volatilization losses to the soil-gas. Lower concentrations are also attributed to slower diffusion-controlled transport from the TNT/DNT source and potential dilution with evaporation replenishment water. Aqueous TNT and DNT were not detected at 60% saturation for 25 nor 35°C. They were, however detected in the gas phase (discussed later). It is suspected that no detection is caused by problems with the chemical analysis of the samples during these experiments.

Comparison of BTCs for NaCl, TNT, and DNT (Figures 55 and 56) indicate retardation (slower movement) of TNT and DNT relative to NaCl (conservative tracer). TNT breakthrough in the upper-most port (port 4) at 45% saturation occurs at about the same time as NaCl. Considering that the TNT source is closer to this port than the NaCl port, TNT would be eluted earlier than NaCl if no retention processes acted on the transport of TNT. Because TNT is eluted at about the same time as NaCl in this port, it is considered that it moves at a slower rate than the NaCl and, therefore, is retarded. For deeper locations (Figure 55 b, c, and d), a marked retardation is noticed for TNT as it is eluted at later times than NaCl. Separation in solute breakthrough of NaCl and TNT seems to increase with depth, suggesting stronger retention mechanisms or non-equilibrium sorption. Similar results are observed for DNT (Figure 56) and for saturated conditions (Figure 57).

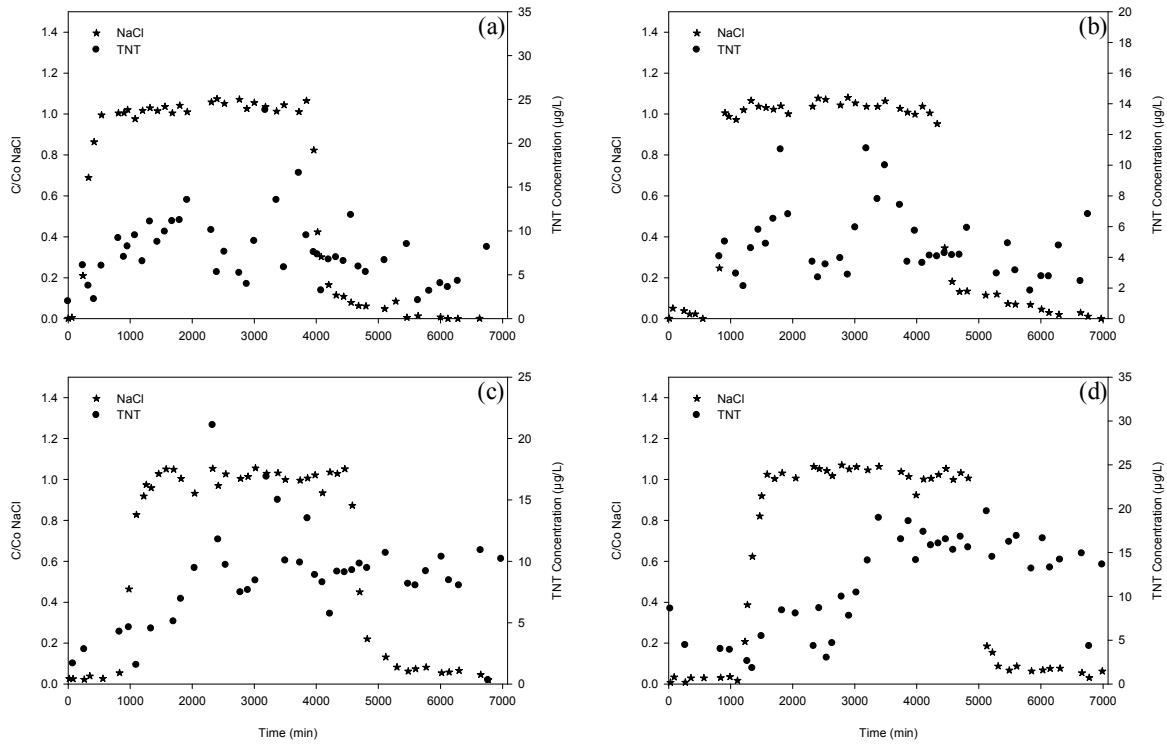


Figure 55. NaCl vs. TNT_W during Infiltration Process for Port 4 (a), Port 3 (b), Port 2 (c) and Port 1 (d), under 45% of Saturation at 25°C (Exp 5)

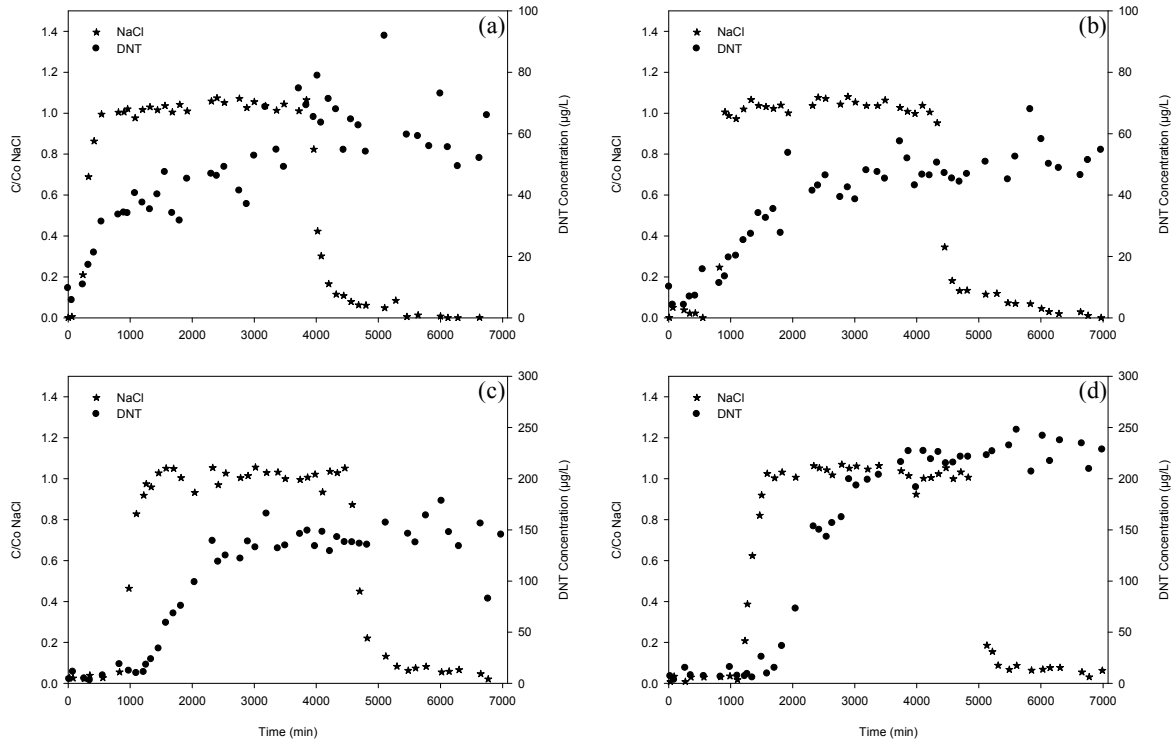


Figure 56. NaCl vs. DNT_W during Infiltration Process for Port 4 (a), Port 3 (b), Port 2 (c) and Port 1 (d), under 45% of Saturation at 25°C (Exp 5)

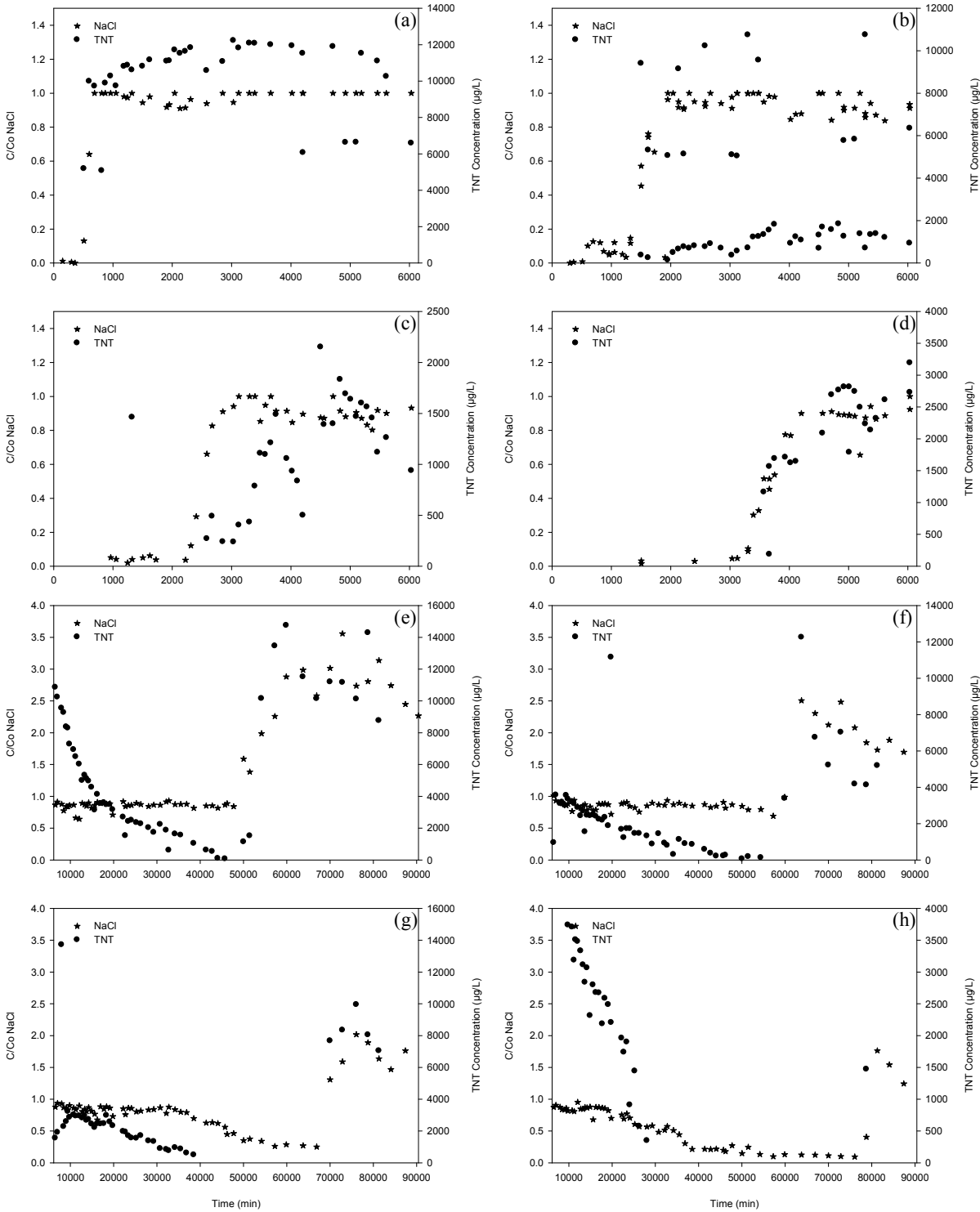


Figure 57. NaCl vs. TNT_w during: Infiltration Process for Port 4 (a), Port 3 (b), Port 2 (c) and Port 1 (d); during Evaporation Process for Port 4 (e), Port 3 (f), Port 2 (g) and Port 1 (h), under Saturated Conditions at 25°C (Exp 3)

Comparison of NaCl and DNT BTCs under saturated conditions during evaporation periods (Figure 57) shows that DNT solute concentration change (decrease) at much greater rates than these for NaCl. This is attributed to dilution (mixing) and volatilization processes. Although, TNT solute concentration may also decrease due to sorption mechanisms. Similar behavior between NaCl and TNT during the solute concentration (accumulation) phase after long periods of evaporation suggest that the accumulation is caused by water evaporation losses, rather than solute (NaCl, TNT, DNT) fate transport processes.

Higher temperatures generally result in greater TNT and DNT solute concentration in water for saturated (compare Figures 47 and 48 with Figures 113 and 114 in the appendix A) and unsaturated conditions (Figures 51 and 52). Greater retardation during infiltration is also observed at higher temperatures (35°C) for saturated (Figures 58 and 59) and unsaturated conditions. TNT seems to be slightly more retarded than DNT at higher temperatures (Figure 60) but not the lower temperatures.

The TNT and DNT mass eluted at port 4 was estimated from zeroth moment analysis of the BTCs. Total mass eluted was higher for saturated experiments and decreased with lower degree of saturation (Table 13). This is due to the higher dissolution rates at higher water contents and losses to the gas-phase at lower water contents. Higher temperatures produce higher dissolution rates, as observed for DNT mass of experiments 7 and 8. For saturated experiments the estimated mass was close to the mass buried in the system at 25°C, but much higher at 35°C. The large difference at higher temperatures is attributed to integration errors caused by high concentration

variability. Greater mass is recovered for DNT than TNT because of the greater solubility kinetics of DNT.

Table 13. TNT and DNT Mass Estimated from Moment Analyses of BTCs in Port 4

Experiment	Temperature (°C)	Degree of Saturation (%)	Q (mL/min)	Water Flux (mL/min.cm ²)	TNT mass (mg)	DNT mass (mg)
3	25	100	2	0.017	128.946	145.987
4	25	75	20	0.228	14.303	40.203
5	25	45	2	0.037	0.103	0.330
6	35	100	2	0.017	667.685	957.529
7	25	60	10	0.136	0.202	3.479
8	35	60	10	0.136	ND	13.845

Note: Initial TNT/DNT mass buried was 180 mg/L for each one (TNT and DNT).
ND – No detected

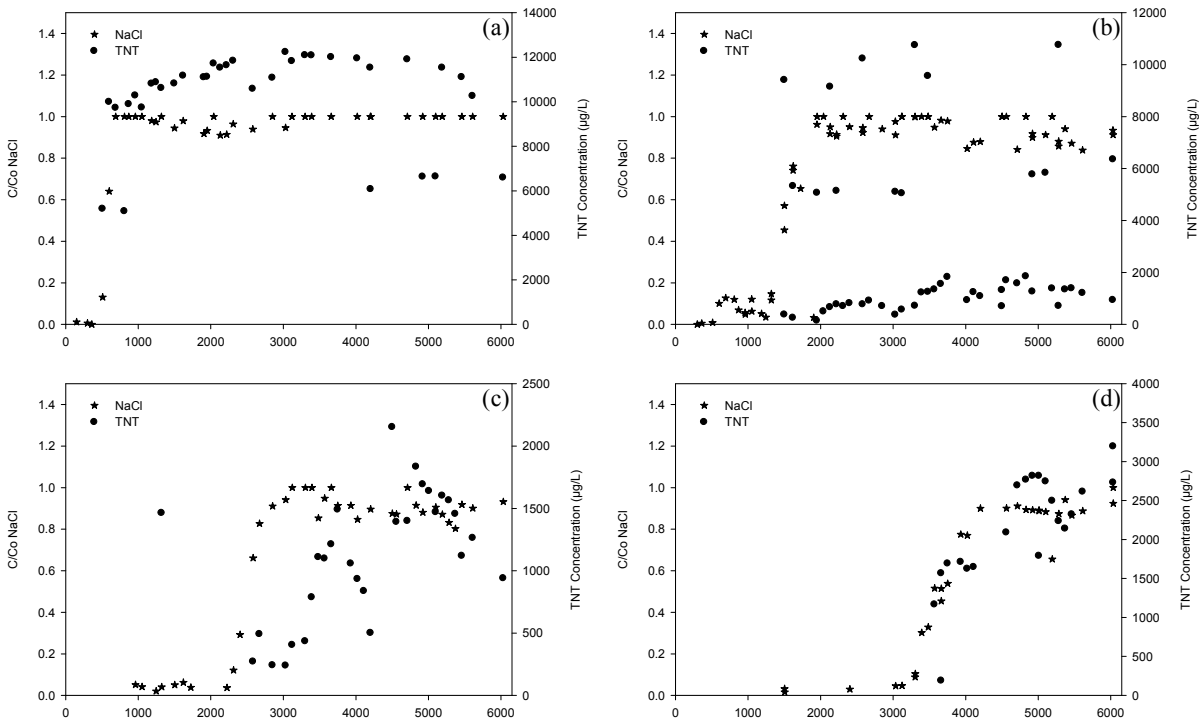


Figure 58. NaCl vs. TNT_w during: Infiltration Process for Port 4 (a), Port 3 (b), Port 2 (c) and Port 1 (d) under Saturated Conditions at 25°C (Exp 3)

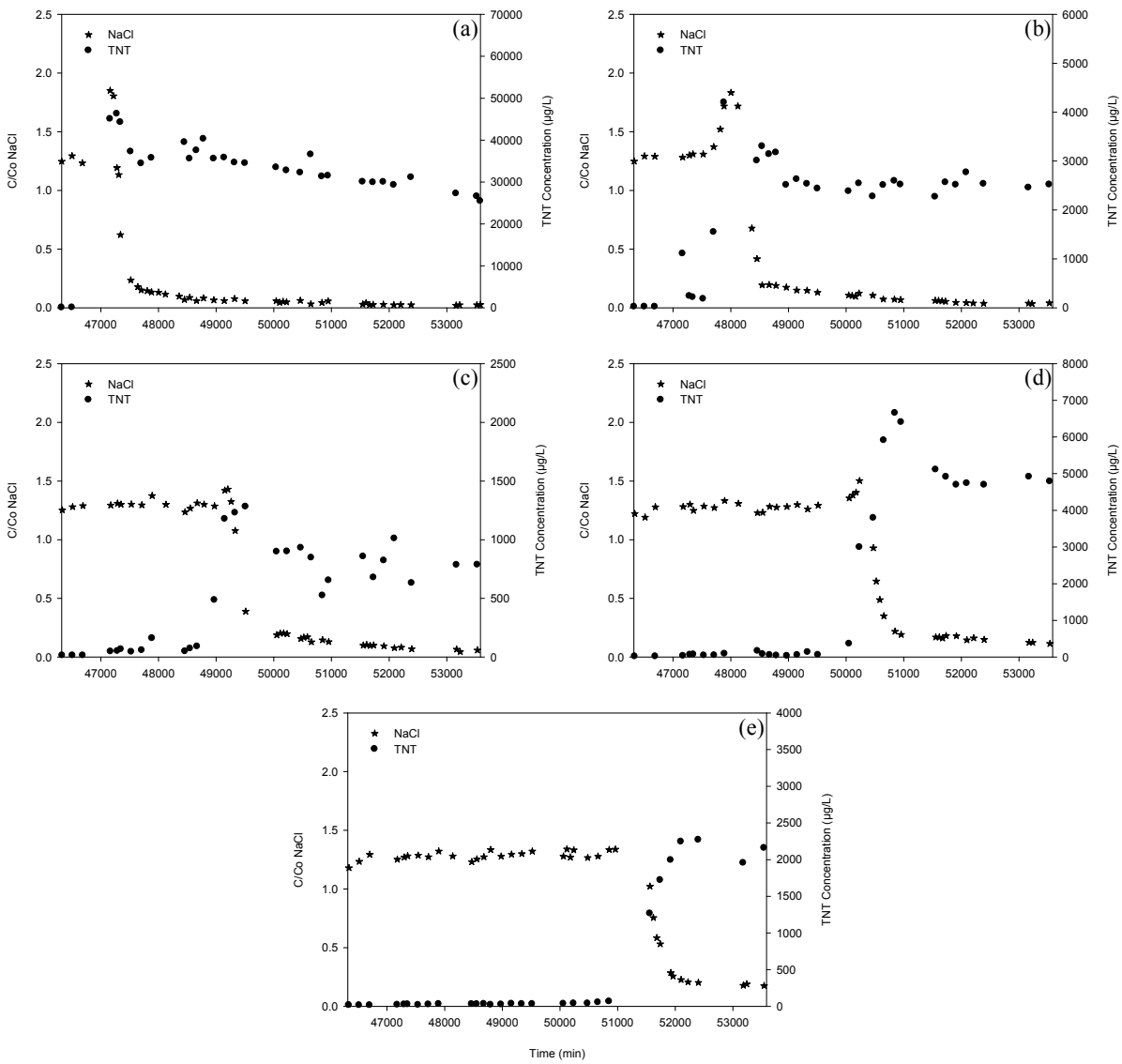


Figure 59. NaCl vs. TNT_w during: Infiltration Process for Port 4 (a), Port 3 (b), Port 2 (c), Port 1 (d) and Port 0 (e) in the Second Stage of the Experiment under Saturated Conditions at 35°C (Exp 6)

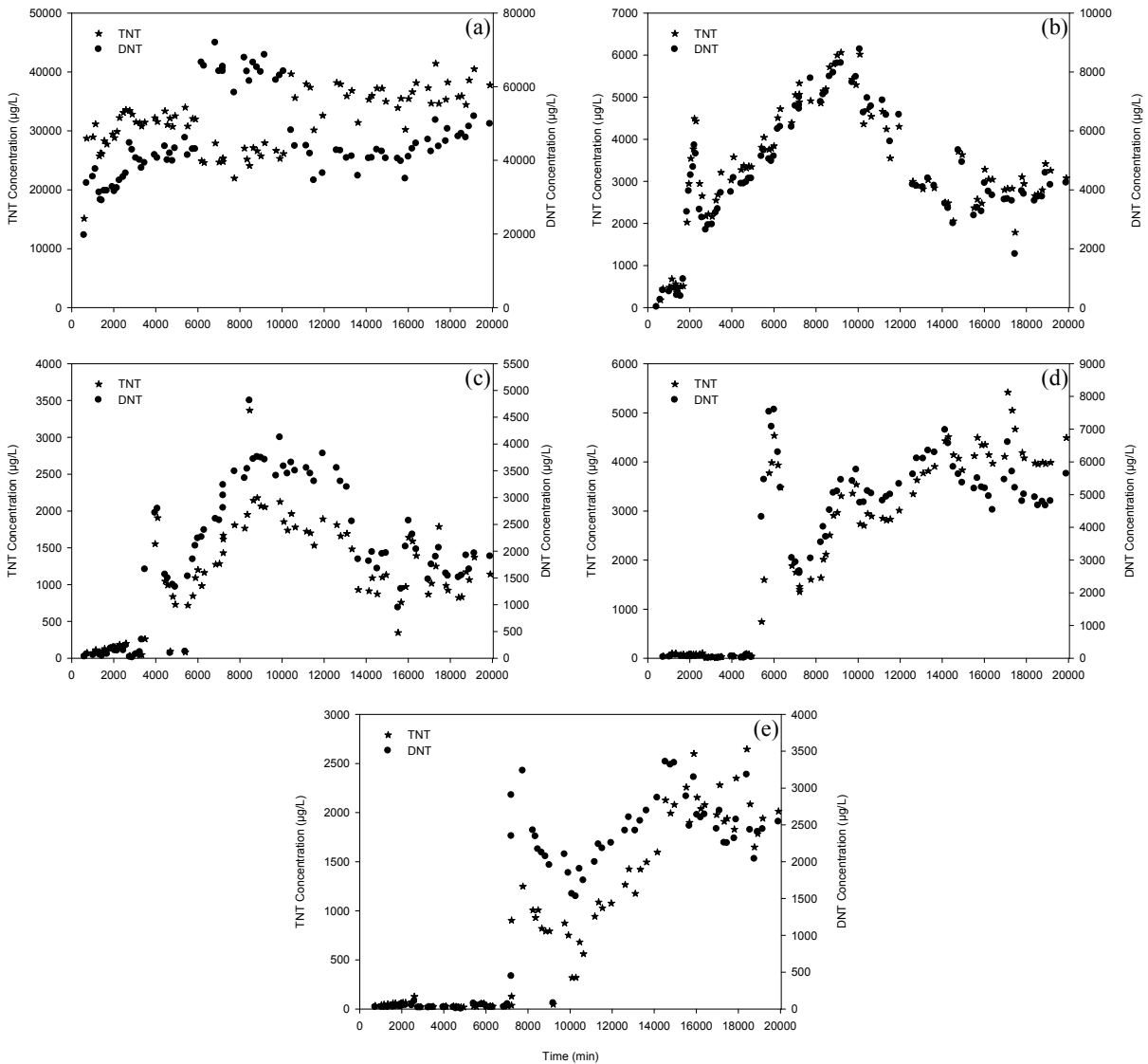


Figure 60. TNT_w vs. DNT_w during: Infiltration Process for Port 4 (a), Port 3 (b), Port 2 (c), Port 1 (d) and Port 0 (e), in the First Stage of the Experiment under Saturated Conditions at 35°C (Exp 6)

4.5.3 Vapor TNT/DNT BTCs

TNT and DNT vapor phase concentrations were measured above the soil surface for saturated and unsaturated experiments and along the soil column during unsaturated conditions.

Limited vapor samples were taken during infiltration periods because of the high water content. Higher number of vapor samples were possible during evaporation periods.

Vapor phase TNT and DNT concentrations are generally highly variable throughout the column and the soil surface (Figure 61). The high variability is attributed to variable volatilization throughout the column depending on water content and flow conditions. Higher DNT vapor concentration variability results from higher vapor pressure gradients and volatilization rates than TNT.

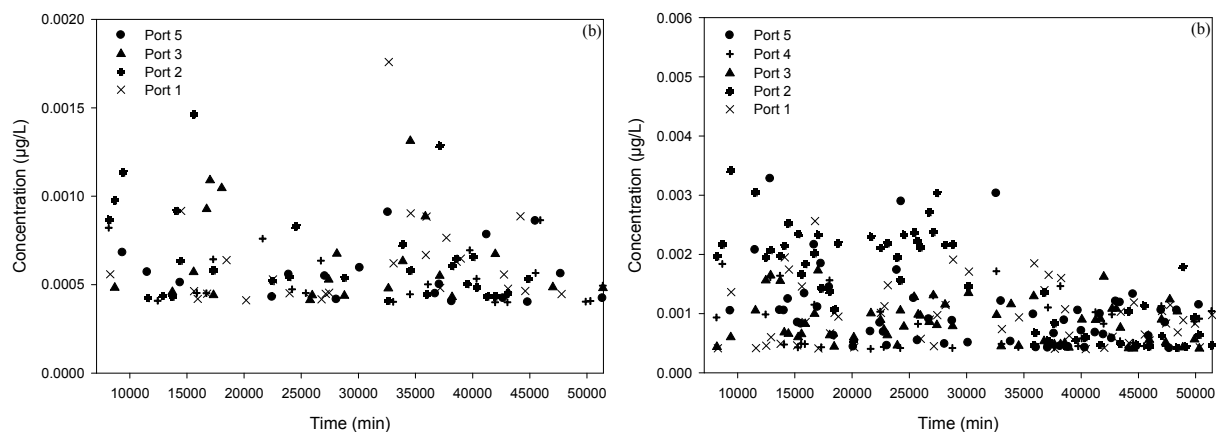


Figure 61. TNT_G (a) and DNT_G (b) BTCs during Evaporation Process under 45% of Saturation at 25°C (Exp 5)

Generally, no major differences are observed in vapor phase concentrations during infiltration events (Figures 62 and 63). Similar behavior is initially observed during evaporation periods, except that vapor concentrations tend to decrease at later times. The decrease is attributed to vapor flux losses to the atmosphere at greater rates that volatilization sources from soil-water.

Average vapor phase concentrations for TNT and DNT (Table 14) show higher values for higher water contents at a given temperature. This corresponds to higher aqueous concentrations at higher water contents and indicate that volatilization from water controls the gas-phase concentrations and fluxes.

Table 14. Vapor-Phase TNT and DNT Average Concentrations

Experiment		TNT		DNT	
		Average Concentration (µg/L)	Standard Deviation	Average Concentration (µg/L)	Standard Deviation
4	Port 5	0.00136	0.00012	0.00170	0.00076
	Port 4	0.00164	0.00044	0.00182	0.00096
	Port 3	0.00152	0.00043	0.00224	0.00134
	Port 2	--	--	--	--
	Port 1	--	--	--	--
5	Port 5	0.00057	0.00015	0.00102	0.00063
	Port 4	0.00041	--	0.00093	0.00081
	Port 3	0.00060	0.00022	0.00110	0.00037
	Port 2	0.00078	0.00025	0.00239	0.00057
	Port 1	0.00049	0.00008	0.00101	0.00080
6	Port 5	0.00920	0.02298	0.03967	0.02298
	Port 4	--	--	--	--
	Port 3	--	--	--	--
	Port 2	--	--	--	--
	Port 1	--	--	--	--
7	Port 5	0.00053	0.00030	0.04081	0.19580
	Port 4	0.00038	0.00013	0.00072	0.00038
	Port 3	0.00035	0.00012	0.00071	0.00040
	Port 2	0.00033	0.00011	0.00087	0.00041
	Port 1	0.00042	0.00038	0.00088	0.00048
8	Port 5	0.00444	0.00788	0.00153	0.00393
	Port 4	0.16641	0.79513	0.08091	0.06360
	Port 3	0.00141	0.00070	0.01158	0.00332
	Port 2	0.00227	0.00341	0.01317	0.00809
	Port 1	0.00406	0.00151	0.02186	0.00856

Higher vapor phase concentrations at higher temperatures result from higher vapor pressures of TNT and DNT. Generally, lower variability is observed in vapor concentration distribution at higher temperatures for saturated (Figure 64) and unsaturated conditions (Figure 65). The lower variability at saturation is caused by homogeneous volatilization through the air-water interface phase at the surface of the soil. The greater volatilization variability caused by

irregular interfacial areas in unsaturated flow, is however masked at higher temperature because of the greater volatilization rates.

Comparison of DNT vapor BTC in the soil near the soil surface and the soil surface (Figure 66) show a very similar but temporally shifted behavior of vapor phase (DNT_G) and aqueous (DNT_W) concentrations. Vapor phase breakthrough lags that of the aqueous phase because it takes time for the buried source. Initial increase in vapor phase concentrations occurs from greater volatilization of the increasing aqueous concentration. Aqueous concentrations reach a peak value and then decrease as solutes are transferred to the vapor phase. The vapor phase concentration decreases after some time due to lower water concentrations and vapor diffusion transport.

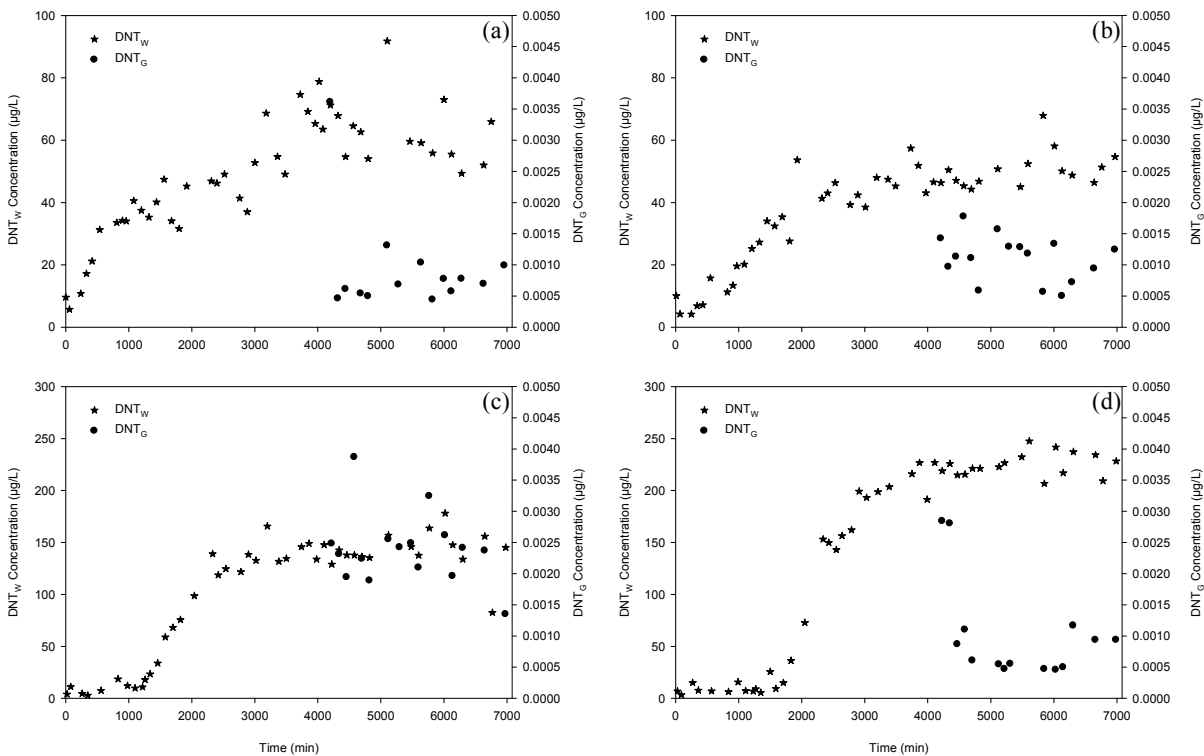


Figure 62. DNT_W vs. DNT_G during Infiltration Process for Port 4 (a), Port 3 (b), Port 2 (c) and Port 1 (d) under 45% of Saturation at 25°C (Exp 5)

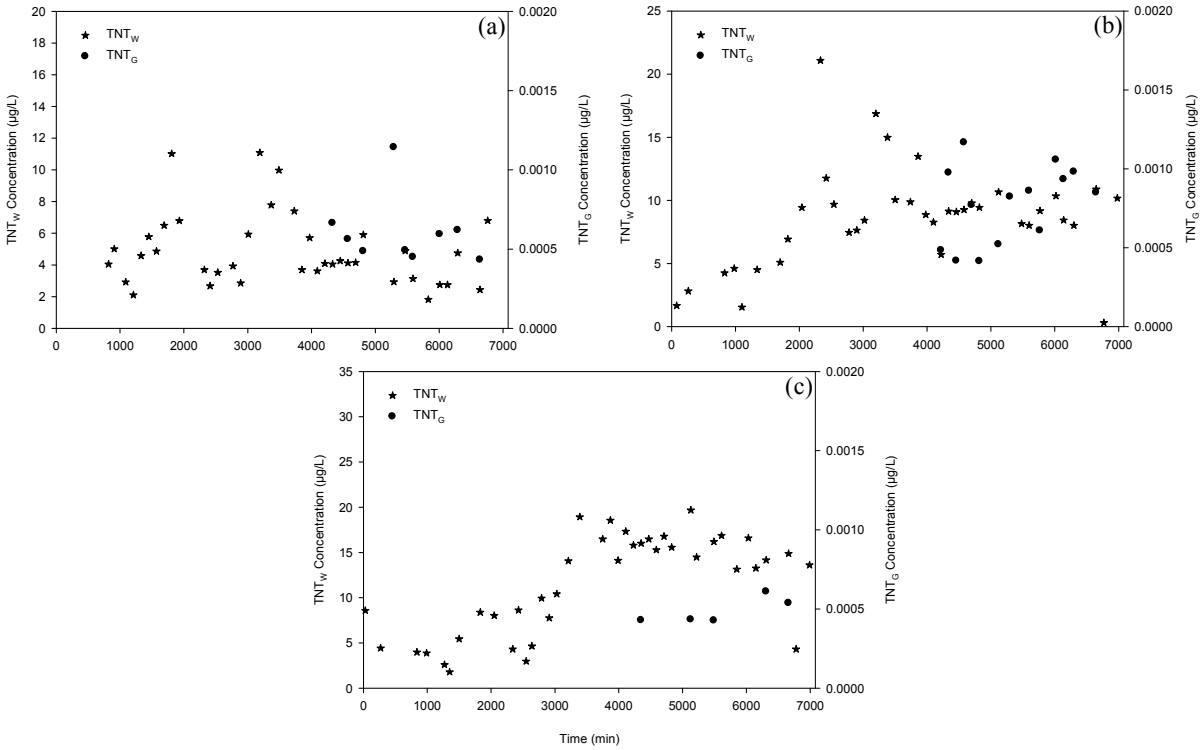


Figure 63. TNT_W vs. TNT_G during Infiltration Process for Port 3 (a), Port 2 (b) and Port 1 (c) under 45% of Saturation at 25°C (Exp 5)

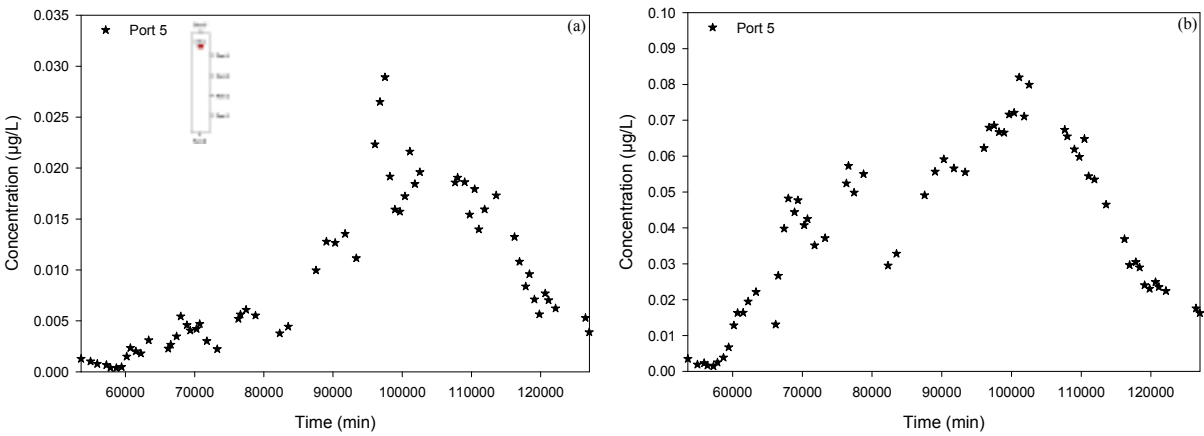


Figure 64. TNT_G (a) and DNT_G (b) BTCs in the Surface of the Soil during Evaporation Process in the Second Stage of the Experiment under Saturated Conditions at 35°C (Exp 6)

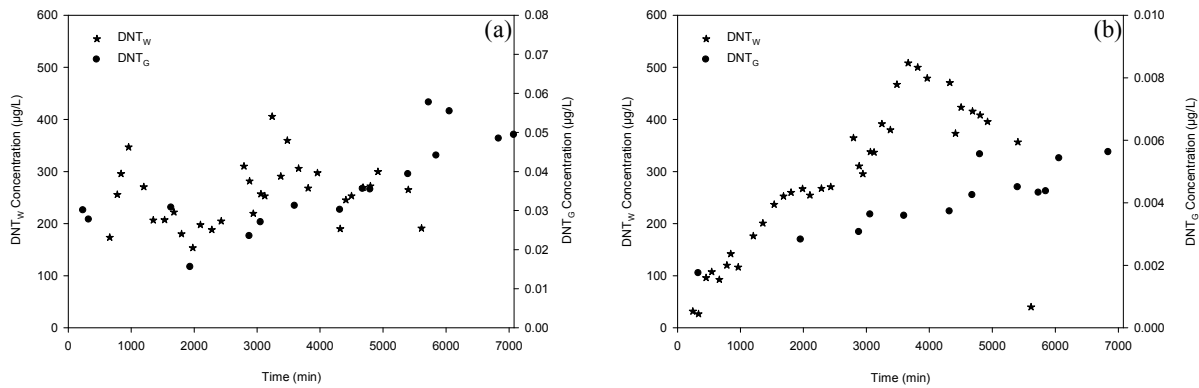


Figure 65. DNT_W vs. DNT_G during Infiltration Process for Port 4 (a) and Port 3 (b), under 60% of Saturation at 35°C (Exp 8)

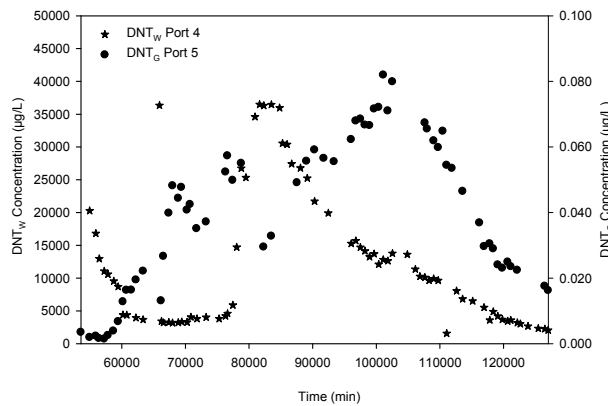


Figure 66. DNT_W vs. DNT_G BTC in the Surface of the Soil during Evaporation Process in the Second Stage of the Experiment under Saturated Conditions at 35°C (Exp 6)

4.5.4 Microbial Activity Test Realized during Experiment 4 (WC 0.28 and 25°C)

Microbial activity was evaluated in ports 1 and 2 (bottom ports) during the infiltration period of experiment 4 (75% saturation at 25°C). Microbial activity was measured in port 2 (Figure 67), which was closest to the TNT/DNT source. There were not observables differences in microbial activity between agar plates prepared with and without explosive mix solution. This suggests that: (1) DNT/TNT are not a limited substrate for potential DNT/TNT degraders; (2)

organisms are not DNT/TNT degraders; and/or (3) the organisms present are not affected by these explosive chemicals.

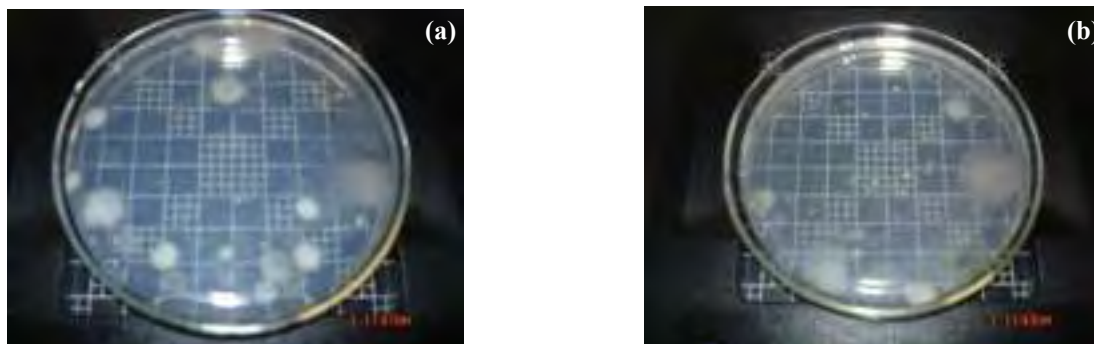


Figure 67. Port 2 without (a) and with (b) initial addition of explosive solution (5 mg/L TNT-DNT)

4.5.5 ERC Degradation

Observable color changes at the surface of the soil (Figure 68) suggest TNT/DNT degradation in the soil, which is observed also in the chromatograms obtained by using Gas Chromatography. Unidentified chromatographic peaks (Figure 69) indicate the presence of potential degradation products.



Figure 68. Degradation on Soil Surface

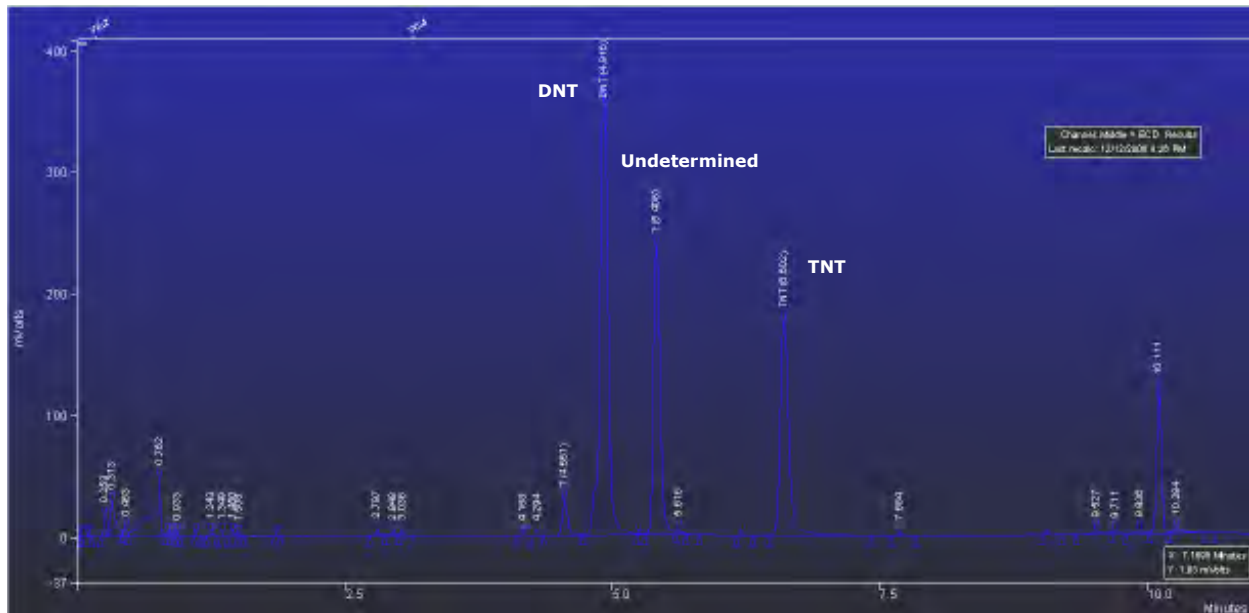


Figure 69. Explosives Chromatogram from Aqueous Phase Samples

4.6 NaCl Simulation

NaCl infiltration data from experiments 3 to 8 were simulated using Hydrus 2D code. Longitudinal dispersion (D_L), immobile water fraction (θ_{imw}) and mass transfer coefficient for NaCl exchange between mobile and immobile water (ω) parameters were fitted using the inverse module of HYDRUS-2D. Figures 70, 71 and 72, show the hydraulic and fate and transport simulation results for experiments 3 and 7. Pressure head and water content forward simulation results (Figure 70) suggest that water flow simulation is in agreement with the results obtained during the experimental period (Figures 21 and 25). They further suggest that soil-hydraulic parameters included into the hydraulic model correspond to the experimental setup (soil column). Simulated pressure heads and water contents for the different experiments are given in Table 15.

Table 15. Simulated Pressure Heads and Water Contents during Infiltration Process

Experiment		θ_w	P (cm)
3	Port 4	0.337	82.0
	Port 3	0.337	62.0
	Port 2	0.337	42.0
	Port 1	0.337	25.0
4	Port 4	0.284	-21.0
	Port 3	0.284	-21.0
	Port 2	0.284	-21.0
	Port 1	0.279	-21.4
5	Port 4	0.180	-40.8
	Port 3	0.180	-40.8
	Port 2	0.189	-40.2
	Port 1	0.222	-37.0
6	Port 4	0.337	82.0
	Port 3	0.337	62.0
	Port 2	0.337	42.0
	Port 1	0.337	25.0
7	Port 4	0.248	-27.2
	Port 3	0.248	-27.2
	Port 2	0.248	-27.2
	Port 1	0.251	-26.9
8	Port 4	0.248	-27.2
	Port 3	0.248	-27.2
	Port 2	0.248	-27.2
	Port 1	0.251	-26.9

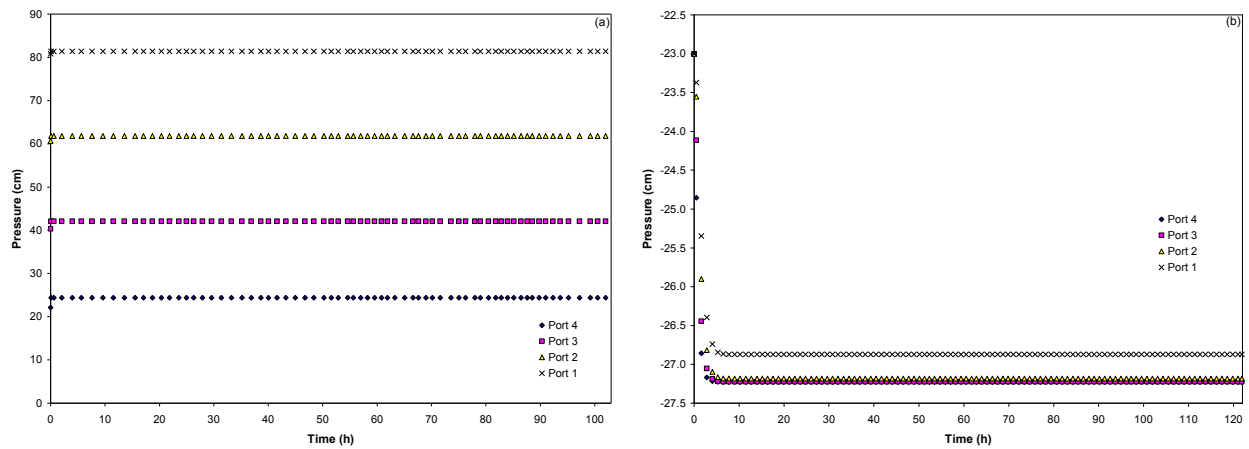


Figure 70. Simulated Pressure Heads for Saturated Conditions (a) and 60% of Saturation (b) at 25°C

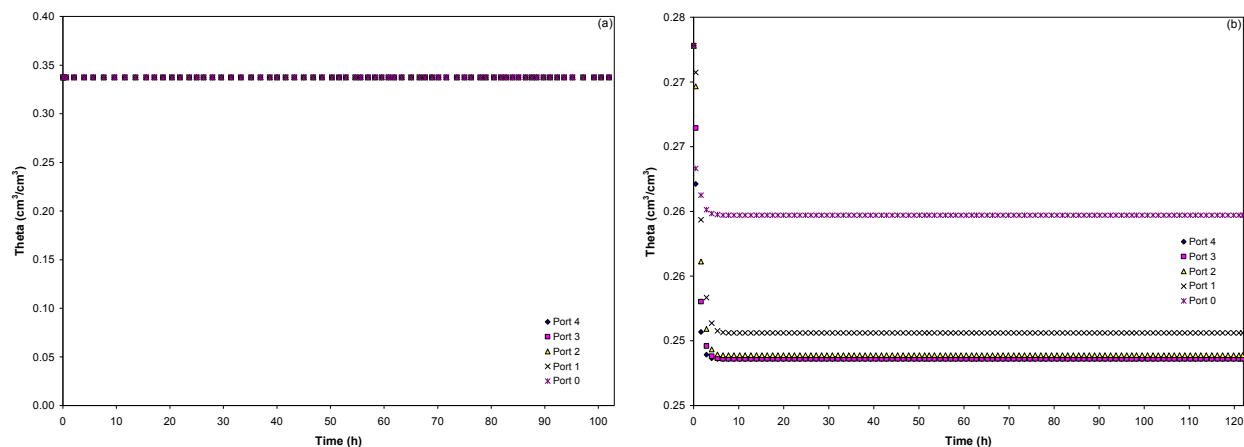


Figure 71. Simulated Water Contents for Saturated Conditions (a) and 60% of Saturation (b) at 25°C

Measured relative NaCl concentration distributions were not properly simulated in the HYDRUS model of the system (Figure 72). Low correlation coefficients for both, saturated conditions and WC 0.23 (0.73601 and 0.82222, respectively) were obtained in the inverse solution. Poor simulation results are attributed to different hydraulic characteristics through the column formed by preferential flow paths. Analysis of NaCl BTCs suggest higher pore-water velocities near the soil surface, potentially caused by preferential flow paths formed near the surface by soil disturbances during ERC source burial (Table 11). Proper simulation of preferential flow would require heterogeneous modeling of fate and transport parameters (e.g., mobile water content).

Plots of simulated NaCl Relative Concentrations vs. NaCl Relative Concentrations Data (Figure 72) show that pore-water velocities through the column length are variable. Generally simulated BTCs are eluted later than measured BTCs in the upper portions of the soil. As NaCl is transported deeper into the soil, the simulated and measured BTCs move closer (i.e., port 1,

Figure 72). At the soil-water outflow point, the simulated BTC is eluted earlier than the measured BTC. This behavior results because the inverse model is minimizing the error of all BTCs at once in an “homogeneously” simulated medium. To improve these results is recommended that each port be fitted for transport parameters separately to obtain best average parameters for each soil section. The overall model can then be developed for heterogeneous conditions.

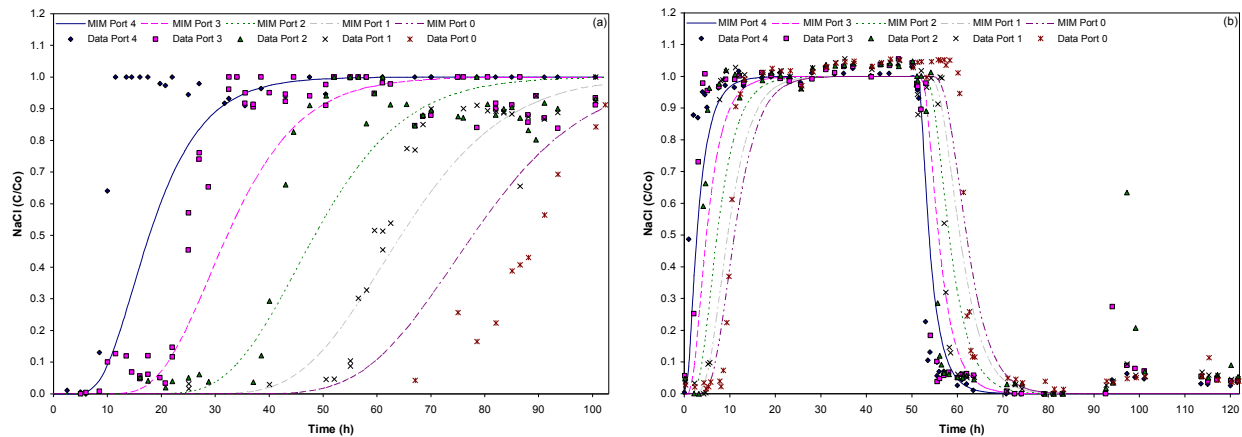


Figure 72. Measured vs Simulated Relative NaCl Concentrations Using Mobile-Immobile Model (MIM) for Saturated Conditions (a) and 60% of Saturation (b) at 25°C

Differences between simulated and moment estimated pore water velocities (Table 16) are attributed to moment-estimation and simulation errors. Pore-estimated velocities using the method of moments were estimated from frontal elution curves (Table 11), which show much greater velocities than those estimated with slug method. Using the slug method during the moment-based and simulated velocities closer together, but are still generally higher than those determined from inverse modeling. Simulation errors arise from the assumption of homogeneous hydraulic properties.

The dispersivity coefficient (α) was estimated from MIM-generated dispersion coefficient (D_L) and velocities. Higher than expected dispersivity values were calculated for saturated values. Previous studies have reported dispersivities between 0.03 and 0.04 cm (Padilla et al. 1999; Fetter, 1999). Dispersivity estimates at 25°C suggest slight decrease with decreasing water contents. This suggests greater hydraulic heterogeneities at higher water contents. The higher dispersivity values for saturated flow and decreasing values at lower water contents suggest boundary induce preferential flow in relatively large pores at high water contents. Once drained, the large pores do not participate in flow and flow hydraulic becomes more homogeneous. This can also be caused by greater water content variations along the length of the column at the higher water contents. At lower water contents, pressure heads show lower water content variations along the column. At higher temperatures, solution degassing and air entrapment may result in greater velocity variation at higher water contents.

Table 16. Estimated Transport Parameters for NaCl during Infiltration Process

Experiment	MOM	MIM using HYDRUS			α (cm)	
	v (cm/h)	v (cm/h)	D_L (cm ² /h)	θ_{imw}		ω (h ⁻¹)
3	2.494	0.423	1.5046	0.1	23.51	3.555
4	34.205	3.622	2.5255	0.1	81.88	0.697
5	6.479	1.969	5.6537	0.1	95.36	2.871
6	1.809	0.423	2.5666	0.1	0.01	6.064
7	15.650	2.438	7.8816	0.1	0.01	3.232
8	23.968	2.439	3.8878	0.1	0.01	1.594

4.7 Integrated Discussion of Results

Transport experiments were conducted to determine the fate and transport behavior of TNT and DNT in soils near the soil-atmospheric interface at different water contents, flow and

temperatures conditions, when subjected to infiltration and evaporation events. Results indicate that TNT and DNT transport is highly influenced by these conditions and events.

When subjected to periods of infiltration and evaporation, the principal component of water flux can be downward, stagnant, or upward. Hydraulic and NaCl concentration measurements indicate that water flow is principally downward during infiltration events. After infiltration periods, water flux may be principally downward, stagnant and/or upward.

Although the sandy soil used in these experiments is relatively homogeneous, water content estimates and NaCl temporal distributions indicate the existence of hydraulic heterogeneities and preferential flow paths in saturated and unsaturated media during infiltration events. Preferential flow paths near the infiltrating surface are attributed to soil disturbance during burial of ERC sources (landmine) and the presence of these sources. Hydraulic heterogeneities form from differences in hydraulic properties as a function of water contents and depend on boundary conditions. Generally, water contents in unsaturated flow decreased with depth at ambient temperatures (25°C) during infiltration periods, but increased with depth at higher temperatures (35°C). The depth-related water content increase at higher temperatures is attributed to water drainage from the upper portions of the soil into lower regions. This drainage is caused by lower soil-water tensions resulting from lower air-water surface tensions and higher sand-water contact angles. Water-content variations with depth result in different hydraulic properties and may induce paths of preferential flow. Preferential flow paths in the system are supported by NaCl temporal concentration distributions along the sand column. Analyses of

these distributions (also known as breakthrough curves - BTCs) indicate variations in solute velocities that are associated with preferential flow.

Preferential flow during infiltration processes is also supported by the results obtained from a moment analysis and HYDRUS 2D numerical model. The model, which simulated homogeneous hydraulic conditions, indicate that NaCl experimental BTCs move faster near the soil surface and slower near the column outlet than simulated BTCs.

Soil-water pressure measurements, total hydraulic heads, and water content estimates indicate that after an infiltration event, water flux is initially downward, depending on soil depth, water content, and temperature. Soils with higher water contents and higher temperature at the end of the infiltration period show higher degree of drainage. Drainage water redistribution was generally followed by a stagnant water flux period during infiltration-evaporation transition in the flux components. This corresponds to a period in which downward drainage redistribution and upward evaporation processes are balanced. Similar to the period following infiltration events, pressure and hydraulic head measurement indicate that the transition period depend on the initial water contents after infiltration, temperature, and depth. The transition is seen initially in the upper ports, and starts earlier for soils with higher initial water contents. The infiltration-evaporation transition period is, however, slower (takes longer) for the higher initial water content soils. After this transition period, evaporation pressures at the surface of the soil controls water flux causing it to be predominantly upward. Evaporate-fluxes toward the end of the experiments are generally higher than infiltration periods under the same conditions.

Generally greater dispersion is observed with solute traveling distance (i.e., with depth for infiltration conditions and upward distance in evaporation conditions). This is attributed to greater velocity variations caused by preferential flow, depth dependent variable flow, and multiple dispersive (mechanical and diffusive) mechanisms. Greater apparent dispersion for evaporation conditions result from additional velocity variation caused by flow reversal processes.

Dispersivity estimates from HYDRUS 2D suggest higher dispersivity values than previously reported for homogeneous sand. The higher-than-expected values suggests preferential flow processes and hydraulic heterogeneity.

TNT and DNT BTCs indicate downward movement with infiltrating water. The infiltrating concentrations are, however, controlled by rate-limited distribution of the ERC source, preferential flow, and incomplete mixing of the solutes. Lower TNT and DNT aqueous concentrations than their solubility values indicate that dissolution of the ERC sources is rate limited. Higher aqueous concentrations at higher water contents and temperature indicate that dissolution kinetics is dependent on water-flux and temperatures. Higher temperatures generally result in greater DNT aqueous concentrations. TNT is however not detected in unsaturated conditions at higher temperatures, suggesting greater losses to sorption or volatilization at higher temperatures.

The downward movement of TNT and DNT with infiltrating water is generally retarded (moves slower) with respect to water (or conservative tracers), indicating sorption of ERC onto the soil and other surfaces present in the system. At higher temperatures TNT is more retarded

than DNT, suggesting greater sorption processes for TNT than DNT. For unsaturated conditions, air-water interfaces can potentially act as sorption surface. Because air-water interfacial areas vary with water content, TNT and DNT sorption at the air-water interface would vary with water content distribution. Variable depth-dependent retardation of TNT and DNT suggest rate-limited sorption, variable sorption capacity, and/or non-linear sorption. Rate-limited sorption may result from preferential flow. Variable sorption capacity may occur as water content and interfacial areas distribution vary with depth. Nonlinear sorption would occur if sorption capacity varies with solute concentration. Further studies would have to be made to discern the mechanistic processes inducing the observed depth-dependent retardation.

Preferential flow and incomplete mixing of the TNT and DNT solutes result in lower concentrations with depth. This also results in greater dispersion of the solutes, indicating greater expansion of the plume.

Variable TNT and DNT aqueous concentration with time after infiltration periods indicate that their fate and transport is influenced by water redistribution, upward movement of solute-free water during evaporation, and solute accumulation caused by water evaporation at the soil surface. Generally, TNT and DNT solute concentration tend to decrease with time after water redistribution processes caused by drainage. The decrease is attributed to slow dissolution kinetics, and sorption, and volatilization losses. Although some degradation losses may be possible, there is no evidence of major degradation processes. Volatilization losses are reflected in TNT and DNT vapor concentrations throughout the soil and above the soil-atmospheric surface.

High variability of TNT and DNT vapors indicate variable volatilization and gas-diffusion rates depending on water content and flow conditions. Vapor-phase concentrations during infiltration experiments indicate some upward gaseous movement controlled by gas-phase diffusion and solute volatilization. TNT and DNT vapor-phase concentrations are related to solute concentration in the aqueous phase, thus it is higher for higher water contents at a given temperature. This behavior indicates that volatilization from water controls the gas-phase concentration and fluxes. Higher vapor concentrations at higher temperatures indicate greater volatilization at the higher temperature.

No significant differences in temporal vapor concentrations are observed during infiltration periods because TNT and DNT are continuously dissolved through time. Decreasing temporal vapor-phase concentrations and redistribution, however, indicate vapor flux losses to the atmosphere.

5 CONCLUSIONS

Results from transport experiments conducted to determine the fate and transport behavior of TNT and DNT from buried sources near soil-atmospheric surfaces indicate that the mobility and persistence of these ERCs is highly influenced by water contents, temperatures, and flow conditions. Results from experimental data and numerical simulations permit the inference of the following conclusions:

- Water movement near TNT and DNT buried sources is the most important processes affecting their fate and transport in soils and near-atmospheric surfaces. Water-flux associated with higher water contents enhances source dissolution, volatilization, and movement of TNT and DNT solutes.
- Dissolution kinetics controls the solute concentration of TNT and DNT in water, indicating that dissolution is rate-limited. Greater dissolution is observed at higher water contents and temperatures. Greater dissolution results in greater gas-phase concentrations, indicating that gas-phase concentrations are controlled by solute volatilization. Higher concentrations in the water and gas-phase as a result of greater dissolution rates enhance the movement of TNT and DNT away from the source.
- Disturbances of soil properties by burial of ERC sources results in hydraulic heterogeneities and preferential flow near the source, which influences their fate and transport away from the source. Preferential flow causes faster movement and greater dispersion of the solutes during infiltration periods. It also causes incomplete mixing near the source, resulting in lower concentrations away from the source.

- The downward movement of TNT and DNT with infiltrating water is generally retarded by sorption processes at soil and air-water surfaces. Retardation processes seem to be influenced by rate-limited sorption, variable sorption capacity, and/or non-linear sorption.
- The fate and transport of TNT and DNT in soils subjected to variable flow and water contents are influenced by dissolution (source-water), volatilization (water-air), and sorption (water-soil) mass transfer limitations. These limitations are further influenced by temperature.
- Upward movement of water during evaporation processes results in upward movement of solutes toward the soil-atmospheric surfaces. Water evaporation near the soil surface result in increased solute concentrations near the soil surface after prolonged evaporation periods. Higher potential evaporation at higher water contents result in higher solute concentrations.
- TNT and DNT concentrations tend to decrease with time after infiltration periods. The decrease is attributed to slow dissolution of ERC source, and greater sorption and volatilization losses.
- Greater dispersion is observed with solute traveling distance during both infiltration and evaporation periods. Greater dispersion is attributed to greater velocity variations caused by preferential flow, depth-dependent variable flow, and multiple dispersive (diffusion and mechanical) mechanisms. Greater apparent dispersion during evaporation periods result from additional velocity variations caused by flow reversal processes.

- TNT and DNT vapor concentrations indicate volatilization and gaseous transport during infiltration periods. During evaporation periods, vapor concentrations tend to decrease with time due to lower concentrations in the water phase.
- Water contents highly influences the fate and transport of TNT and DNT in soils. Greater water contents result in higher dissolution rates of ERC buried sources and higher aqueous and gaseous concentrations and transport.
- Higher temperature affects the fate and transport of DNT and TNT by influencing hydraulic properties, increasing water drainage and evaporation, and enhancing dissolution and volatilization rates, sorption processes, and diffusion-controlled vapor transport.
- Infiltration and evaporation events affect the fate and transport of TNT and DNT by affecting dissolution rates, water advection rates, and direction, and causing greater dispersion of chemicals.
- Reverse flow during infiltration and evaporation result in greater dispersion of solutes.

6 RECOMMENDATIONS

Several recommendations are provided to further advance the knowledge in processes affecting the fate and transport of ERCs in soils. They are listed below.

Sampling

- Water sampling methodologies must take into account sampling volumes at low water contents and fluxes.
- Employ water content and temperature sensors placed in the soil to better assess environmental conditions affecting the fate and transport of ERCs in soils.
- Locate sampling port above the explosive source to determine the ERCs behavior due to explosive emanations to gas and liquid phases upward flow.
- Use of more sensitive pressure sensors.

Experimental

- Expand the range of experimental water contents and temperature.
- Use slug tracer injections to characterize physical transport in the soil.
- Develop experimental replicates to increase the reliability of the data collected. Although, is known that this kind of experiments can not be exactly replicated because of differences during the experimental setup, data collection and data analysis, the overall behavior can support or reject the given hypothesis.
- Conduct infiltration and evaporation experiments with shorter cyclic variations.

Analytical

- Use the incomplete (frontal) breakthrough data to calculate the moments from $t=0$ up to $t=t_{\max}$, where t_{\max} is the time of the last data point. Then, use the truncated moment equations for an appropriate model to calculate the moment from $t=t_{\max}$ to $t=\infty$.
- Develop a moment method for high concentration measured variability to estimate DNT and TNT mean arrival times.
- Estimate evaporation water velocities.
- Develop a HYDRUS 2D model for heterogeneous hydraulic properties in soil.
- Model NaCl transport during evaporation period using HYDRUS 2D.
- Simulate TNT and DNT fate and transport using heterogeneous hydraulic model in HYDRUS 2D with dissolution, volatilization, and sorption mass transfer processes.
- Increase the range of water contents and temperature.

7 REFERENCES

- Amrhein M., B. Srinivasan, D. Bonvin, M.M. Schumacher, M.H. Behringer, J. Grifoll and Y. Cohen. "Contaminant Migration in the Unsaturated Soil Zone: the Effect of Rainfall and Evapotranspiration". *Journal of Contaminant Hydrology*, 23:185-211, 1996.
- Anaya A., I. Padilla and S. Hwang. "Influence of Environmental Conditions on the Fate and Transport of ERCs in a Physical 3D Model: Spatial and Temporal Assessment Effects in a Sandy Soil", *Proceedings of SPIE on Detection and Remediation Technologies for Mines and Minelike Targets, XII SPIE Defense and Security Symposium, Orlando, FL, Vol. 6553*, 2007.
- Armstrong J.E., E.O. Frind and R.D. McClellan. "Nonequilibrium Mass Transfer between the Vapor, Aqueous, and Solid Phases in Unsaturated Soils during Vapor Extraction". *Water Resources Research*, 30:355-368, 1994.
- Bachmann J., R. Horton, S.A. Grant and R.R. van der Ploeg. "Temperature Dependence of Water Retention Curves for Wettable and Water-Repellent Soils". *Soil Science Society of America Journal*, 66:44-52, 2002.
- Bajracharya K. and D.A. Barry. "Nonequilibrium Solute Transport Parameters and their Physical Significance: Numerical and Experimental Results". *Journal of Contaminant Hydrology*, 24:(3-4):185-204, 1997.
- Bonazountas M. and J. Wagner. *SESOIL: A Seasonal Soil Compartment Model. Draft Report. Office of Toxic Substances, US Environmental Protection Agency, Washington, DC, PB86112406*, 1984.
- Bond W.J. and P.J. Wierenga. "Immobile Water during Solute Transport in Unsaturated Sand Columns". *Water Resources Research*, 26:2475-2481, 1990.
- Borrero E., J.G. Briano, M. Castro and S.P. Hernández. "Numerical Simulation of the Chemical-Signature-Compounds Transport from a Mine Field". *Proceedings of the SPIE, Detection and Remediation Technologies for Mines and Minelike Targets IX*, 5415:533-544, 2004.
- Bourgeois J. and G.S. Smith. "A Complete Electromagnetic Simulation of the Separated-Aperture Sensor for Detecting Buried Land Mines". *IEEE Transactions on Antennas and Propagation*, 46(10):1419-1426, 1998.
- Brannon J.M., C.B. Price and A. Charolett. "Abiotic and Biotic TNT Transformations". *US Army Corps of Engineers, Waterways Experimental Station, Miscellaneous Paper IRRP-97-3*, 1997.

- Brannon J.M., P. Deliman, C. Ruiz, C.B. Price, M. Qasim, J.A.Gerald, C. Hayes and S. Yost. "Conceptual Model and Process Descriptor Formulations for Fate and Transport of UXO". US Army Corps of Engineers, Waterways Experimental Station, Technical Report IRRP-99-1, 1999.
- Brannon J.M., C.B. Price, P. S. Yost, C. Hayes and B. Porter. "Comparison of Environmental Fate and Transport Process Descriptors of Explosives in Saline and Freshwater Systems". *Marine Pollution Bulletin* 50:247–251, 2005.
- Cattaneo M.V., J.C. Pennington, J.M. Brannon, D. Gunnison, D.W. Harrelson and M. Zikikhani. "Natural Attenuation of Explosives, in Remediation Engineering of Contaminated Soils". Wise, L.J., ed, Pages 949-970, New York, Marcel Decker Press, 2000.
- Choi J.W., F.D. Tillman Jr. and J.A. Smith. "Relative Importance of Gas-Phase Diffusive and Advective Trichloroethene (TCE) Fluxes in the Unsaturated Zone under Natural Conditions". *Environmental Science & Technology*, 36:3157-3164, 2002.
- Comfort S.D., P.J. Shea, L.S. Hundal, Z. Li, B.L. Woodbury, J.L. Martin and W.L. Powers. "TNT Transport and Fate in Contaminated Soil". *Journal of Environmental Quality*, 24:1174-1182, 1995.
- Costanza M. and M.L. Brusseau. "Influence of Adsorption at the Air-Water Interface on the Transport of Volatile Contaminants in Unsaturated Porous Media". *Environmental Science and Technology*, 34(1):1-11, 2000.
- Cragin J.H. and D.C. Leggett. "Diffusion and Flux of Explosive-Related Compounds in Plastic Mine Surrogates". US Army Corps of Engineers, Engineer Research and Development Center, Cold Region Research & Engineering Laboratory, ERDC/CRREL TR-03-12, 2003.
- Cumming C.J., C. Aker, M. Fisher, M. Fox, M.J. la Grone, D. Reust, M.G. Rockley, T.M. Swager, E. Towers and V. Williams. "Using Novel Fluorescent Polymers as Sensory Materials for Above-Ground Sensing of Chemical Signature Compounds Emanating from Buried Landmines". *IEEE Transactions on Geoscience and Remote Sensing*, 39(6):1119-1128, 2001.
- Dillert R., M. Brandt, I. Fornefett, U. Siebers and D. Bahnemann. "Photo Catalytic Degradation of TNT and other Nitroaromatic Compounds". *Chemosphere*, 30(12):2333-2341, 1995.
- Dontsova K.M., S.L. Yost, J. Šimůnek, J.C. Pennington and C.W. Williford. "Dissolution and Transport of TNT, RDX, and Composition B in Saturated Soil Columns". *Journal of Environmental Quality*, 35:2043–2054, 2006.

- Ericksson J. and U. Skyllberg. "Binding of 2,4,6-Trinitrotoluene and its Degradation Products in a Soil Organic Matter Two-Phase System". *Journal of Environmental Quality*, 30:2053-2061, 2001.
- Esteve-Núñez A., A. Caballero and J.L. Ramos. "Biological Degradation of 2,4,6-Trinitrotoluene". *Microbiology and Molecular Biology Reviews*, 65(3):335-352, 2001.
- Fetter C.W. *Contaminant Hydrogeology*, Prentice Hall Inc., New Jersey, 500 p., 1999.
- Fisher M. and C. Cumming. "Detection of Trace Concentration of Vapour Phase Nitroaromatic Explosive by Fluorescence Quenching of Novel Polymer Materials". *Nomadics, Inc.*, 7th International Symposium on the Analysis and Detection of Explosives, Edinburgh Scotland, UK., June 2001.
- George V., T.F. Jenkins, D.C. Leggett, J.H. Cragin, J. Phelan, J. Oxley and J. Pennington. "Progress on Determining the Vapor Signature of a Buried Landmine," *Proceedings of the SPIE, Detection and Remediation Technologies for Mines and Minelike Targets IV*, 3710(2):258-269, 1999.
- Grant S.A. and A. Salehzadeh. "Calculations of Temperature Effects on Wetting Coefficients of Porous Solids and their Capillary Pressure Functions". *Water Resources Research*, 32:261-270, 1996.
- Grifoll J., J.M. Gastó and Y. Cohen. "Non-isothermal Soil Water Transport and Evaporation". *Advances in Water Resources*, 28(11):1254-1266, 2005.
- Havis R.N., R.E. Smith and D.D. Adrian. "Partitioning Solute Transport between Infiltration and Overland Flow under Rainfall". *Water Resources Research*, 28(10):2569-2580, 1992.
- Hawari J., S. Beaudet, A. Halasz, S. Thibouto and G. Ampleman. "Microbial Degradation of Explosives: Biotransformation versus Mineralization". *Applied Microbiology and Biotechnology*, 54:605-618, 2000.
- Hoff J.T., D. Mackay, R.W. Gillham and W.Y. Shiu. "Partitioning of Organic Chemicals at the Air Water Interface in Environmental Systems". *Environmental Science and Technology*, 27(10):2171-2180, 1993a.
- Hoff J.T., R.W. Gillham, D. Mackay and W.Y. Shiu. "Sorption of Organic Vapours in a Sand Aquifer Material". *Environmental Science and Technology*, 27(13):2789-2794, 1993b.
- Hopmans J.W. and J.H. Dane. "Temperature Dependence of Soil Hydraulic Properties". *Journal of Soil Science Society of America*, 50:4-9, 1986.

- Hutson J. L. and R. J. Wagenet. Leaching Estimation and Chemistry Model. A Process Based Model of Water and Solute Movement Transformations, Plant Uptake and Chemical Reactions in the Unsaturated Zone. Department of Agronomy, Cornell University, New York, Version 20, 148, 1989.
- Hwang H.M., S.M. Slaughter, S.M. Cook and H. Cui. "PhotoChemical and Microbial Degradation of 2,4,6- Trinitrotoluene (TNT) in a Freshwater Environment". Bulletin of Environmental Contamination and Toxicology, 65:228-235, 2000.
- Irrazábal M., E. Borrero, J.G. Briano, M. Castro and S.P. Hernández. "3D Numerical Simulation of the Transport of Chemical-Signature-Compounds from Buried Landmines". Proceedings of the SPIE, Detection and Remediation Technologies for Mines and Minelike Targets X, 5794:738-744, 2005.
- Irrazábal M., V. Florián, M. Castro, S.P. Hernández and J.G. Briano. "Effect of Environmental Parameters on the Chemical Signature of TNT in Soil". Proceedings of the SPIE, Detection and Remediation Technologies for Mines and Minelike Targets XII, 6553, 2007.
- Jawitz J.W. "Moments of Truncated Continuous Univariate Distributions". Advances in Water Resources, 27: 269–281, 2004.
- Jenkins T.F., D.C. Leggett and T.A. Ranney. "Vapor Signatures from Military Explosives". US Army Corps of Engineers, Special Report 99-21, 1999.
- Jenkins T.F., M.E. Walsh, P.H. Miyares, J.A. Kopczynski, T.A. Ranney, V. George, J. Pennington and T.E. Berry. "Analysis of Explosives-Related Chemical Signatures in Soil Samples Collected near Buried Landmines". US Army Corps of Engineers, Engineer Research and Development Center, Cold Region Research & Engineering Laboratory, ERDC/CRREL Technical Report TR-00-5, 2000.
- Jenkins T.F., J.C. Pennington, T.A. Ranney, T.E. Berry Jr., P.H. Miyares, M.E. Walsh, A.D. Hewitt, N.M. Perron, L.V. Parker, C.A. Hayes and E.G. Wahlgren. "Characterization of Explosives Contamination at Military Firing Ranges". US Army Corps of Engineers, Engineer Research and Development Center, Technical Report No. 01-05, 2001.
- Jenkins T.F., J.C. Pennington, G.Ampleman, S. Thiboutot, M.R. Walsh, E. Diaz, K.M. Dontsova, A.D. Hewitt, M.E. Walsh, S.R. Bigl, S. Taylor, D.K. MacMillan, J.L. Clausen, D. Lambert, N.M. Perron, M.C. Lapointe, S. Brochu, M. Brassard, R. Stowe, R. Farinaccio, A. Gagnon, A. Marois, D. Gilbert, D. Faucher, S. Yost, C. Hayes, C.A. Ramsey, R.J. Rachow, J.E. Zufelt, C.M. Collins, A.B. Gelvin and S.P. Saari. "Characterization and Fate of Gun and Rocket Propellant Residues on Testing and Training Ranges. Interim Report 1". US Army Corps of Engineers, Engineer Research and Development Center, Technical Report ERDC TR-07-1, 2007.

- Jury W.A. and R. Horton. *Soil Physics*, 6th edition, John Wiley & Sons, Inc., p. 370, 2004.
- Keeley R. *Understanding Landmines and Mine Action*. (An extract from the publication “The Economics of Landmine Clearance” published by dissertation.de, October 2006), 2006.
- Larson R.A. “Effects of Surfactants on Reduction and Photolysis (>290 nm) of Nitro Aromatic Compounds”. *Journal of Environmental Science and Technology*, 34(3):505-508, 2000.
- Leggett D.C., T.F. Jenkins, A.W. Hogan and T.A. Ranney. “External Contamination of Landmines by Organic Nitro-Compounds”. US Army Corps of Engineers, Engineering Research and Development Center, Technical Report ERDC/CRREL TR-00-2, 2000.
- Leggett D.C., J.H. Cragin, T.F. Jenkins and T. Ranney. “Release of Explosive-Related Vapors from Land Mines”. US Army Corps of Engineers, Engineering Research and Development Center, Cold Regions Research and Engineering Laboratory, Technical Report ERDC/CRREL TR-01-6, 2001.
- Lynch J.C., J.M. Brannon and J.J. Delfino. “Dissolution Rates of Three High Explosive Compounds: TNT, RDX, and HMX”. *Chemosphere*, 47:725–734, 2002.
- Massol A., D. Pérez, E. Pérez, M. Berrios and E. Díaz. “Trace Elements Analysis in Forage Samples from a US Navy Bombing Range (Vieques, Puerto Rico)”. *International Journal of Environmental Research and Public Health*, 2(2):263–266, 2005.
- McGrath C.J. “Review of Formulations for Processes Affecting Subsurface Transport of Explosives”. US Army Corps of Engineers, Waterways Experiment Station, Vicksburg, MS., Technical Report IRRP-95-2, 1995.
- Miyares P.H. and T.F. Jenkins. “Estimating the Half-Lives of Key Components of the Chemical Vapor Signatures of Land Mines”. U.S. Army Corps of Engineers, Engineer Research and Development Center, Cold Region Research & Engineering Laboratory, ERDC/CRREL TR-00-17, 2000.
- Molina G., I. Padilla, M. Pando and D. Pérez. “Field Lysimeters for the Study of Fate and Transport of Explosive Chemical in Soils under Variable Environmental Conditions”. Paper Number: 6217-137, in *Detection and Remediation Technologies for Mines and Minelike Targets XI*, SPIE Defense and Security Symposium, Orlando, FL. April 17-21, 2006.
- Morley M.C., H. Yamamoto, G.E. Speitel Jr. and J. Clausen. “Dissolution Kinetics of High Explosives Particles in a Saturated Sandy Soil”. *Journal of Contaminant Hydrology*, 85(3-4):141-158, 2006.

- Myers T.E., J.M. Brannon, J.C. Pennington, W.M. Davis, K.F. Myers, D.M. Townsend and M.K. Ochman. "Laboratory Studies of Soil Sorption/Transformation of TNT, RDX, and HMX". US Army Corp of Engineers, Waterways Experiment Station, Vicksburg, MS., Technical Report IRRP-98-8, 1998.
- Padilla I. Y. "Transport of Nonreactive and Volatile Solutes in Unsaturated Porous Media under Wetting and Draining Conditions". Dissertation Thesis, The University of Arizona, 1998.
- Padilla I.Y., T.C. Jim Yeh and M.H. Conklin. "The Effect of Water Content on Solute Transport in Unsaturated Porous Media". *Water Resources Research*, 35(11):3303–3313, 1999.
- Padilla A.C., I.Y. Padilla and I. Santiago. "Multiphase Extraction Sampling of Explosives in Unsaturated Soils". Paper Number: 6217-139, Proceedings of SPIE, Detection and Remediation Technologies for Mines and Minelike Targets XI, SPIE Defense and Security Symposium, April 17-21 2006 in Orlando, FL, Volume 6217, 62173C, Pages 1-11, 2006.
- Pella, P.A. "Measurement of the Vapor Pressures of TNT, 2,4-DNT, 2,6-DNT and EGDN". *Journal of Chemical Thermodynamics*, 9:301-305, 1977.
- Pennington J.C and W.H. Patrick. "Adsorption and Desorption of 2,4,6 Trinitrotoluene by Soils". *Journal of Environmental Quality*, 19:559-567, 1990.
- Pennington J.C., T.F. Jenkins, G. Ampleman, S. Thiboutot, J.M. Brannon, J. Lewis, J.E. DeLaney, J. Clausen, A.D. Hewitt, M.A. Hollander, C.A. Hayes, J.A. Stark, A. Marois, S. Bochu, H.Q. Dinh, D. Lambert, A. Gagnon, M. Bouchard and Martel. "Distribution and Fate of Energetics on DoD Test and Training Ranges: Interim Report 3". US Army Corps of Engineers, Engineer Research and Development Center, Technical Report ERDC TR-03-2, 2003.
- Petersen L.W., Y.H. El-Farhan, P. Moldrup, D.E. Rolston and T. Yamaguchi. "Transient Diffusion, Adsorption, and Emission of Volatile Organic Vapors in Soils with Fluctuating Low Water Content". *Journal of Environmental Quality*, 25:1054-1063, 1996.
- Phelan J.M. and S.W. Webb. "Environmental Fate and Transport of Chemical Signatures from Buried Landmines - Screening Model Formulation and Initial Simulations". Sandia National Laboratories, Sand Report SAND97-1426, 1997.
- Phelan J.M. and S.W. Webb. "Chemical Detection of Buried Landmines". Mine Warfare Association, Proceeding of the 3rd International Symposium on Technology and the Mine Problem, April 6-9, 1998.

- Phelan J.M., M. Gozdor, S.W. Webb and M. Cal. "Laboratory Data and Model Comparisons of the Transport of Chemical Signatures from Buried Landmines/UXO". Proceedings of the SPIE Conference on Detecting and Remediation Technologies for Mines and Minelike Targets V, April 24-28, 2000.
- Phelan J.M. and J.L. Barnett. "Phase Partitioning of TNT and DNT in Soils". Sandia National Laboratories, Sand Report SAND2001-0310, 2001.
- Phelan J.M., S.W. Webb, M. Gozdor, M. Cal and J.L. Barnett. "Effect of Soil Wetting and Drying on DNT Vapor Flux – Laboratory Data and T2TNT Model Comparisons". Proceedings of the SPIE Conference on Detecting and Remediation Technologies for Mines and Minelike Targets V, April 16-20, 2001.
- Phelan J.M. and S.W. Webb. "Chemical Sensing for Buried Landmines – Fundamental Processes Influencing Trace Chemical Detection". Sandia Laboratories, Sand Report SAND2002-0909, 2002.
- Porro I., P.J. Wierenga and R.G. Hills. "Solute Transport through Large Uniform and Layered Soil Columns". Water Resources Research, 29(4):1321-1330, 1993.
- Price, A.R., C.J. Pennington, L.S. Larson, D. Neumann and A.H. Charolett. "Uptake of RDX and TNT by Agronomy Plants". Soil and Sediment Contamination, 11(3):307-326, 2002.
- Ravikrishna, R., S.L. Yost, C.B. Price, K.T. Valsaraj, J.M. Brannon and P. Miyares. "Vapor Phase Transport of Unexploded Ordnance Compounds through Soils". Environmental Toxicology and Chemistry, 21(10):2020-2026, 2002.
- Reichman R., Y. Mahrer and R. Wallach. "A Combined Soil-Atmosphere Model for Evaluating the Fate of Surface Applied Pesticides 2. The Effect of Varying Environmental Conditions". Environmental Science & Technology, 34:1321-1330, 2000.
- Rensselaer Polytechnic Institute. Architectural Acoustics.
<<http://symphony.arch.rpi.edu/acoustics/research.html>> [Accessed on April 12, 2007].
- Roberson J.A. and C.T. Crowe. Engineering Fluid Mechanics, Houghton Mifflin Company, 4th Edition, 747 p., 1990.
- Rodríguez S., I. Padilla and I. Santiago. "Development of a Multi-Scale Packing Methodology for Evaluating Fate and Transport Processes of Explosive-Related Chemicals in Soil Physical Models". Paper Number: 6217-77, Proceedings in Detection and Remediation Technologies for Mines and Minelike Targets XI, SPIE Defense and Security Symposium, Orlando, FL., April 17-21, 2006.

- Roero C. "Contact Angle Measurements of Sessile Drops Deformed by a DC Electric Field". Proceedings of the 4th International Symposium on Contact Angle, Wettability and Adhesion, Philadelphia, USA, 2004.
- Roth K. and K. Hammel. "Transport of Conservative Chemical through an Unsaturated Two Dimensional Miller-Similar Medium with Steady State Flow". Water Resources Research, 32(6):1653-1663, 1996.
- Sandia National Laboratories. Sandia Labs Developing Means to Sniff Out Mines Chemically and Electronically. <<http://www.sandia.gov/media/landmine.htm>> [Accessed on April 12, 2007].
- Schaap M.G., F.J. Leij and M.Th. van Genuchten. "ROSETTA: A Computer Program for Estimating Soil Hydraulic Parameters with Hierarchical Pedotransfer Functions". Journal of Hydrology, 251:163-176, 2001.
- Schmelling D.C., K.A. Gray and P.V. Kamat. "Role of Reduction in the Photo Catalytic Degradation of TNT". Journal of Environmental Science and Technology, 30(83):2547-2555, 1996.
- Schwarzenbach R.P., P.M. Gschwend and D.M. Indoben. Environmental Organic Chemistry, John Wiley & Sons, Inc., 1309 p., 2003.
- Sheremata T.W., S. Thiboutot, G. Ampleman, L. Paquet, A. Halasz and J. Hawari. "Fate of 2,4,6-Trinitrotoluene and its Metabolites in Natural and Model Soil Systems". Environmental Science & Technology, 33:4002-4008, 1999.
- Šimůnek J., N.J. Jarvis, M.Th. van Genuchten and A. Gärdenäs. "Review and Comparison of Models for Describing non-equilibrium and Preferential Flow and Transport in the Vadose Zone". Journal of Hydrology, 272:14–35, 2003.
- Šimůnek J., M. Šejna and M.Th. van Genuchten. The Hydrus 1-D Software Package for Simulating the One-Dimensional Movement of Water, Heat, and Multiple Solutes in Variably-Saturated Media, version 3.0, HYDRUS Software Series 1, Department of Environmental Sciences, University of California Riverside, Riverside, California, USA, 2005.
- Šimůnek J., M. Šejna and M.Th. van Genuchten. The HYDRUS Software Package for Simulating the Two- and Three-Dimensional Movement of Water, Heat, and Multiple Solutes in Variably-Saturated Media, version 1.0, U.S. Salinity Laboratory, Riverside, California, 2006.

- Skaggs T.H. and F.J. Leij. Solute transport: Theoretical Background In: Methods of Soil Analysis, Part 1, Physical Methods, Chapter 6.3, Eds. J.H. Dane and G.C. Topp, Third edition, SSSA, Madison, WI, 1353-1380, 2002.
- Thibaud C., C. Erkey and A. Akgerman. "Investigation of the Effect of Moisture on the Sorption and Desorption of Chlorobenzene and Toluene from Soil". Environmental Science & Technology, 27:2373-2380, 1993.
- Torres A., I. Padilla and S. Hwang. "Physical Modeling of 2,4-DNT Gaseous Diffusion through Unsaturated Soil". Proceedings of SPIE, Detection and Remediation Technologies for Mines and Minelike Targets XII, SPIE Defense and Security Symposium, Orlando, FL., April 9-13, 6553, 2007.
- Unicef. Clases de Minas. <<http://www.unicef.org/co/masartemenosminas/4.htm>> [Accessed on April 15, 2007].
- US EPA. Handbook on the Management of Ordnance and Explosives at Closed, Transferring, and Transferred Ranges and Other Sites, 222 p., 2002.
- van Genuchten M.Th. and P.J. Wierenga. "Mass Transfer Studies in Sorbing Porous Media: I. Analytical Solutions". Journal of Soil Science Society of America, 40(4): 473-480, 1976.
- Vanderborght J., A. Timmerman and J. Feyen. "Solute Transport for Steady-State and Transient Flow in Soils with and without Macropores". Soil Science Society of America, 64:1305-1317, 2000.
- Webb S.W., S.A. Finsterle, K. Pruess and J.M. Phelan. "Prediction of TNT-Signature from Buried Landmines". Proceeding of the TOUGH Workshop'98, Lawrence Berkeley National Laboratory, Berkeley, CA., Report LBNL-41995, 1998.
- Webb S.W., K. Pruess, J.M. Phelan and S.A. Finsterle. "Development of a Mechanistic Model for the Movement of Chemical Signatures from Buried Landmines/UXO". Proceedings of the SPIE, Conference on Detecting and Remediation Technologies for Mines and Minelike Targets IV, April 5-9, 1999.
- Webb S.W. and J.M. Phelan. "Effect of Diurnal and Seasonal Weather Variations on the Chemical Signatures from Buried Landmines/UXO". Proceedings of the SPIE, Conference on Detecting and Remediation Technologies for Mines and Minelike Targets V, April 24-28, 2000.
- Wierenga P.J. and M.Th. van Genuchten. "Solute Transport through Small and Large Unsaturated Columns". Ground Water, 27(1): 35-42, 1989.

- Wildenschild D. and K.H. Jensen. "Laboratory Investigations of Effective Flow Behavior in Unsaturated Heterogeneous Sands". *Water Resources Research*, 35.1:17-28, 1999.
- Young D.F. and W.P. Ball. "Column Experimental Design Requirements for Estimating Model Parameters from Temporal Moments under Nonequilibrium Conditions". *Advances in Water Resources*, 23:449-460, 2000.
- Yoshikawa K., K. Masuda, Y. Yamamoto, T. Takamatsu, H. Toku, K. Nagasaki, E. Hotta, K. Yamauchi, M. Ohnishi and H. Osawa. "Research & Development of Technology for Humanitarian Landmine Detection by a Compact IEC Fusion Neutron Source". IC/P6-54, 5th US-Japan Workshop on Inertial Electrostatic Confinement Fusion, U. Wisconsin, Madison, 2002.
- Zyvoloski G., Z. Dash and S. Kelkar. FEHM: Finite Element Heat and Mass Transfer Code. Los Alamos National Laboratory, LA-11224-MS, 1988.

APPENDIXES

Appendix A. Graphs Obtained from Experimental Data

A. Experiment 1 (Saturated, 25°C, Infiltration, TNT solution injected)

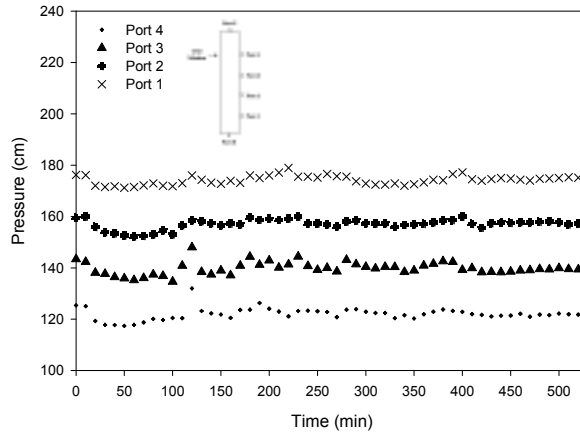


Figure 73. Pressures during Infiltration Process under Saturated Conditions at 25°C (Exp 1)

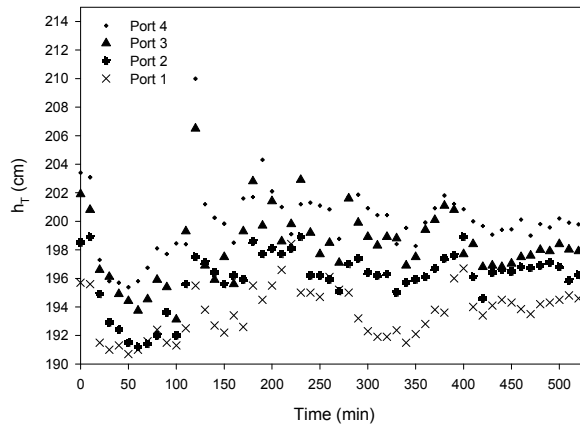


Figure 74. Total Hydraulic Heads during Infiltration Process under Saturated Conditions at 25°C (Exp 1)

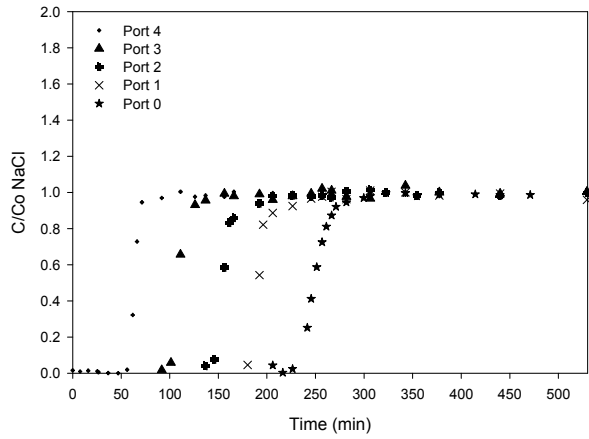


Figure 75. NaCl BTC during Infiltration Process under Saturated Conditions at 25°C (Exp 1)

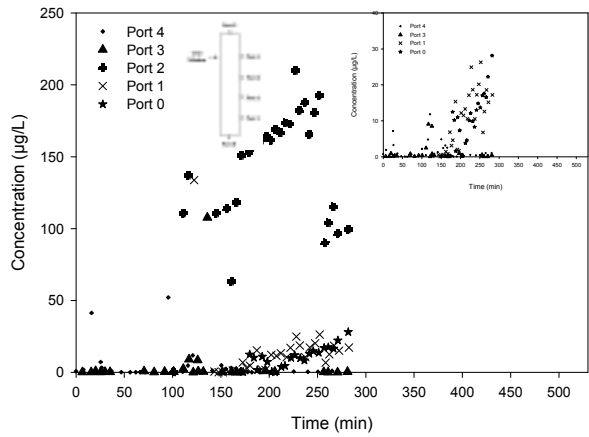


Figure 76. TNT_W BTC during Infiltration Process under Saturated Conditions at 25°C (Exp 1)

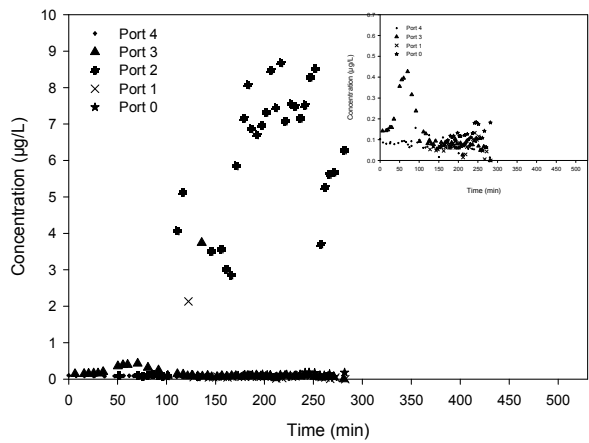


Figure 77. DNT_W BTC during Infiltration Process under Saturated Conditions at 25°C (Exp 1)

B. Experiment 2 (Saturated, 25°C, Infiltration-Reverse Flow, TNT solution injected)

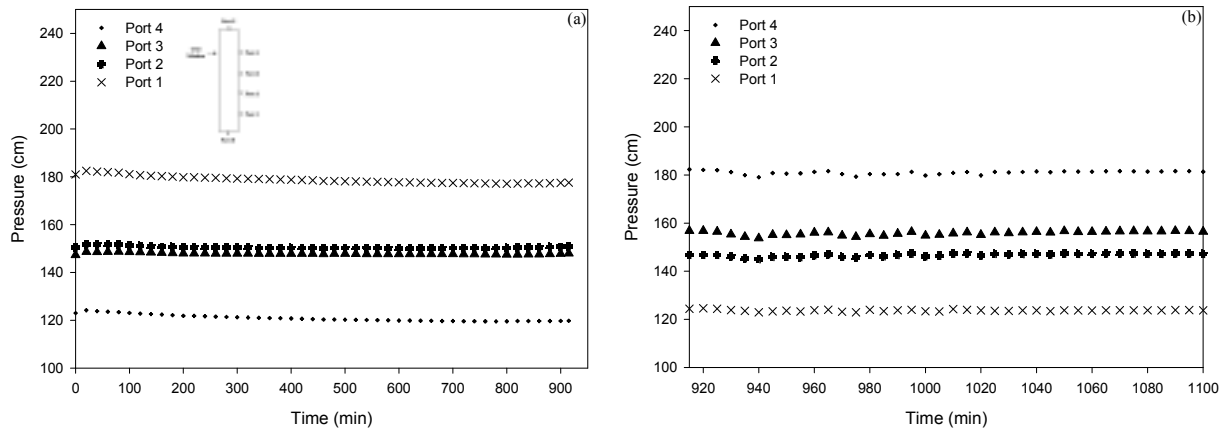


Figure 78. Pressures during Infiltration (a) and Reverse Flow (b) Processes under Saturated Conditions at 25°C (Exp 2)

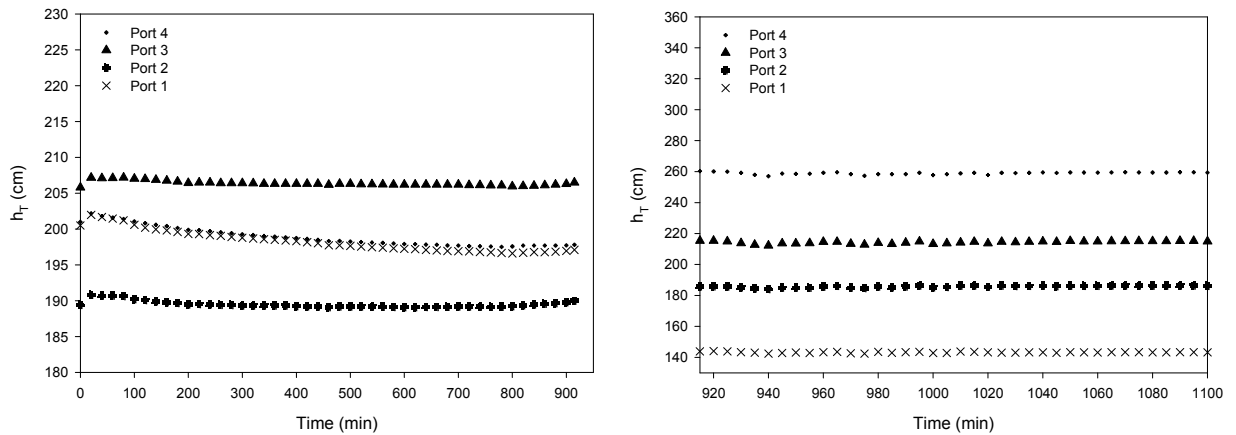


Figure 79. Total Hydraulic Heads during Infiltration (a) and Reverse Flow (b) Processes under Saturated Conditions at 25°C (Exp 2)

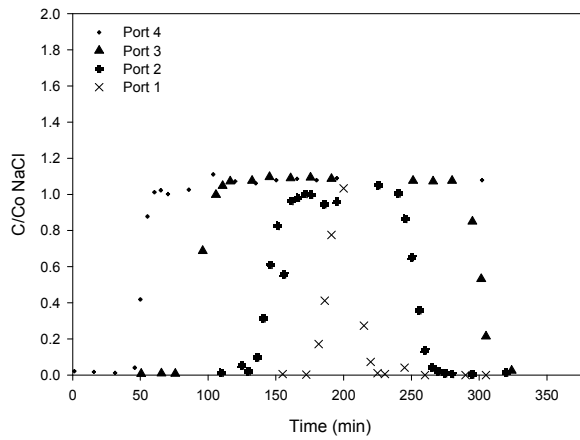


Figure 80. NaCl BTC during Infiltration and Reverse Flow Processes under Saturated Conditions at 25°C (Exp 2)

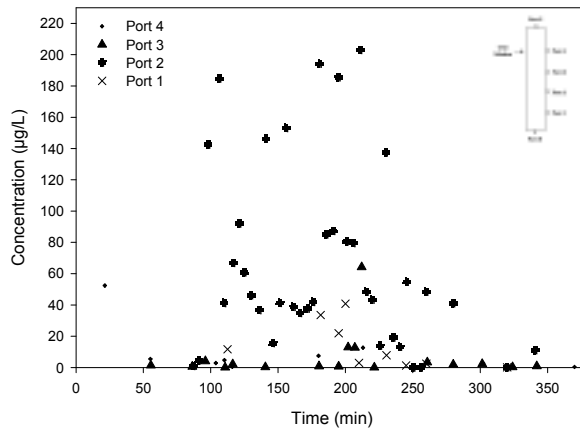


Figure 81. TNT_w BTC during Infiltration and Reverse Flow Processes under Saturated Conditions at 25°C (Exp 2)

C. *Experiment 3 (Saturated, 25°C, Infiltration-Evaporation, TNT-DNT source buried)*

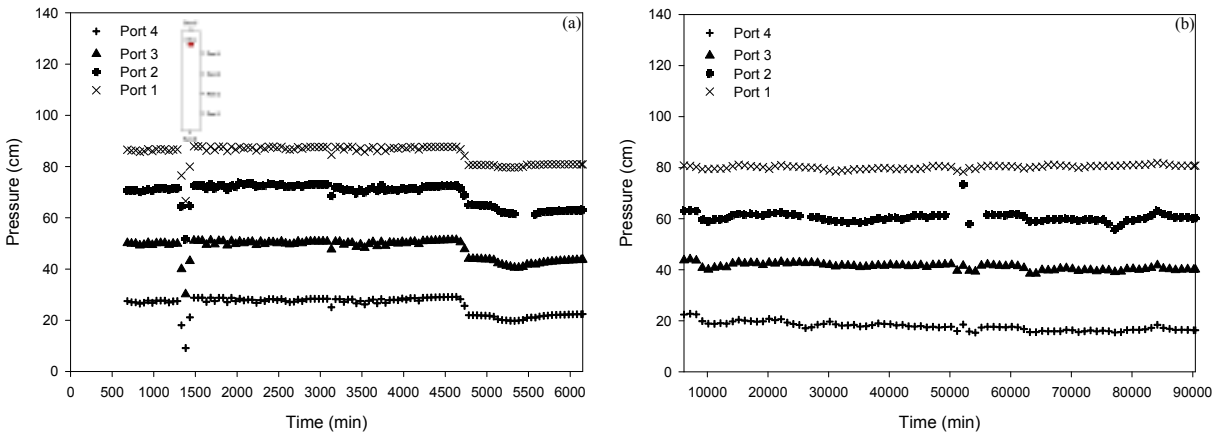


Figure 82. Pressures during Infiltration (a) and Evaporation (b) Processes under Saturated Conditions at 25°C (Exp 3)

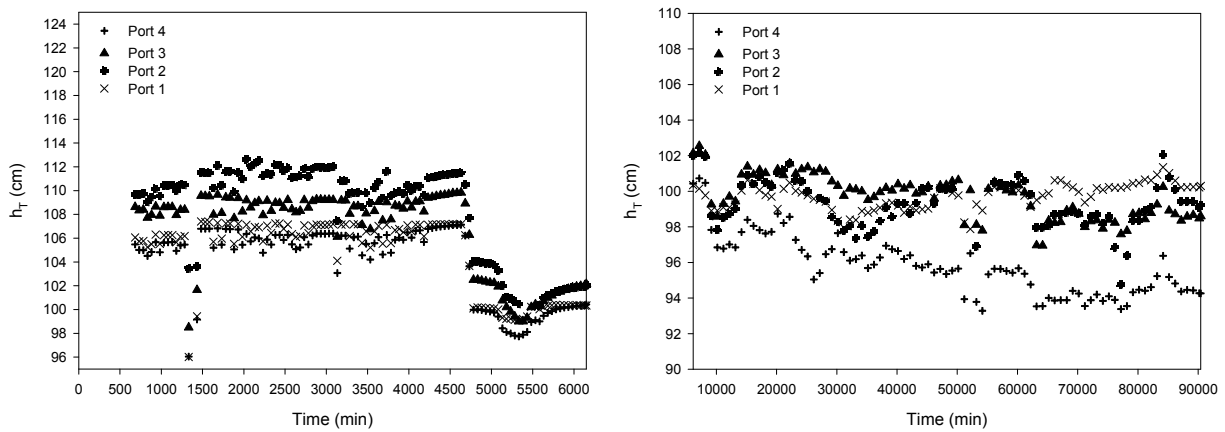


Figure 83. Total Hydraulic Heads during Infiltration (a) and Reverse Flow (b) Processes under Saturated Conditions at 25°C (Exp 2)

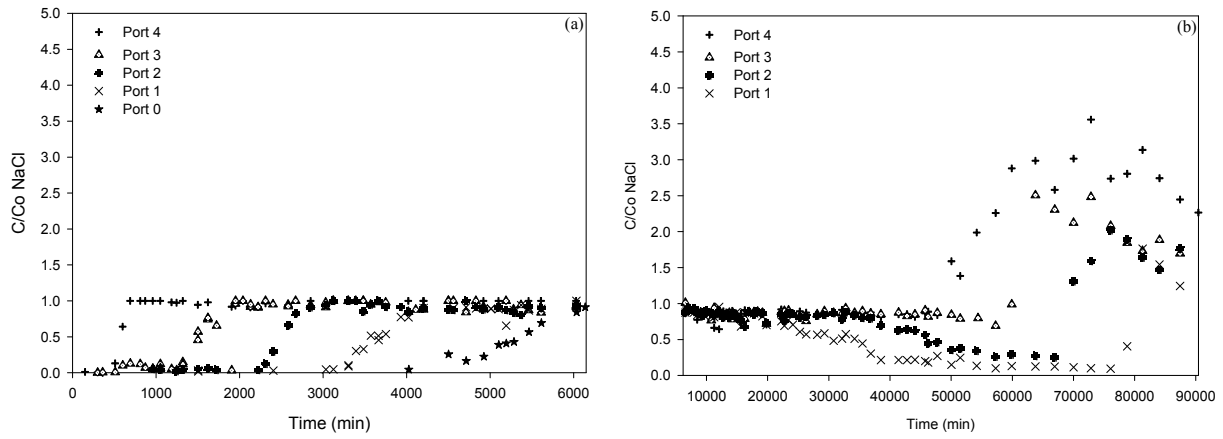


Figure 84. NaCl BTC during Infiltration (a) and Evaporation (b) Processes under Saturated Conditions at 25°C (Exp 3)

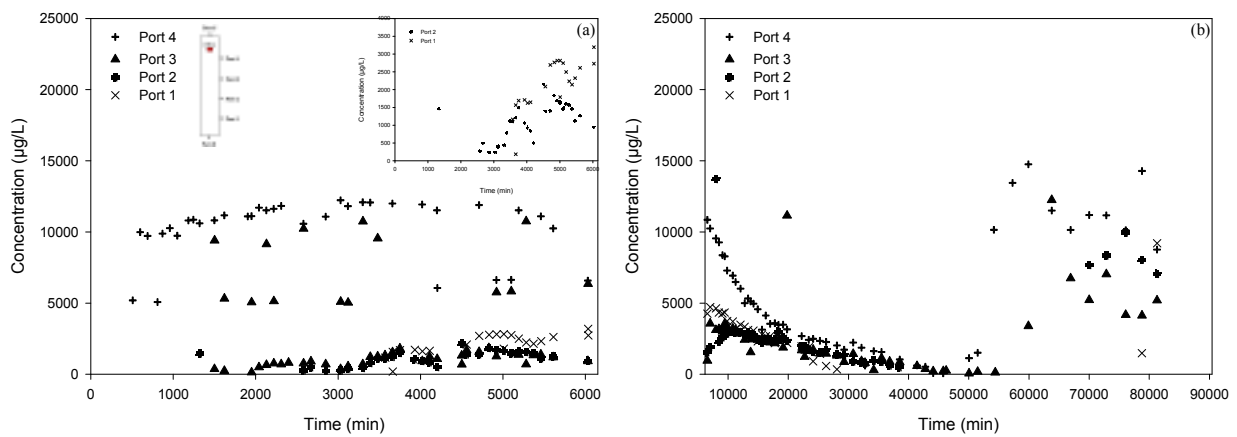


Figure 85. TNT_w BTC during Infiltration (a) and Evaporation (b) Processes under Saturated Conditions at 25°C (Exp 3)

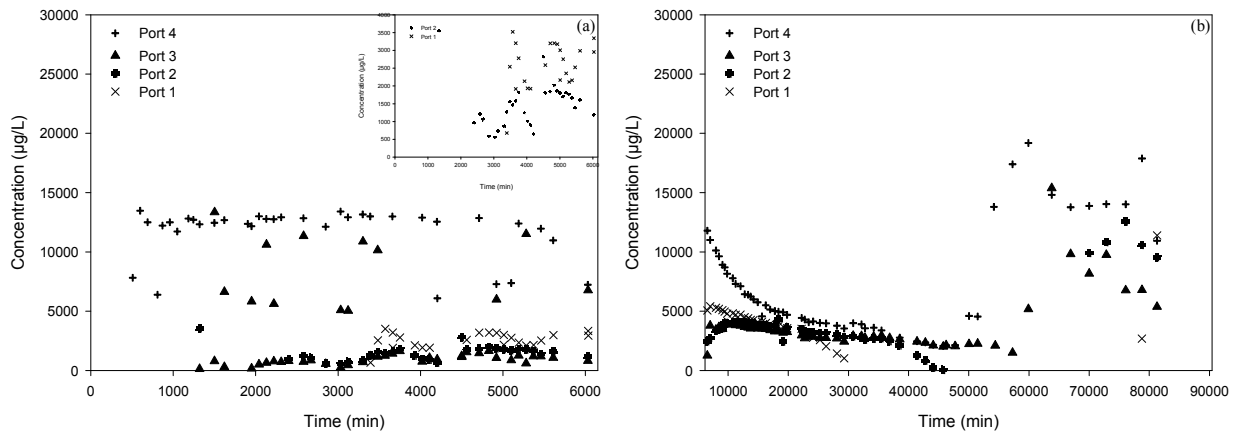


Figure 86. DNT_w BTC during Infiltration (a) and Evaporation (b) Processes under Saturated Conditions at 25°C (Exp 3)

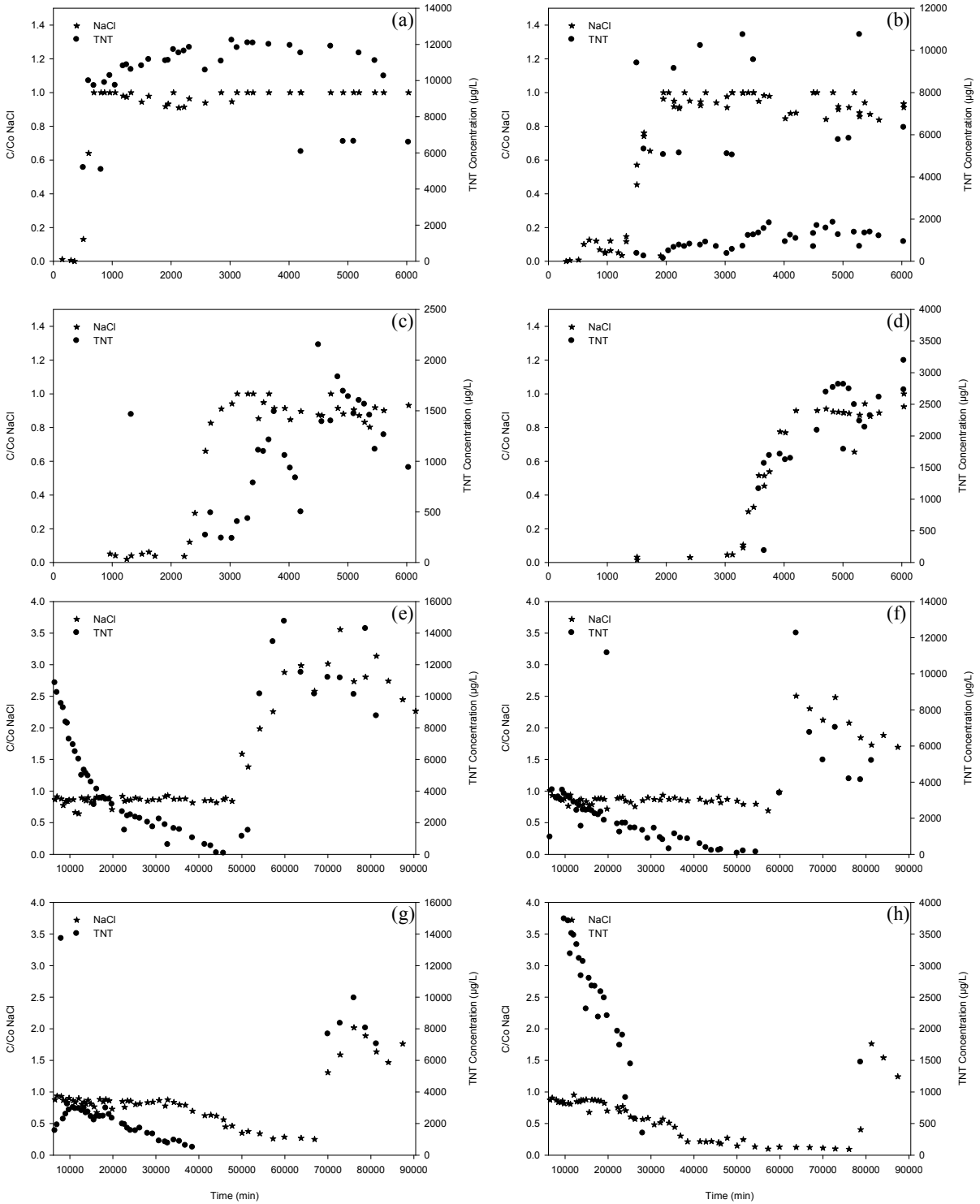


Figure 87. NaCl vs. TNT_w during: Infiltration Process for Port 4 (a), Port 3 (b), Port 2 (c) and Port 1 (d); during Evaporation Process for Port 4 (e), Port 3 (f), Port 2 (g) and Port 1 (h), under Saturated Conditions at 25°C (Exp 3)

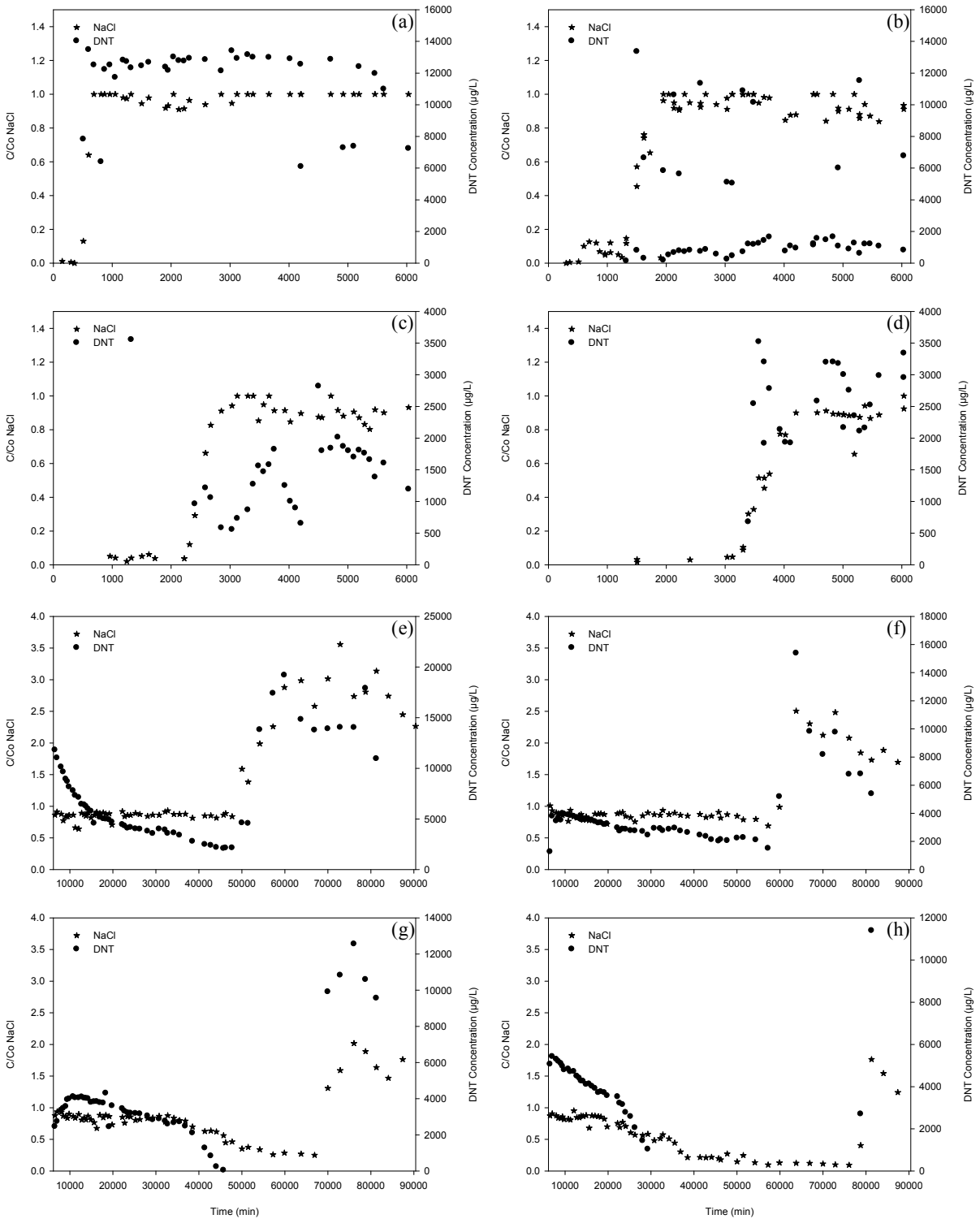


Figure 88. NaCl vs. DNT_w during: Infiltration Process for Port 4 (a), Port 3 (b), Port 2 (c) and Port 1 (d); during Evaporation Process for Port 4 (e), Port 3 (f), Port 2 (g) and Port 1 (h), under Saturated Conditions at 25°C (Exp 3)

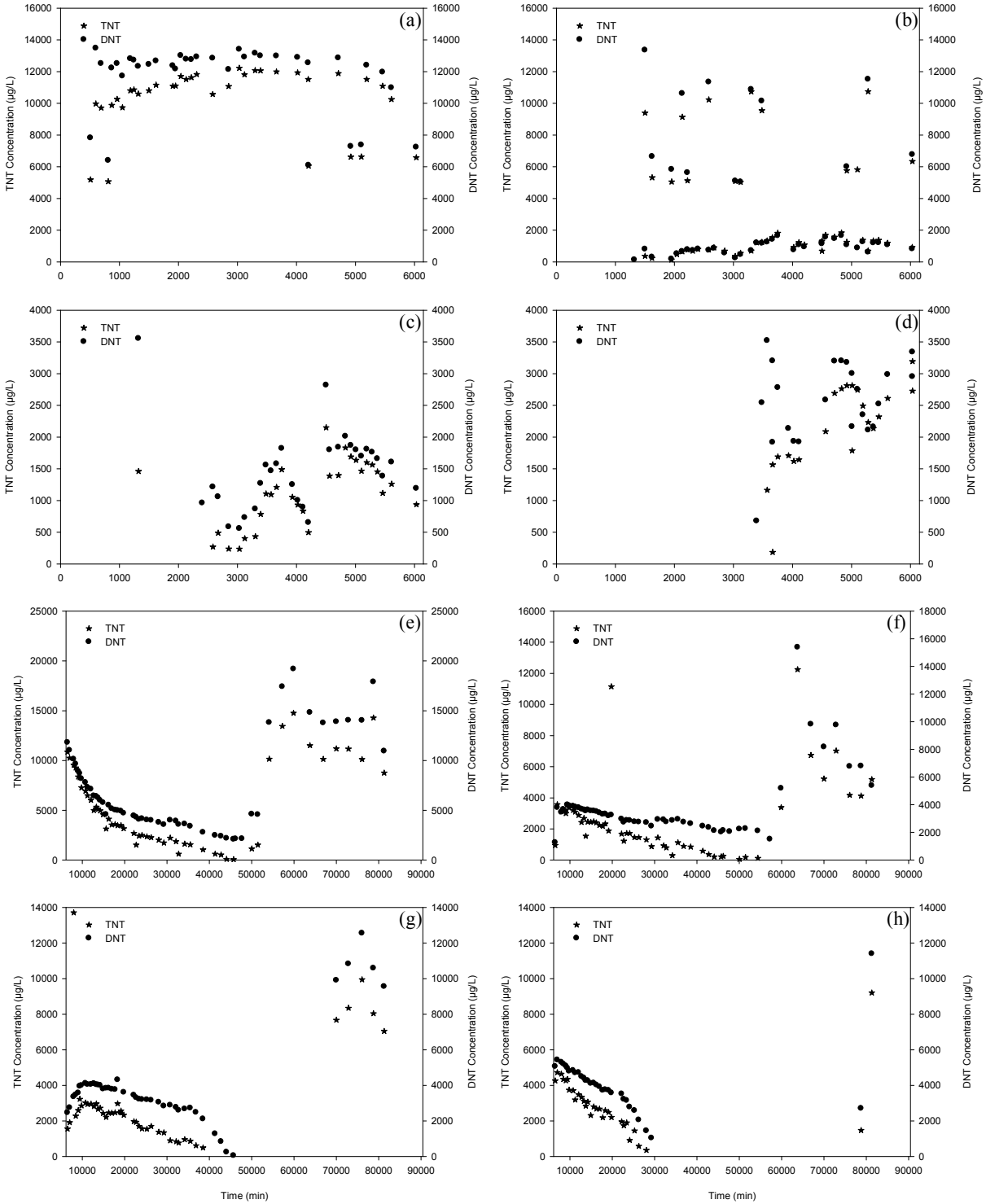


Figure 89. TNT_W vs. DNT_W during: Infiltration Process for Port 4 (a), Port 3 (b), Port 2 (c) and Port 1 (d); during Evaporation Process for Port 4 (e), Port 3 (f), Port 2 (g) and Port 1 (h), under Saturated Conditions at 25°C (Exp 3)

D. Experiment 4 (75% of Saturation, 25°C, Infiltration-Evaporation, TNT-DNT source buried)

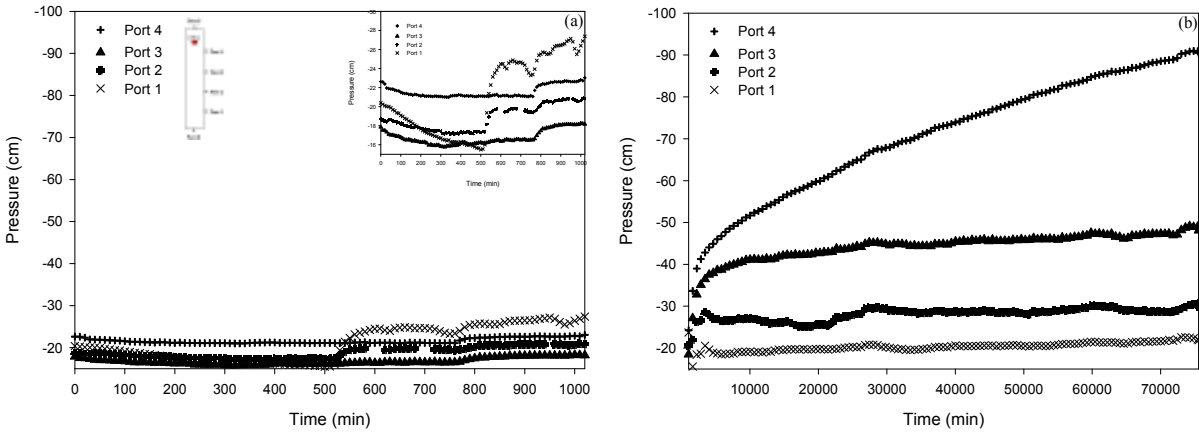


Figure 90. Pressures during Infiltration (a) and Evaporation (b) Processes under 75% of Saturation at 25°C (Exp 4)

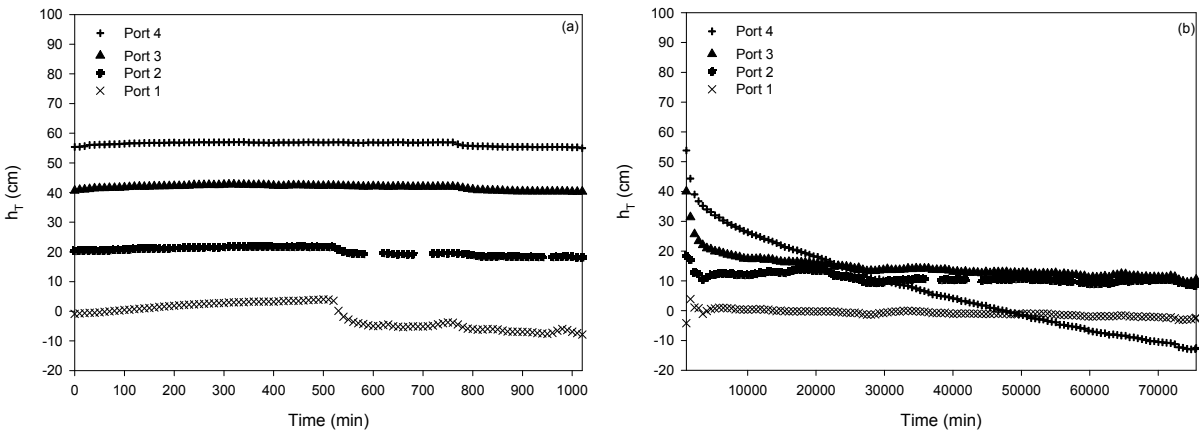


Figure 91. Total Hydraulic Heads during Infiltration (a) and Evaporation (b) Processes under 75% of Saturation at 25°C (Exp 4)

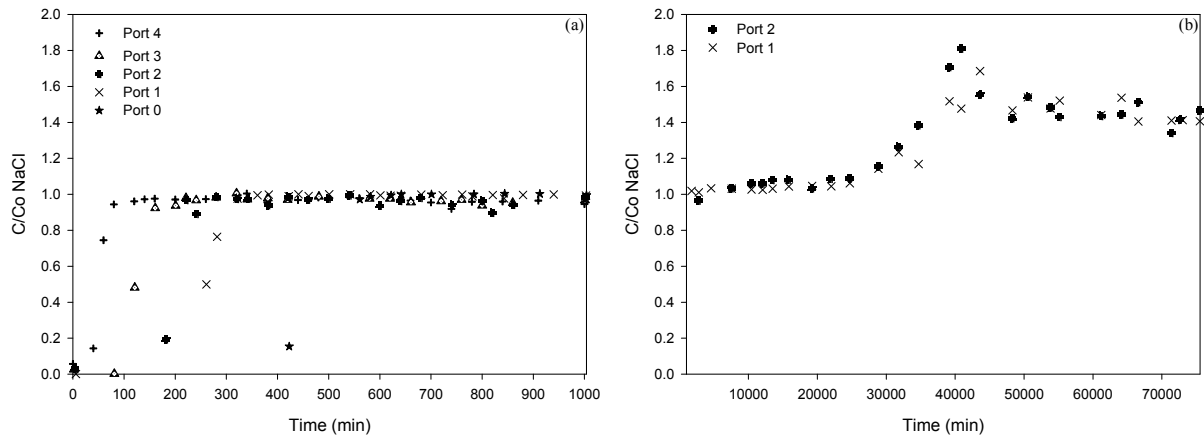


Figure 92. NaCl BTC during Infiltration (a) and Evaporation (b) Processes under 75% of Saturation at 25°C (Exp 4)

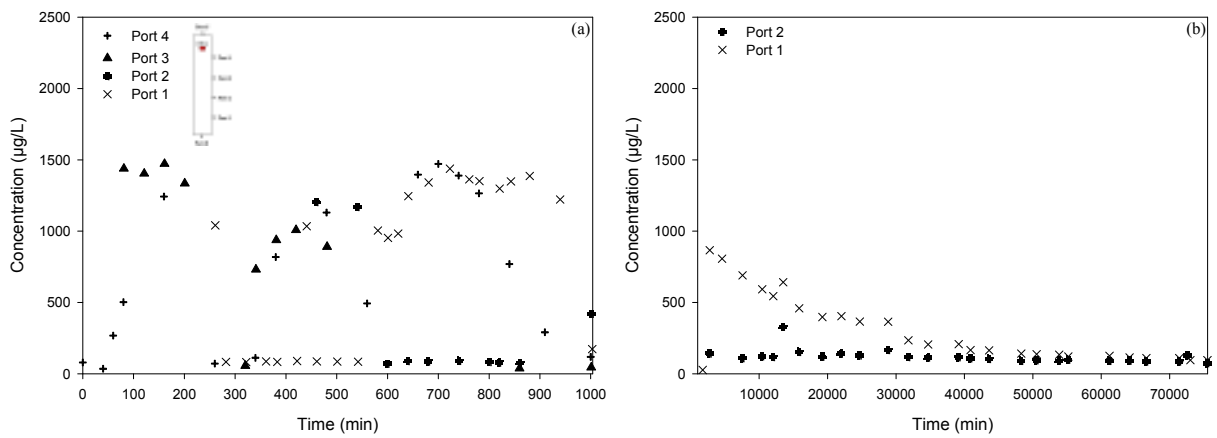


Figure 93. TNT_w BTC during Infiltration (a) and Evaporation (b) Processes under 75% of Saturation at 25°C (Exp 4)

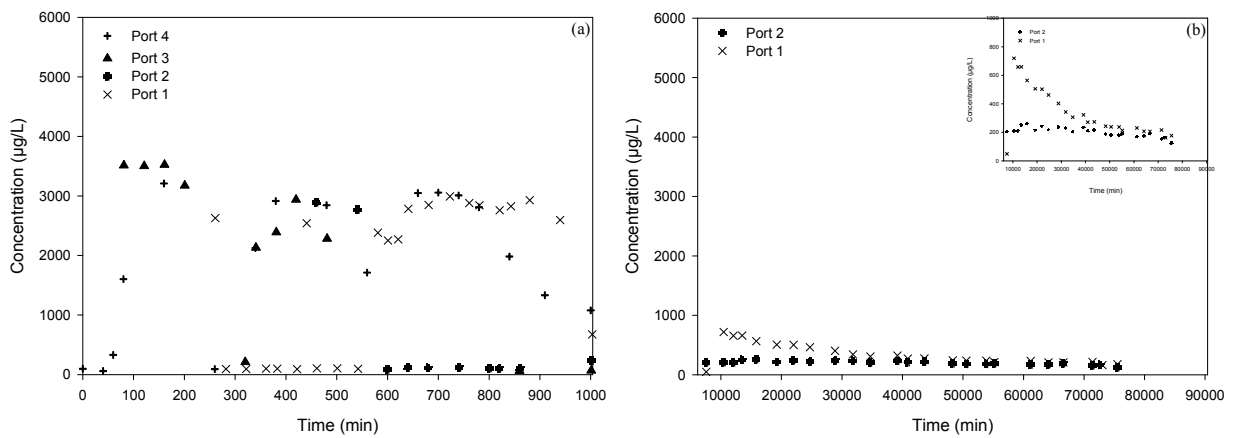


Figure 94. DNT_w BTC during Infiltration (a) and Evaporation (b) Processes under 75% of Saturation at 25°C (Exp 4)

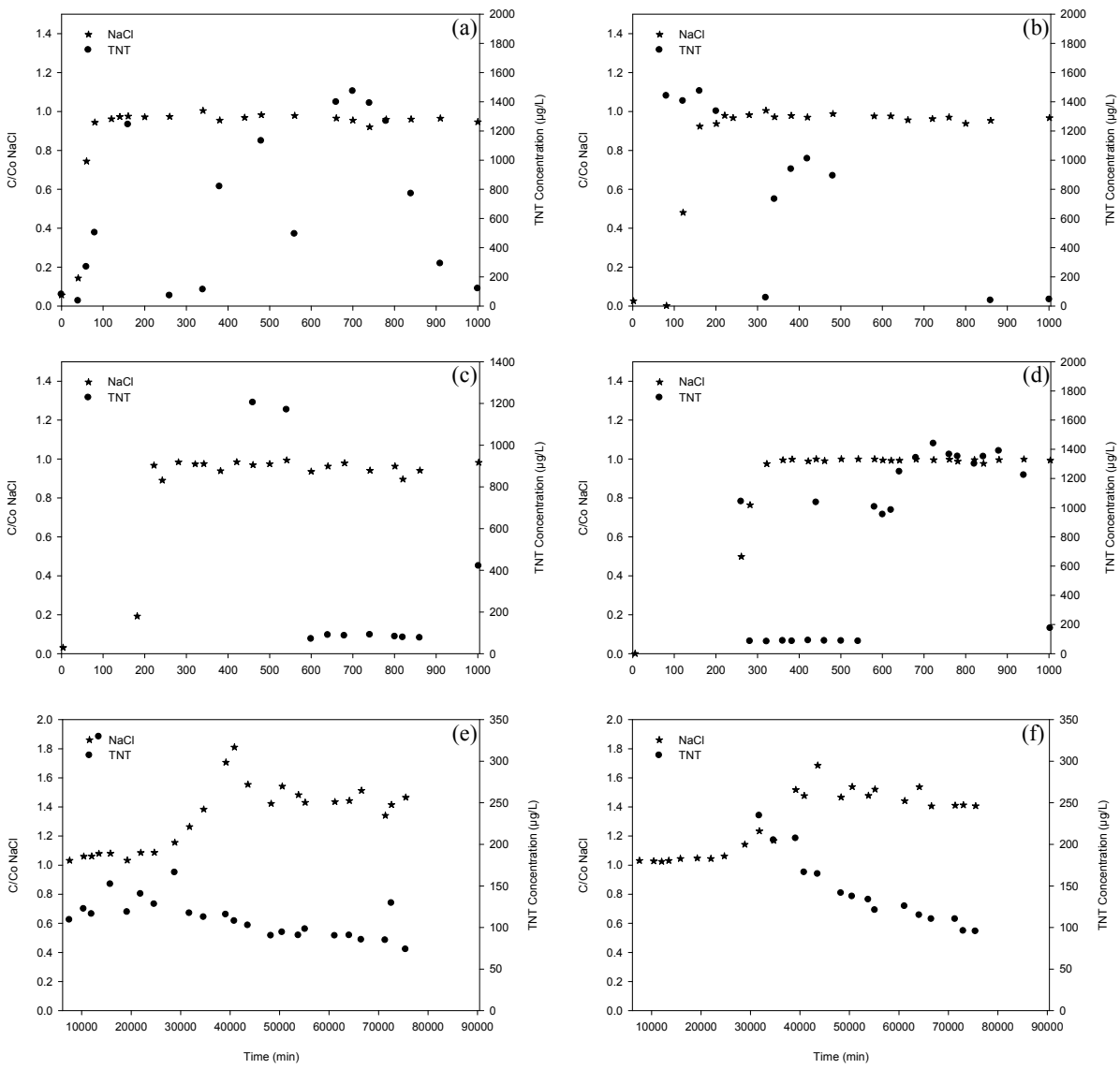


Figure 95. NaCl vs. TNT_w during: Infiltration Process for Port 4 (a), Port 3 (b), Port 2 (c) and Port 1 (d); during Evaporation Process for Port 2 (e) and Port 1 (f), under 75% of Saturation at 25°C (Exp 4)

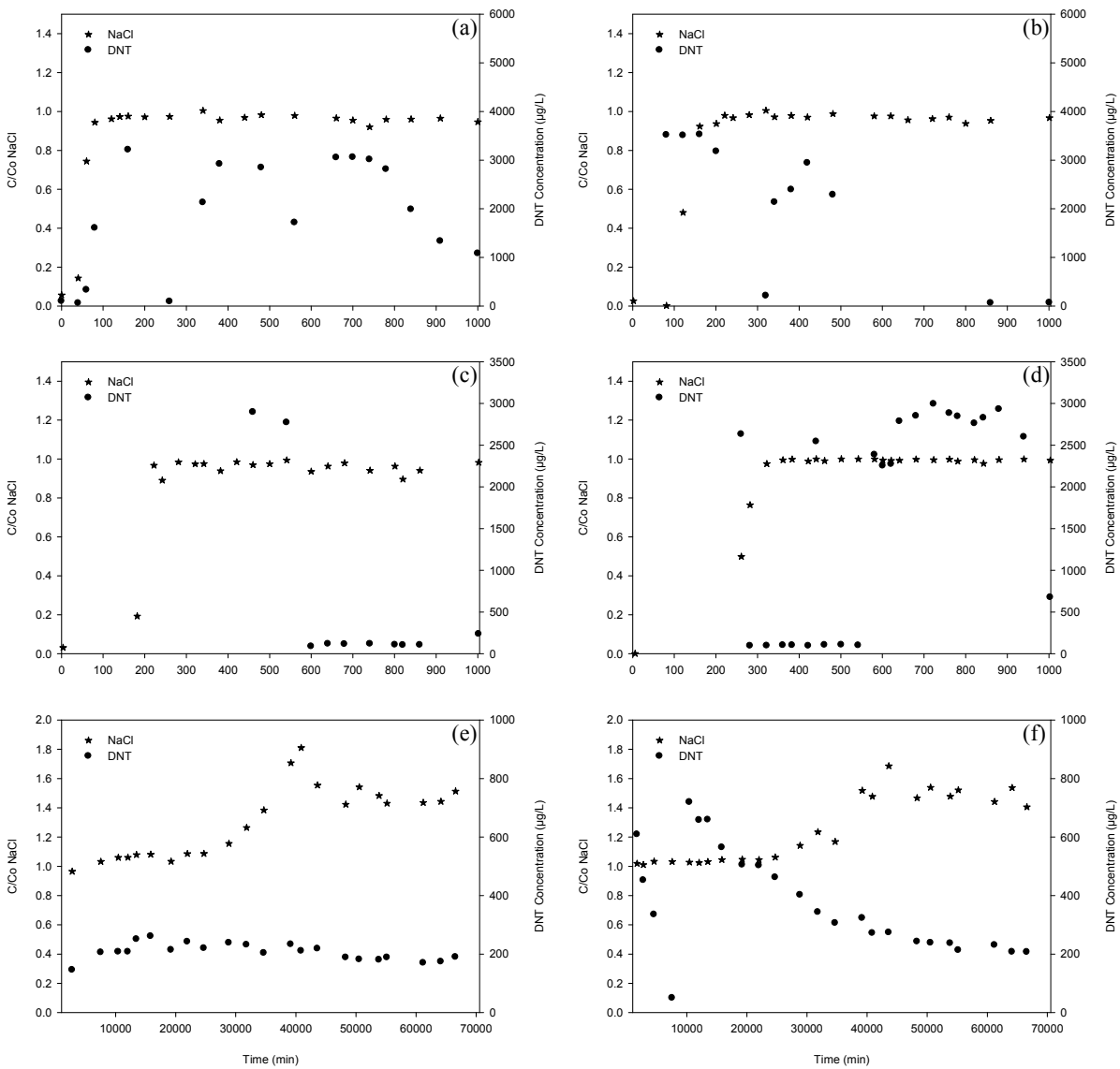


Figure 96. NaCl vs. DNT_w during: Infiltration Process for Port 4 (a), Port 3 (b), Port 2 (c) and Port 1 (d); during Evaporation Process for Port 2 (e) and Port 1 (f), under 75% of Saturation at 25°C (Exp 4)

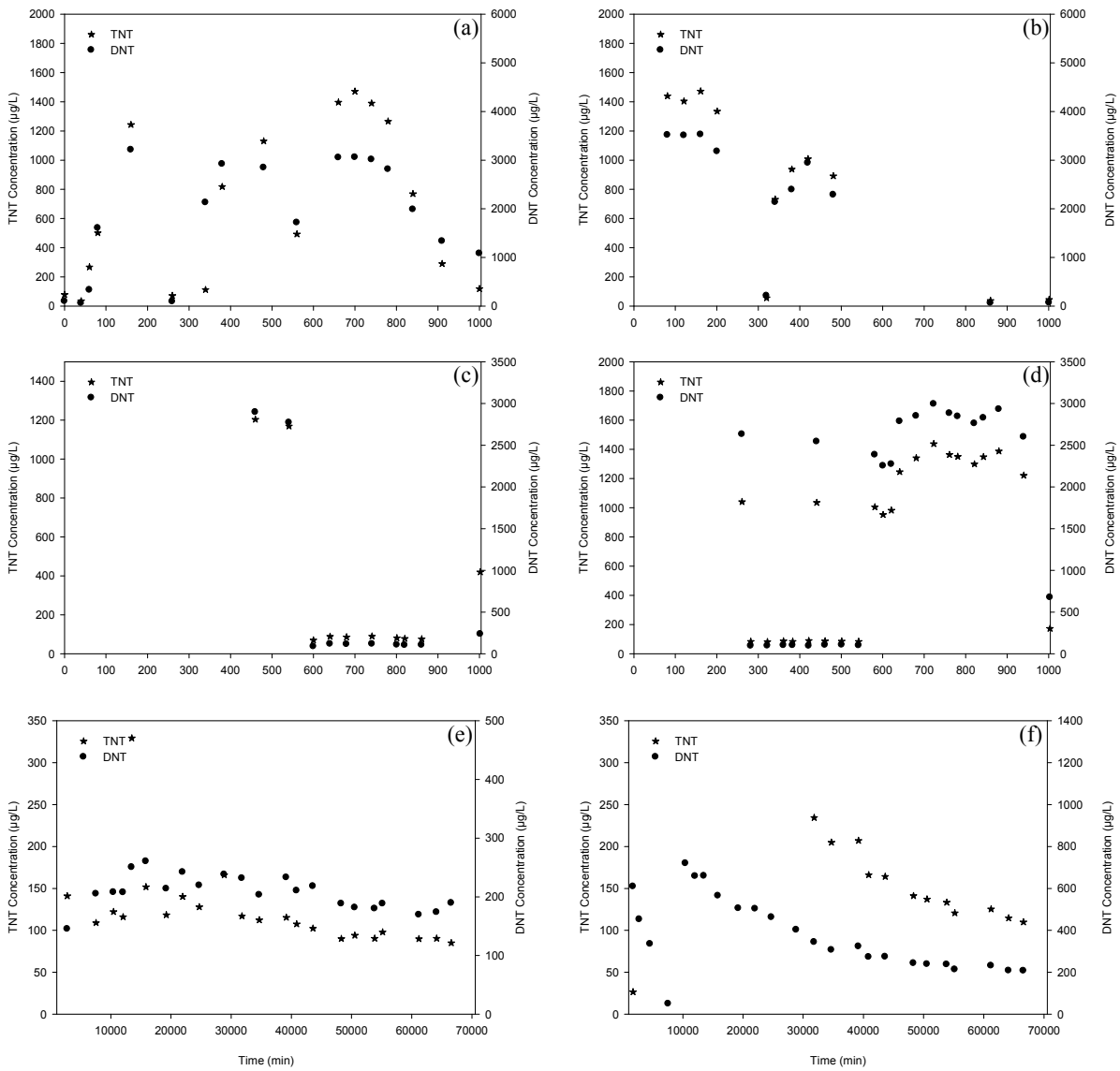


Figure 97. TNT_w vs. DNT_w during: Infiltration Process for Port 4 (a), Port 3 (b), Port 2 (c) and Port 1 (d); during Evaporation Process for Port 2 (e) and Port 1 (f), under 75% of Saturation at 25°C (Exp 4)

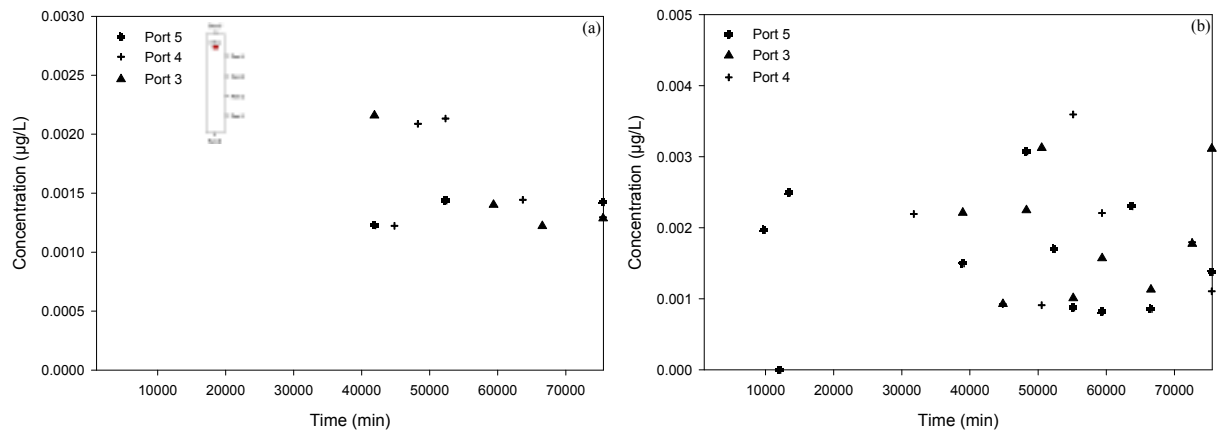


Figure 98. TNT_G (a) and DNT_G (b) BTCs during Evaporation Process under 75% of Saturation at 25°C (Exp 4)

E. Experiment 5 (45% of Saturation, 25°C, Infiltration-Evaporation, TNT-DNT source buried)

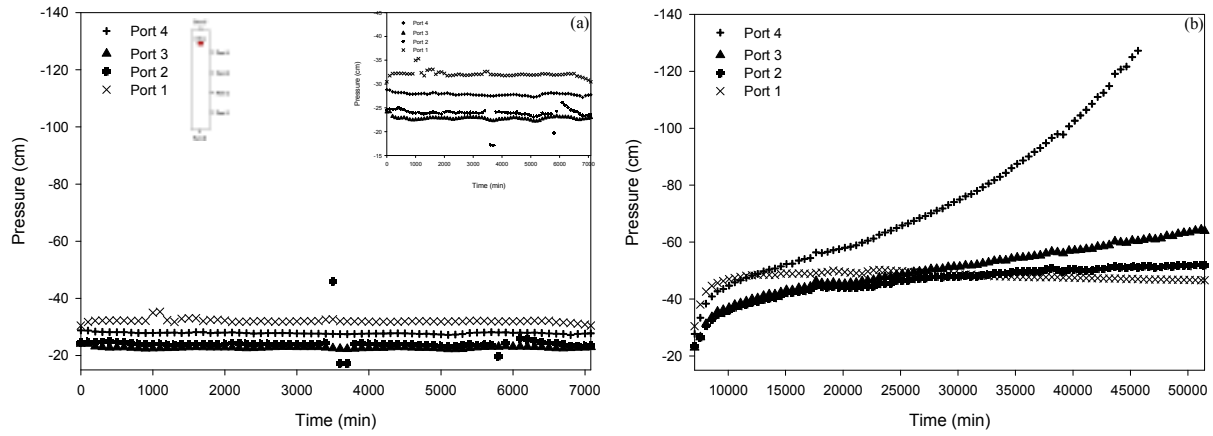


Figure 99. Pressures during Infiltration (a) and Evaporation (b) Processes under 45% of Saturation at 25°C (Exp 5)

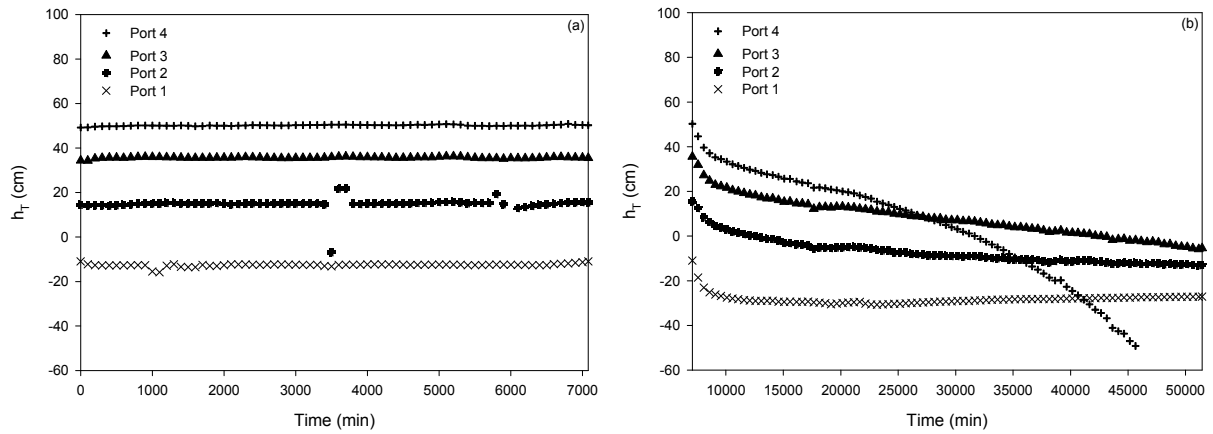


Figure 100. Total Hydraulic Heads during Infiltration (a) and Evaporation (b) Processes under 45% of Saturation at 25°C (Exp 5)

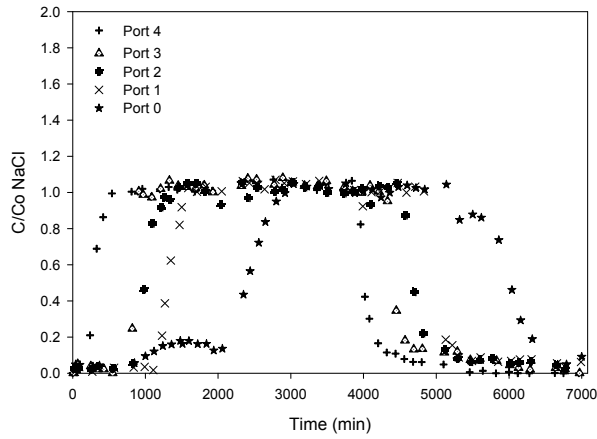


Figure 101. NaCl BTC during Infiltration Process under 45% of Saturation at 25°C (Exp 5)

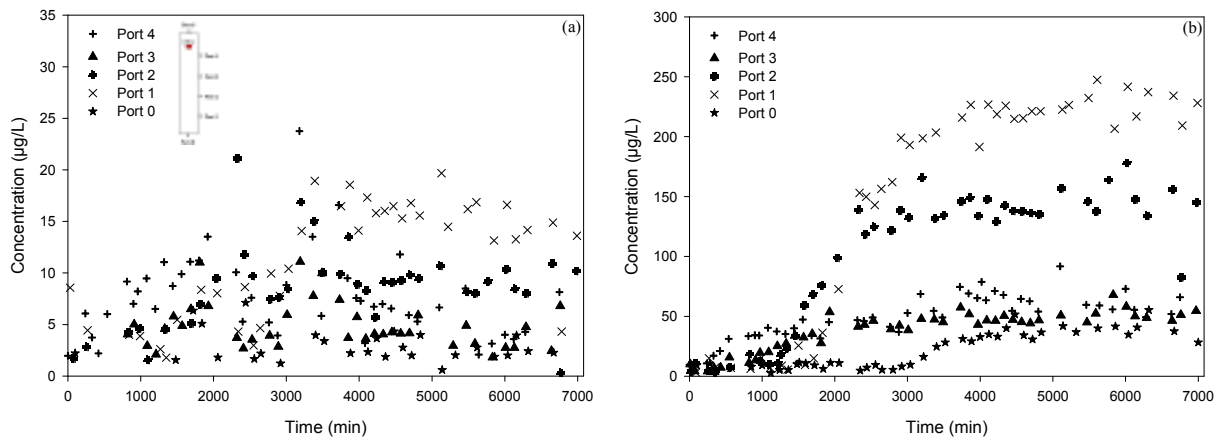


Figure 102. TNT_w (a) and DNT_w (b) BTCs during Infiltration Process under 45% of Saturation at 25°C (Exp 5)

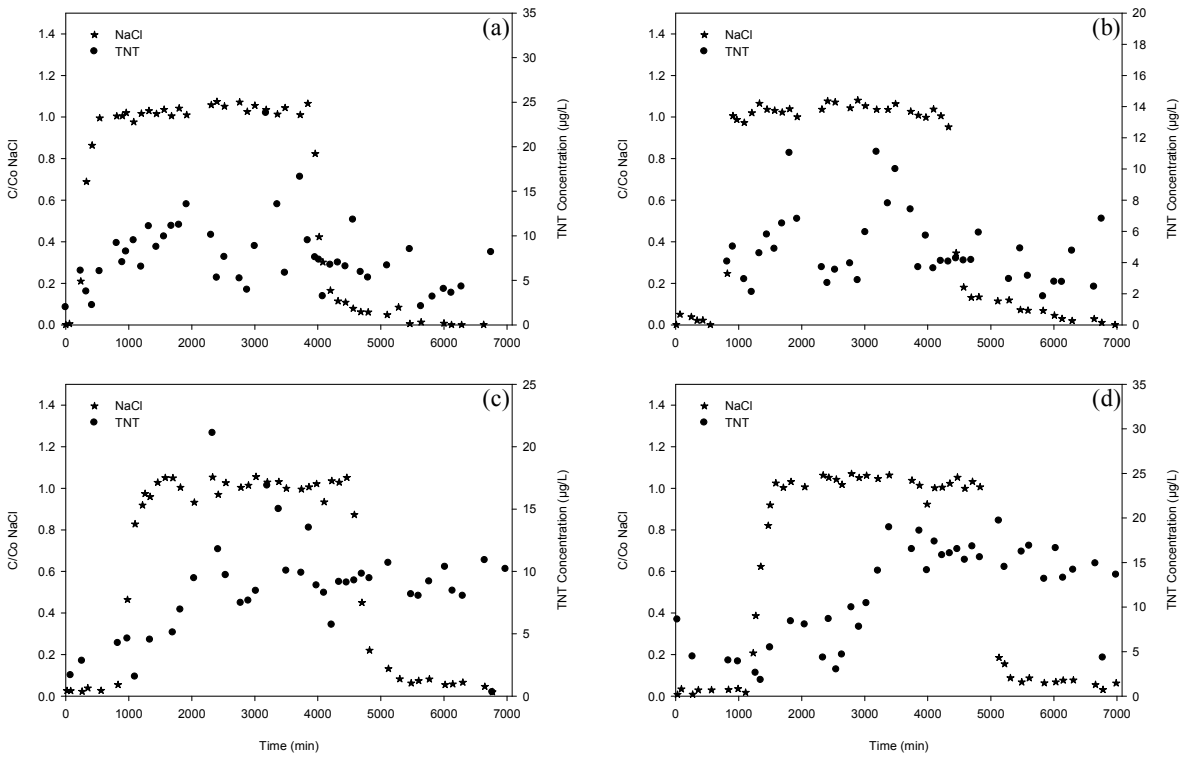


Figure 103. NaCl vs. TNT_w during Infiltration Process for Port 4 (a), Port 3 (b), Port 2 (c) and Port 1 (d), under 45% of Saturation at 25°C (Exp 5)

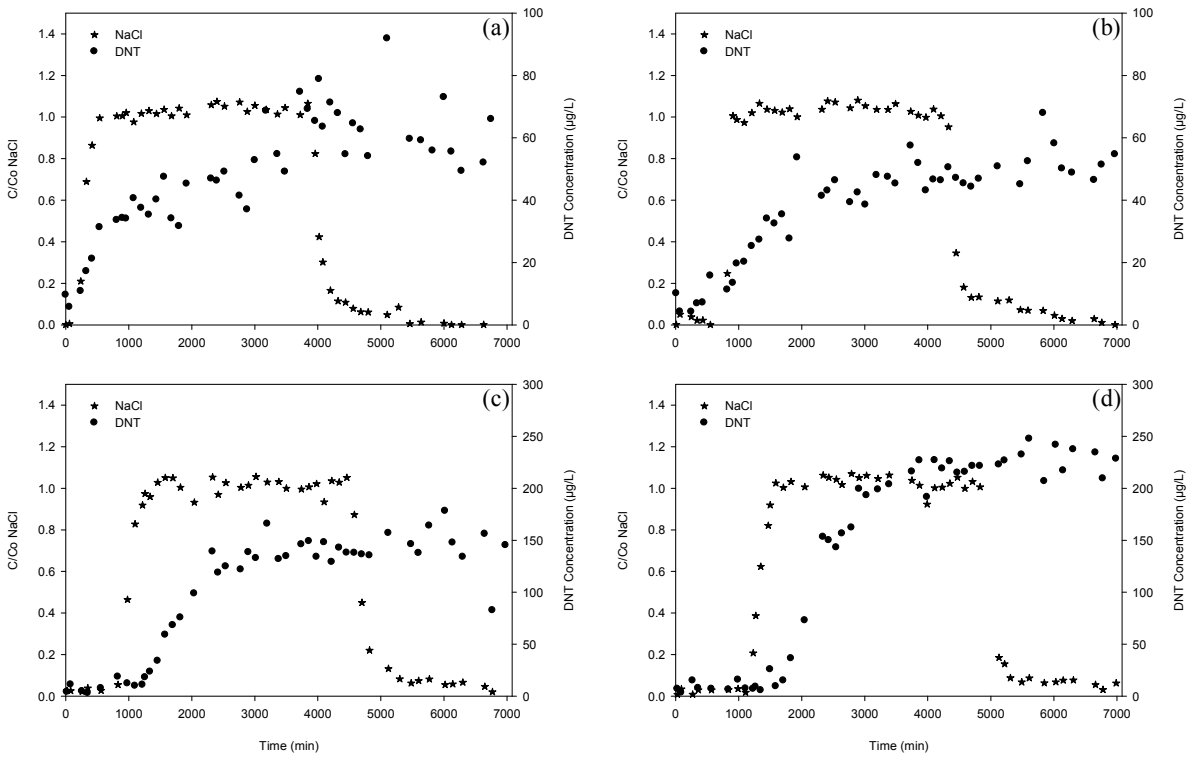


Figure 104. NaCl vs. DNT_w during Infiltration Process for Port 4 (a), Port 3 (b), Port 2 (c) and Port 1 (d), under 45% of Saturation at 25°C (Exp 5)

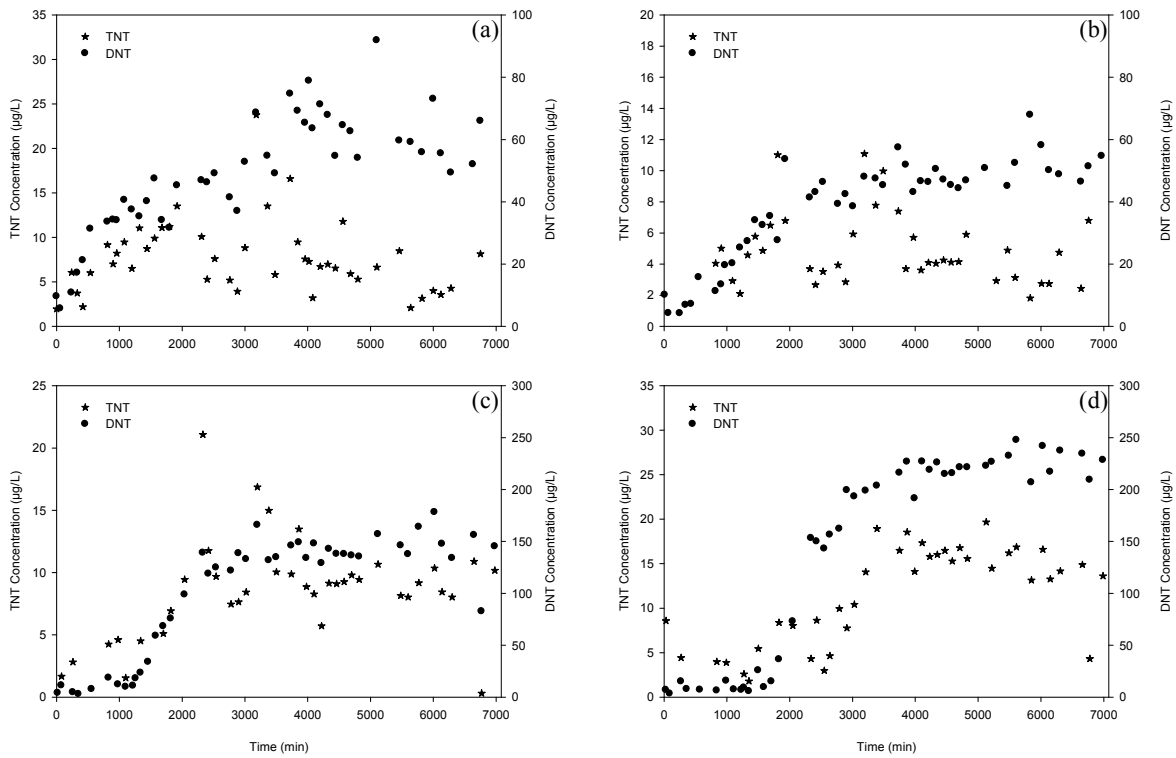


Figure 105. TNT_W vs. DNT_W during Infiltration Process for Port 4 (a), Port 3 (b), Port 2 (c) and Port 1 (d), under 45% of Saturation at 25°C (Exp 5)

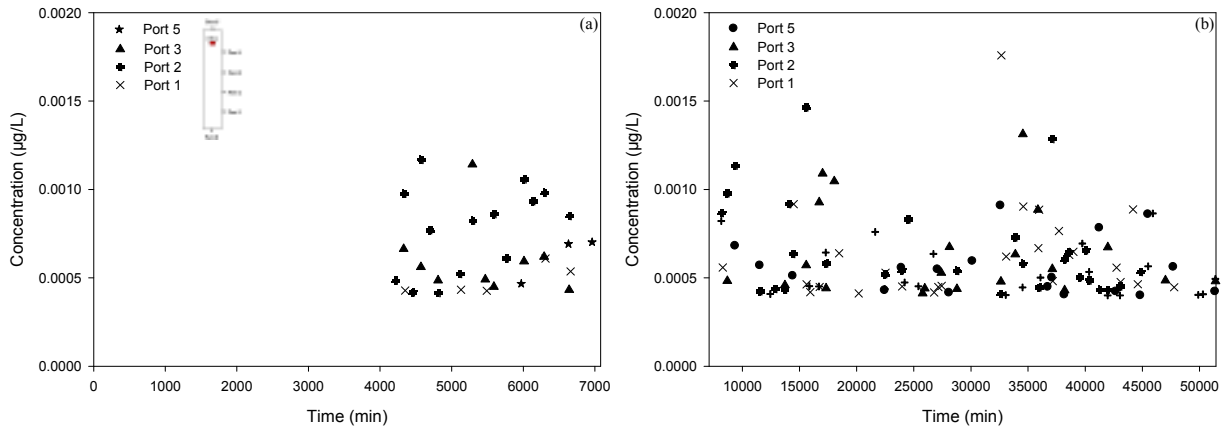


Figure 106. TNT_G BTC during Infiltration (a) and Evaporation (b) Processes under 45% of Saturation at 25°C (Exp 5)

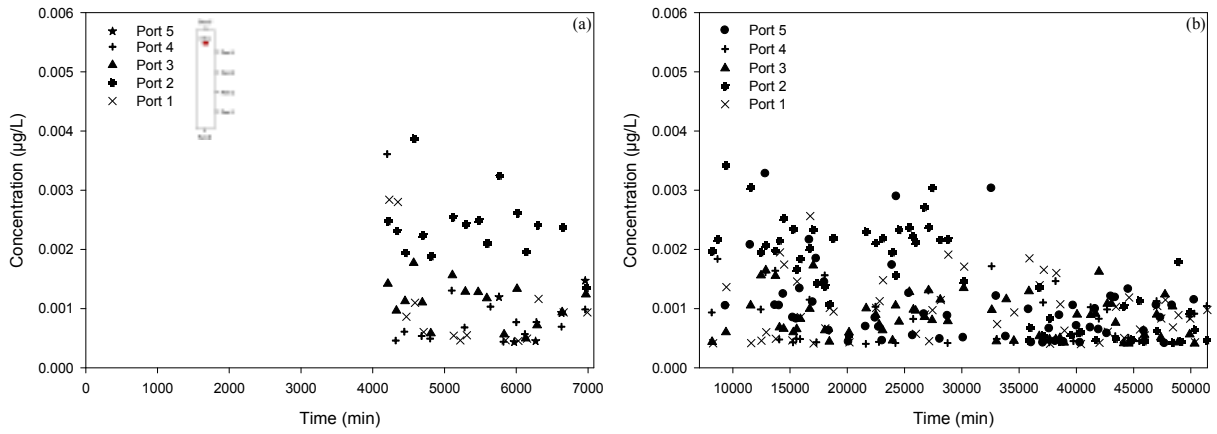


Figure 107. DNT_G BTC during Infiltration (a) and Evaporation (b) Processes under 45% of Saturation at 25°C (Exp 5)

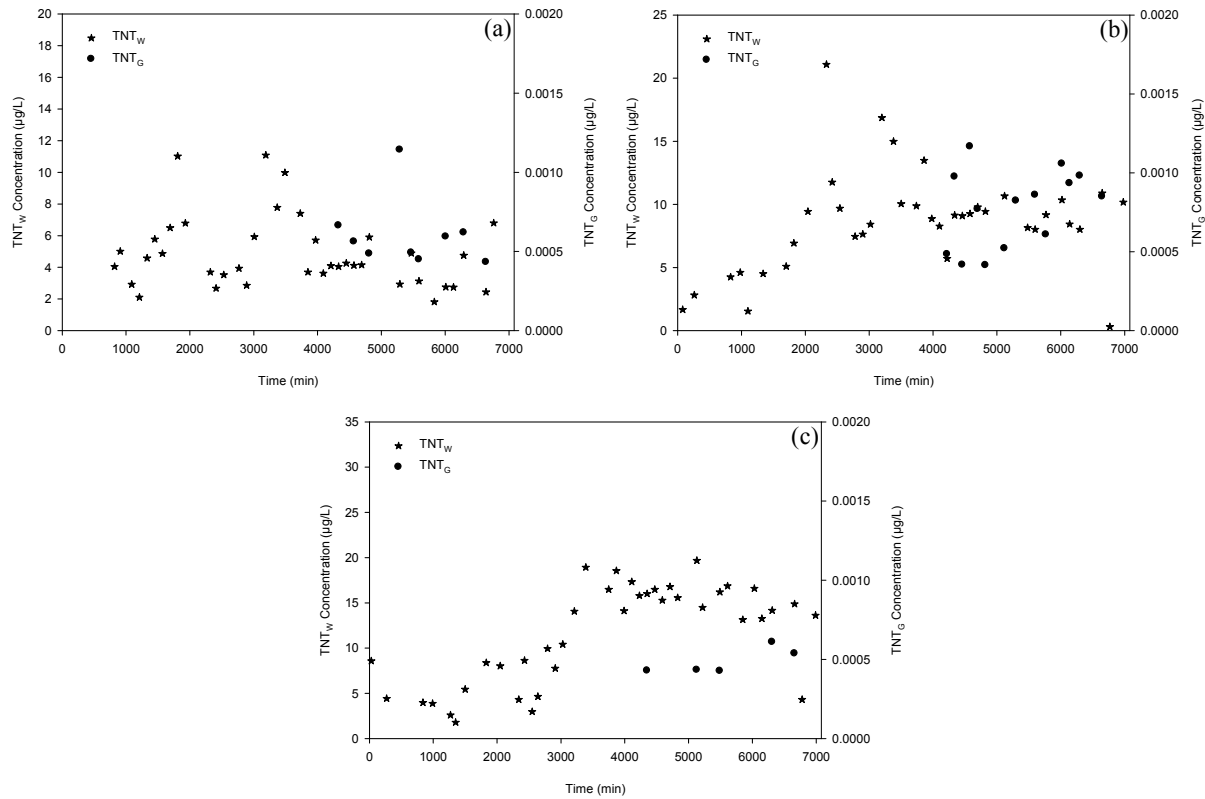


Figure 108. TNT_w vs. TNT_G during Infiltration Process for Port 3 (a), Port 2 (b) and Port 1 (c) under 45% of Saturation at 25°C (Exp 5)

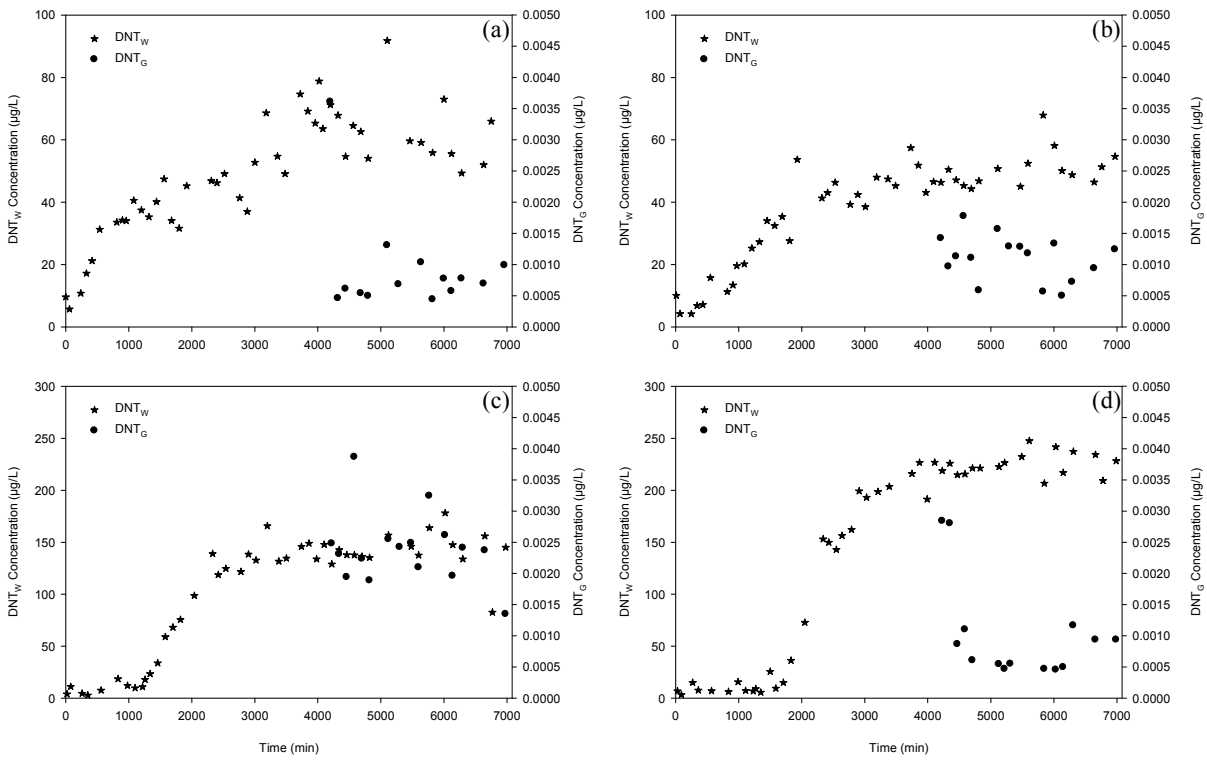


Figure 109. DNT_W vs. DNT_G during Infiltration Process for Port 4 (a), Port 3 (b), Port 2 (c) and Port 1 (d) under 45% of Saturation at 25°C (Exp 5)

F. Experiment 6 (Saturated, 35°C, Infiltration-Evaporation, TNT-DNT source buried)

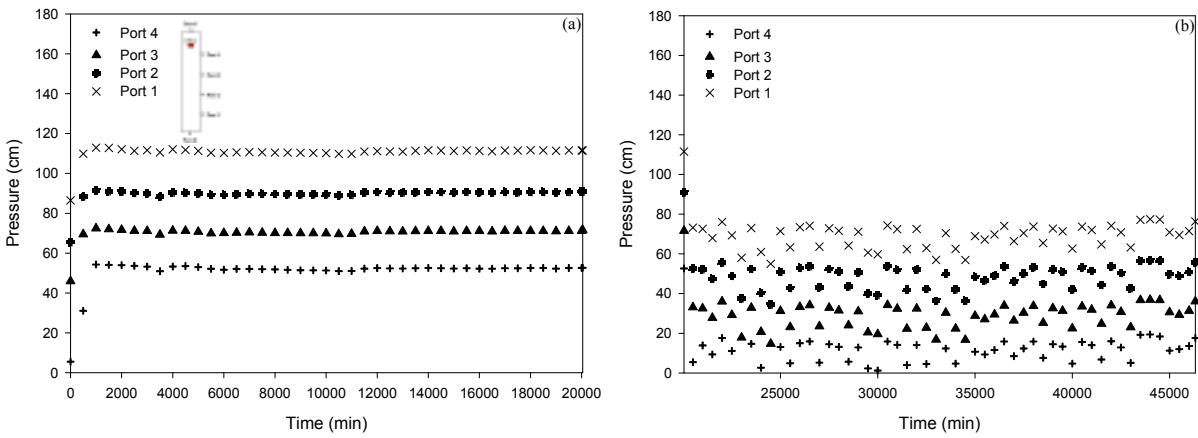


Figure 110. Pressures during Infiltration (a) and Evaporation (b) Processes in the First Stage of the Experiment under Saturated Conditions at 35°C (Exp 6)

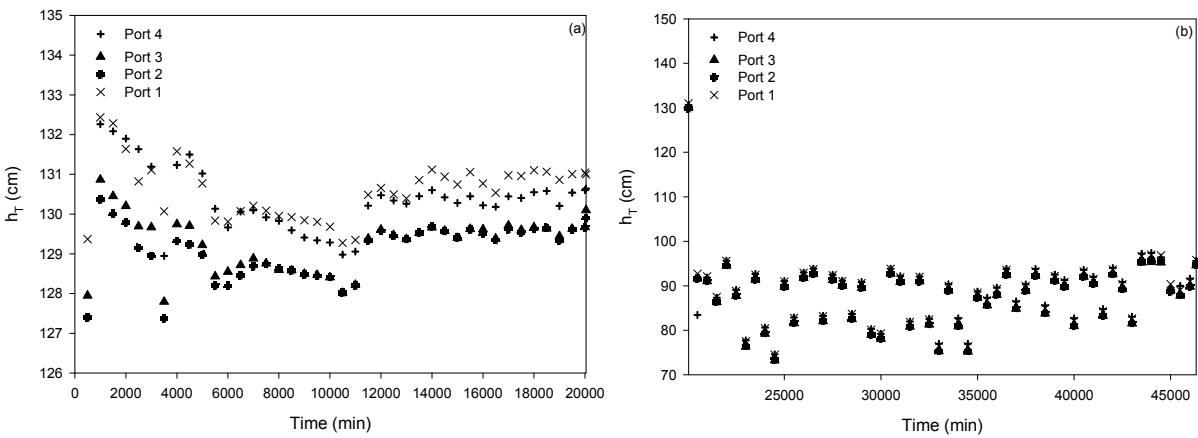


Figure 111. Total Hydraulic Heads during Infiltration (a) and Evaporation (b) Processes in the First Stage of the Experiment under Saturated Conditions at 35°C (Exp 6)

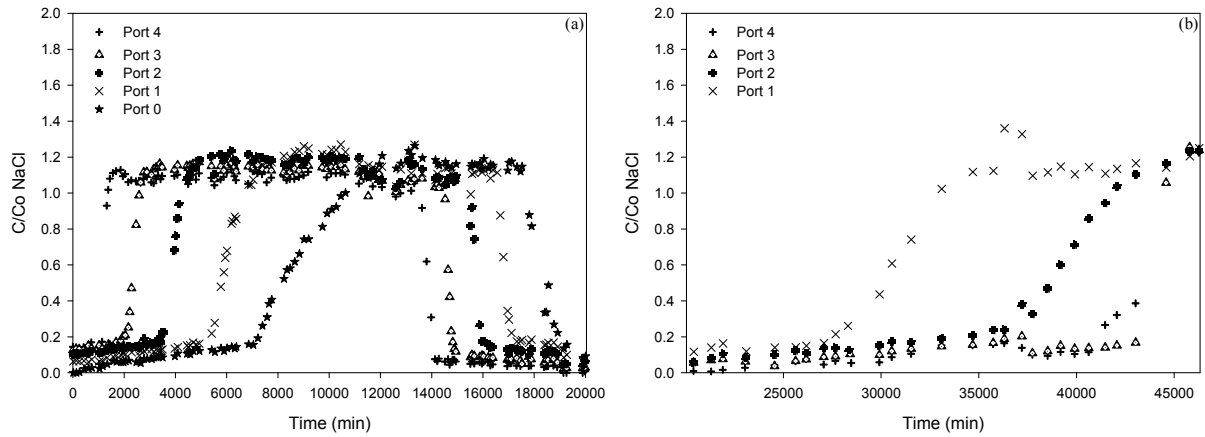


Figure 112. NaCl BTC during Infiltration (a) and Evaporation (b) Processes in the First Stage of the Experiment under Saturated Conditions at 35°C (Exp 6)

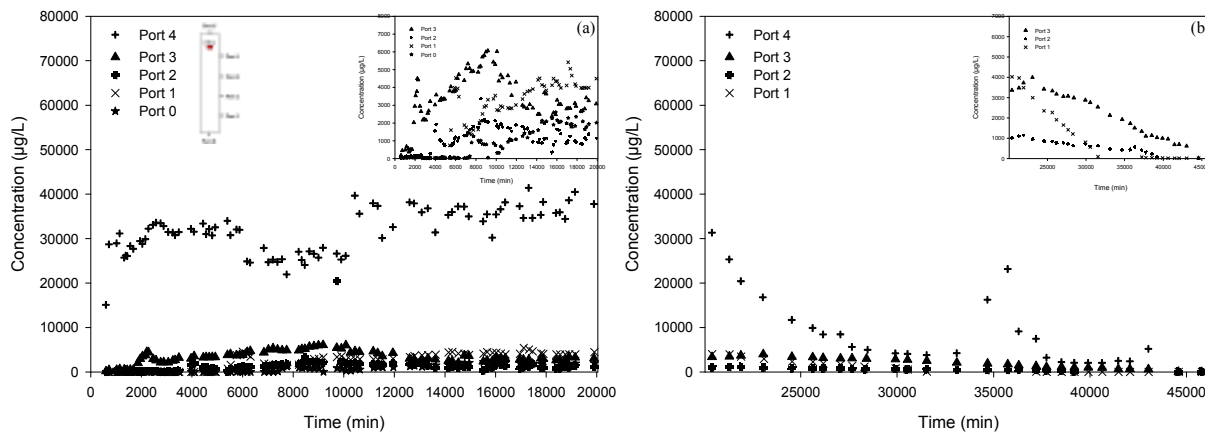


Figure 113. TNT_w BTC during Infiltration (a) and Evaporation (b) Processes in the First Stage of the Experiment under Saturated Conditions at 35°C (Exp 6)

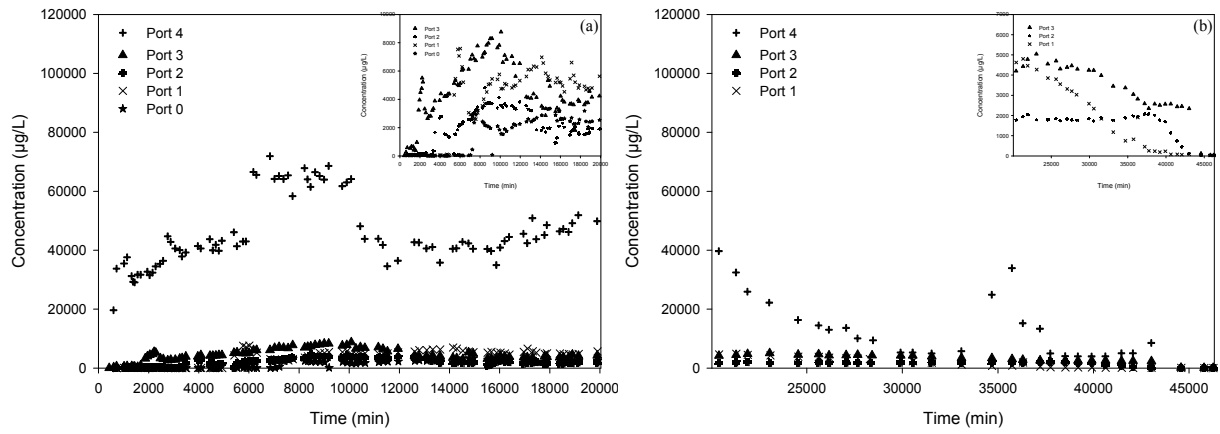


Figure 114. DNT_w BTC during Infiltration (a) and Evaporation (b) Processes in the First Stage of the Experiment under Saturated Conditions at 35°C (Exp 6)

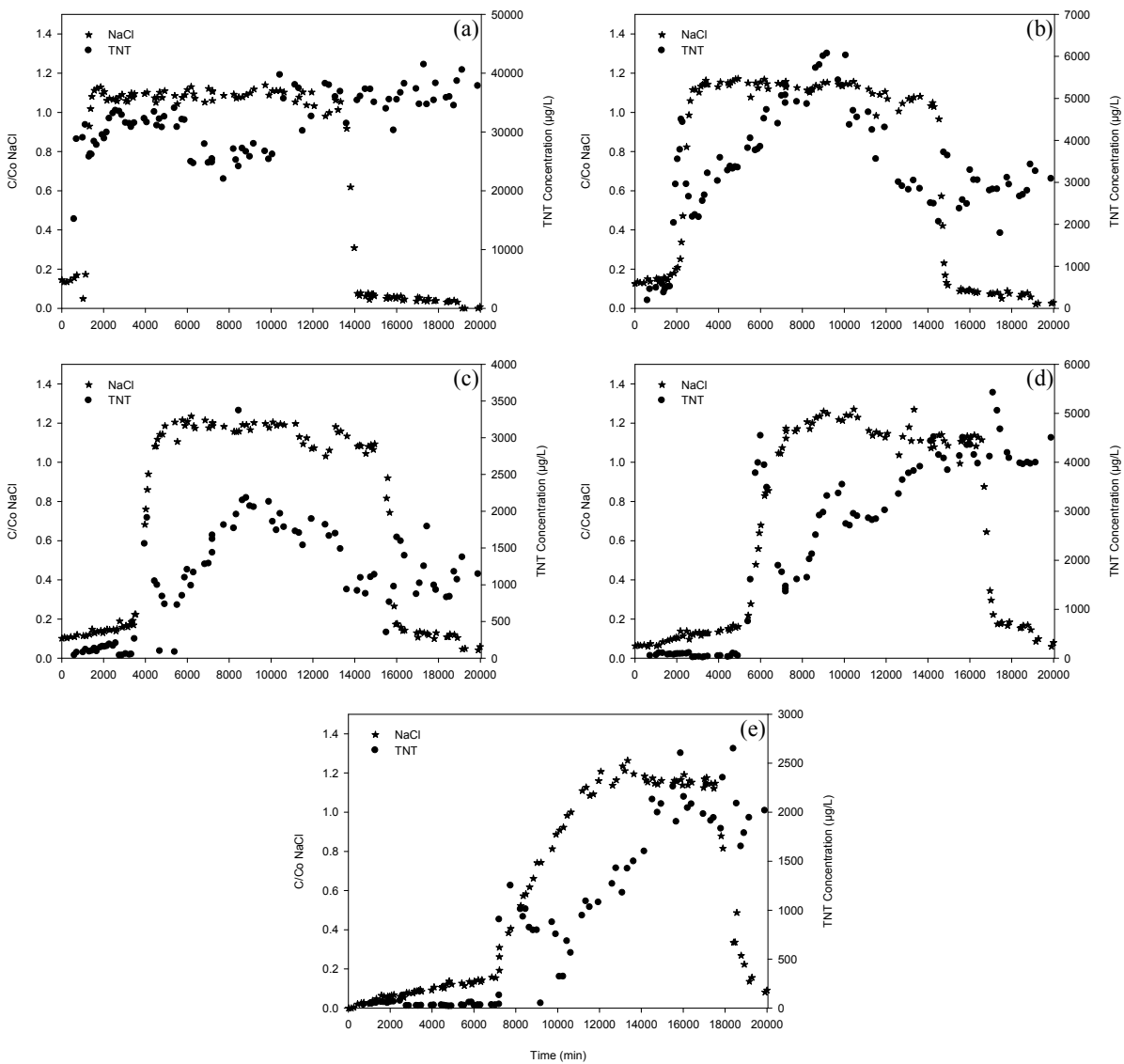


Figure 115. NaCl vs. TNT_w during: Infiltration Process for Port 4 (a), Port 3 (b), Port 2 (c), Port 1 (d) and Port 0 (e), in the First Stage of the Experiment under Saturated Conditions at 35°C (Exp 6)

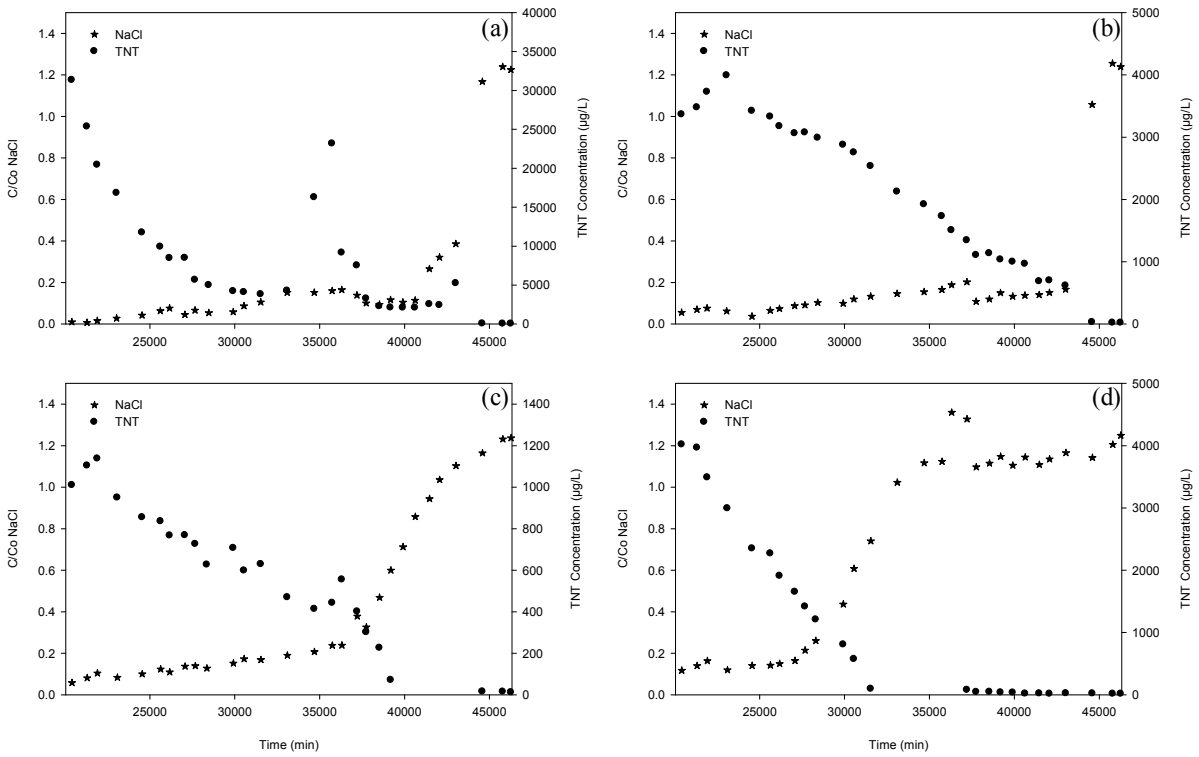


Figure 116. NaCl vs. TNT_w during Evaporation Process for Port 4 (a), Port 3 (b), Port 2 (c) and Port 1 (d), in the First Stage of the Experiment under Saturated Conditions at 35°C (Exp 6)

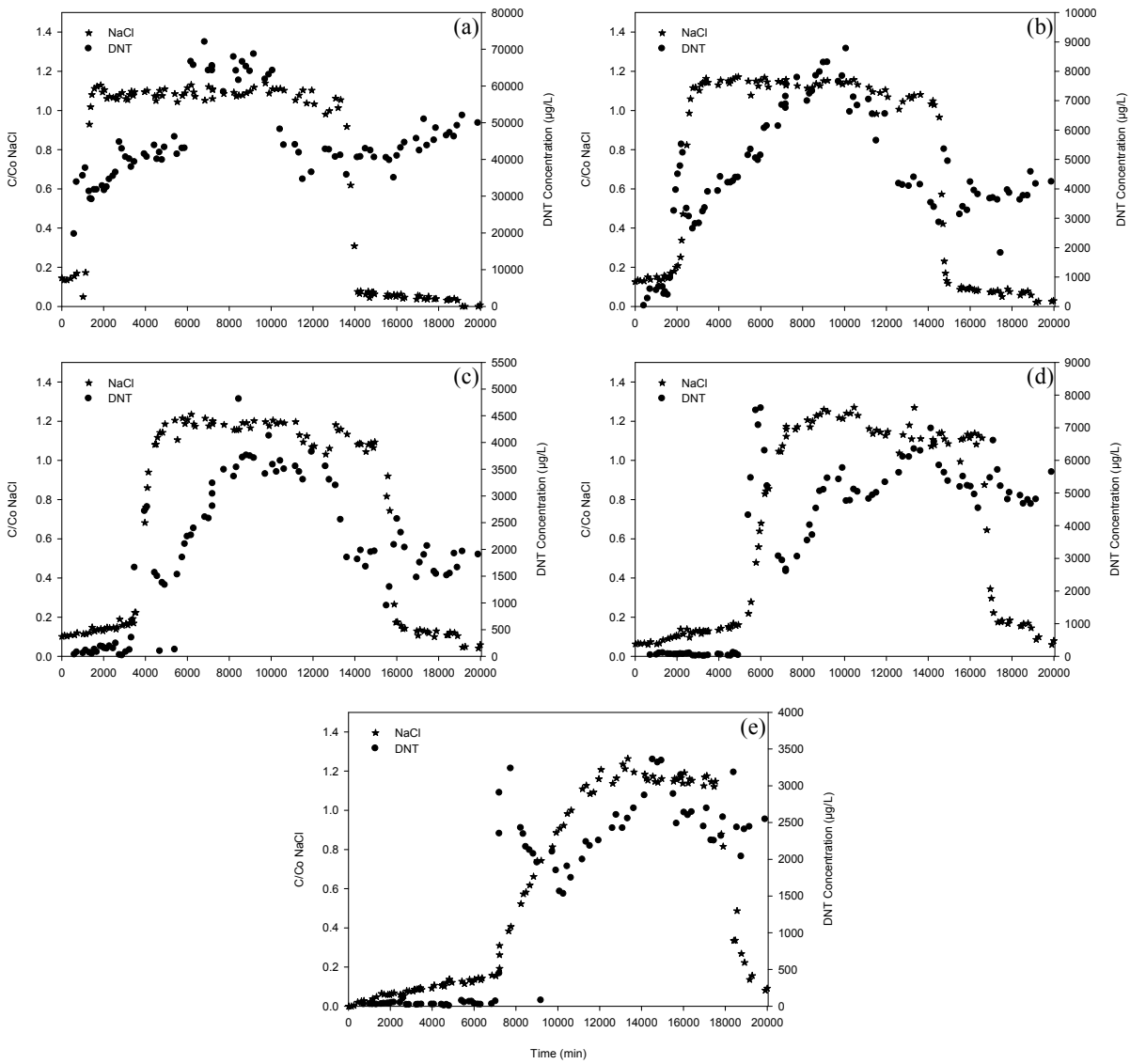


Figure 117. NaCl vs. DNT_w during Infiltration Process for Port 4 (a), Port 3 (b), Port 2 (c), Port 1 (d) and Port 0 (e), in the First Stage of the Experiment under Saturated Conditions at 35°C (Exp 6)

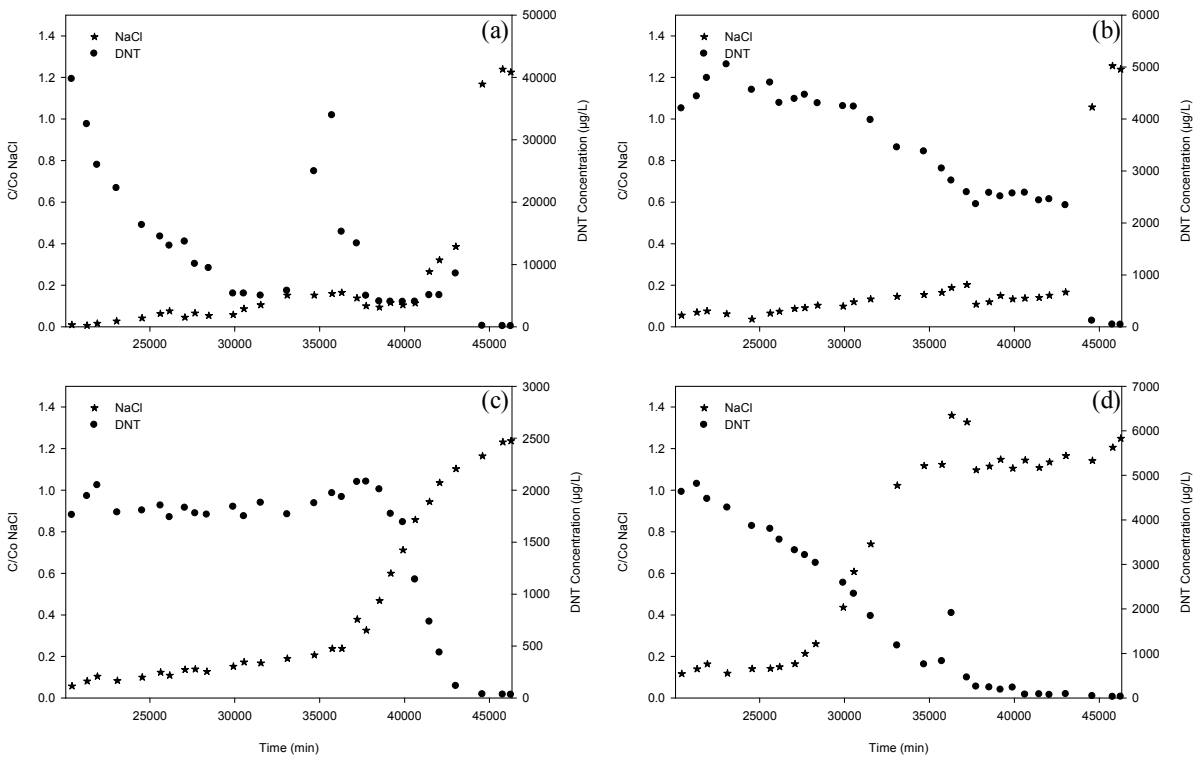


Figure 118. NaCl vs. DNT_w during Evaporation Process for Port 4 (a), Port 3 (b), Port 2 (c) and Port 1 (d), in the First Stage of the Experiment under Saturated Conditions at 35°C (Exp 6)

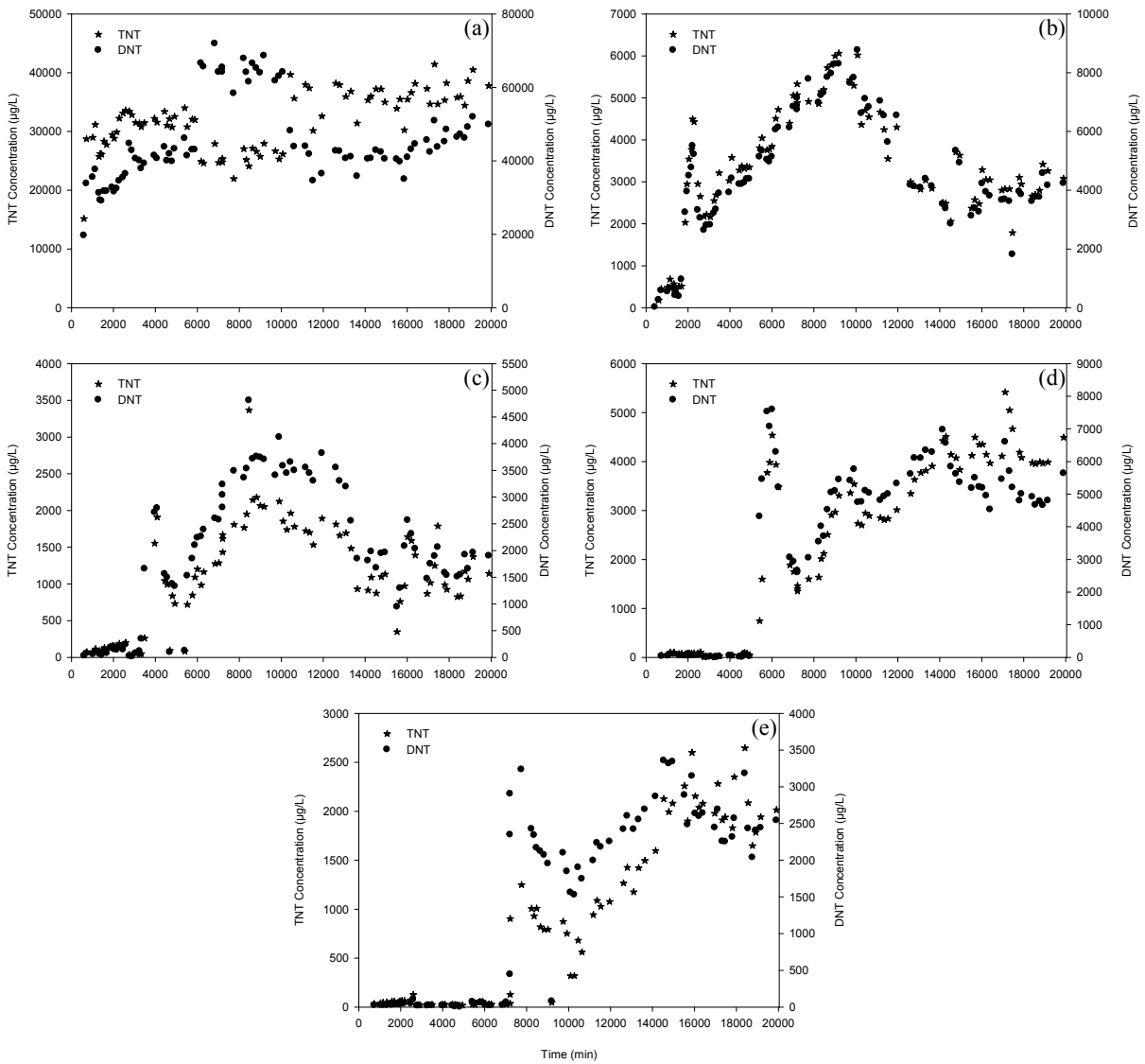


Figure 119. TNT_w vs. DNT_w during Infiltration Process for Port 4 (a), Port 3 (b), Port 2 (c), Port 1 (d) and Port 0 (e), in the First Stage of the Experiment under Saturated Conditions at 35°C (Exp 6)

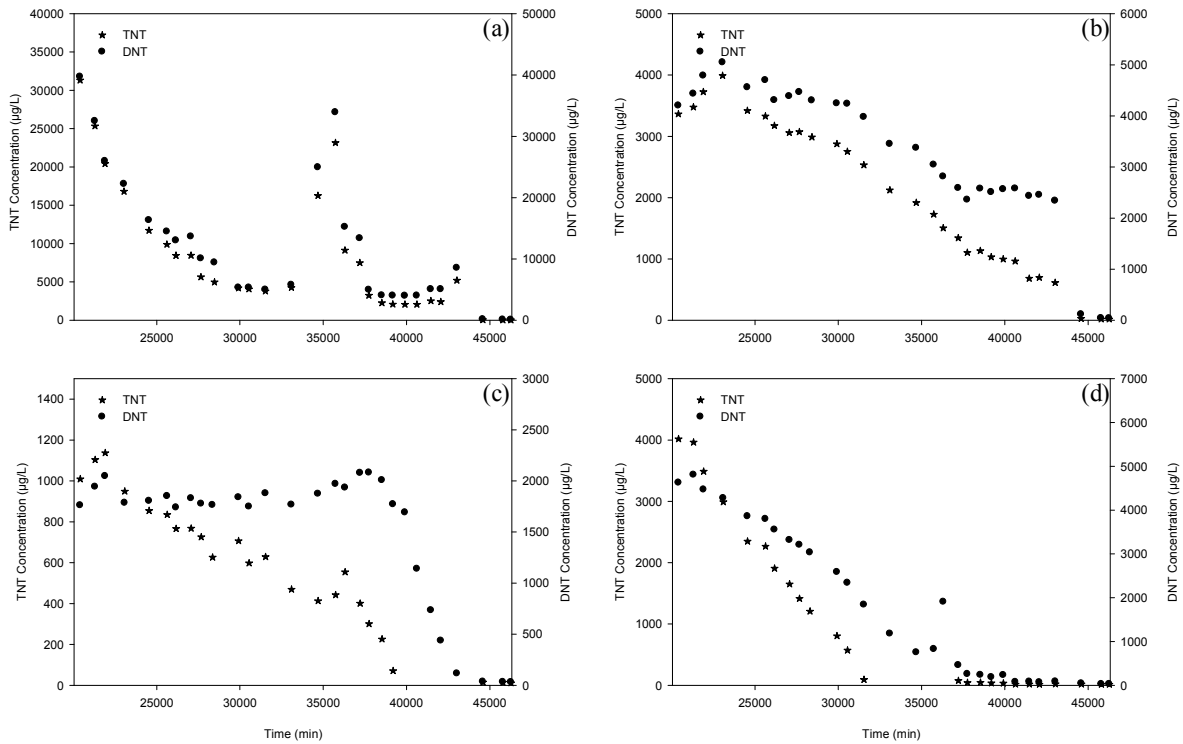


Figure 120. TNT_W vs. DNT_W during Evaporation Process for Port 4 (a), Port 3 (b), Port 2 (c) and Port 1 (d), in the First Stage of the Experiment under Saturated Conditions at 35°C (Exp 6)

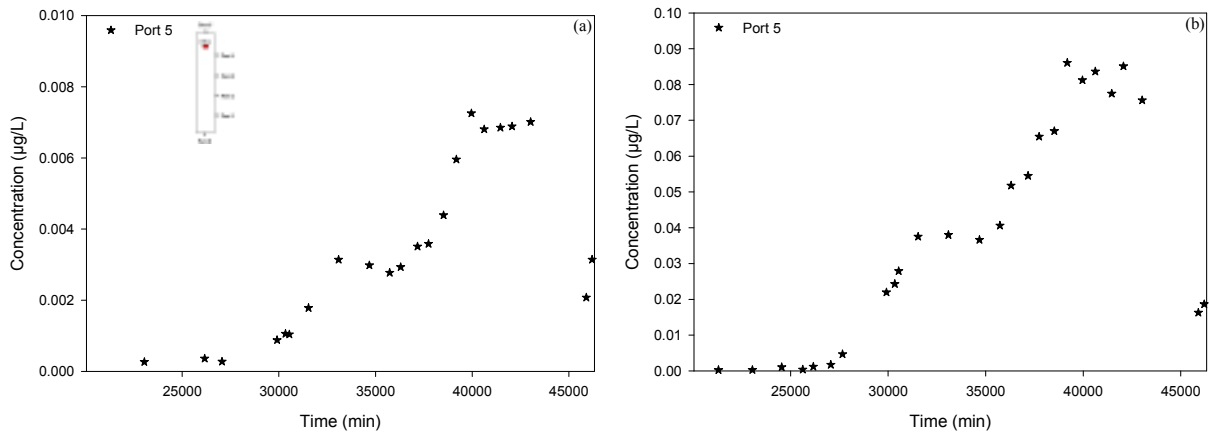


Figure 121. TNT_G (a) and DNT_G (b) BTCs in the Surface of the Soil during Evaporation Process in the First Stage of the Experiment under Saturated Conditions at 35°C (Exp 6)

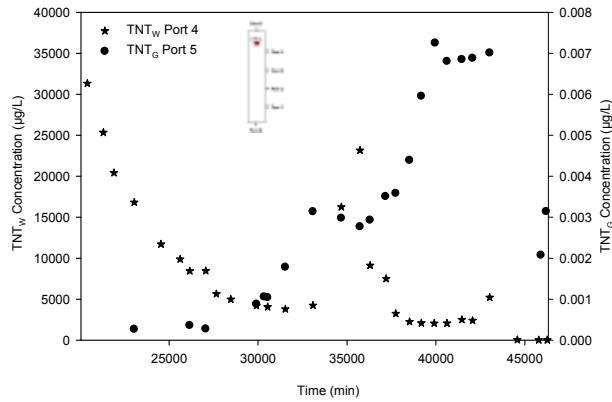


Figure 122. TNT_W vs. TNT_G BTC in the Surface of the Soil during Evaporation Process in the First Stage of the Experiment under Saturated Conditions at 35°C (Exp 6)

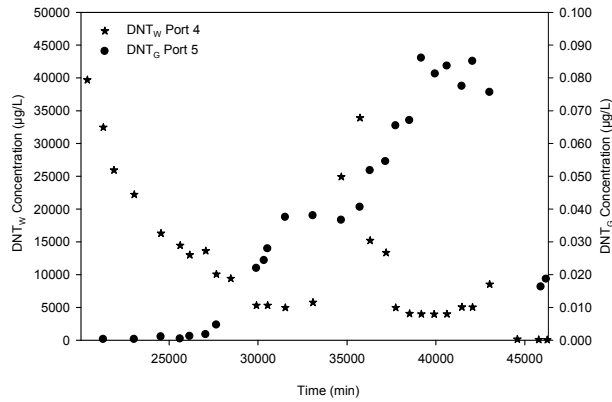


Figure 123. DNT_W vs. DNT_G BTC in the Surface of the Soil during Evaporation Process in the First Stage of the Experiment under Saturated Conditions at 35°C (Exp 6)

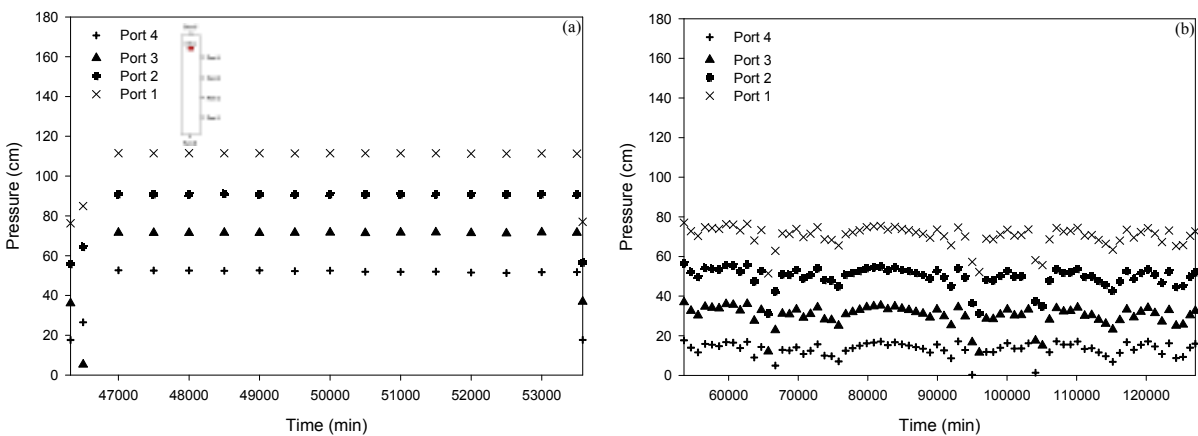


Figure 124. Pressures during Infiltration (a) and Evaporation (b) Processes in the Second Stage of the Experiment under Saturated Conditions at 35°C (Exp 6)

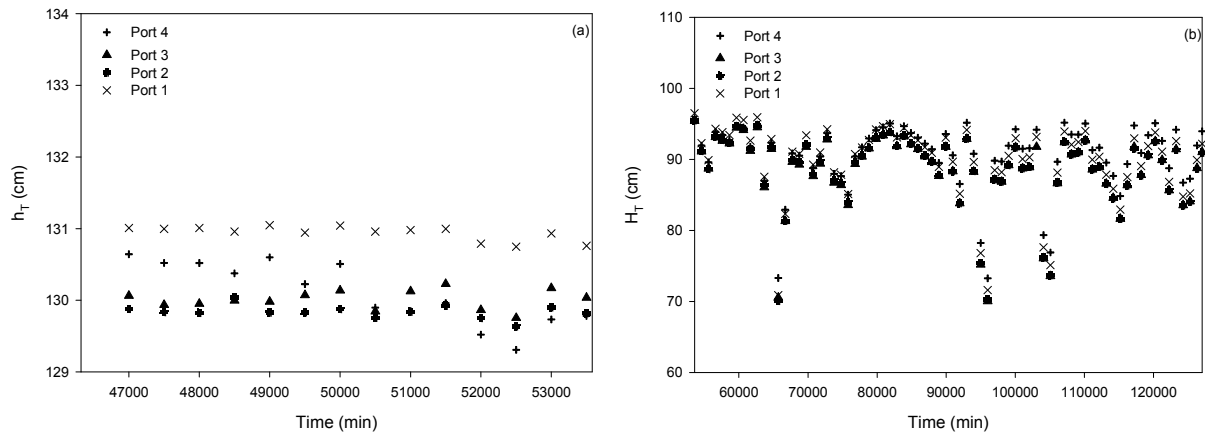


Figure 125. Total Hydraulic Heads during Infiltration (a) and Evaporation (b) Processes in the Second Stage of the Experiment under Saturated Conditions at 35°C (Exp 6)

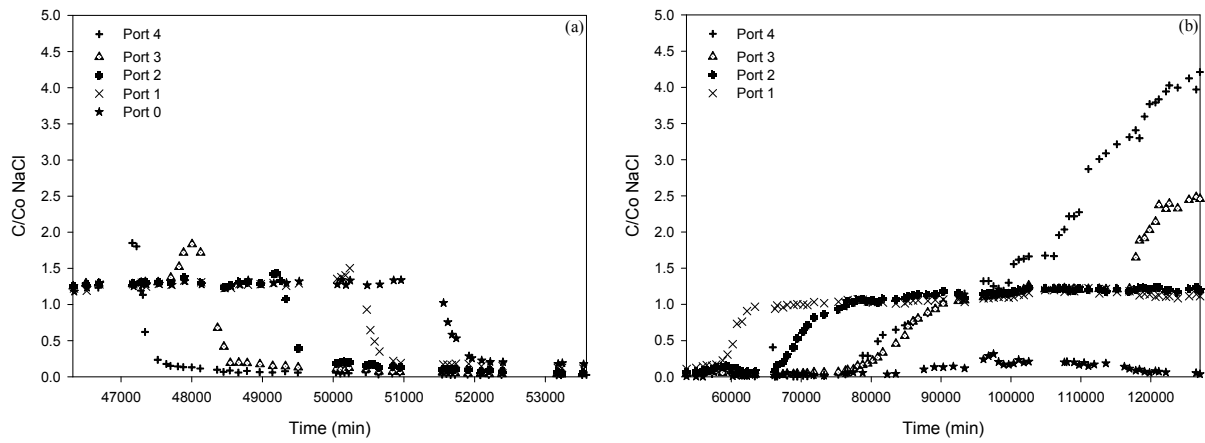


Figure 126. NaCl BTC during Infiltration (a) and Evaporation (b) Processes in the Second Stage of the Experiment under Saturated Conditions at 35°C (Exp 6)

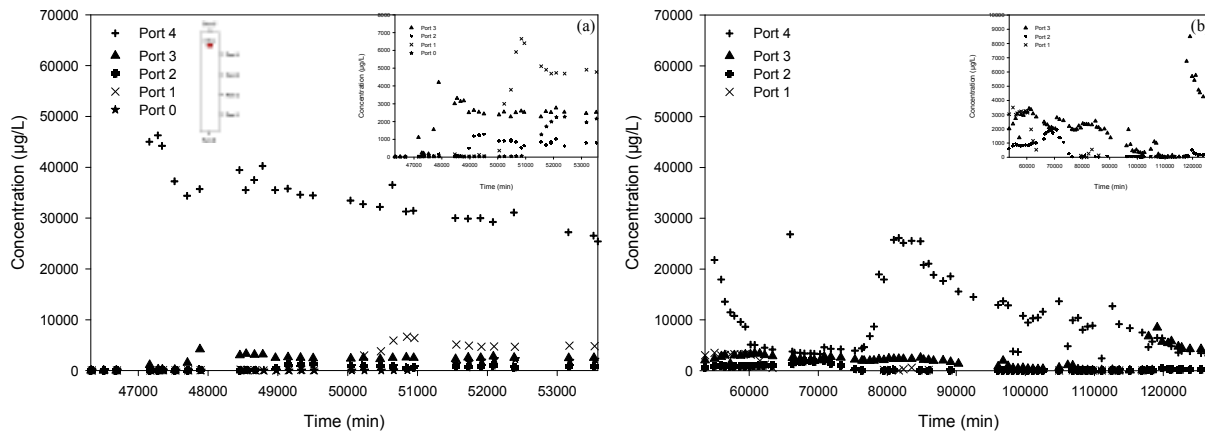


Figure 127. TNT_w BTC during Infiltration (a) and Evaporation (b) Processes in the Second Stage of the Experiment under Saturated Conditions at 35°C (Exp 6)

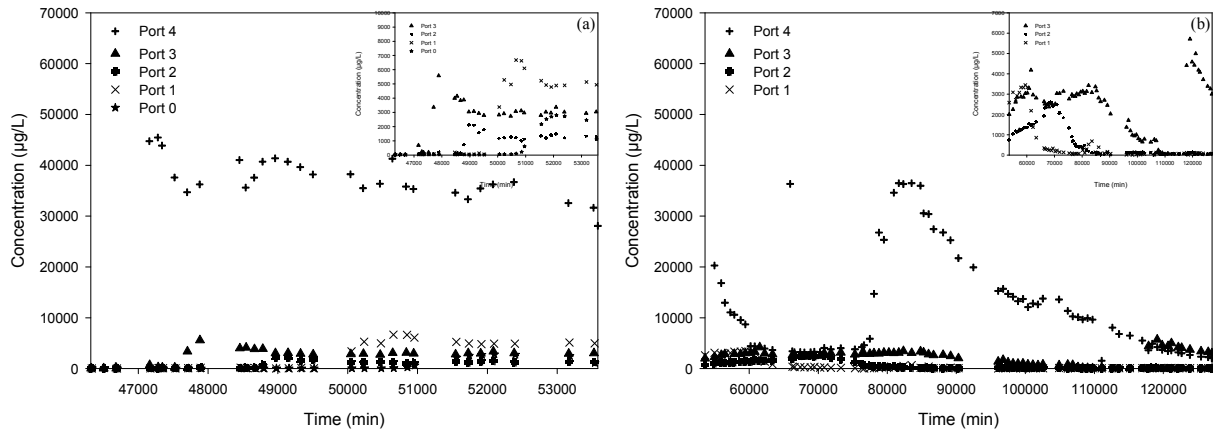


Figure 128. DNT_w BTC during Infiltration (a) and Evaporation (b) Processes in the Second Stage of the Experiment under Saturated Conditions at 35°C (Exp 6)

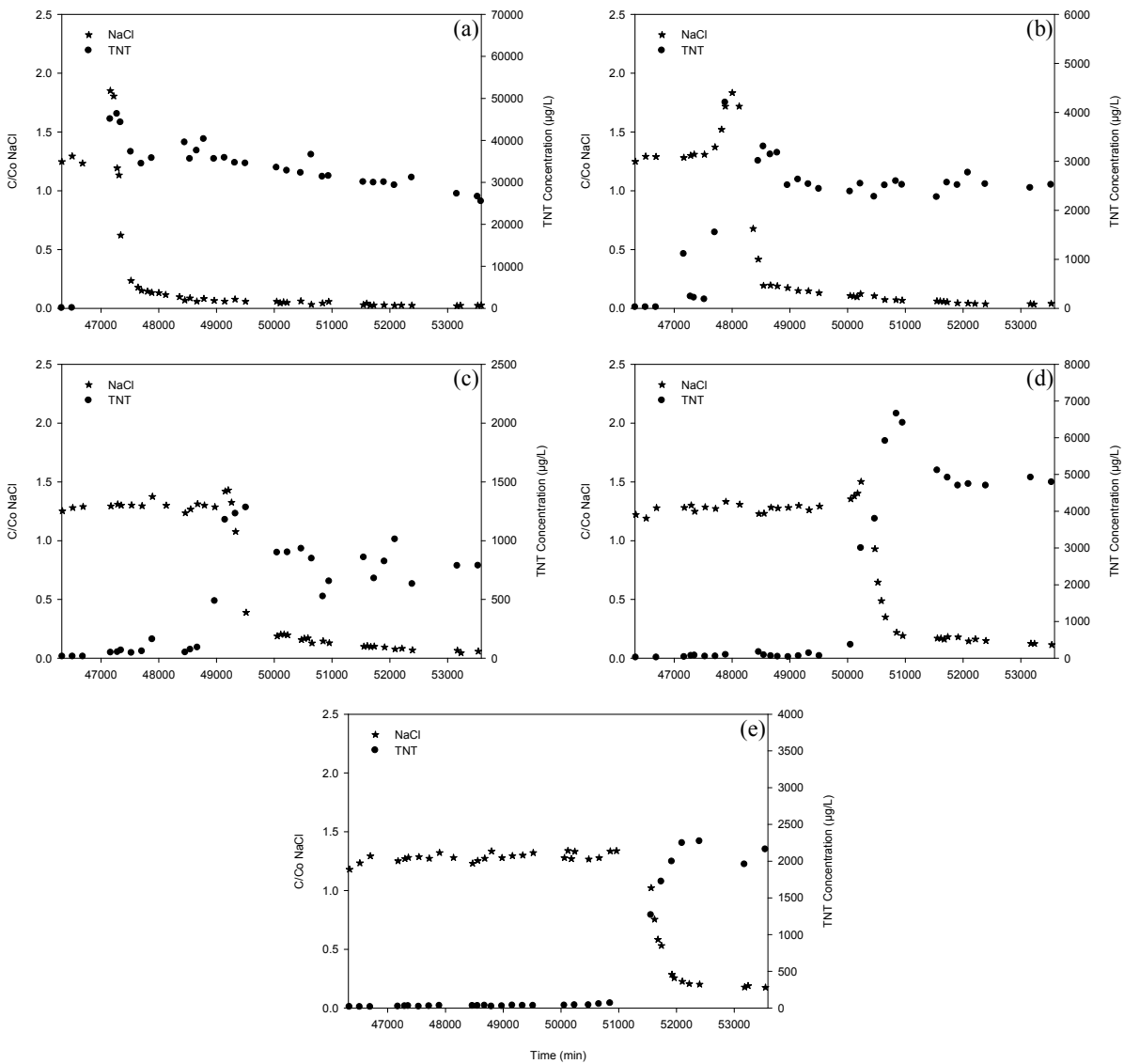


Figure 129. NaCl vs. TNT_w during Infiltration Process for Port 4 (a), Port 3 (b), Port 2 (c), Port 1 (d) and Port 0 (e), in the Second Stage of the Experiment under Saturated Conditions at 35°C (Exp 6)

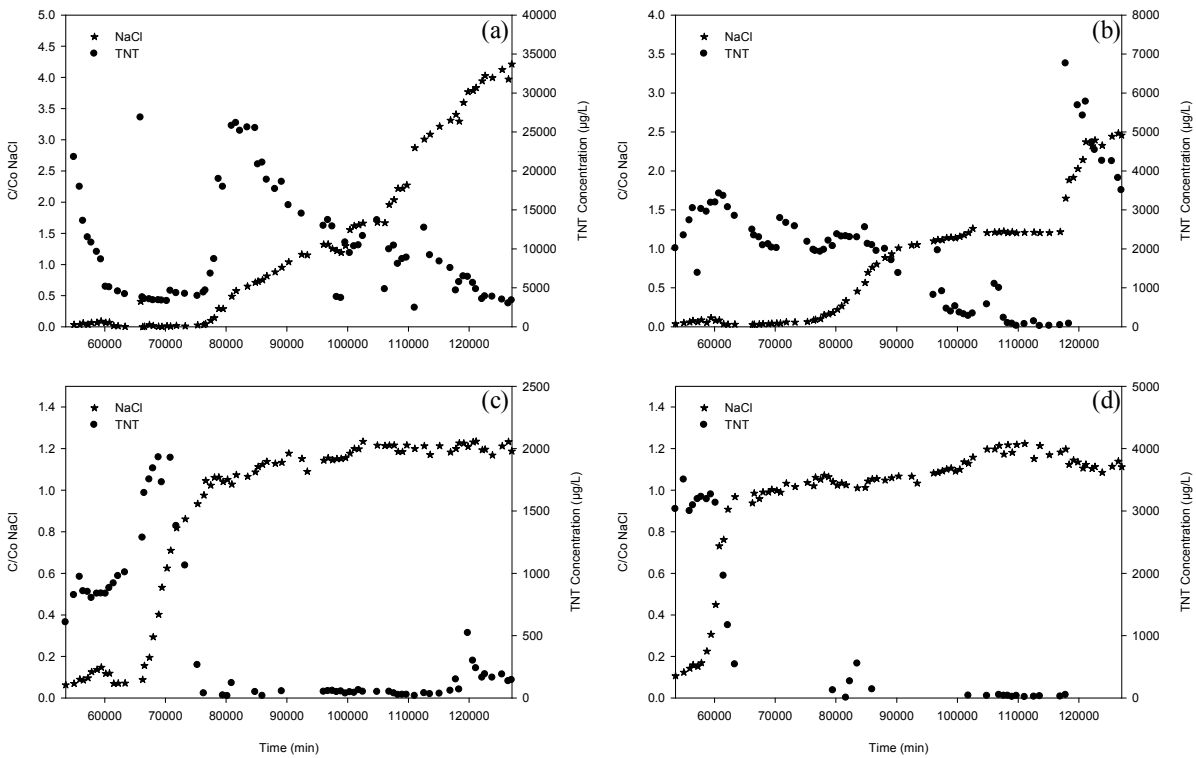


Figure 130. NaCl vs. TNT_w during Evaporation Process for Port 4 (a), Port 3 (b), Port 2 (c) and Port 1 (d), in the Second Stage of the Experiment under Saturated Conditions at 35°C (Exp 6)

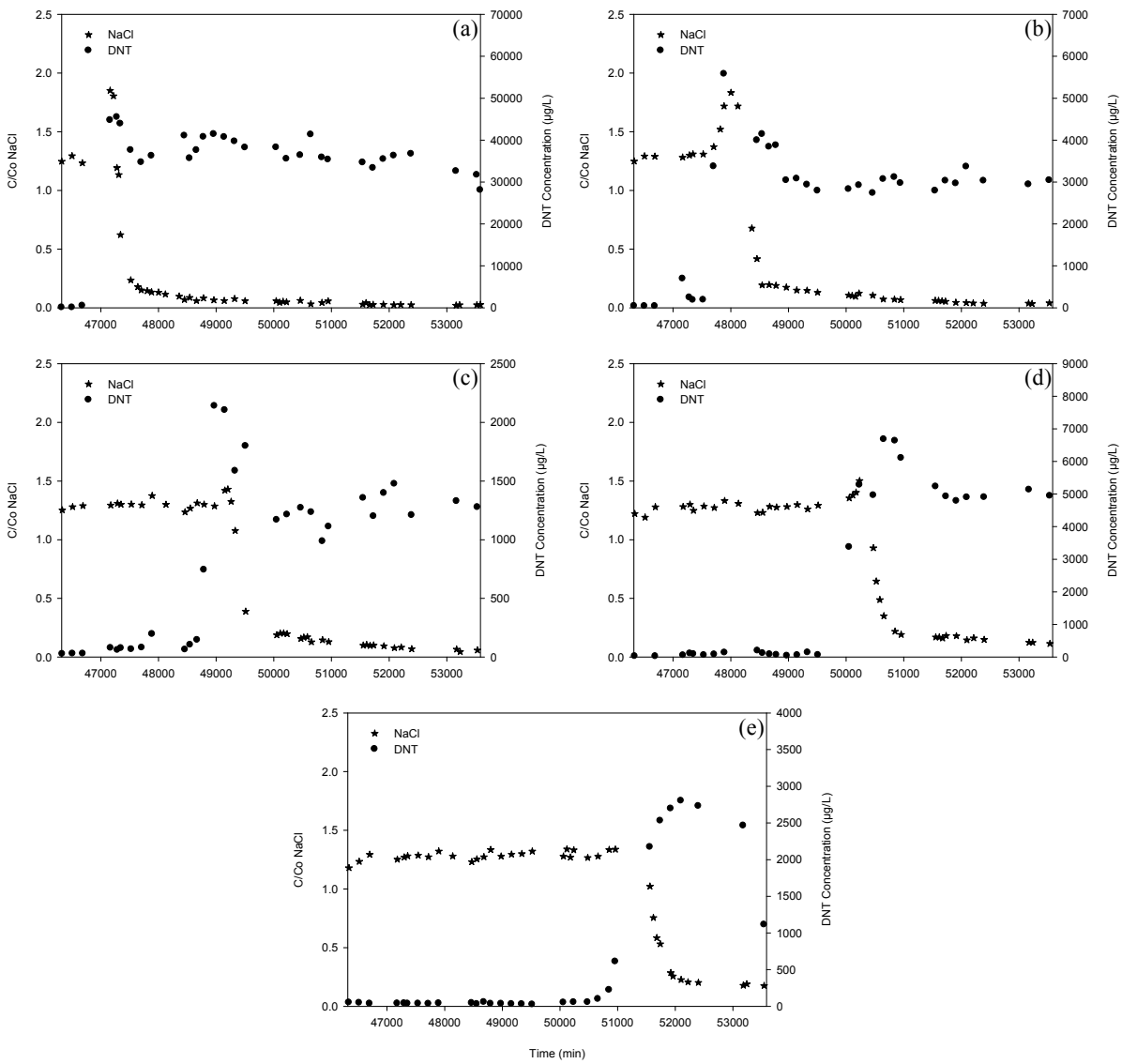


Figure 131. NaCl vs. DNT_w during Infiltration Process for Port 4 (a), Port 3 (b), Port 2 (c) and Port 1 (d), in the Second Stage of the Experiment under Saturated Conditions at 35°C (Exp 6)

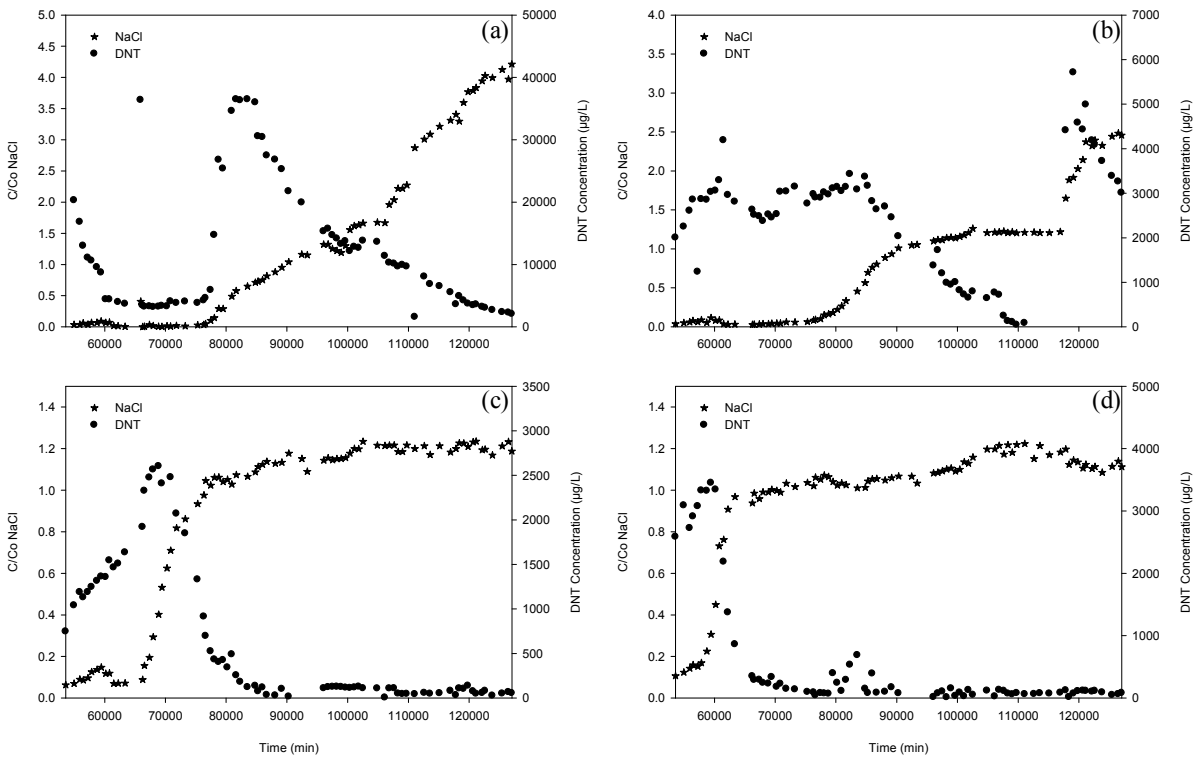


Figure 132. NaCl vs. DNT_w during Evaporation Process for Port 4 (a), Port 3 (b), Port 2 (c) and Port 1 (d), in the Second Stage of the Experiment under Saturated Conditions at 35°C (Exp 6)

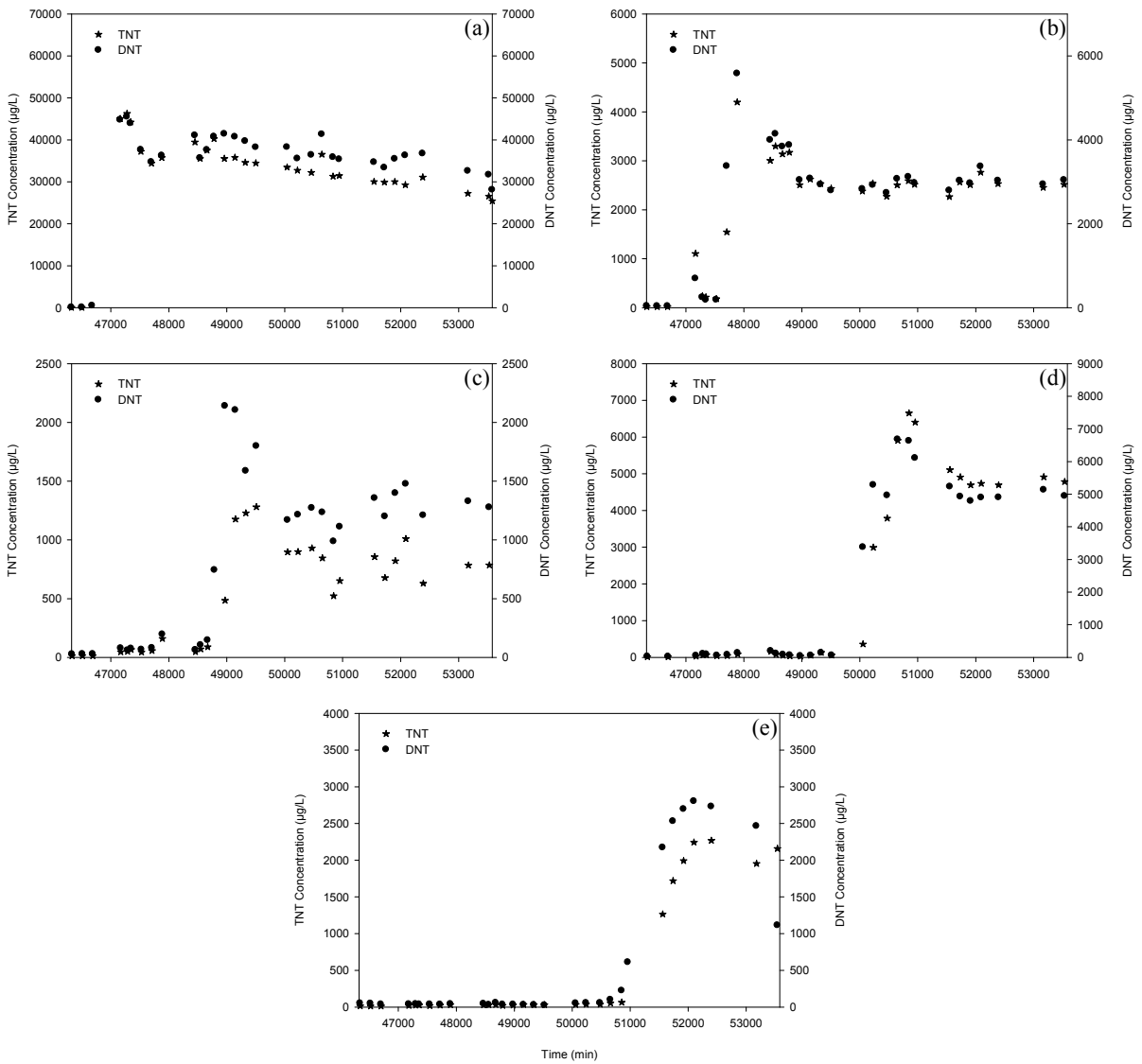


Figure 133. TNT_W vs. DNT_W during Infiltration Process for Port 4 (a), Port 3 (b), Port 2 (c), Port 1 (d) and Port 0 (e), in the Second Stage of the Experiment under Saturated Conditions at 35°C (Exp 6)

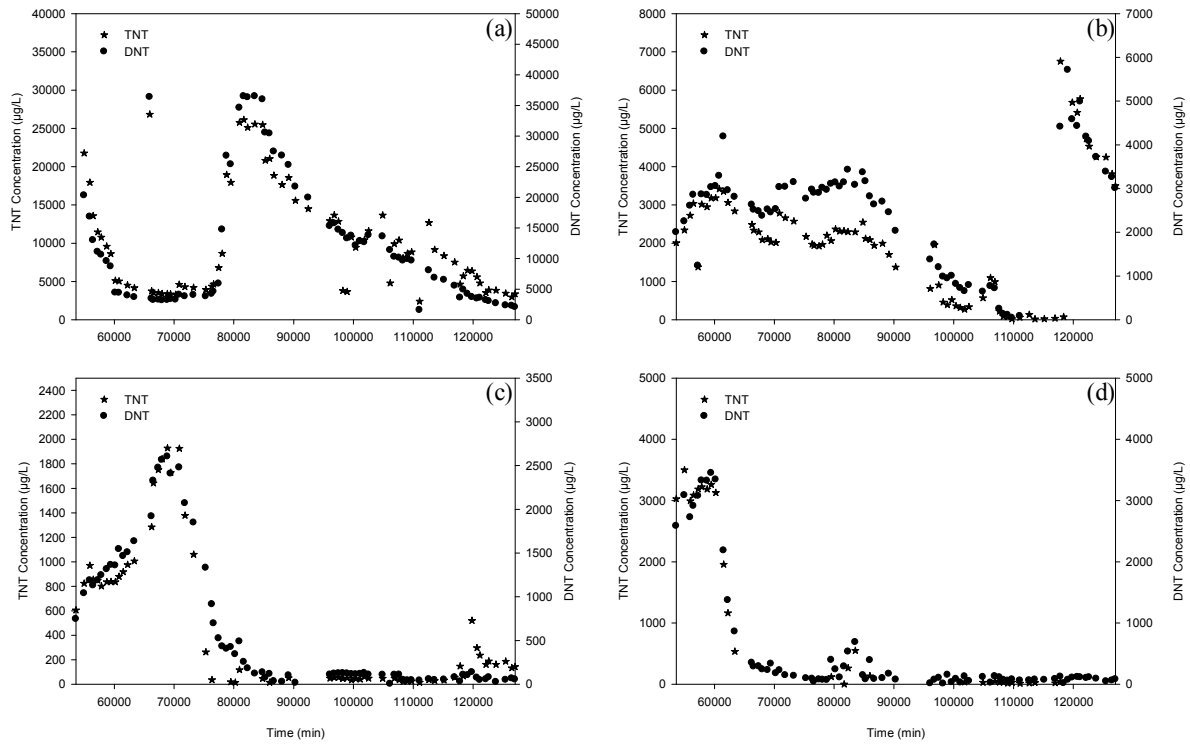


Figure 134. TNT_W vs. DNT_W during Evaporation Process for Port 4 (a), Port 3 (b), Port 2 (c) and Port 1 (d), in the Second Stage of the Experiment under Saturated Conditions at 35°C (Exp 6)

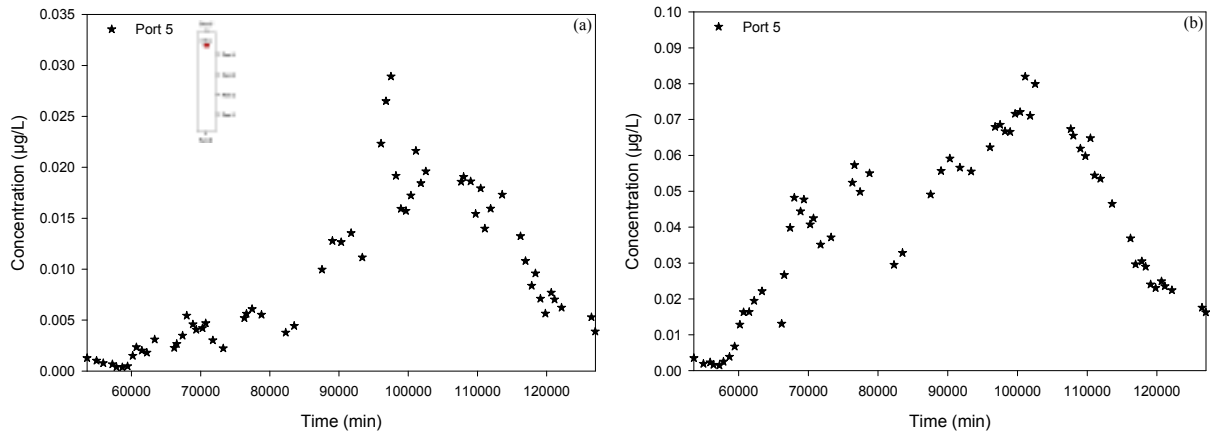


Figure 135. TNT_G (a) and DNT_G (b) BTCs in the Surface of the Soil during Evaporation Process in the Second Stage of the Experiment under Saturated Conditions at 35°C (Exp 6)

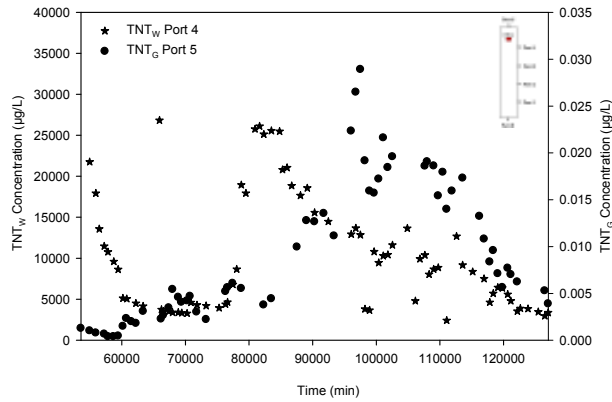


Figure 136. TNT_w vs. TNT_g BTC in the Surface of the Soil during Evaporation Process in the Second Stage of the Experiment under Saturated Conditions at 35°C (Exp 6)

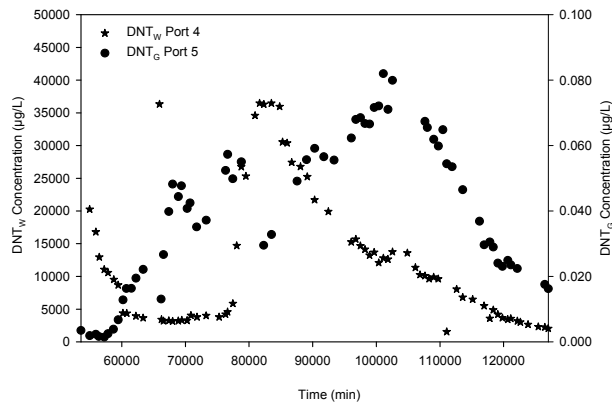


Figure 137. DNT_w vs. DNT_g BTC in the Surface of the Soil during Evaporation Process in the Second Stage of the Experiment under Saturated Conditions at 35°C (Exp 6)

G. Experiment 7 (60% of Saturation, 25°C, Infiltration-Evaporation, TNT-DNT source buried)

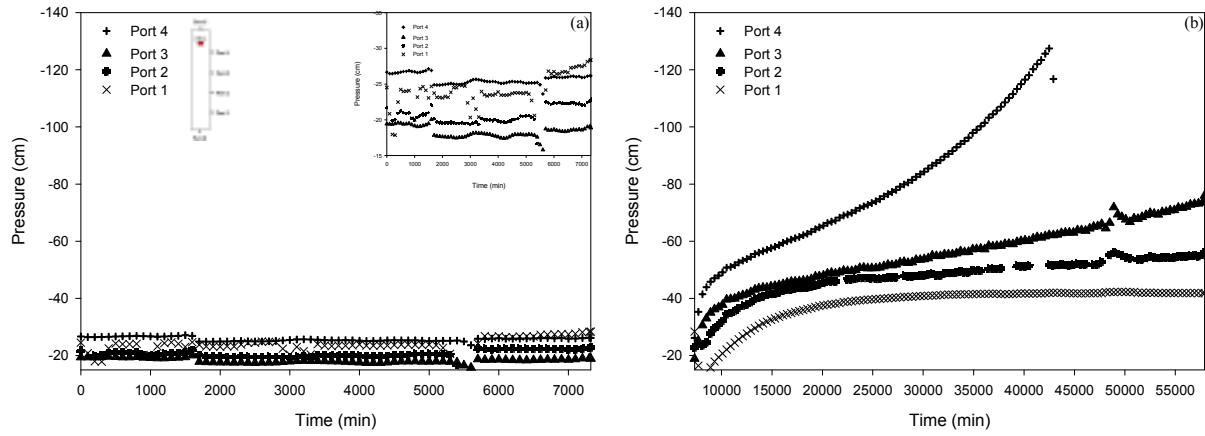


Figure 138. Pressures during Infiltration (a) and Evaporation (b) Processes under 60% of Saturation at 25°C (Exp 7)

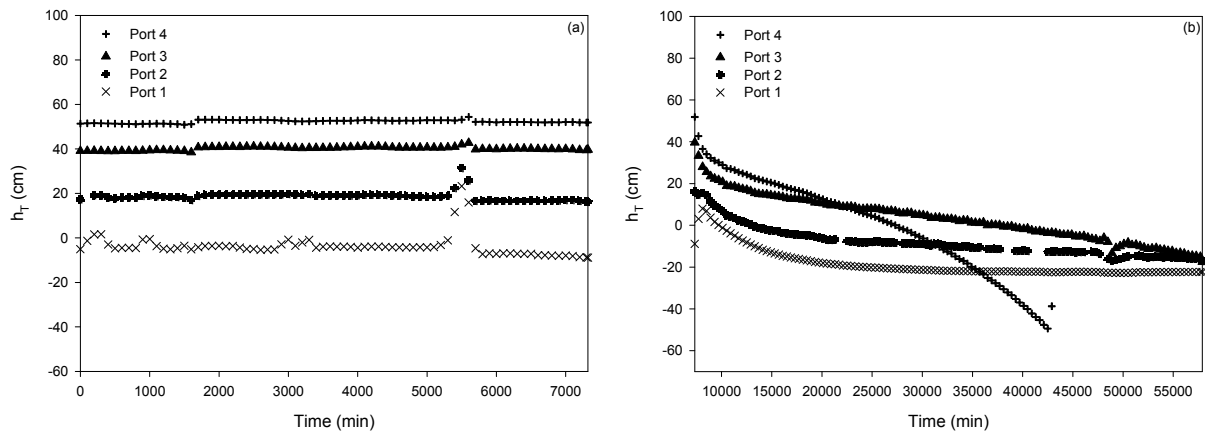


Figure 139. Total Hydraulic Heads during Infiltration (a) and Evaporation (b) Processes under 60% of Saturation at 25°C (Exp 7)

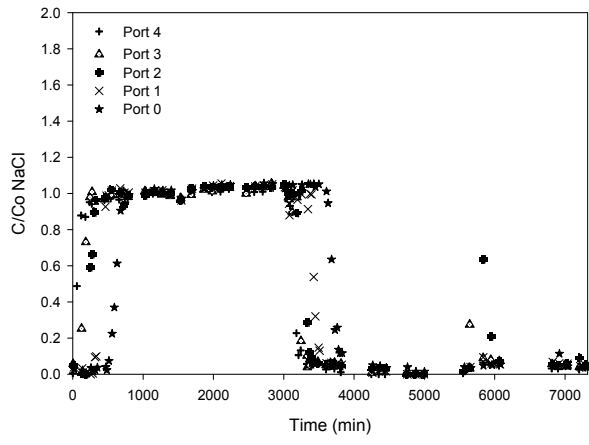


Figure 140. NaCl BTC during Infiltration Process under 60% of Saturation at 25°C (Exp 7)

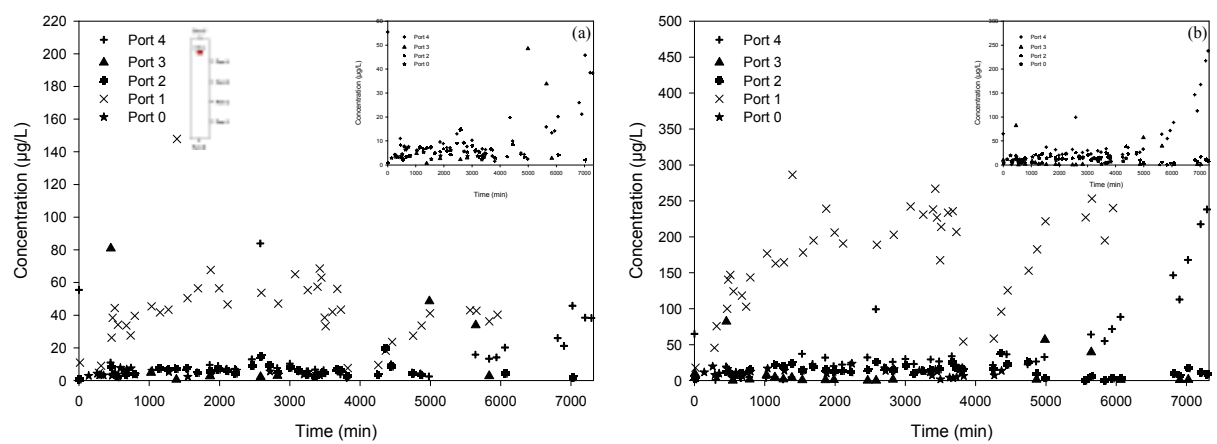


Figure 141. TNT_w (a) and DNT_w (b) BTCs during Infiltration Process under 60% of Saturation at 25°C (Exp 7)

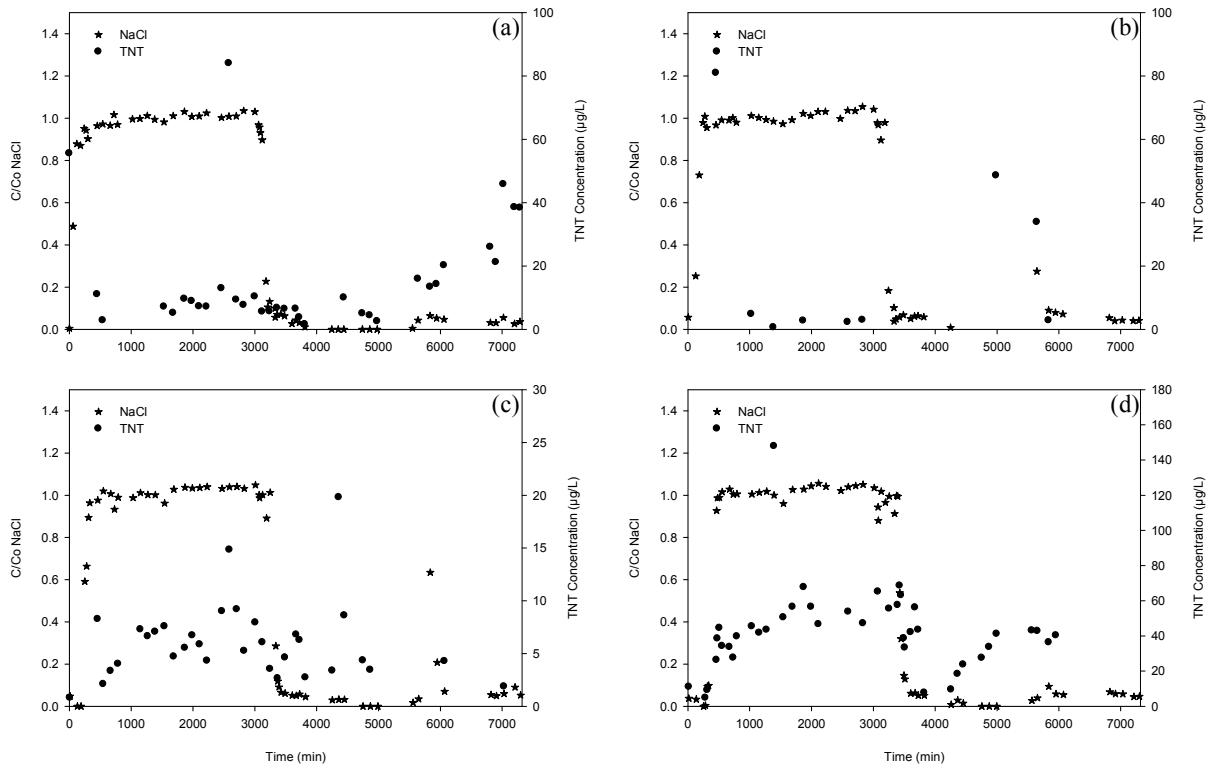


Figure 142. NaCl vs. TNT_w during Infiltration Process for Port 4 (a), Port 3 (b), Port 2 (c) and Port 1 (d), under 60% of Saturation at 25°C (Exp 7)

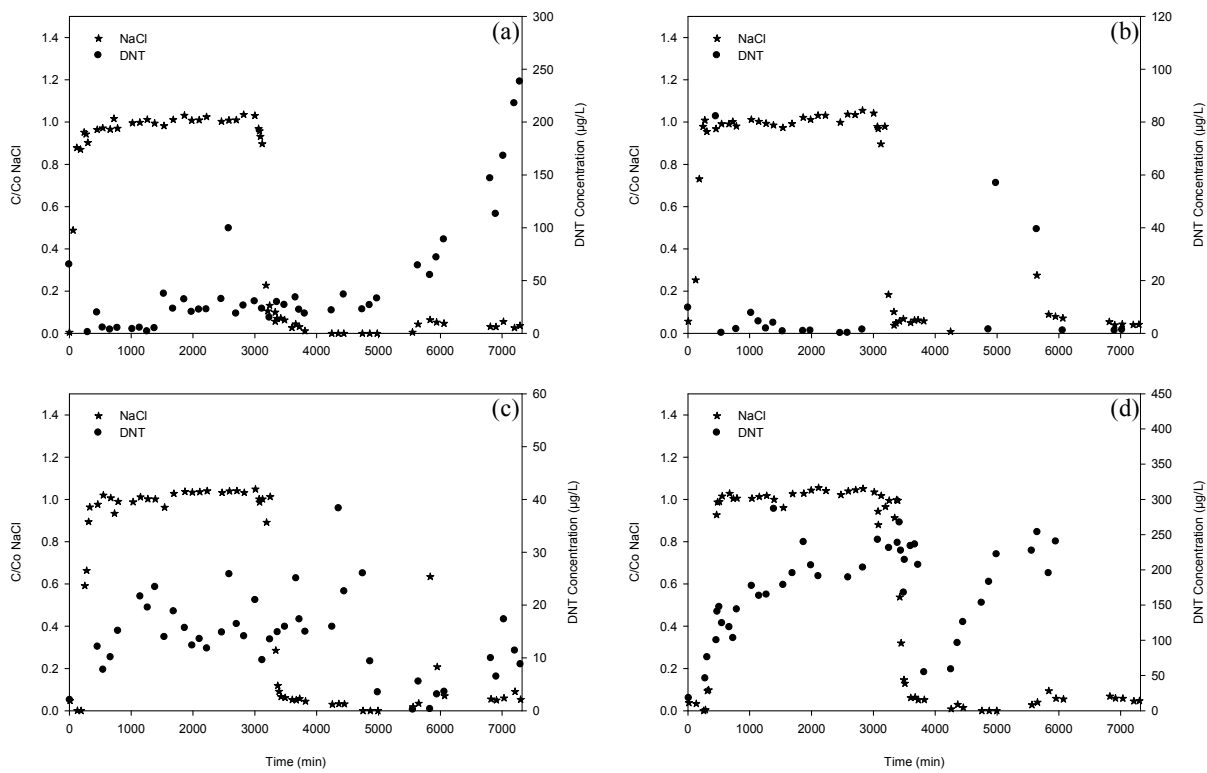


Figure 143. NaCl vs. DNT_w during Infiltration Process for Port 4 (a), Port 3 (b), Port 2 (c) and Port 1 (d), under 60% of Saturation at 25°C (Exp 7)

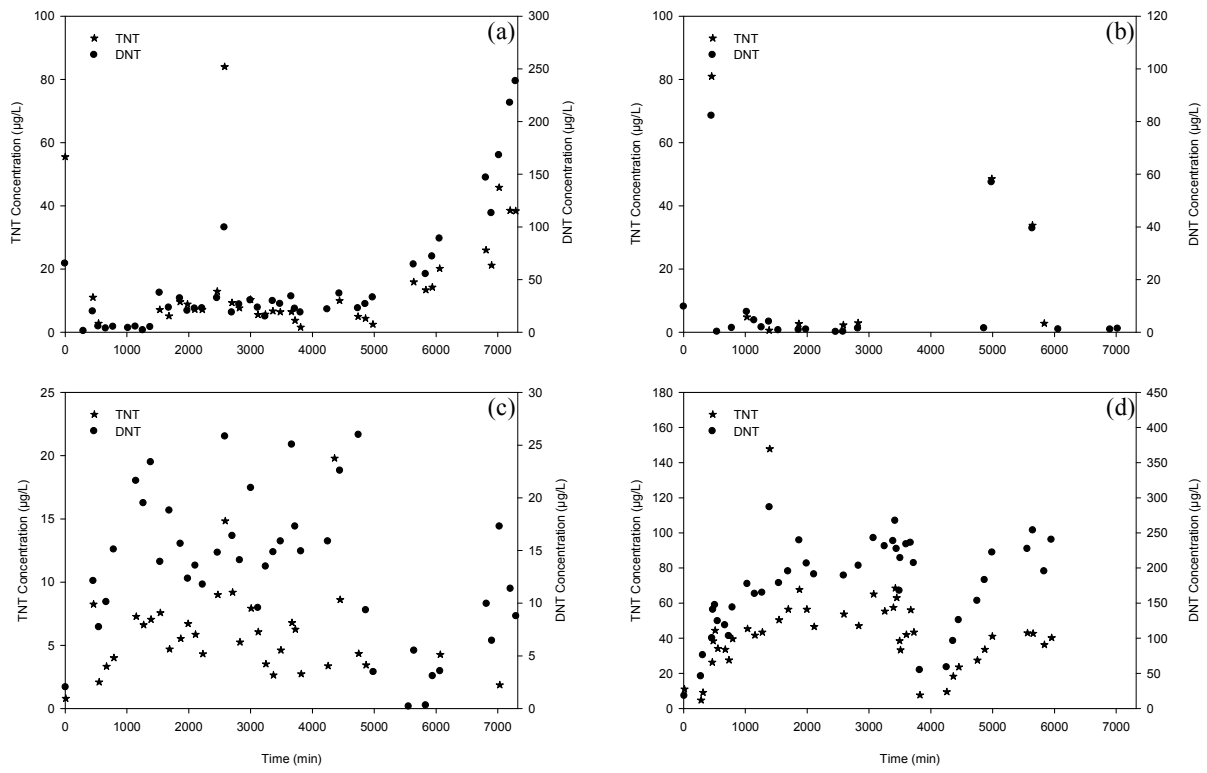


Figure 144. TNT_W vs. DNT_W during Infiltration Process for Port 4 (a), Port 3 (b), Port 2 (c) and Port 1 (d), under 60% of Saturation at 25°C (Exp 7)

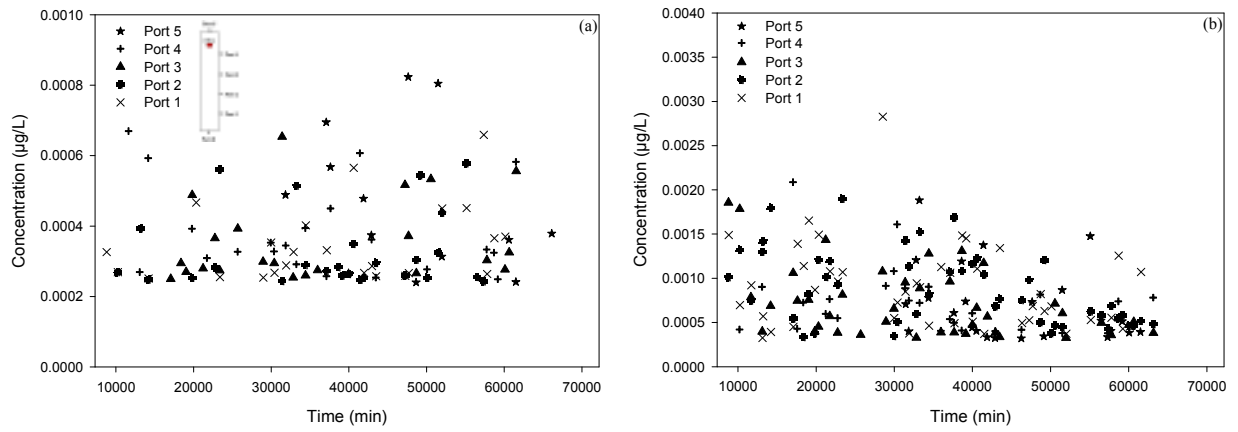


Figure 145. TNT_G (a) and DNT_G (b) BTCs during Evaporation Process under 60% of Saturation at 25°C (Exp 7)

H. Experiment 8 (60% of Saturation, 35°C, Infiltration-Evaporation, TNT-DNT source buried)

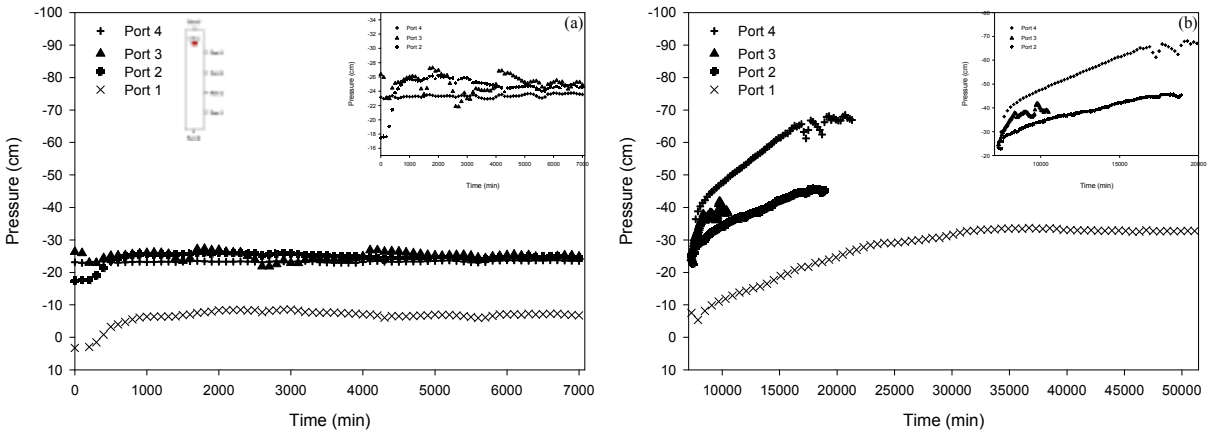


Figure 146. Pressures during Infiltration (a) and Evaporation (b) Processes under 60% of Saturation at 35°C (Exp 8)

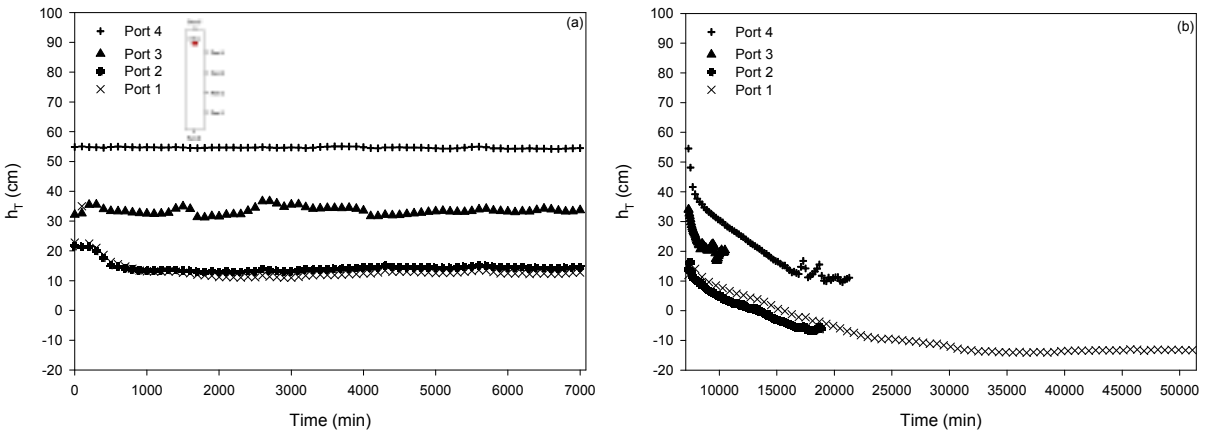


Figure 147. Total Hydraulic Heads during Infiltration (a) and Evaporation (b) Processes under 60% of Saturation at 35°C (Exp 8)

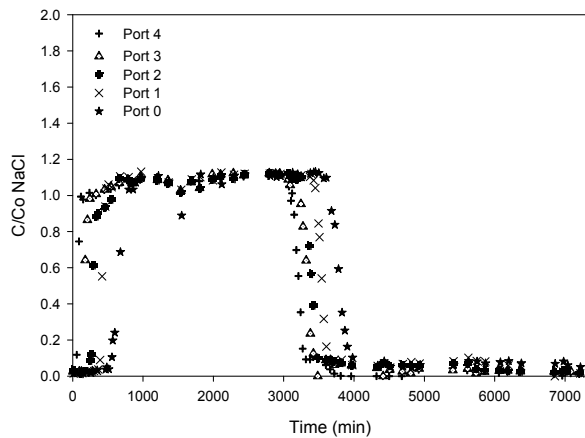


Figure 148. NaCl BTC during Infiltration Process under 60% of Saturation at 35°C (Exp 8)

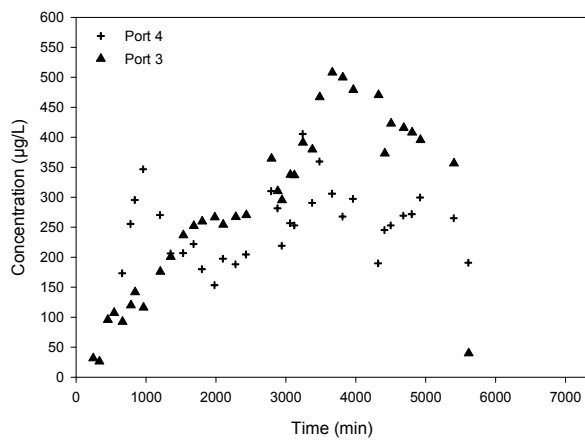


Figure 149. DNT_w BTC during Infiltration Process under 60% of Saturation at 35°C (Exp 8)

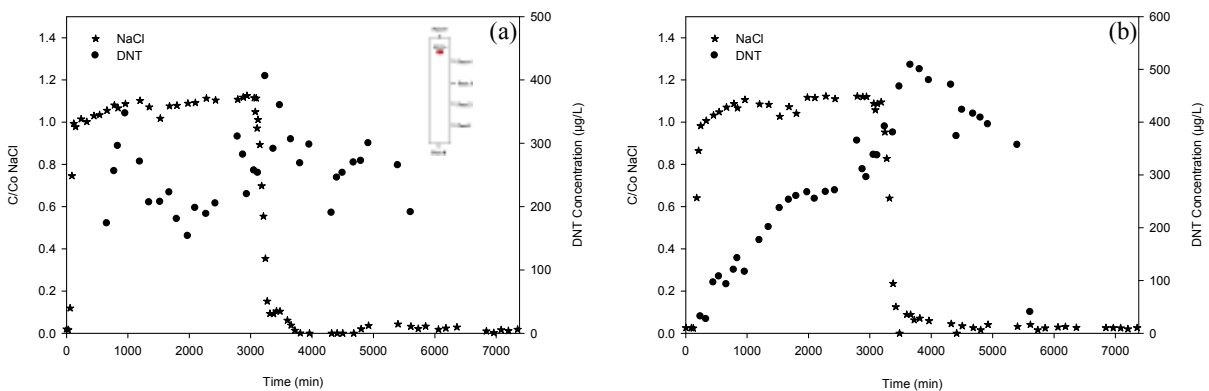


Figure 150. NaCl vs. DNT_w during Infiltration Process for Port 4 (a) and Port 3 (b), under 60% of Saturation at 35°C (Exp 8)

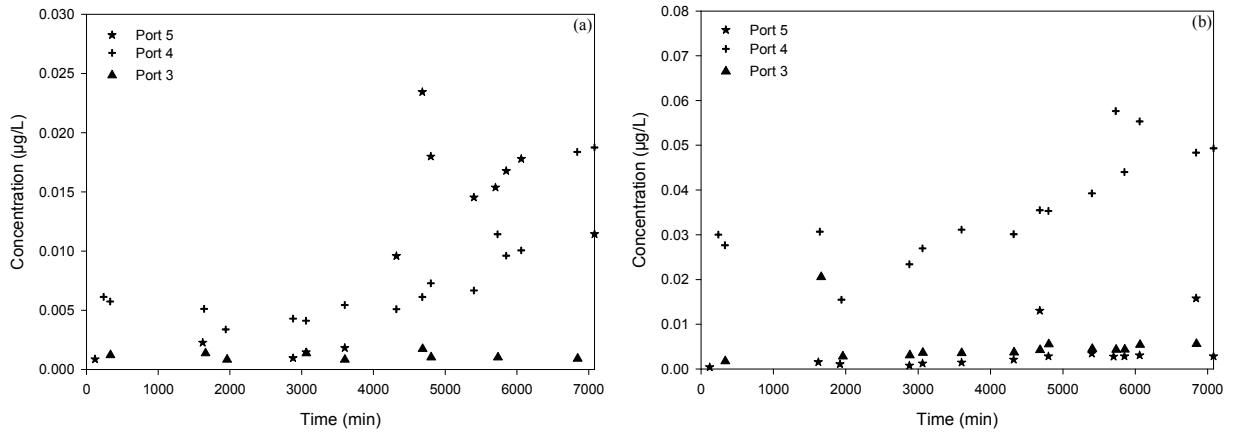


Figure 151. TNT_G (a) and DNT_G (b) BTCs during Infiltration Process under 60% of Saturation at 35°C (Exp 8)

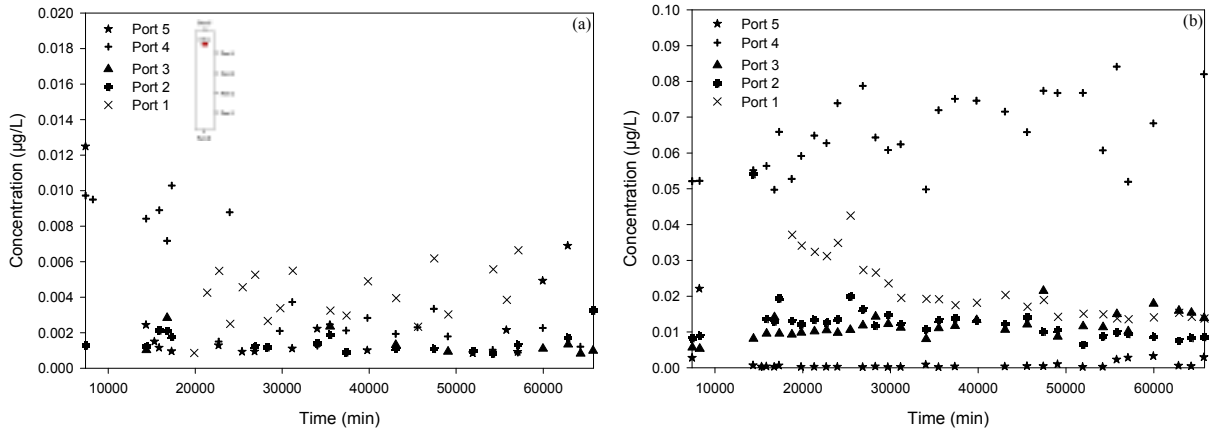


Figure 152. TNT_G (a) and DNT_G (b) BTCs during Evaporation Process under 60% of Saturation at 35°C (Exp 8)

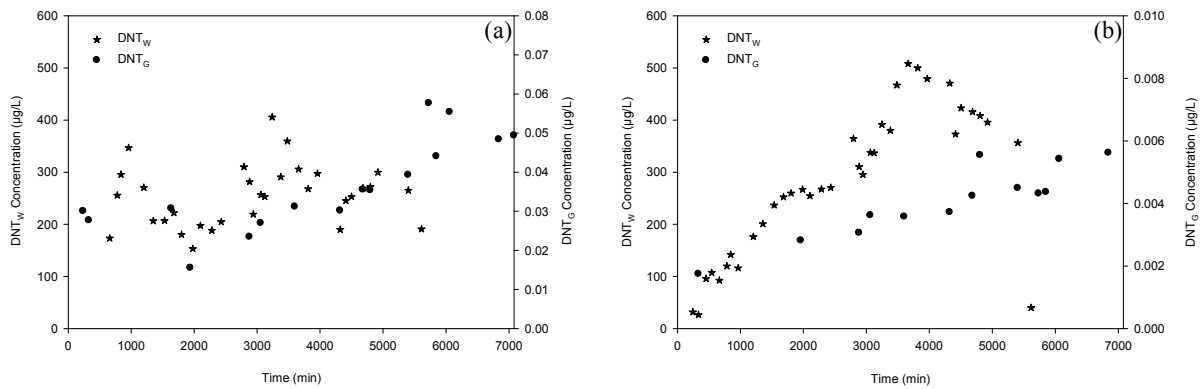


Figure 153. DNT_W vs. DNT_G during Infiltration Process for Port 4 (a) and Port 3 (b), under 60% of Saturation at 35°C (Exp 8)

Appendix B. TNT/DNT Water Calibration Curves

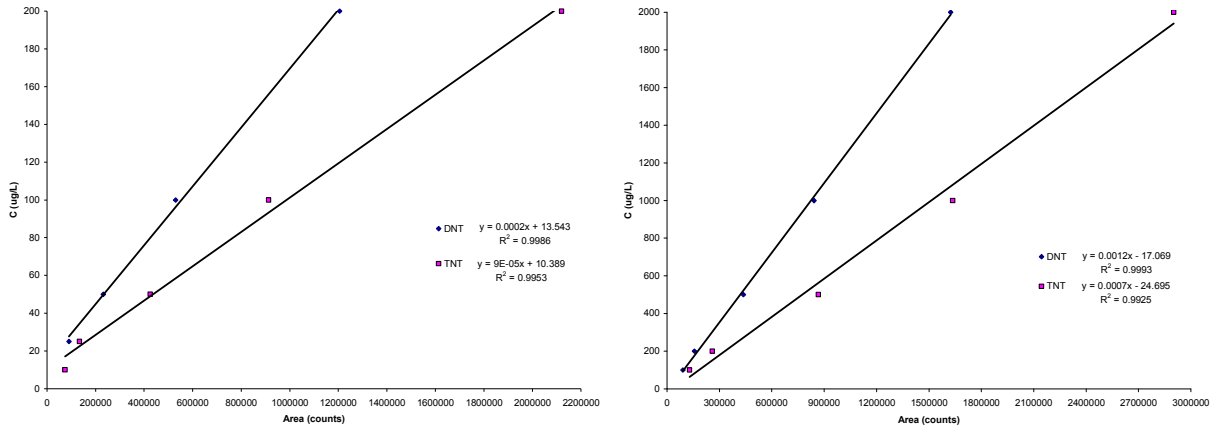


Figure 154. TNT/DNT Water Calibration Curves for ECD Sensitivity 1 and Sensitivity 10

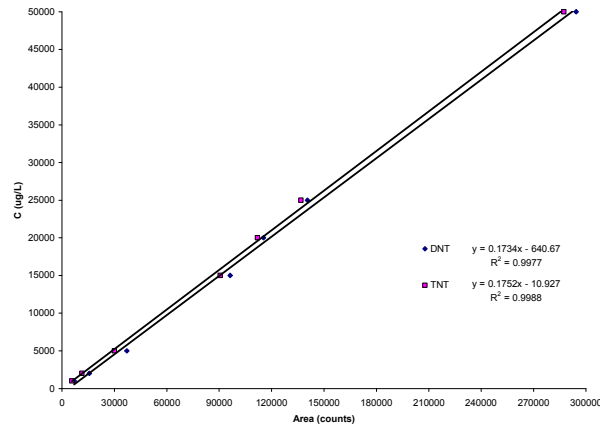


Figure 155. TNT/DNT Water Calibration Curves for TSD Sensitivity 12

Appendix C. TNT/DNT Gas Calibration Curves

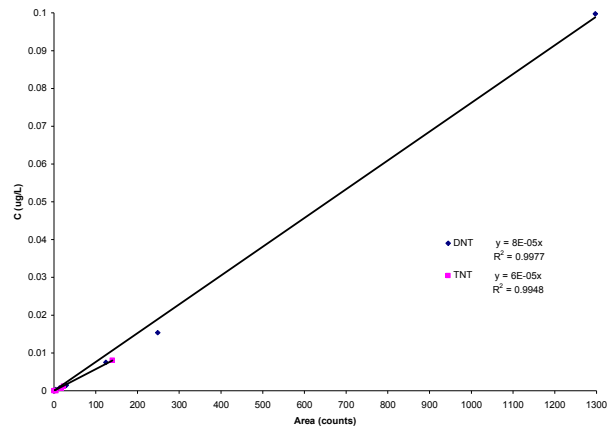


Figure 156. TNT/DNT Gas Calibration Curves for ECD Sensitivity 1

**Appendix D. Mass Balance Information for Inverse Solution Results from NaCl
Transport at Saturated Conditions and 25°C (Exp 3)**

Program parameters

Max. iterations	(MIT)	10
No. of observations	(NOBb)	182

Solute transport parameters

Bulk density	(RO)	0.167E+01
Longitudinal dispersivity	(DISPL)	0.140E+01
Transfer dispersivity	(DISPT)	0.300E-01
Type-1 adsorption sites fraction	(FRAC)	0.000E+00
Immobile water content	(THIMOB)	0.100E+00
Diffusion in water	(DIFW)	0.139E+01
Diffusion in gas	(DIFG)	0.000E+00
First adsorption coefficient	(KD)	0.000E+00
Second adsorption coefficient	(NU)	0.000E+00
Third adsorption coefficient	(BETA)	0.100E+01
Henry law constant	(HENRY)	0.000E+00
First-order reaction (liquid)	(SNKL1)	0.000E+00
First-order reaction (solid)	(SNKS1)	0.000E+00
First-order reaction (gas)	(SNKG1)	0.000E+00
Chain first-order reaction (liquid)	(SNKL1')	0.000E+00
Chain first-order reaction (solid)	(SNKS1')	0.000E+00
Chain first-order reaction (gas)	(SNKG1')	0.000E+00
Zero-order reaction (liquid)	(SNKL0)	0.000E+00
Zero-order reaction (solid)	(SNKS0)	0.000E+00
Zero-order reaction (gas)	(SNKG0)	0.000E+00
Mass-transfer coefficient	(ALPHA)	0.100E+00

Parameter estimation with the 1. initial estimate

Iteration	SSQ	DISPL	THIMOB	ALPHA
0	0.3123D+00	1.40E+00	1.00E-01	1.00E-01
1	0.3122D+00	1.50E+00	1.00E-01	2.51E+01
2	0.3122D+00	1.51E+00	1.00E-01	2.35E+01

No further reduction in SSQ obtained, optimization stopped

Mass balance error in FE solution during final run was 0.0089 %

Correlation matrix

	1	2	3
1	1		
2	0	0	
3	-0.5729	0	1

Non-linear least-squares analysis: final results

Variable	Value	95% Confidence limits		
		S.E.Coeff.	Lower	Upper
DISPL	1.50E+00	5.97E-01	3.26E-01	2.68E+00
THIMOB	1.00E-01	4.18E-17	1.00E-01	1.00E-01
ALPHA	2.35E+01	7.96E+02	-1.55E+03	1.60E+03

Contributions to the final objective function

Measurement Set 4: 0.3122E+00

RSQUARE for regression of predicted vs observed =0.73601

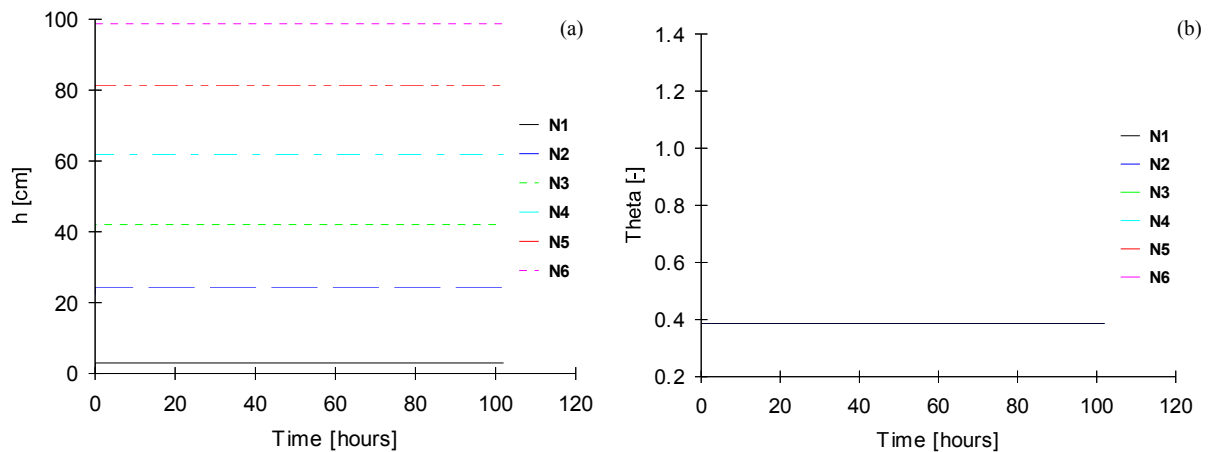


Figure 157. Simulated Pressure Heads (a) and Water Contents (b) for Saturated Conditions at 25°C (N1=Port 5, N2=Port 4, N3=Port 3, N4=Port 2, N5=Port 1, and N6=Port 0)

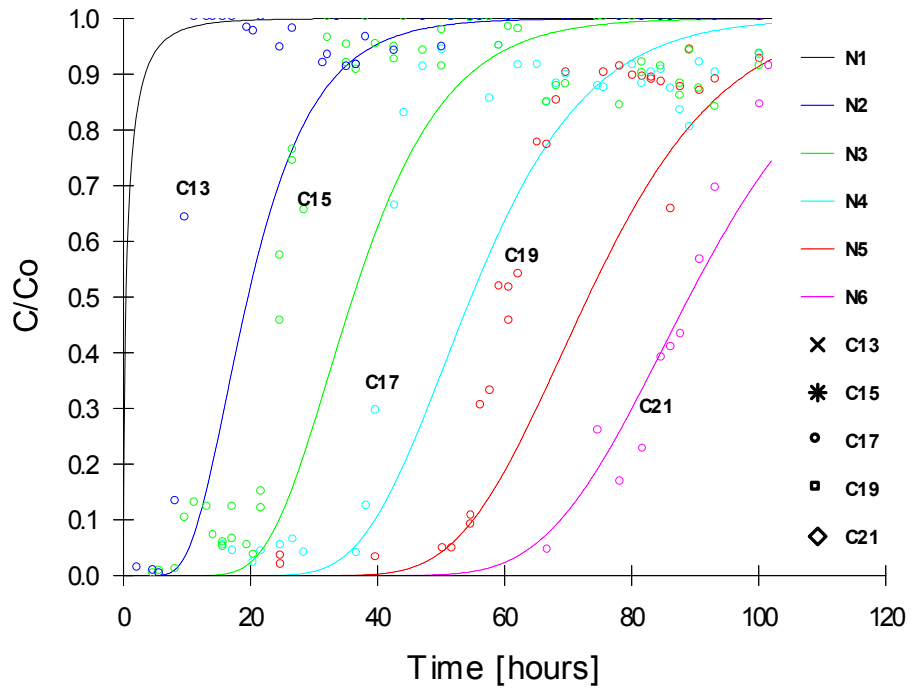


Figure 158. Measured vs Simulated Relative NaCl Concentrations Using Mobile-Immobile Model (MIM) for Saturated Conditions at 25°C (For Simulated Data: N1=Port 5, N2=Port 4, N3=Port 3, N4=Port 2, N5=Port 1, and N6=Port 0; For Experimental Data: C13=Port 4, C15=Port 3, C17=Port 2, C19=Port 1, and C21=Port 0)

**Appendix E. Mass Balance Information for Inverse Solution Results from NaCl
Transport at 75% of Saturation and 25°C (Exp 4)**

Program parameters

Max. iterations	(MIT)	20
No. of observations	(NOBb)	96

Solute transport parameters

Bulk density	(RO)	0.167E+01
Longitudinal dispersivity	(DISPL)	0.140E+01
Transfer dispersivity	(DISPT)	0.300E-01
Type-1 adsorption sites fraction	(FRAC)	0.000E+00
Immobile water content	(THIMOB)	0.100E+00
Diffusion in water	(DIFW)	0.139E+01
Diffusion in gas	(DIFG)	0.000E+00
First adsorption coefficient	(KD)	0.000E+00
Second adsorption coefficient	(NU)	0.000E+00
Third adsorption coefficient	(BETA)	0.100E+01
Henry law constant	(HENRY)	0.000E+00
First-order reaction (liquid)	(SNKL1)	0.000E+00
First-order reaction (solid)	(SNKS1)	0.000E+00
First-order reaction (gas)	(SNKG1)	0.000E+00
Chain first-order reaction (liquid)	(SNKL1')	0.000E+00
Chain first-order reaction (solid)	(SNKS1')	0.000E+00
Chain first-order reaction (gas)	(SNKG1')	0.000E+00
Zero-order reaction (liquid)	(SNKL0)	0.000E+00
Zero-order reaction (solid)	(SNKS0)	0.000E+00
Zero-order reaction (gas)	(SNKG0)	0.000E+00
Mass-transfer coefficient	(ALPHA)	0.100E+00

Parameter estimation with the 1. initial estimate

Iteration	SSQ	DISPL	THIMOB	ALPHA
0	0.4572D+00	1.40E+00	1.00E-01	1.00E-01
1	0.4392D+00	2.60E+00	1.00E-01	8.48E-01
2	0.4388D+00	2.53E+00	1.00E-01	1.54E+01
3	0.4388D+00	2.53E+00	1.00E-01	8.20E+01
4	0.4388D+00	2.52E+00	1.00E-01	8.19E+01

No further reduction in SSQ obtained, optimization stopped

Mass balance error in FE solution during final run was 0.001 %

Correlation matrix

	1	2	3
1	1		
2	0	0	
3	-0.097	0	1

Non-linear least-squares analysis: final results

Variable	Value	95% Confidence limits		
		S.E.Coeff.	Lower	Upper
DISPL	2.52E+00	8.43E-01	8.49E-01	4.20E+00
THIMOB	1.00E-01	6.87E-17	1.00E-01	1.00E-01
ALPHA	8.19E+01	2.96E+03	-5.80E+03	5.96E+03

Contributions to the final objective function

Measurement Set 4: 4.39E-01

RSQUARE for regression of predicted vs observed = 0.70977

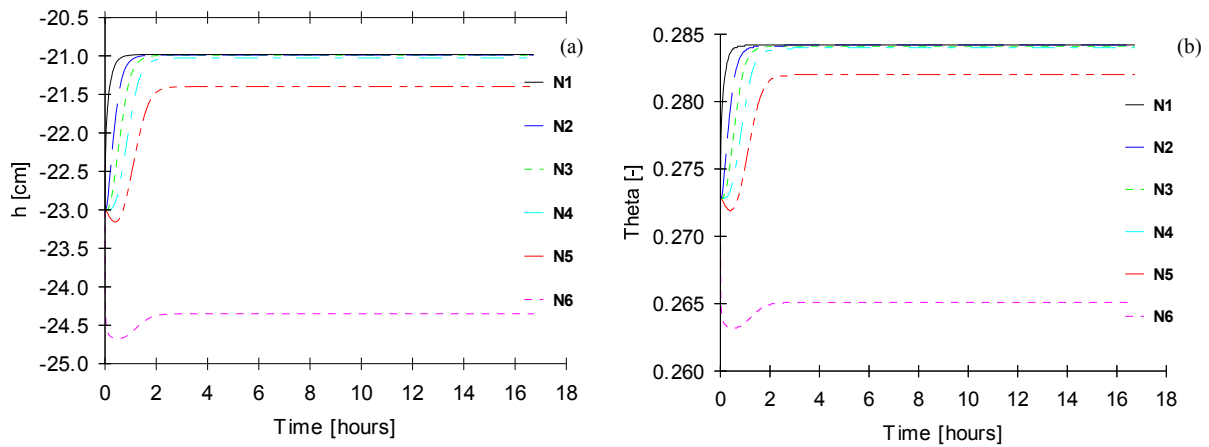


Figure 159. Simulated Pressure Heads (a) and Water Contents (b) for 75% of Saturation at 25°C (N1=Port 5, N2=Port 4, N3=Port 3, N4=Port 2, N5=Port 1, and N6=Port 0)

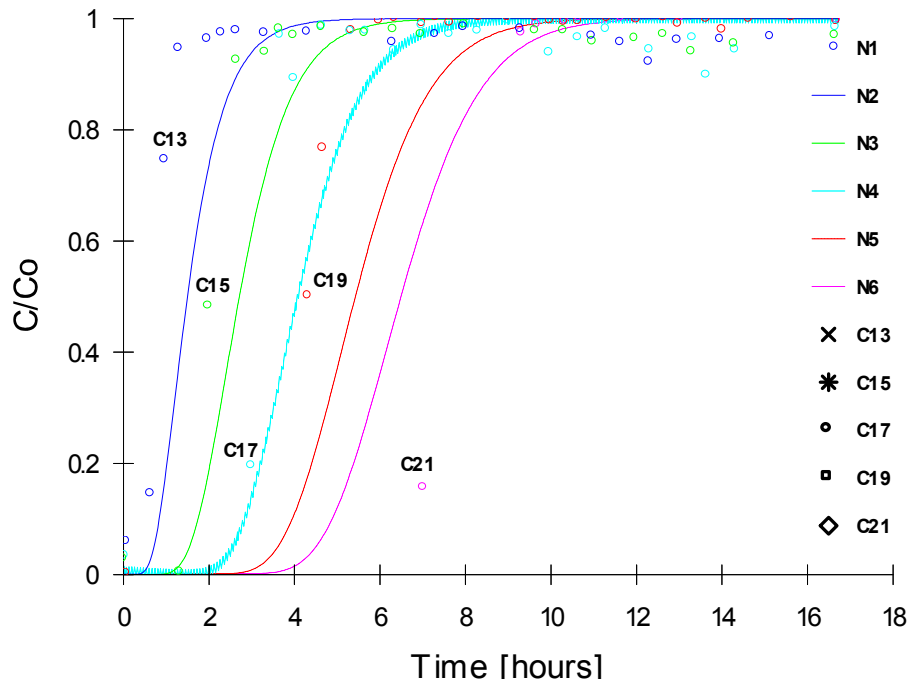


Figure 160. Measured vs Simulated Relative NaCl Concentrations Using Mobile-Immobile Model (MIM) for 75% of Saturation at 25°C (For Simulated Data: N2=Port 4, N3=Port 3, N4=Port 2, N5=Port 1, and N6=Port 0; For Experimental Data: C13=Port 4, C15=Port 3, C17=Port 2, C19=Port 1, and C21=Port 0)

**Appendix F. Mass Balance Information for Inverse Solution Results from NaCl
Transport at 45% of Saturation and 25°C (Exp 5)**

Program parameters

Max. iterations	(MIT)	20
No. of observations	(NOBb)	235

Solute transport parameters

Bulk density	(RO)	0.167E+01
Longitudinal dispersivity	(DISPL)	0.140E+01
Transfer dispersivity	(DISPT)	0.300E-01
Type-1 adsorption sites fraction	(FRAC)	0.000E+00
Immobile water content	(THIMOB)	0.100E+00
Diffusion in water	(DIFW)	0.139E+01
Diffusion in gas	(DIFG)	0.000E+00
First adsorption coefficient	(KD)	0.000E+00
Second adsorption coefficient	(NU)	0.000E+00
Third adsorption coefficient	(BETA)	0.100E+01
Henry law constant	(HENRY)	0.000E+00
First-order reaction (liquid)	(SNKL1)	0.000E+00
First-order reaction (solid)	(SNKS1)	0.000E+00
First-order reaction (gas)	(SNKG1)	0.000E+00
Chain first-order reaction (liquid)	(SNKL1')	0.000E+00
Chain first-order reaction (solid)	(SNKS1')	0.000E+00
Chain first-order reaction (gas)	(SNKG1')	0.000E+00
Zero-order reaction (liquid)	(SNKL0)	0.000E+00
Zero-order reaction (solid)	(SNKS0)	0.000E+00
Zero-order reaction (gas)	(SNKG0)	0.000E+00
Mass-transfer coefficient	(ALPHA)	0.100E+00

Parameter estimation with the 1. initial estimate

Iteration	SSQ	DISPL	THIMOB	ALPHA
0	0.3813D+00	1.40E+00	1.00E-01	1.00E-01
1	0.3389D+00	3.87E+00	1.00E-01	1.00E-02
2	0.3341D+00	6.15E+00	1.00E-01	1.41E+01
3	0.3340D+00	5.64E+00	1.00E-01	7.04E+00
4	0.3340D+00	5.69E+00	1.00E-01	1.00E+02
5	0.3340D+00	5.68E+00	1.00E-01	9.84E+01
6	0.3340D+00	5.65E+00	1.00E-01	9.54E+01

No further reduction in SSQ obtained, optimization stopped

Mass balance error in FE solution during final run was 0.0314 %

Correlation matrix

	1	2	3
1	1		
2	0	0	
3	-0.1188	0	1

Non-linear least-squares analysis: final results

Variable	Value	95% Confidence limits		
		S.E.Coeff.	Lower	Upper
DISPL	5.65E+00	1.30E+00	3.09E+00	8.22E+00
THIMOB	1.00E-01	3.79E-17	1.00E-01	1.00E-01
ALPHA	9.54E+01	4.66E+02	-8.23E+02	1.01E+03

Contributions to the final objective function

Measurement Set 4: 3.34E-01

RSQUARE for regression of predicted vs observed = 0.68115

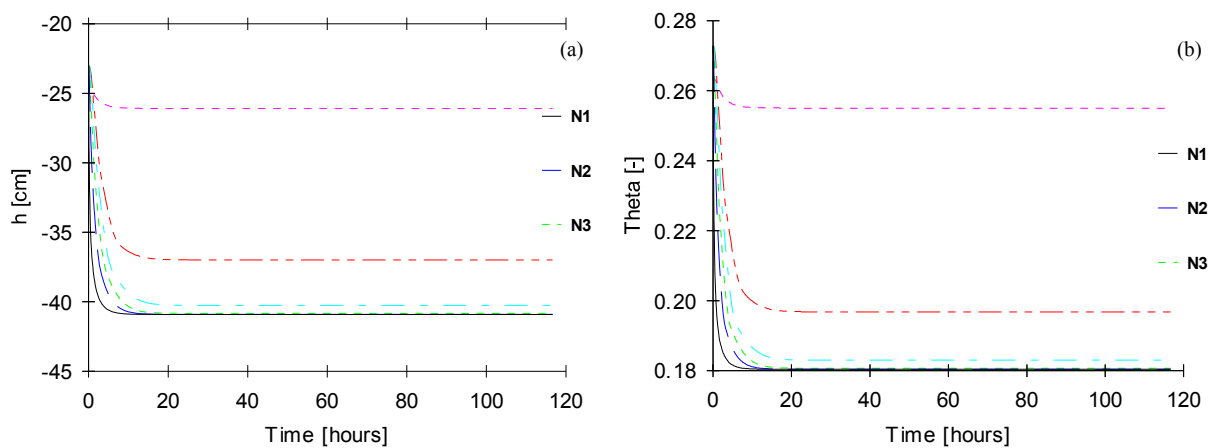


Figure 161. Simulated Pressure Heads (a) and Water Contents (b) for 45% of Saturation at 25°C (N1=Port 5, N2=Port 4, N3=Port 3, N4=Port 2, N5=Port 1, and N6=Port 0)

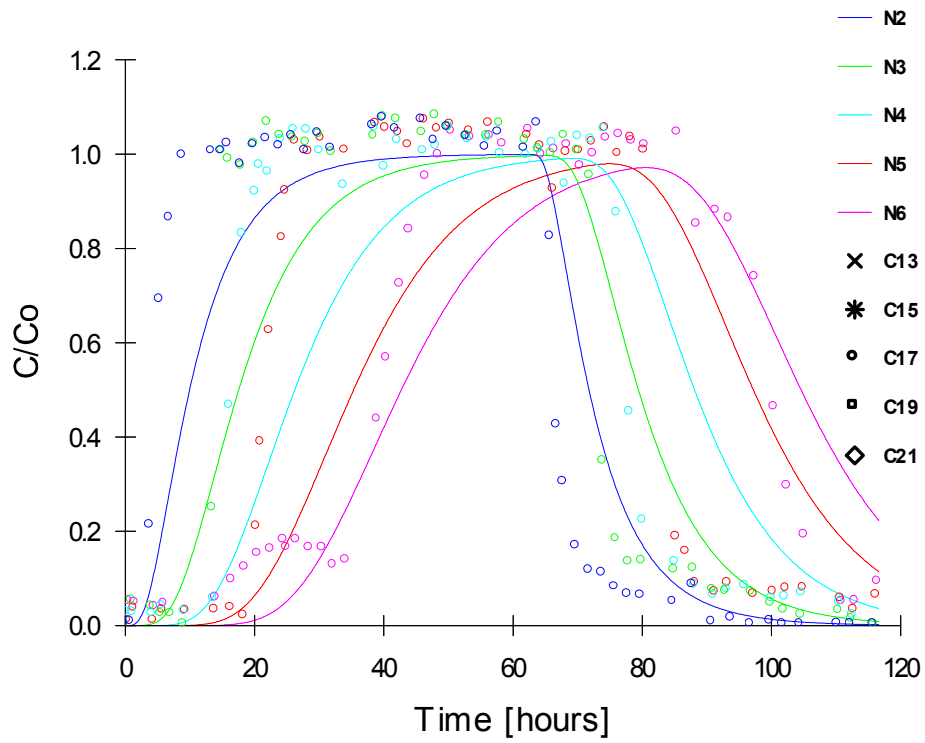


Figure 162. Measured vs Simulated Relative NaCl Concentrations Using Mobile-Immobile Model (MIM) for 45% of Saturation at 25°C (For Simulated Data: N2=Port 4, N3=Port 3, N4=Port 2, N5=Port 1, and N6=Port 0; For Experimental Data: C13=Port 4, C15=Port 3, C17=Port 2, C19=Port 1, and C21=Port 0)

**Appendix G. Mass Balance Information for Inverse Solution Results from NaCl
Transport at Saturated Conditions and 35°C (Exp 6)**

Program parameters

Max. iterations	(MIT)	10
No. of observations	(NOBb)	563

Solute transport parameters

Bulk density	(RO)	0.167E+01
Longitudinal dispersivity	(DISPL)	0.140E+01
Transfer dispersivity	(DISPT)	0.300E-01
Type-1 adsorption sites fraction	(FRAC)	0.000E+00
Immobile water content	(THIMOB)	0.100E+00
Diffusion in water	(DIFW)	0.139E+01
Diffusion in gas	(DIFG)	0.000E+00
First adsorption coefficient	(KD)	0.000E+00
Second adsorption coefficient	(NU)	0.000E+00
Third adsorption coefficient	(BETA)	0.100E+01
Henry law constant	(HENRY)	0.000E+00
First-order reaction (liquid)	(SNKL1)	0.000E+00
First-order reaction (solid)	(SNKS1)	0.000E+00
First-order reaction (gas)	(SNKG1)	0.000E+00
Chain first-order reaction (liquid)	(SNKL1')	0.000E+00
Chain first-order reaction (solid)	(SNKS1')	0.000E+00
Chain first-order reaction (gas)	(SNKG1')	0.000E+00
Zero-order reaction (liquid)	(SNKL0)	0.000E+00
Zero-order reaction (solid)	(SNKS0)	0.000E+00
Zero-order reaction (gas)	(SNKG0)	0.000E+00
Mass-transfer coefficient	(ALPHA)	0.100E+00

Parameter estimation with the 1. initial estimate

Iteration	SSQ	DISPL	THIMOB	ALPHA
0	0.2340D+00	1.40E+00	1.00E-01	1.00E-01
1	0.2320D+00	2.61E+00	1.00E-01	1.00E+02
2	0.2320D+00	2.59E+00	1.00E-01	1.00E-02
3	0.2320D+00	2.57E+00	1.00E-01	1.00E-02

No further reduction in SSQ obtained, optimization stopped

Mass balance error in FE solution during final run was 0.009 %

Correlation matrix

	1	2	3
1	1		
2	0	0	
3	-0.1954	0	1

Non-linear least-squares analysis: final results

Variable	Value	95% Confidence limits		
		S.E.Coeff.	Lower	Upper
DISPL	2.57E+00	5.67E-01	1.45E+00	3.68E+00
THIMOB	1.00E-01	2.04E-17	1.00E-01	1.00E-01
ALPHA	1.00E-02	1.01E+01	-1.98E+01	1.99E+01

Contributions to the final objective function

Measurement Set 4: 2.32E-01

RSQUARE for regression of predicted vs observed = 0.77755

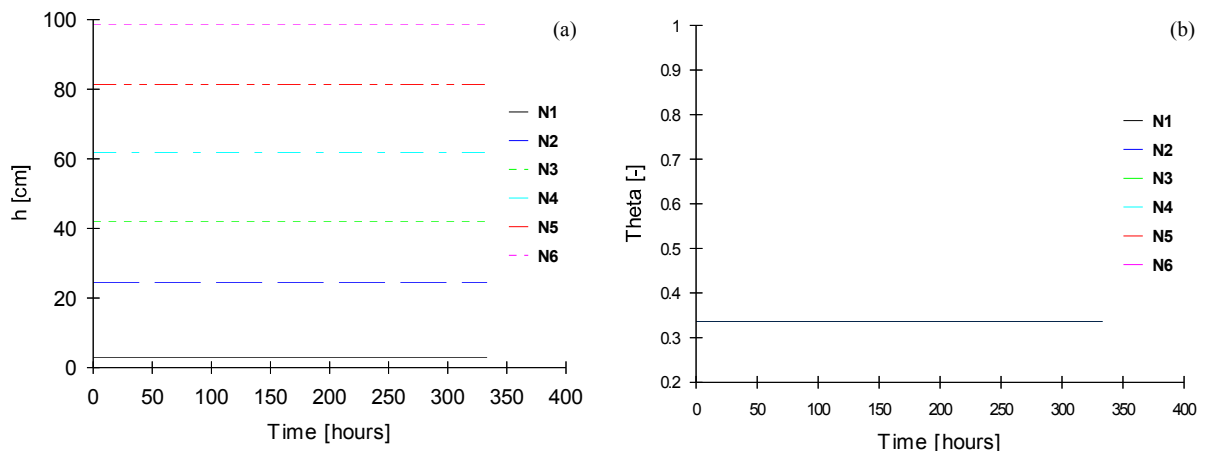


Figure 163. Simulated Pressure Heads (a) and Water Contents (b) for Saturated Conditions at 25°C (N1=Port 5, N2=Port 4, N3=Port 3, N4=Port 2, N5=Port 1, and N6=Port 0)

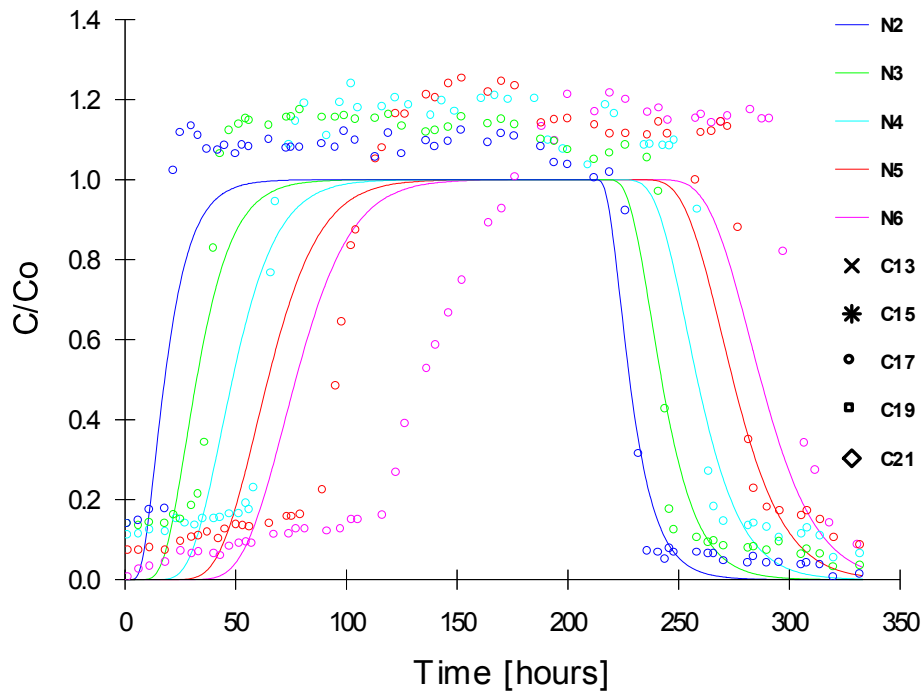


Figure 164. Measured vs Simulated Relative NaCl Concentrations Using Mobile-Immobile Model (MIM) for Saturated Conditions at 25°C (For Simulated Data: N2=Port 4, N3=Port 3, N4=Port 2, N5=Port 1, and N6=Port 0; For Experimental Data: C13=Port 4, C15=Port 3, C17=Port 2, C19=Port 1, and C21=Port 0)

**Appendix H. Mass Balance Information for Inverse Solution Results from NaCl
Transport at 60% of Saturation and 25°C (Exp 7)**

Program parameters

Max. iterations	(MIT)	20
No. of observations	(NOBb)	295

Solute transport parameters

Bulk density	(RO)	0.167E+01
Longitudinal dispersivity	(DISPL)	0.140E+01
Transfer dispersivity	(DISPT)	0.300E-01
Type-1 adsorption sites fraction	(FRAC)	0.000E+00
Immobile water content	(THIMOB)	0.100E+00
Diffusion in water	(DIFW)	0.139E+01
Diffusion in gas	(DIFG)	0.000E+00
First adsorption coefficient	(KD)	0.000E+00
Second adsorption coefficient	(NU)	0.000E+00
Third adsorption coefficient	(BETA)	0.100E+01
Henry law constant	(HENRY)	0.000E+00
First-order reaction (liquid)	(SNKL1)	0.000E+00
First-order reaction (solid)	(SNKS1)	0.000E+00
First-order reaction (gas)	(SNKG1)	0.000E+00
Chain first-order reaction (liquid)	(SNKL1')	0.000E+00
Chain first-order reaction (solid)	(SNKS1')	0.000E+00
Chain first-order reaction (gas)	(SNKG1')	0.000E+00
Zero-order reaction (liquid)	(SNKL0)	0.000E+00
Zero-order reaction (solid)	(SNKS0)	0.000E+00
Zero-order reaction (gas)	(SNKG0)	0.000E+00
Mass-transfer coefficient	(ALPHA)	0.100E+00

Parameter estimation with the 1. initial estimate

Iteration	SSQ	DISPL	THIMOB	ALPHA
0	0.2216D+00	1.40E+00	1.00E-01	1.00E+00
1	0.1832D+00	5.11E+00	1.00E-01	1.00E-02
2	0.1797D+00	8.00E+00	1.00E-01	1.00E-02
3	0.1797D+00	7.88E+00	1.00E-01	1.00E-02

No further reduction in SSQ obtained, optimization stopped

Mass balance error in FE solution during final run was 0.0013 %

Correlation matrix

	1	2	3
1	1		
2	0	0	
3	0.2933	0	1

Non-linear least-squares analysis: final results

Variable	Value	95% Confidence limits		
		S.E.Coeff.	Lower	Upper
DISPL	7.88E+00	1.77E+00	4.39E+00	1.14E+01
THIMOB	1.00E-01	2.48E-17	1.00E-01	1.00E-01
ALPHA	1.00E-02	1.41E+00	-2.77E+00	2.79E+00

Contributions to the final objective function

Measurement Set 4: 1.80E-01

RSQUARE for regression of predicted vs observed = 0.82222

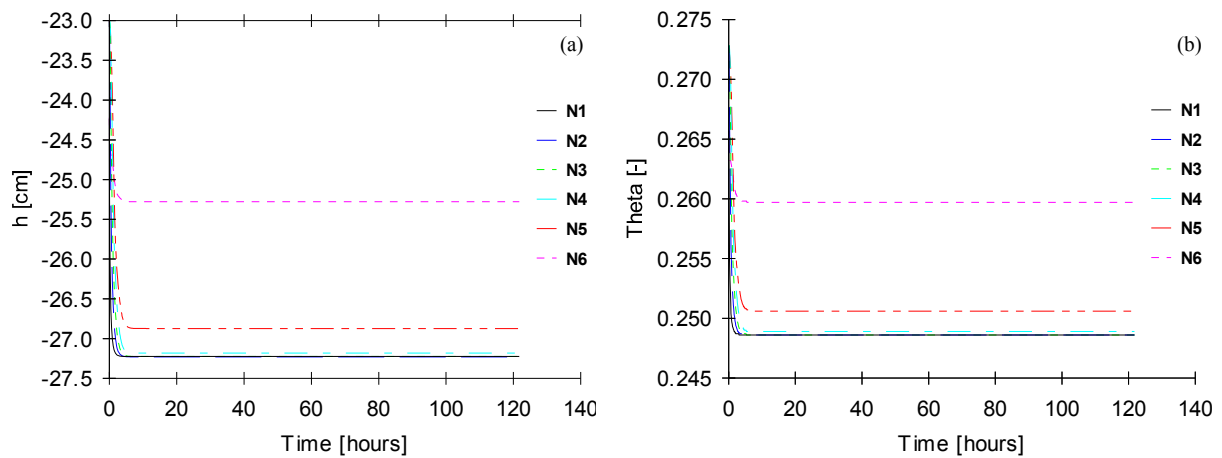


Figure 165. Simulated Pressure Heads (a) and Water Contents (b) for 60% of Saturation at 25°C (N1=Port 5, N2=Port 4, N3=Port 3, N4=Port 2, N5=Port 1, and N6=Port 0)

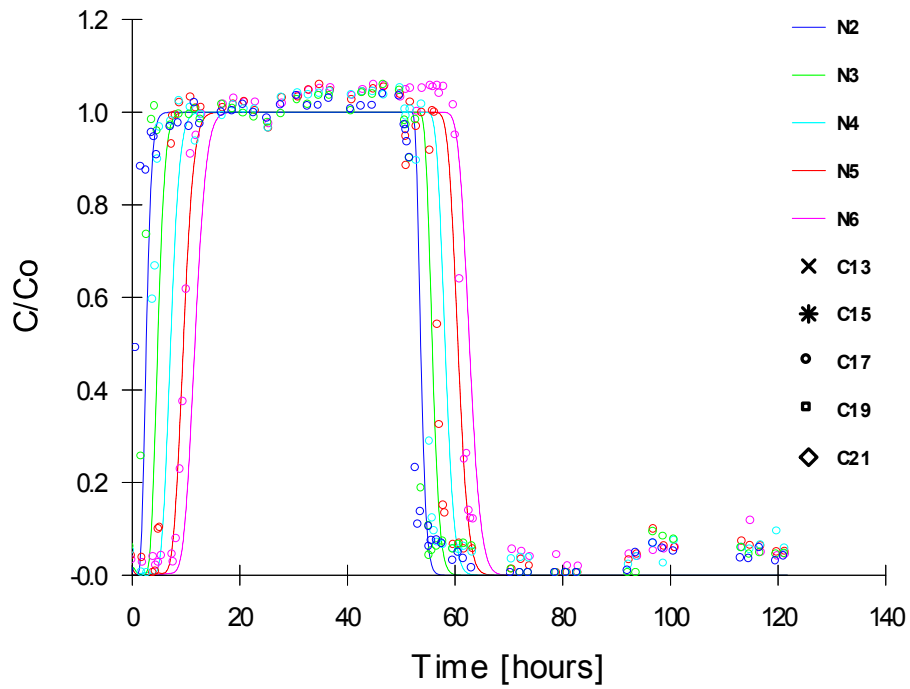


Figure 166. Measured vs Simulated Relative NaCl Concentrations Using Mobile-Immobile Model (MIM) for 60% of Saturation at 25°C (For Simulated Data: N2=Port 4, N3=Port 3, N4=Port 2, N5=Port 1, and N6=Port 0; For Experimental Data: C13=Port 4, C15=Port 3, C17=Port 2, C19=Port 1, and C21=Port 0)

Appendix I. Mass Balance Information for Inverse Solution Results from NaCl Transport at 60% of Saturation and 35°C (Exp 8)

Program parameters

Max. iterations	(MIT)	20
No. of observations	(NOBb)	307

Solute transport parameters

Bulk density	(RO)	0.167E+01
Longitudinal dispersivity	(DISPL)	0.140E+01
Transfer dispersivity	(DISPT)	0.300E-01
Type-1 adsorption sites fraction	(FRAC)	0.000E+00
Immobile water content	(THIMOB)	0.100E+00
Diffusion in water	(DIFW)	0.139E+01
Diffusion in gas	(DIFG)	0.000E+00
First adsorption coefficient	(KD)	0.000E+00
Second adsorption coefficient	(NU)	0.000E+00
Third adsorption coefficient	(BETA)	0.100E+01
Henry law constant	(HENRY)	0.000E+00
First-order reaction (liquid)	(SNKL1)	0.000E+00
First-order reaction (solid)	(SNKS1)	0.000E+00
First-order reaction (gas)	(SNKG1)	0.000E+00
Chain first-order reaction (liquid)	(SNKL1')	0.000E+00
Chain first-order reaction (solid)	(SNKS1')	0.000E+00
Chain first-order reaction (gas)	(SNKG1')	0.000E+00
Zero-order reaction (liquid)	(SNKL0)	0.000E+00
Zero-order reaction (solid)	(SNKS0)	0.000E+00
Zero-order reaction (gas)	(SNKG0)	0.000E+00
Mass-transfer coefficient	(ALPHA)	0.100E+00

Parameter estimation with the 1. initial estimate

Iteration	SSQ	DISPL	THIMOB	ALPHA
0	0.1306D+00	1.40E+00	1.00E-01	1.00E+00
1	0.1190D+00	3.46E+00	1.00E-01	1.00E-02
2	0.1190D+00	3.89E+00	1.00E-01	1.00E-02
3	0.1190D+00	3.89E+00	1.00E-01	1.00E-02

No further reduction in SSQ obtained, optimization stopped

Mass balance error in FE solution during final run was 0.0014 %

Correlation matrix

	1	2	3
1	1		
2	0	0	
3	-0.1993	0	1

Non-linear least-squares analysis: final results

Variable	Value	95% Confidence limits		
		S.E.Coeff.	Lower	Upper
DISPL	3.89E+00	7.74E-01	2.37E+00	5.41E+00
THIMOB	1.00E-01	1.98E-17	1.00E-01	1.00E-01
ALPHA	1.00E-02	2.96E+00	-5.81E+00	5.83E+00

Contributions to the final objective function

Measurement Set 4: 1.19E-01

RSQUARE for regression of predicted vs observed = 0.90811

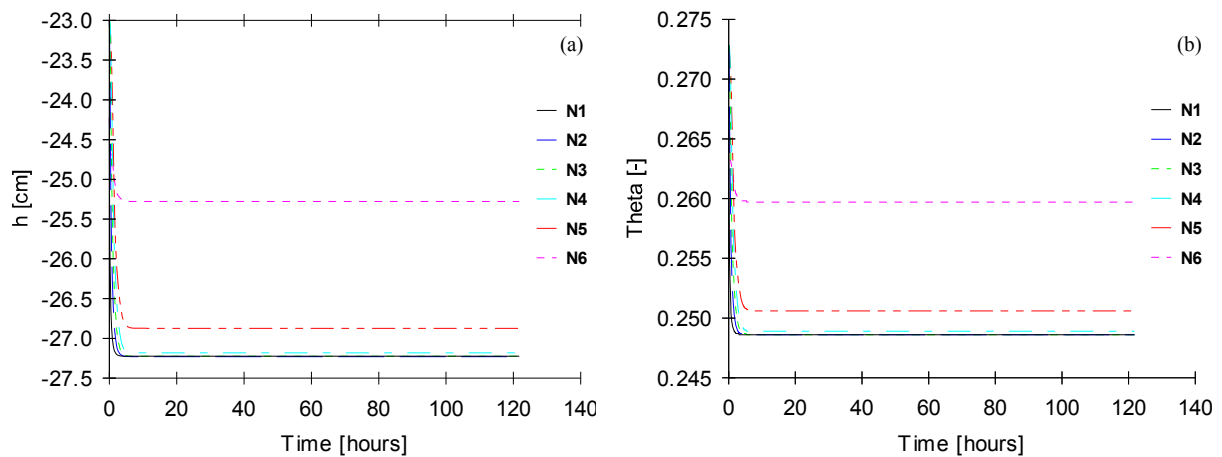


Figure 167. Simulated Pressure Heads (a) and Water Contents (b) for 60% of Saturation at 35°C (N1=Port 5, N2=Port 4, N3=Port 3, N4=Port 2, N5=Port 1, and N6=Port 0)

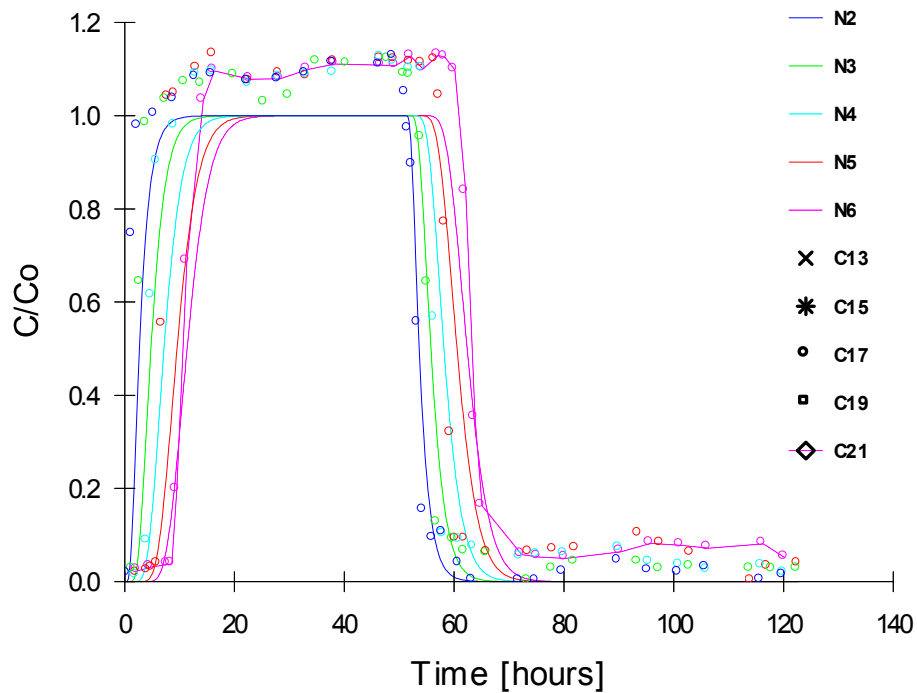


Figure 168. Measured vs Simulated Relative NaCl Concentrations Using Mobile-Immobile Model (MIM) for 60% of Saturation at 35°C (For Simulated Data: N2=Port 4, N3=Port 3, N4=Port 2, N5=Port 1, and N6=Port 0; For Experimental Data: C13=Port 4, C15=Port 3, C17=Port 2, C19=Port 1, and C21=Port 0)

Appendix J. Pressure and Temperature Sensors Wiring Diagram for Data Logger and Multiplexer

CR23X Wiring Diagram for Multiplexer.SCH
(Wiring details can be found in the help file.)

1H	AM16/32 (2x32 mode) COM ODD H	7H	VoltsDiff (6) High
1L	AM16/32 (2x32 mode) COM ODD L	7L	VoltsDiff (6) Low
Ground		Ground	
2H	VoltsDiff (1) High	8H	VoltsDiff (7) High
2L	VoltsDiff (1) Low	8L	VoltsDiff (7) Low
Ground		Ground	
3H	VoltsDiff (2) High	9H	VoltsDiff (8) High
3L	VoltsDiff (2) Low	9L	VoltsDiff (8) Low
Ground		Ground	
4H	VoltsDiff (3) High	10H	VoltsDiff (9) High
4L	VoltsDiff (3) Low	10L	VoltsDiff (9) Low
Ground		Ground	
5H	VoltsDiff (4) High	11H	VoltsDiff (10) High
5L	VoltsDiff (4) Low	11L	VoltsDiff (10) Low
Ground		Ground	
6H	VoltsDiff (5) High	12H	VoltsDiff (11) High
6L	VoltsDiff (5) Low	12L	VoltsDiff (11) Low
Ground		Ground	
G	VoltsDiff (1) Shield	Ground	
	VoltsDiff (2) Shield	EX1	
	AM16/32 (2x32 mode) Gnd	EX2	
	AM16/32 (2x32 mode) COM Ground	Ground	
3V		EX3	
G	VoltsDiff (3) Shield	EX4	
	VoltsDiff (4) Shield	Ground	
	VoltsDiff (5) Shield	CA01	
	VoltsDiff (6) Shield	CA02	
SW12		Ground	
G	VoltsDiff (7) Shield	P1	
	VoltsDiff (8) Shield	Ground	
	VoltsDiff (9) Shield	P2	
	VoltsDiff (10) Shield	Ground	
12V	AM16/32 (2x32 mode) 12V	P3	
12V		Ground	
G	VoltsDiff (11) Shield	P4	
C1	AM16/32 (2x32 mode) Res	Ground	
C2	AM16/32 (2x32 mode) Clk		
C3			
C4			
G			
C5			
C6			
C7			
C8			
G			

CR23X

1 Sensors 2 Wiring Diagram 3 Wiring Test

AM16/32 Multiplexer (2x32 mode) Wiring Diagram for Multiplexer.SCW
 (Wiring details can be found in the help file.)

1H	VoltsDiff (1) High	RES	CR23X C1
1L	VoltsDiff (1) Low	CLK	CR23X C2
Ground		GND	CR23X G
2H	VoltsDiff (2) High	12V	CR23X 12V
2L	VoltsDiff (2) Low	COM ODD H	CR23X 1H
Ground		COM ODD L	CR23X 1L
3H	VoltsDiff (3) High	COM Ground	CR23X G
3L	VoltsDiff (3) Low	COM EVEN H	
Ground		COM EVEN L	
4H	VoltsDiff (4) High	COM Ground	
4L	VoltsDiff (4) Low	13H	
Ground		13L	
5H	VoltsDiff (5) High	Ground	
5L	VoltsDiff (5) Low	14H	
Ground		14L	
6H	VoltsDiff (6) High	Ground	
6L	VoltsDiff (6) Low	15H	
Ground		15L	
7H	VoltsDiff (7) High	Ground	
7L	VoltsDiff (7) Low	16H	
Ground		16L	
8H	VoltsDiff (8) High	Ground	
8L	VoltsDiff (8) Low	17H	
Ground		17L	
9H	VoltsDiff (9) High	Ground	
9L	VoltsDiff (9) Low	18H	
Ground		18L	
10H		Ground	
10L		19H	
Ground		19L	
11H		Ground	
11L		20H	
Ground		20L	
12H		Ground	
12L			
Ground			
21H			
21L			
Ground			
22H			
22L			
Ground			
23H			
23L			
Ground			
24H			
24L			
Ground			
25H			
25L			
Ground			
26H			
26L			
Ground			
27H			
27L			
Ground			
28H			
28L			
Ground			
29H			
29L			
Ground			
30H			
30L			
Ground			
31H			
31L			
Ground			
32H			
32L			
Ground			

AM16/32